Electronic Theses and Dissertations

Theses, Dissertations, and Major Papers

6-29-2018

Failure Mechanisms in Tribological Coatings and Energy Materials Subjected to Different Environments and Temperatures

Guanhong Sun
University of Windsor

Follow this and additional works at: https://scholar.uwindsor.ca/etd

Failure Mechanisms in Tribological Coatings and Energy Materials Subjected to Different Environments and Temperatures

By

Guanhong Sun

A Dissertation

Submitted to the Faculty of Graduate Studies
through the Department of Mechanical, Automotive & Materials Engineering
in Partial Fulfillment of the Requirements for
the Degree of Doctor of Philosophy
at the University of Windsor

Windsor, Ontario, Canada

2018

Failure Mechanisms in Tribological Coatings and Energy Materials Subjected to

Different Environments and Temperatures

by

Guanhong Sun

APPROVED BY:

_____
S. Park, External Examiner
University of Calgary

_____
D. Green
Department of Mechanical, Automotive & Materials Engineering

_____
H. Hu
Department of Mechanical, Automotive & Materials Engineering

_____
V. Stoilov
Department of Mechanical, Automotive & Materials Engineering

_____
A. Alpas, Advisor
Department of Mechanical, Automotive & Materials Engineering

June 8, 2018

DECLARATION OF CO-AUTHORSHIP/PREVIOUS PUBLICATION

I. Co-Authorship

I hereby declare that this dissertation incorporates documentation of research performed by the author under the supervision of Prof. Ahmet T. Alpas. Mr. B. McClory (General Motors Powertrain) and Mr. D. R. White (General Motors Powertrain) assisted in obtaining samples and provided insights into impact of experimental results in Chapter 2 and 3. The experiments in Chapters 4-6 were performed in collaboration with Dr. S. Bhowmick (University of Windsor). The experiments and analysis in Chapters 7 were performed in collaboration with Dr. S. Bhattacharya (University of Windsor).

I am aware of the University of Windsor Senate Policy on Authorship and I certify that I have properly acknowledged the contribution of other researchers to my thesis, and have obtained written permission from each of the co-author(s) to include the above material(s) in my thesis.

I certify that, with the above qualification, this thesis, and the research to which it refers, is the product of my own work.

II. Previous Publication

This thesis includes 6 original papers that have been previously published/to be submitted for publication in peer reviewed journals, as follow:

Chapter	Publication title/full citation	Publication status
2	G. Sun, D. R. White, B. McClory, A. T. Alpas, Fracture Behaviour and Toughness Measurement of Thermal Spray Coatings by In-situ Observation of Bending Tests, Materials Science and Engineering: A	To be submitted

3	G. Sun, S. Bhattacharya, D. R. White, B. McClory, A. T. Alpas, Indentation fracture behaviour of low carbon thermal spray coatings: Role of dry sliding-induced tribolayer, Materials Science and Engineering: A	To be submitted
4	S. Bhowmick, G. Sun, A. T. Alpas, Low friction behaviour of boron carbide coatings (B4C) sliding against Ti–6Al–4V, Surface and Coatings Technology, 307 (2016) 316-327.	Published
5	G. Sun, S. Bhowmick, A. T. Alpas, Effect of Atmosphere and Temperature on the Tribological Behavior of the Ti Containing MoS2 Coatings Against Aluminum, Tribology Letters, (2017) 65:158. https://doi.org/10.1007/s11249-017-0934-5	Published
6	G. Sun, S. Bhowmick, A. T. Alpas, Boundary Lubricated sliding behaviour of Ti containing MoS2 coatings against an aluminum alloy, Tribology Letters.	To be submitted
7	G. Sun, S. Bhattacharya, A. T. Alpas, Cyclic strain-induced crack growth in graphite during electrochemical testing in propylene carbonate-based Li-ion battery electrolytes, Journal of Material Science, 53 (2018) 1297-1309.	Published

I certify that I have obtained a written permission from the copyright owners to include the above published materials in my thesis. I certify that the above material describes work completed during my registration as a graduate student at the University of Windsor.

III. General

I declare that, to the best of my knowledge, my thesis does not infringe upon anyone's copyright nor violate any proprietary rights and that any ideas, techniques, quotations, or any other material from the work of other people included in my thesis, published or otherwise, are fully acknowledged in accordance with the standard referencing practices. Furthermore, to the extent that I have included copyrighted material that surpasses the bounds of fair dealing within the meaning of the Canada Copyright Act, I certify that I have

obtained a written permission from the copyright owners to include such materials in my thesis.

I declare that this is a true copy of my thesis, including any final revisions, as approved by my thesis committee and the Graduate Studies office, and that this thesis has not been submitted for a higher degree to any other University or Institution.

ABSTRACT

The objective of this research is to develop advanced material characterization and mechanical testing methods for C-, Mo- based and ferrous tribological coatings to be used in lightweight engines, and manufacturing of lightweight materials. These new characterization methods are also applied to the investigation of damage processes in energy materials, namely to investigate degradation in C- based electrodes used in Li-ion batteries. Evaluations of the damage mechanisms in these materials under static and sliding contact stress conditions, as well as under different environments and temperatures encountered under the actual service conditions create several challenges. Accordingly, an in-situ mechanical testing set-up was developed to study the fracture behaviour of coating materials under different strain gradients simulating sliding contact and voltage gradients stimulating lithium batteries' operation conditions.

Thermal spray low carbon steel coatings were used for mass reduction in powertrains to replace iron liners. The crack initiation and propagation processes were captured and fracture mechanisms were delineated. Cracks were formed at oxide layers, whose propagation behaviour were described by a mixed mode I and mode II with stress intensity factors K_I and K_{II} used to determine the crack propagation direction. According to the experimental results, new guidelines for the coating design consisting of distribution, angle and length of oxide stringers were proposed for optimization of the coatings' fracture resistance. Dry wear tests were performed on the coatings to simulate the oil starvation condition in combustion engines. The tribolayer formed acted as an energy-absorbing entity and reduced the driving force necessary for FeO stringer separation in the low carbon coating.

Wear maps for these Ti-MoS$_2$ and B$_4$C coatings along with the DLC were constructed as a function of temperature and for different environments, and these maps provided engineering guidelines for optimization of the working conditions of these coatings. MoS$_2$ coatings exhibited

low coefficient of friction (COF) when sliding against aluminum, however, their COF showed high sensitivity to moisture. A MoS_2 transfer layer was formed on the counterface and maintained low wear rate and low COF (<0.1) throughout the temperature range from 25 to 400 °C in an oxygen free environment (dry N_2). C- based coatings namely B_4C were subjected to sliding tests under different environments. In high humidity atmospheres where sliding induced graphitization occurred --as observed by Raman, FTIR and XPS--the passivation of graphitized tribolayers maintained a low COF for B_4C. An increase in the humidity from 25% to 85% RH resulted in reduction of COF to 0.18. The lowest COF values of 0.07 were achieved in iso-propyl alcohol as the OH- radicals passivated the surfaces.

Lithiation/de-lithiation cycles induced cracks in isostatically pressed graphite electrode and reduced the capacity of lithium battery. The crack-growth rate, da/dt, depended on the stress intensity factor at the crack tip and could be expressed as $da/dt = A\Delta K_I^n$. A two-stage crack-growth behaviour was determined with n=51.3 in the first stage and n=9.9 in the second stage. The reduction of ΔK to ΔK_{eff} and reduced the crack-growth rates in the second stage are caused by a rough crack face morphology and generation of thick solid electrolyte reduction products on the crack flanks resulted in premature closing of cracks, indicating the battery performance degradation could be slowed down by this phenomenon.

From a practical point of view, by exploring the failure mechanisms and tribological properties of thermal spray coatings, the work presented in this dissertation has provided guidelines for designing stable and wear resistant microstructures. For C- and Mo- based coatings, operating temperatures and environment conditions were determined to help with establishing processing windows for manufacturing applications. Battery electrodes for energy applications, selections of electrolytes and electrode materials for a longer life time were suggested.

DEDICATION

I dedicate this work to my parents,

Mr. Zhongqiu Sun and Mrs. Yubin Wang

and

my family and close friends.

Thank you for your unconditional love and constant support.

ACKNOWLEDGEMENTS

TABLE OF CONTENTS

LIST OF TABLES

LIST OF FIGURES

LIST OF ABBREVIATIONS/SYMBOLS

Abbreviations

ASTM American Society for Testing and Materials

BS-SEM Back Scattered Scanning Electron Microscopy

COF Coefficient of friction

CV Cyclic Voltammetry

CVD Chemical vapour deposition

DLC Diamond-like Carbon

E* Composite elastic modulus between two bodies

EDS Energy Dispersive X-ray Spectroscopy

FFT Fast Fourier Transform

H-DLC Hydrogenated DLC

NH-DLC Non-hydrogenated DLC

ORL Oil-residue layer

PTWA Plasma Transferred Wire Arc

PVD Physical vapour deposition

SEM Scanning electron microscope

TCR Top compression rings

WT Wear Track

XPS X-ray Photoemission Spectroscopy

ZDDP Zinc Dialkyl-DithioPhosphate

Symbols

K_I Mode I stress intensity factor

K_{II} Mode II stress intensity factor

K_{III} Mode III stress intensity factor

K_{IC} Fracture toughness

α Viscosity constant of lubricating oil

λ Film thickness ratio

μ_R Average steady state coefficient of friction

μ_S Maximum running-in coefficient of friction

h_{min} Lubrication film thickness

r* Composite surface roughness of two contacting bodies

a.u. Arbitrary units

CHAPTER 1
RESEARCH BACKGROUND

1.1   Background and Motivation

In order to alleviate the negative effects of global warming and energy shortage problems, it is necessary to reduce energy consumption and greenhouse gas emissions. The automotive industry is one of the industrial sectors that must reduce atmospheric emissions and fuel consumption because government regulations have been introduced that mandate the improvement of fuel efficiency. The Energy Independence and Security Act of 2007 increased the Corporate Average Fuel Economy (CAFE) standard by 40% for new vehicles, which must be met by 2020 [1, 2]. To address this, automotive engineers and researchers have focused on three approaches to reducing the energy consumption and emissions: reducing the engine frictional energy losses in traditional internal combustion engines by the application of the tribological coatings, trimming down the weight of the vehicles by using lightweight materials, and using lithium batteries and developing hybrid powertrains to improve energy efficiency.

The word "tribology" was first introduced by Jost [3], and refers to the science and engineering methods that focus on the friction, lubrication, and wear of interacting surfaces. Friction causes energy loss, while wear is the cause of material wastage and degradation of mechanical performance. It is estimated that friction causes one-third of the world's energy resources. Usually, the objective of tribology is to reduce the friction and wear between the surfaces contact as shown in **Figure 1.1**.
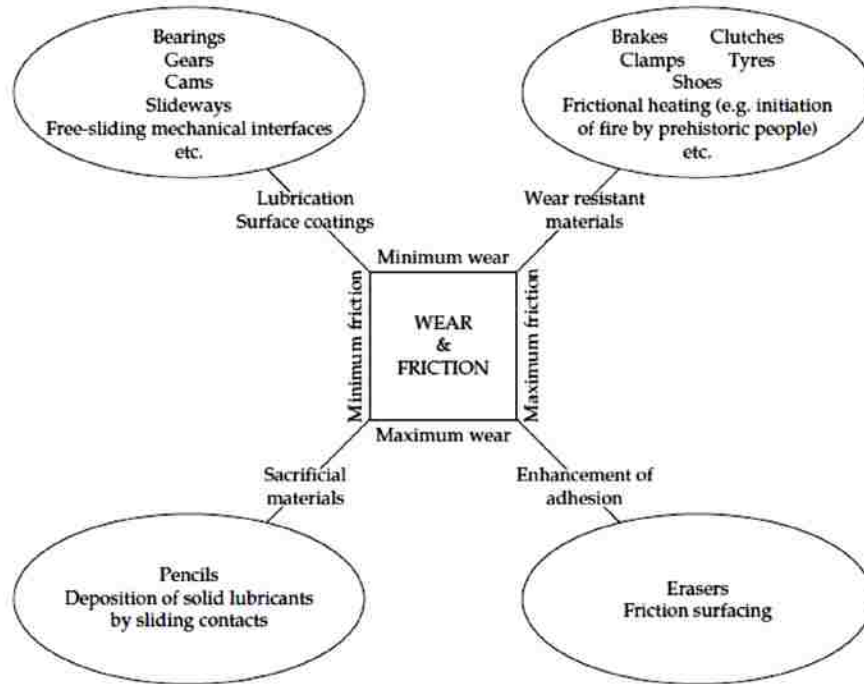
Figure 1.1 Research prospects and practical applications of tribology [4].

In the automotive industry, significant research has focused on the decrease of the friction in vehicle components. As shown in **Figure 1.2**, data compiled by Anderson [5] demonstrates that only 12% of the available energy in the fuel finally reaches the driving wheels, with about 15% being dissipated as friction loss [6]. Based on the fuel consumption data presented, a 10% reduction in mechanical losses would lead to a 1.5% reduction in fuel consumption. **Figure 1.3** shows the energy consumption distribution within the engine, where friction losses occupy 48% of the overall energy consumption developed [7]. By addressing and solving tribological problems within the automotive systems, especially in powertrain parts, effective strategies can be developed that reduce the energy consumption.
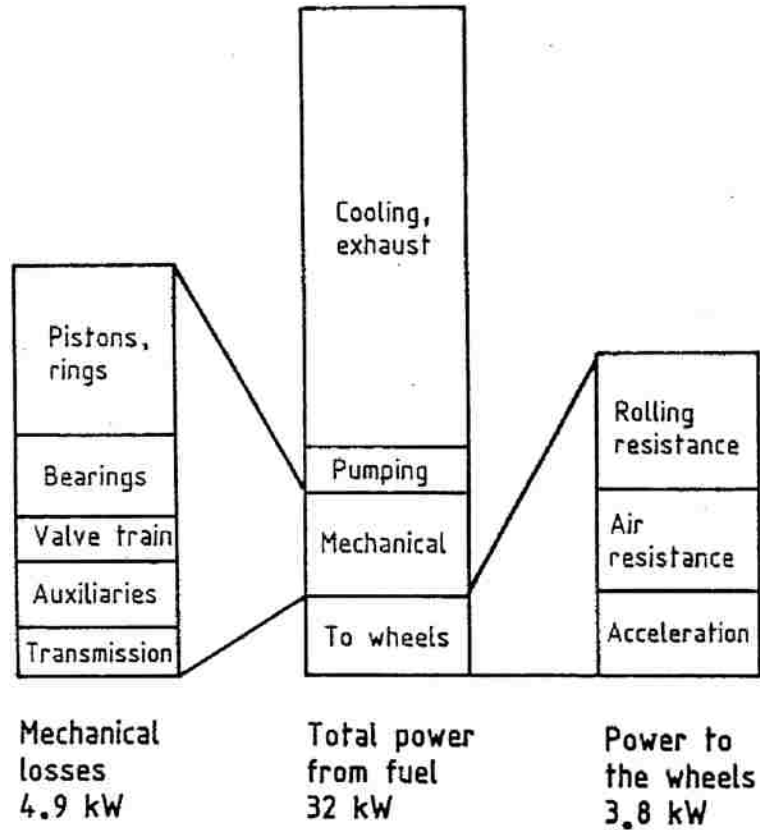
Figure 1.2 Fuel energy distribution for a medium size passenger car during an urban cycle [5].
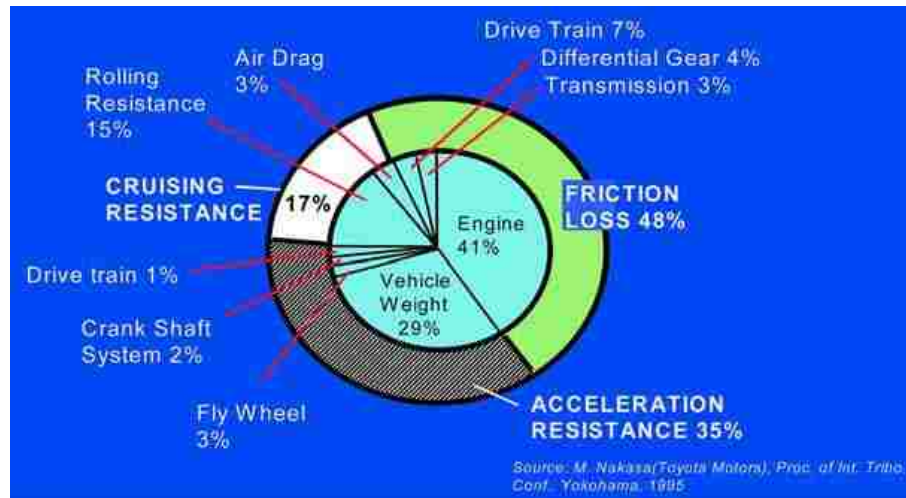
Figure 1.3 Energy consumption developed in an engine [7].

Diamond-like carbon coatings (DLC) typically display low coefficient of friction (COF) and high wear resistance, and because of these tribological properties, they have been used as friction reducing coatings for automotive applications, albeit to a limited extent. Konca et al. [8-10] studied the friction behaviour of non-hydrogenated DLC (NH-DLC, less than 2% H) coatings sliding against Al, Mg and Ti alloys under different environments and temperatures. A low COF of 0.015 was found in a H_2 atmosphere, and low COF of 0.12 was obtained in ambient air with 40% RH for NH-DLC sliding against Al alloy. During the sliding contact, the coating transferred to the counterface forming a tribolayer. The dissociation of H_2/H_2O then reacted with the tribolayer: this is called passivation and is a mechanism that maintains the low COF of NH-DLC coatings. Abou Gharam et al. [11] examined the effect of oxygen and humidity on the wear behaviour of NH-DLC coatings and found that oxidation would occur on the NH-DLC coating. This resulted in a high COF of 0.35 under dry oxygen atmosphere, whereas with 45%RH under an oxygen atmosphere, the COF was reduced to 0.12 due to the effect of passivation.

Abou Gharam et al. [12] also explored the high temperature tribological performance of tungsten doped DLC (W-DLC) coating. They found a low COF of 0.12 at 400 ºC because of the formation of WO_3 tribolayer. Since the use of ethanol based bio-fuels reduces greenhouse and polluting gas emissions, Banerji et al. [13, 14] studied the wear behaviour of DLC coatings with E85 fuel (85% ethanol and 15% gasoline). Banerji et al. studied wear behaviour of Ti-MoS_2 coatings, and found the transferlayer maintained a COF of 0.05 at 200 ºC [15]. This type of fundamental work is needed to provide guidelines when determining which tribological coatings and lubricants are suitable in different environments and temperatures. The current study seeks to contribute to these efforts for the improvement of fuel economy and emission reduction for automotive and other applications.

Decreases in fuel consumption and greenhouse gas emissions could also be accomplished by reducing the weight of vehicles. To this end, Al-Si alloys are already being used as engine block

material [16, 17]. Wear mechanism maps and wear transition maps were constructed for Al-Si alloys and Al-Si alloy based composite materials [18, 19], although most of these engines use cast iron liners for wear protection. Edrisy et al. [20] examined the effect of load and velocity on the plastic deformation, heat localization and wear rates, as well as the mechanism that control the wear behaviour of Al-Si alloys. The silicon particles in eutectic/hypereutectic Al-Si alloys were found to act as load bearing elements during sliding contact, and can be used as linerless engine blocks. Chen et al. [21-23] summarized that there are three stages of ultra-mild wear regimes for hypereutectic Al-Si sliding against AISI 52100 steel: the sinking of silicon particles, the wear of the aluminum matrix, and the formation of a stable oil residue layer. However, hypoeutectic Al-Si alloys, which have a Si<10 %, are prone to wear damage. Thus, either iron liners or new protective coatings such as thermal spray coatings are needed for the contact surface of hypoeutectic Al-Si cylinder bores.

Furthermore, during the manufacturing processes of lightweight alloys, high local temperatures and high stress can cause adhesion and wear damage to the machining tools, resulting in short tool life times and increased manufacturing costs. Advanced coatings like DLC, Ti-MoS$_2$, and B$_4$C could be employed on machining tools to reduce these problems [24-26]. In addition, MoS$_2$ coatings have extremely low COF in high vacuum, oxygen free environments. Thus, the low COF of MoS$_2$ coatings could be maintained up to 400 ºC. These features make them excellent in aerospace applications such as bearings and wheels coatings [27, 28]. A successful application of these coatings could make vehicles more lightweight. This thesis contributes to these efforts by investigating the wear behaviour of these coatings under different environments and temperatures.

The third approach in energy savings in vehicles is to uses hybrid vehicles with lithium batteries to assist with the traditional combustion engines. Lithium ion batteries have highly efficient electrochemical energy storage ability. C-based electrodes (anodes) are widely used in lithium batteries; however, the capacity of the batteries decreases with the number of

charging/discharging cycles. The lithium-ion-intercalation-induced strains cause damage to the anode during the first few cycles. Electrolyte deposition products also form and are responsible for the capacity fading [29-31]. Currently, no optimum material design method exists to make selections for durable and high capacity anodes. Nevertheless, some works have examined new materials for the anode. Sn and Si are good candidates as anode materials. Si has a high capacity of 4200 mAh/g, though it suffers from a volume expansion of 400%, which results in mechanical damage [32-34]. Bhattacharya [35, 36] studied the performance of Si-Al anodes in different electrolyte compositions and voltage scan rates. It was found that the Al surrounding Si particles served to arrest the crack at Al/Si interface. The electrochemical capacity changes of Sn-carbon fibre composite anode were also examined, and a higher capacity was observed for Sn-carbon composite than bulk Sn electrodes [37]. Bhattacharya [38, 39] also found a pre-treatment with Li_2CO_3 particles containing aqueous solution could effectively reduce the capacity fading problem. The details of lithium batteries will be reviewed in section 1.4. However, a direct measurement of damage and crack growth rate for lithium battery anode has not been performed. Direct crack growth rate measurement focusing on the capacity reduction mechanism of widely used graphite anodes will provide fundamental information for improving current battery performance.

The overall goal of the current study is to develop advanced material characterization and mechanical testing methods for C-based, Mo-based and ferrous tribological coatings to be used in lightweight engines and in the manufacturing of lightweight materials. These new characterization methods are also applied to the investigation of damage processes in energy materials, namely to investigate degradation in C-based electrodes used in Li-ion batteries. Evaluation of the damage mechanisms in these materials under static and sliding contact stress conditions, as well as under different environments and temperatures encountered under actual service conditions, will contribute to friction reduction, effective machining of lightweight materials, and battery electrodes with higher capacity and extended life cycle. By examining the failure mechanisms and tribological

behaviours of these materials, a guideline on utilizing these materials to achieve less energy consumption and greenhouse gas emission automotive systems could be developed.

In sections 1.2 and 1.3, tribological materials, mechanical properties and measurements and environmental effects on tribological behaviours will be introduced. Section 1.4 will discuss the mechanisms of graphite electrode lithium battery including the intercalation, anode material selection, and capacity-fading phenomenon.

1.2   Tribological Coatings for Lightweight Materials

New coatings have been designed to achieve better lubricity and longer wear life in demanding tribological applications [40]. They include coatings produced by thermal spray, physical vapour deposition (PVD), and chemical vapour deposition (CVD) processes [41].

The thermal spray steel coatings that are being considered by automotive manufacturers are built up particle by particle, resulting in the formation of coatings with highly anisotropic layered structures [42]. PVD techniques—such as magnetron sputtering, cathodic arc deposition and electron beam physical vapor deposition—are widely used for thin, hard films in the manufacturing of machining tools [43, 44]. The coating material is vaporized from a solid or liquid source in vacuum or under low pressure gases and then condenses to the substrate to form the coating. CVD, involves occurrence of chemical reactions in the vapor phase. The products of these reactions condense onto the substrate to form the coating [45]. Typical applications of CVD coatings are producing SiO_2 for the semiconductor industry, synthesis of graphene and DLC coatings for manufacturing, and automotive applications [46].

Among PVD and CVD coatings, DLC coatings are particularly important as they have low COF and high wear resistance. They also mitigate adhesion of light metals to the counterfaces. DLC coatings typically consist of a mixture of sp2 and sp3 types of C bonds [47]. Depending on

7

the hydrogen content, they can be divided into two groups: hydrogenated DLC (H-DLC) with about 40 at.% hydrogen and non-hydrogenated DLC (NH-DLC) with <2 at.% hydrogen). These two groups have different tribolayer formation and passivation mechanisms during sliding; therefore, they have different responses to the environmental changes, especially to the moisture when used in tribological applications [8, 48, 49].

MoS$_2$ coatings have low COF because their layered structure is like graphite [50]. During sliding, the MoS$_2$ coating can be readily transferred to the counterface and forms a transfer layer to reduce friction. The COF of MoS$_2$ could be maintained at a low and stable level until 400 °C in oxygen free environments [51]. However, the moisture could damage the layered structure of MoS$_2$ coatings cause an increase in the COF [15, 27, 52, 53]. Thus, the environmental factors and dissociative absorption of water molecules should be taken into account [54, 55] because the tribological behaviour of layered materials does not depend only on "easy shear" mechanisms [56, 57], as has been commonly suggested.

Boron carbide (B$_4$C) is a widely used ceramic with a high hardness, high elastic modulus, and high melting point [58]. More importantly, the passivation of carbon causes it to have low adhesion to titanium. High hardness (~29 GPa) and low adhesion make B$_4$C an ideal candidate for titanium machining [59]. The hardness could also remain constant up to 1000 °C while maintaining a relatively low COF [60].

The current study explores thermal spray ferrous coatings with compositions similar to those of low carbon steel (0.1% C and 0.3% C). Internal combustion engines made from hypoeutectic Al-Si alloys with Si content less than 10 wt% suffer from scuffing failure [17, 61, 62]. Thermal spray coatings have higher hardness than the Al-Si substrate, and the coating is normally much thinner than iron liners. Therefore, thermal spray coatings are being developed to replace iron liners to further reduce the weight of the engines [63-67]. In thermal spray coatings, oxide layers, cracks,

and porosities delineate the unique microstructure, and the mechanical and wear tests established correlations between these microstructural features and their performance [68, 69].

1.2.1 Thermal Spray Cylinder Bore Steel Coatings

Lightweight materials such as Al-Si are replacing cast iron in the production of engine blocks, resulting in approximately 30% mass reduction [70]. Hypoeutectic Al-Si alloys with 6-8wt% Si suffer from low wear resistance when the piston rings blocks come into contact with the engine block cylinder wall, whereas hypereutectic Al-Si alloys are wear-resistant hard to machine [23]. Cast iron liners are the traditional option. However, the increased weight and local heat transfer may increase fuel consumption, emissions, and manufacturing costs. Ferrous thermal spray coatings with a lower weight (much thinner than iron liners), high hardness (~3 GPa) and better tribological performance can be used as a replacement for iron liners [63, 64]. **Figure 1.4** shows thermal spray plasma transferred wire arc (PTWA) coating being applied to cylinder bores of a BMW M62 engine [71].

Figure 1.4 PTWA coating of the bores of a BMW M62 gasoline engine [71].

An additional benefit of the thermal spray technology is that it is an economical method, as this process does not require a controlled environment or vacuum deposition like PVD process [72]. It is also possible to coat large surface areas and curved surfaces. Plasma-sprayed ceramic coatings have been widely used for many applications in order to improve resistance to wear, corrosion, oxidization, erosion, and heat [73, 74]. During plasma spraying process, a layer is formed on a substrate surface by spraying melted or partially melted powders at a high speed using a high temperature plasma heat source, which can reach 10,000 K. **Figure 1.5** shows a typical microstructure of thermal spray coatings incorporated pores, oxide and unmelted particles [75].
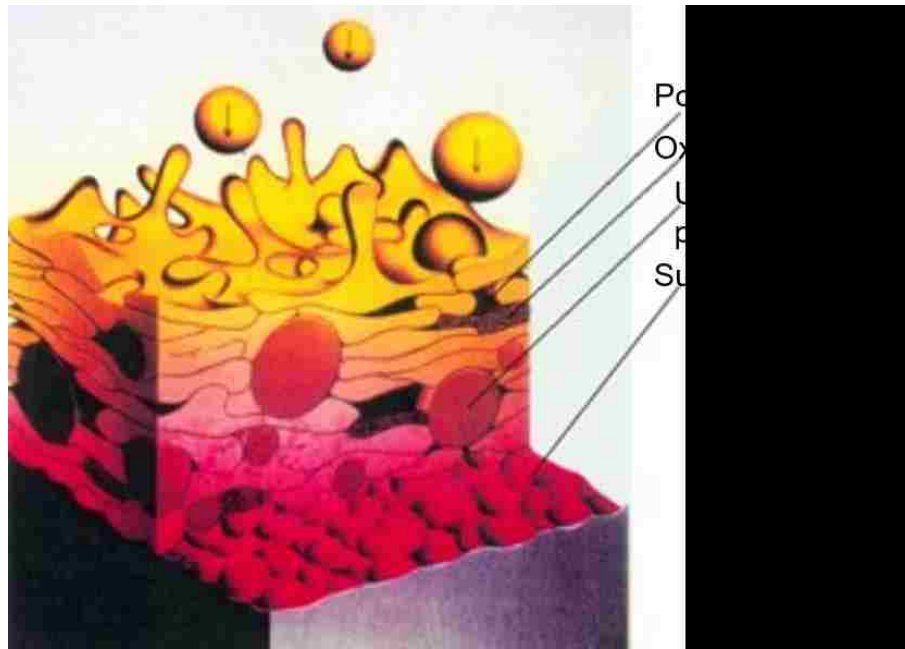
Figure 1.5 Classical microstructure of thermal spray coatings [75].

The PTWA process is a common spray deposition technique and uses a spray jet in rotational motion that goes up and down inside a cylinder bore. The schematic of PTWA system is shown in **Figure 1.6** [71]. The feed stock materials are in a wire form [76], and the coatings deposited using thermal spray technique have a lamellar structure consisting of iron splats, which results from flattening of molten metal droplets as they hit the surface and the separated by iron oxide (FeO) stringers [77]. Few studies in the past have investigated the failure mechanisms of the ferrous coatings deposited by PTWA. Wedge impression tests [77-79] have been used to investigate failure mechanisms of thermal spray thermal barrier coatings. The low fracture toughness of the interfacial oxide could cause splat delamination. The delamination of the coating increases the rate of wear debris production and may lead to the scuffing of the coating [63].

11
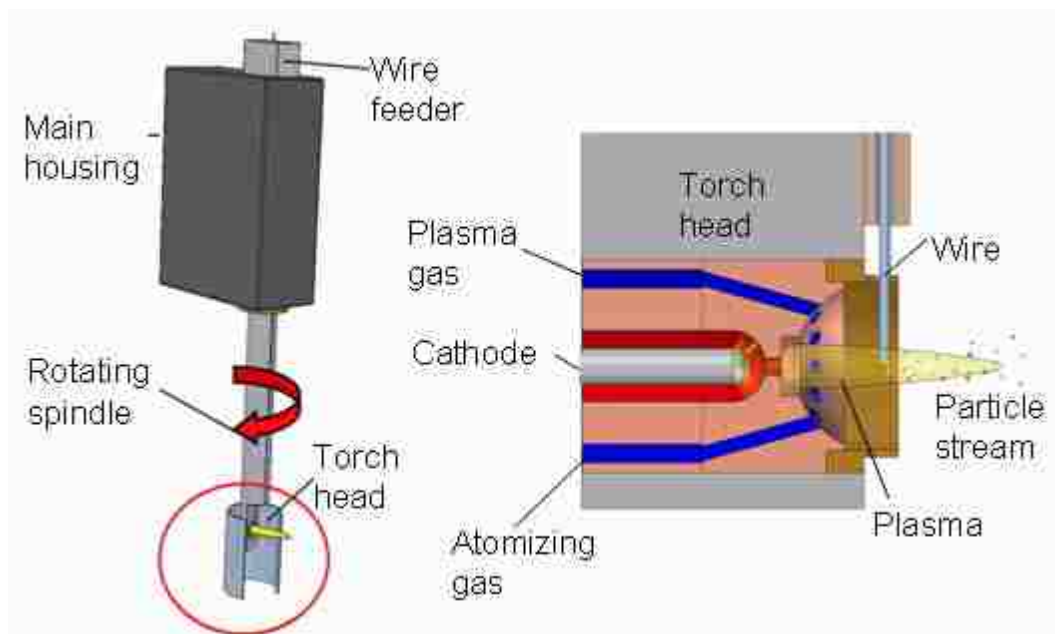
Figure 1.6 Schematics of the PTWA system and the torch head [71].

As the thermal spray coating has a unique lamellar microstructure that incorporates oxide layers, [80, 81] these layers act both as potential crack propagation paths and as crack barriers, depending on their orientation in the coating. The fracture mechanism of the coating is therefore complex due to the variations of these oxide layers.

Faisal et al. [82] performed Vickers indentations on different thermal spray coatings, and measured surface crack lengths, classifying them into three types: radial, edge, and other cracks. Accordingly, Faisal et al. proposed a model based on different types of cracks to determine fracture toughness of thermal spray coatings. The prevalence of radial, edge and surface cracks were ranked, then the total surface crack length was used to determine the fracture toughness of thermal spray coatings. Lin and Berndt [83] have summarized four different methods that have been used to measure the adhesion of thermal spray coatings: the tensile adhesion test, scratch test, indentation test, and the bending test. Howard and Clyne [84] measured the interfacial fracture toughness of thermal spray titanium coatings by using a notched four point bending specimen. An artificially introduced crack at the interface was caused to propagate under the four-point bending

arrangement. Afterwards, interfacial fracture energy and critical stress intensity factor were evaluated from the load-displacement data. Rabiei [77] performed wedge impression tests on thermal spray ferrous coatings with a WC wedge indenter. K_I fracture toughness < 1 MPa·m$^{1/2}$ was measured, indicating a weak interface between oxides and α-Fe in the coating.

High velocity oxygen fuel (HVOF) is another process of thermal spray. Fuel and oxygen are fed into the chamber, which generates the high pressure to accelerate the feeding powders up to 800 m/s [85]. Edrisy and Alpas [65] studied the microstructure and wear resistance of HVOF and PTWA thermal spray coatings. It was found that in dry sliding conditions, the surface oxidation and oxide fracture were the wear mechanisms controlling the wear rate. The coating with higher initial iron oxide was prone to having a higher surface temperature in wear contact, which promoted surface oxidation. Edrisy and Perry [66] investigated the scuffing damage to the HVOF thermal spray coating, concluding that the delamination of the tribolayers was the primary mechanism for scuffing damage. Furthermore, they [64] studied the effect of humidity on the wear behaviour of PTWA coating; lower wear rates were found at high humidity for all loading conditions. Due to high humidity, the metallic contact areas were smoother resulting in less surface damage and splat fracture. Edrisy et al. [66] also found that the delamination of tribolayers consisting of deformed nanocrystalline grains was the primary source of material removal during scuffing.

1.2.2   Carbon Based Coatings-DLC Coatings

Graphite as a common form of carbon material has a layered structure [86]. As shown in **Figure 1.7**, it has a hexagonal, ABAB layer stacking (2H) with c=6.70 $\mathring{A}$, and a= 2.46 $\mathring{A}$. The strong covalent bonds connect atoms in the basal planes, while weak Van der Waals cohesive forces connect the basal planes. This means that, the basal planes will slide over one another under shear force. The adhesion between the basal planes is small due to the low surface energy [52, 87, 88]. Buckley [88] confirmed that when graphite slides against metallic surfaces in high vacuum, it will

create a low COF. However, when the basal planes are damaged, the high energy lamellar sites are exposed, causing adhesion and resulting in increase of COF. The low COF will be maintained when these high energy sites are passivated by water or other vapors [89, 90].
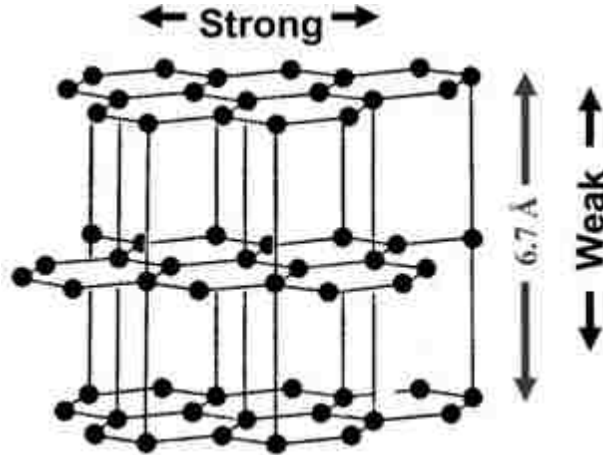
Figure 1.7 Lamellar crystal structure of graphite [89].

Carbon can be used in the synthesis of numerous hard coatings, including diamond, DLC, carbon nitride, transition metal carbides and boron carbide [91]. DLC is a metastable form of amorphous carbon containing some fraction of sp^3 bonds combined with sp^2 bonds [92]. It can have a high mechanical hardness, chemical inertness, and optical transparency, and it is a wide band gap semiconductor. DLC coatings have widespread applications as protective coatings in areas such as optical windows, magnetic storage disks, car parts, biomedical coatings and micro-electromechanical devices (MEMs) [93]. Because of low friction and high wear resistance, these coatings have attracted interest in recent years from both the industrial and scientific communities, and their friction and wear properties have been the subject of numerous scientific studies [94]. The application of suitable DLC coatings in automotive parts such as piston coatings have the potential to reduce the friction and energy consumption [95].

Carbon forms a large variety of crystalline as well as disordered structures because it is able to exist in three hybridization states: sp^3, sp^2 and sp^1. The extreme physical properties of diamond

derive from its strong, directional σ bonds. Diamond has a wide 5.5 eV band gap, the largest bulk modulus of any solid, the highest atom density, the largest room temperature thermal conductivity, smallest thermal expansion coefficient, and largest limiting electron and hole velocities of any semiconductor. Graphite has strong intra-layer σ bonding and weak Van der Waals bonding between its layers.

Figure 1.8 classifies various coatings with respect to their hardness and friction characteristics and shows that most carbon films are capable of providing not only high hardness but also low friction [96]. In **Figure 1.8**, a-C stands for amorphous carbon DLC, a-C:H is hydrogenated DLC and "nc-coatings" means nanocrystalline coatings. In particular, DLC films appear to provide the broadest range of hardness and friction values, while some of the recently developed nanocomposite coatings are able to provide superhardness but lack lubricity or low friction. [97]
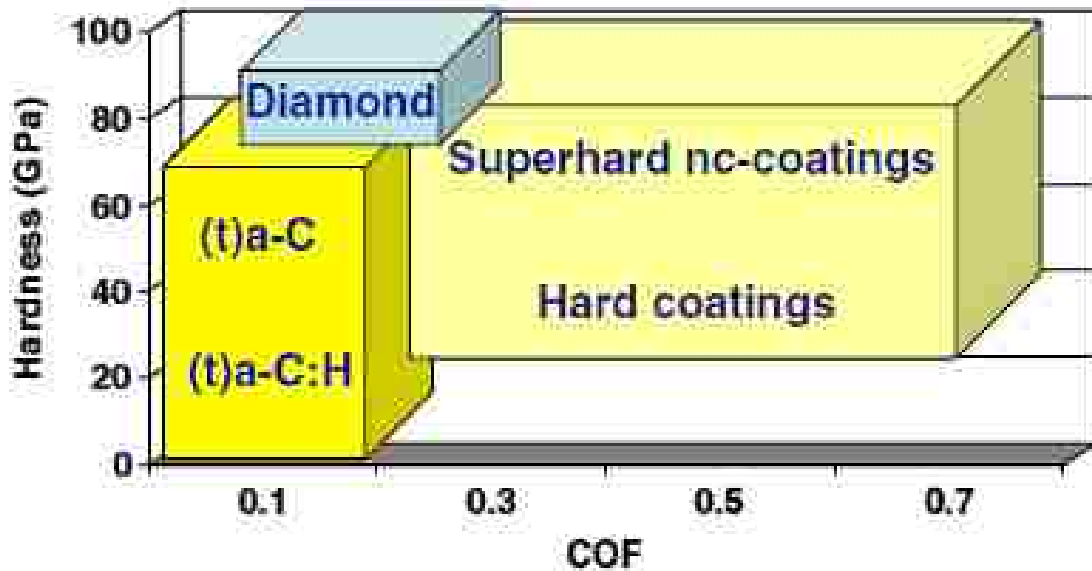
Figure 1.8 A schematic representation of hardness and coefficients of friction (COF) of carbon-based and other hard coatings [96].

Typical properties of the various forms of DLC are compared to diamond and graphite in

Table 1.1.

Table 1.1 Comparison of major properties of amorphous carbons with those of reference materials diamond, graphite, C60 and polyethylene [98].

	sp^3 (%)	H (%)	Density $(g \cdot cm^{-3})$	Gap (eV)	Hardness (GPa)
Diamond	100	0	3.515	55	100
Graphite	0	0	2.267	0	-
C60	0	0		1.6	-
Glassy C	0	0	1.3-1.55	0.01	3
Evaporated C	0	0	1.9	0.4-0.7	3
Sputtered C	5	0	2.2	0.5	-
ta-C	80-88	0	3.1	2.5	80
a-C:H hard	40	30-40	1.6-2.2	1.1-1.7	10-20
a-C:H soft	60	40-50	1.2-1.6	1.7-4	<10
ta-C:H	70	30	2.4	2.0-2.5	50
Polyethylene	100	67	0.92	6	0.01

The sp^3 bonding of DLC confers on it many of the beneficial properties of diamond itself, such as its mechanical hardness, chemical and electrochemical inertness, and wide band gap. DLC consists of both the amorphous carbons (a-C) and the hydrogenated alloys, a-C:H. **Figure 1.9** displays the compositions of the various forms of amorphous C-H alloys on a ternary phase diagram as in which was developed by Robertson [93]. There are many a-Cs with disordered graphitic ordering, such as soot, chars, glassy carbon, and evaporated a-C, featured in the lower left-hand corner of **Figure 1.9**. The two hydrocarbon polymers polyethylene $(CH_2)_n$ and polyacetylene $(CH)_n$ define the limits of a triangle in the right hand corner of **Figure 1.9**, beyond which only molecules can, meaning that C-C networks cannot. Deposition methods have been developed to produce a-Cs

with increasing degrees of sp^3 bonding. Sputtering can extend from sp^2 bonding some way towards sp^3 bonding. When the fraction of sp^3 bonding reaches a high degree, McKenzie [99] suggests that the a-C should be denoted as tetrahedral amorphous carbon (ta-C) in order to distinguish it from sp^2 a-C. Plasma enhanced chemical vapour deposition (PECVD), which produces a-C:H, is able to reach into the interior of the triangle. Although diamond-like, **Figure 1.9** demonstrates that the content of sp^3 bonding is actually not so large but that its hydrogen content is. Thus, Weiler [98] refers to a more sp^3 bonded material with less hydrogen, which can be produced by high plasma density PECVD reactors, as a hydrogenated tetrahedral amorphous carbon (ta-C:H).
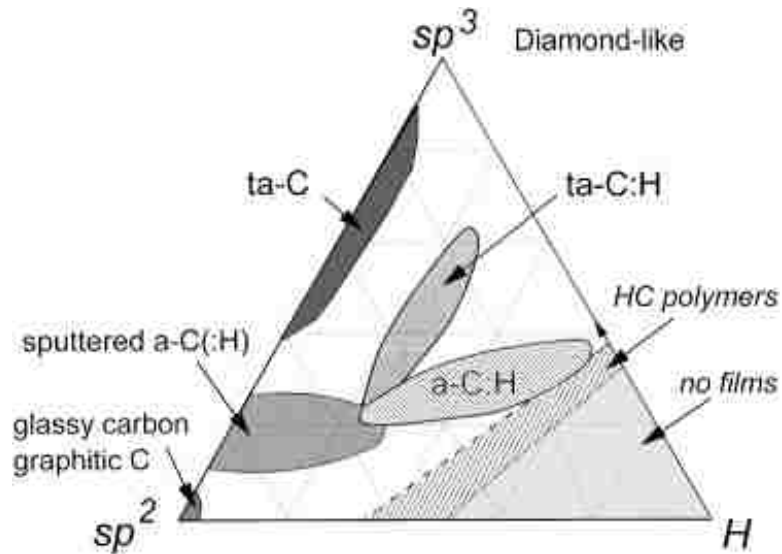
Figure 1.9 Ternary phase diagram of bonding in amorphous carbon–hydrogen alloys [93].

Figure 1.10 presents the Raman-spectra of the DLC-systems. When using the analysis method presented by Ferrari and Robertson [100], the ratio between the D- and the G-peaks (I(D)/I(G)-ratio) of all samples with a Bias voltage between 100 and 150 V is similar and the G-peak positions are between 1545 and 1597 cm^{-1}. The resolution of the graph does not allow it to determine an influence of the changing Bias voltage between 100 and 150 V. Compared to non-hydrogenated DLC-layer processed with a Bias voltage of 25 V, the G-peak position of this system

shifts to higher values while the I(D)/ I(G)-ratio is nearly the same. It can be concluded that higher

Bias voltage leads to higher sp^3-fractions within the DLC systems.
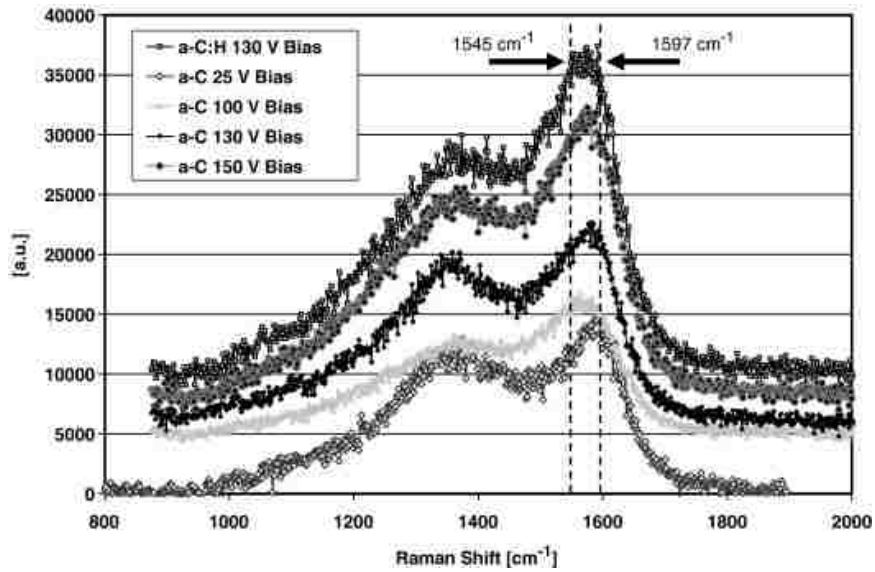
Figure 1.10 Raman spectra of the examined DLC systems [100].

Figure 1.11 illustrates the hardness and Young's modulus values of the different DLC-coating systems [101]. The increasing the Bias voltage in the a-C-process from 25 V to 100 V causes an increasing of hardness as well as Young's modulus by the factor of at least 3. Deng et al. [102] analyzed the influence of the bias voltage on the hardness of DLC coatings.
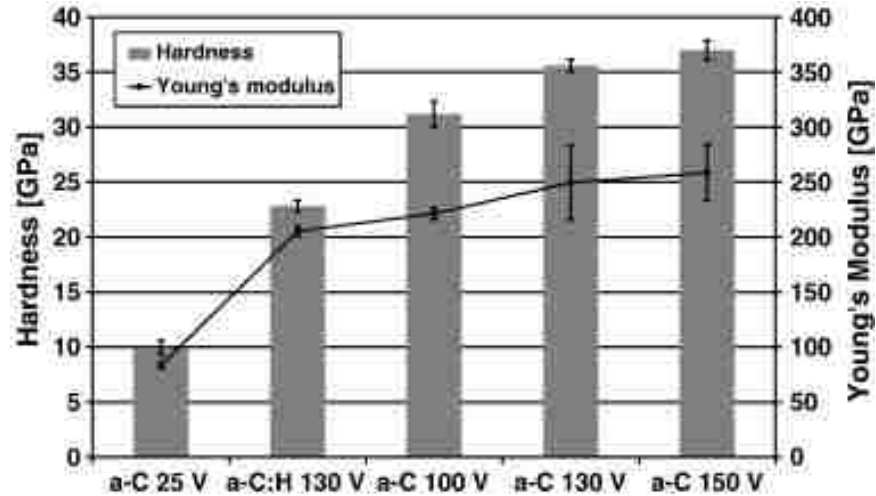
Figure 1.11 Nanoindentation results of the deposited DLC-layers [101].

The tribological behaviour of DLC coatings may vary greatly deal from one type to another. Test conditions and environments can also play a major role in their friction and wear. In particular, the friction values reported for various DLC coatings span the range of 0.001–0.7. The environmental conditions—namely, humidity level, oxygen level, and temperatures—are essential to control the friction behaviour of DLC coatings.

Liu [103] studied the friction behaviour of DLC coatings conducted under 0%, 40% and 100% relative humidity levels. The wear induced graphitization was found to be the reason for the low friction of the DLC coatings. High humidity impedes the graphitization process, resulting in a higher COF. Andersson [104, 105] investigated the friction performance of ta-C and H-DLC coatings in high vacuum, where ta-C exhibited high friction of 0.6 and H-DLC had a low COF of 0.01. This was because the addition of hydrogen reduced the effect of strong covalent bond interactions [48, 106]. Sanchez [107] conducted friction tests in ambient air, dry air, and dry nitrogen: he found the lowest COF was observed in dry nitrogen on H-DLC coating with highest H content. Konca [8-10] studied the friction behaviour of non-hydrogenated DLC coatings against Al, Mg, and Ti alloys in different environments and temperatures. An extreme low COF of 0.015

was found in H$_2$, and low COF of 0.12 was obtained in ambient air with 40% RH for DLC against Al alloy. The coating transfer, dissociation of H$_2$/H$_2$O and passivation were considered as mechanisms controlling the wear behaviour of DLC coatings. Tillmann et al. [108] developed and analyzed DLC-coatings with low wear and friction behaviour under a humid environment, which is needed to maximize the efficiency of wood machining tools. They used Raman spectroscopy to characterize the layered microstructure and examined the effect of sp^3 bonding fraction on the tribology property of DLC films [108].

Erdemir [109] performed wear tests at elevated temperatures for DLC coated SiC, then found that DLC coatings could reduce the COF by factors of 3-5 up to 300 ℃. Likewise, Konca [9] investigated the friction performance of NH-DLC coatings against 319-Al at 25 ℃, 120 ℃, 300 ℃, and 400 ℃: he found that the coating ceased to operate at 120 ℃. Moreover, Banerji et al. [110] studied the high temperature performance of W-DLC coatings sliding against titanium alloys and found the low COF of 0.07 at 400 ℃ and 500 ℃ was attributed to the formation of a WO$_3$ layer, which also reduced the adhesion of titanium. Bhowmick et al. [111] examined the high temperature wear behaviour of Si, O doped H-DLC coatings, at 200 ℃ They attributed a low COF of 0.04 to the mitigating Al adhesion. Finally, Sen et al. [112] used first-principles calculations with an interface model predicted wear behaviour of F doped H-DLC coating, and the wear tests confirmed that during sliding contact, F would transfer to the counterfaces.

1.2.3   Molybdenum Disulfide Coatings with Layered Structure

Transition metal dichalcogenides (TMD) are well-known for their solid lubricating behaviour [57]. Similar to graphite, MoS$_2$ has a lamellar structure with a layer of molybdenum atoms sandwiched between two layers of sulfur. [113] Each S-Mo-S sandwich layer is connected by covalent bonds, while Van der Walls forces connect between the sandwich layers, as shown in **Figure 1.12**. Therefore, the basal planes slide easily due to shearing force, which forms a transfer

layer on the counterface and reduces COF. Martin et al. [28] note that the low friction (COF<0.005) of MoS_2 coatings under high vacuum is attributed to the "easy shear" basal planes of the MoS_2 crystal structure, which are oriented parallel to the contact surface. Other studies [50, 51] have reported that MoS_2 coatings tested in vacuum had low COF values between 0.01-0.04.
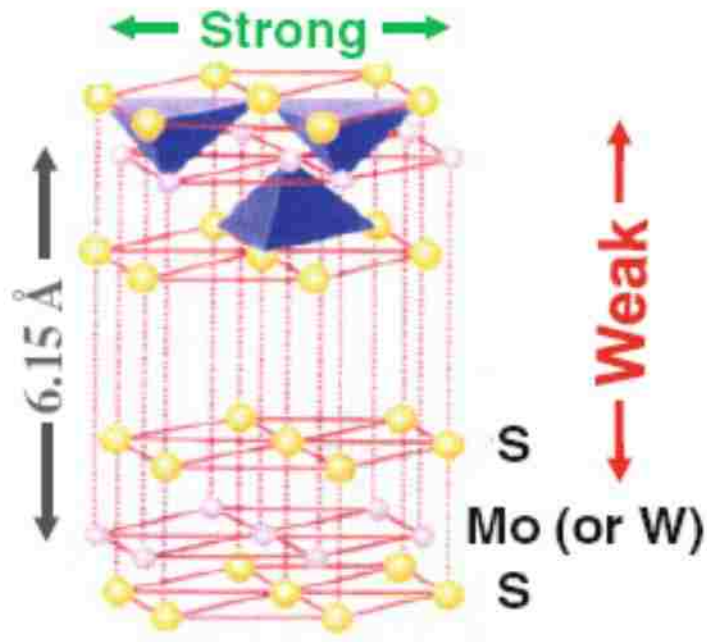
Figure 1.12 Crystal structure of MoS_2.

However, environmental conditions could seriously affect the friction behaviour of MoS_2 because MoS_2 coatings have low COF when in inert gases and high vacuum testing conditions [27, 28, 114, 115]. If moisture is introduced, the COF could be increased when water reacts with dangling bonds on the edge of basal planes in MoS_2 coatings [90, 116]. It was proposed that when in humid environments, the water molecules would diffuse into the inter-lamella gap and restrain the easy shear basal planes [117]. Donnet et al. [54] found a COF of 0.15 under ambient air (40% RH) condition for MoS_2 sliding against 52100 steel. In contrast, under high vacuum (5×10^{-8} Pa) condition, an ultra-low COF of 0.003 was recorded. Khare et al. [118] discovered that COF values increased with increasing moisture when MoS_2 coatings slide against 440C steel in temperatures

below 100 °C. Deacon and Goodman [52] proposed that the increase of COF is attributed to the bonding between water and the edge sites of MoS_2 layers, which restrains the shear movement.

MoS$_2$ is not only used as solid lubricant coating for aerospace applications: it is also used as additives for engine oil and helps to form an effective surface-lubricating film under boundary-lubricating conditions. Thus, MoS_2 plays an important role in engine lubricants. As a decomposition product of MoDTC [119, 120], MoS_2 could be formed during the generation of tribolayers at the contact surfaces and help to maintain low friction and wear [121-124]. MoDTC only decomposes to from MoS_2 at 300 °C under thermal conditions, however, under sliding contact with pressure, MoS_2 could be formed at 100 °C [125]. A high contact temperature of > 40 ℃ is necessary for the formation of MoS_2. Moreover, the oxide MoO_3 and residual MoDTC could be detected in the tribofilms [23].

The addition of Ti to MoS_2 (Ti-MoS_2) coatings could eliminate the moisture in the deposition chamber and consume the water for MoS_2 in order to reduce the sensitivity of the wear behaviour to the humidity [126]. Ti-MoS_2 maintained a low COF of 0.07 when tested against WC-Co counterface at 50% RH. When 9.5 at.% Ti was added to MoS_2 the coating maintained low COF values of 0.03-0.08 during sliding test under environments with RH between 25% and 75%; alternately, relatively higher COF values were observed for monolithic MoS_2 coating under the same test conditions using an Al_2O_3 counterface [127]. The presence of Ti atoms in MoS_2 coatings may reduce the propensity of water vapour entering interlamellar spaces [127]. Wang et al. [128] found that pure MoS_2 tested against Si_3N_4 counterfaces at room temperature with 38% relative humidity showed a high COF of 0.82; however, when 15.3at.% Ti was added to MoS_2, the COF was reduced to 0.16 under the same test conditions.

Mechanical properties of the MoS_2 coatings were also found to improve with the addition of Ti [129]. For example, hardness increase from 4.9 GPa for MoS_2 to 8.3 GPa for Ti-MoS_2 with 15.3 at.% Ti. This increased further to 10.35 GPa for Ti-MoS_2 with the addition of 19.5 at.% Ti [128].

Although researchers have examined lubricating properties of MoS_2 against steel or ceramic based counterfaces in air and vacuum, only a few studies have considered the high temperature wear behaviour of MoS_2 coating. Kubart et al [130] found that the COF values of MoS_2 coatings against 52100 steel decreased from 0.14 at 28 ˚C (50% RH) to 0.04 at 100 ˚C. Likewise, Arslan [131] showed that the COF values of MoS_2 coatings tested against Al_2O_3 counterfaces decreased from 0.07 at 25 ˚C to 0.03 at 300 ˚C, although they increased abruptly to above 0.45 at 500 ˚C. Wong et al. [132] found that MoS_2 coatings against A2 steel tested at 35% RH had a low COF of ≤0.11 at temperatures up to 320 ˚C, which was attributed to the formation of a sulphur rich transfer layer on the counterface. At temperatures higher than 400 ˚C, the MoS_2 layers oxidized completely to MoO_3 due to combined effects of high temperatures and sliding induced shear deformation, resulting in the increase of the COF values to above 0.35. A recent study showed that when temperatures were between 25 °C and 200 °C, Ti-MoS_2 coatings showed low COF values of 0.05–0.11 against Al-6.5% Si (Al 319) [15]. However, the COF increased from 0.11 to 0.15 at the temperature range of 250 °C to 350 °C due to the formation of MoO_3 on the contact surfaces. At above 400 °C, the Ti-MoS_2 coatings began to disintegrate and the 319 Al began to adhere to the coating surface. Consequently, the elimination of O_2 from the test atmosphere is expected to stabilize the friction in the temperature range of 250 °C to 350 °C.

Both MoS_2 coatings as solid lubrication films and MoDTC additives for engine oil are widely studied. However, few studies considered Ti-MoS_2 coatings used in conditions were MoDTC was used as lubricant. In this condition, the mechanisms dominate the wear behaviour: MoS_2 transfer to counterfaces, MoDTC decomposition and the oxidation of MoS_2 occurs. MoS_2 transfer and

MoDTC decomposition commonly result in decreased COF, whereas oxidation may increase the COF.

In this dissertation, friction and the adhesion mechanisms of Ti-MoS$_2$ coatings against Al-6.5% Si alloys were investigated in the temperature range between 25 ˚C and 400 ˚C in a N$_2$ atmosphere. The purpose of conducting SEM, EDS and micro-Raman analyses of the pristine coating and worn surfaces is to delineate the friction mechanisms of Ti-MoS$_2$ coatings experiments tested under a N$_2$ atmosphere at different temperatures. In addition, wear tests were performed on Ti-MoS$_2$ coatings sliding against 319 Al pins at 25 and 100 °C. The COF values of the tests were recorded, and worn surfaces were examined by SEM, EDS mapping and micro-Raman analyses to study the mechanisms of Ti-MoS$_2$ coatings in lubricated wear conditions.

1.2.4 Boron Carbide Coatings

B$_4$C is a well-known ceramic material with many industrial applications [133] and is among one of the hardest materials with high elastic modulus and low specific gravity [134, 135]. It has been used for cutting tools coatings, ceramic composites, and lightweight armor material. B$_4$C is also considered an effective coating for titanium machining tools, and because of the passivation of carbon, it has low adhesion to titanium [136, 137].

The B$_4$C crystal structure, depicted in **Figure 1.13**, consists of 9–20 at.% carbon with melting point of 2490–2375 °C [59]. Erdemir [133] investigated the self-lubricating mechanism of B$_4$C coating. In a vacuum, B$_4$C has a high COF of 0.4 when sliding against yttria/partially stabilized zirconia. In contrast, at 800 °C, a lower COF of 0.20 was observed [138] because of formation of boron acid. In ambient air, the COF of B$_4$C was determined as 0.21 according to tests done at room temperature and decreased to 0.11 at 800 °C. When the temperature was increased to 827 °C, a continuous film of boron hydroxide was formed on top of the B$_4$C surface. However, after annealing B$_4$C at 800 °C for one hour, the COF of B$_4$C was found to be as low as 0.05 at room

temperature [133, 138]. The low COF was attributed to the presence of lubricious boron hydroxide film at the sliding interface. Therefore, the formation of the boron hydroxide compound during wear contact at elevated temperatures controls the COF and wear behaviour of B_4C coatings. Abou Gharam et al. [139] investigated the wear behaviour of B4C coatings against 319 Al up to 400 ℃. A high COF ranging from 0.42-0.65 was observed from room temperature to 350 ℃, and excessive adhesion of Al was the reason for the high COF.
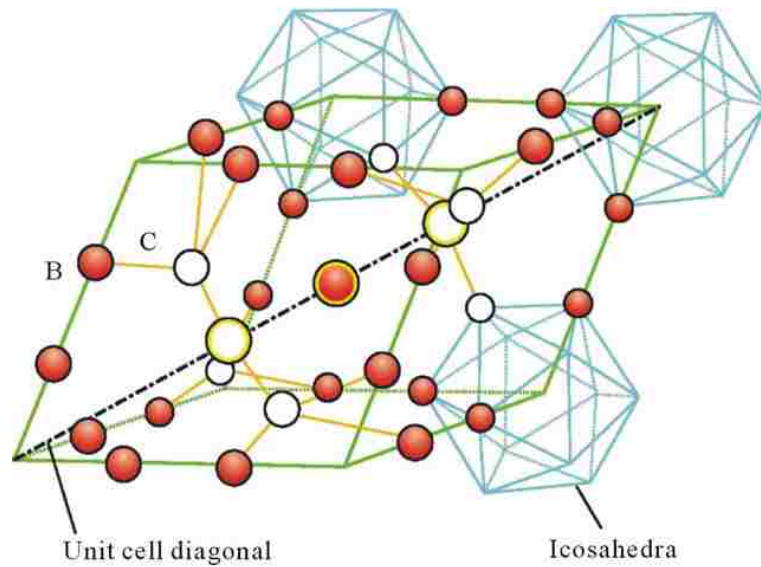
Figure 1.13 Crystal structure of boron carbide [140].

In this dissertation, the friction behaviour of B_4C sliding against Ti-6Al-4V under different environments and lubrications will be discussed. This study also seeks to provide suitable machining methods for manufacturing lightweight alloy products.

1.3   Application of Fracture Mechanics and Test Methods

Fracture mechanics is a powerful tool for analysing important failure mechanisms related to surface contact and wear for evaluating the performance and life time of tribological coatings. Fracture mechanics is concerned with the study of the propagation of cracks in materials. There are

three modes of loading that can be applied to the crack faces: Mode I fracture, which is the opening mode where a tensile stress is applied in the normal direction to the faces of the crack; Mode II fracture, which is sliding mode where shear stress is applied to the normal leading edge of the crack; and Mode III fracture, which is the tearing mode where a shear stress is applied parallel to the leading edge of the crack. **Figure 1.14** illustrates the three modes [141].
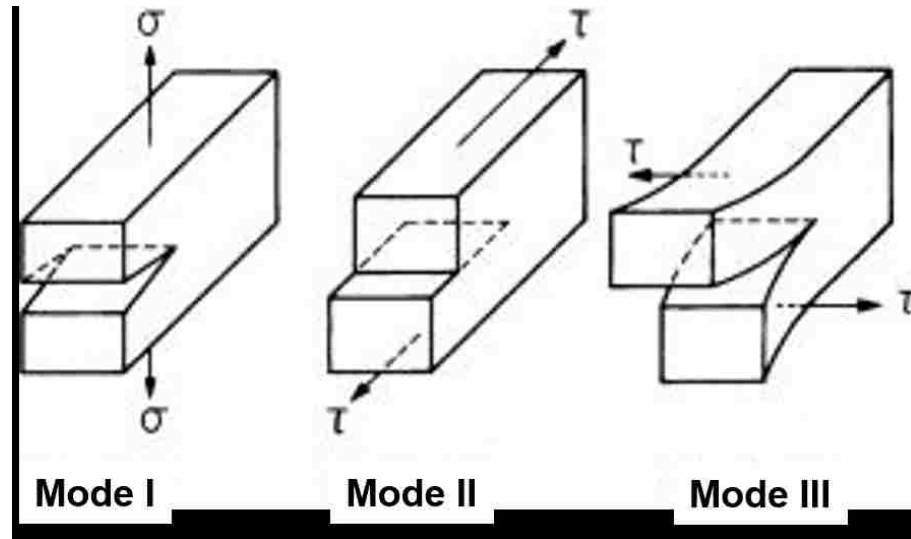
Figure 1.14 The three fracture modes [142].

1.3.1   Griffith Theory and Strain-Energy Release Rate

Griffith [143] proposed a criterion for the propagation of a crack in a perfectly brittle material considering the energy needed for creating new surface. The Griffith criterion can be stated as follows: a crack will propagate when the rate of decrease in elastic strain energy due to crack growth is equal to or larger than the rate of increase in the energy for creating new crack surfaces. The Griffith crack model is shown in **Figure 1.15**. The thickness of the material is taken as unity, so it is a plane stress problem (thin plate). The crack length inside the material is *2c*.

Figure 1.15 Griffith crack model.

The stress required to propagate the crack is given by:

$$\sigma = \left(\frac{2E\gamma_s}{\pi c}\right)^{\frac{1}{2}} \tag{1-1}$$

where σ is the far field tensile stress, E is the elastic modulus of the material and γ_s is the surface energy per unit area. From this equation, the fracture stress can be predicted for a crack with a given crack length, also, the critical crack length required to cause fracture could be determined for a given stress.

Orowan [144] explored whether plastic work can extend the cracks in quasi-brittle mechanics. Because the plastic work expended at the tip of the crack is much larger than the surface energy, the surface energy term is neglected in the equation:

$$\sigma = \left(\frac{E\gamma_p}{\pi c}\right)^{\frac{1}{2}} \tag{1-2}$$

where γ_p is the plastic work.

Irwin [145] modified the equation by introducing the strain energy release rate G_c as a general term for crack resistance that include both γ_s and γ_p.

$$\sigma = \left(\frac{E G_c}{\pi c}\right)^{\frac{1}{2}} \tag{1-3}$$

Then, the fracture condition can be stated as $G=G_c$ as follows:

$$G_c = \frac{\pi c \sigma_c^2}{E} \tag{1-4}$$

The critical value of strain energy release rate G that corresponds to the fracture of the material where $\sigma = \sigma_c$, G_c is called fracture toughness. The lowest value of G_c is G_{IC}, which was achieved in plane strain condition (thick plate). G_{IC} is a material property. Based on his analysis, Irwin [146] suggested that the local stresses near a crack tip depend on the nominal stress, the crack length, and the angular position of the crack. The stress intensity factor K captures the distribution of the stresses at the crack tip, in its simplest form:

$$K_I = \sigma\sqrt{\pi c} \tag{1-5}$$

The critical stress intensity factor designated as K_{IC} is the plane strain fracture toughness of the material in Mode I's crack opening mode. Thus $K_I = K_{IC}$ defines fracture condition. This is a material property and is independent of the load, sample thickness and crack length. It changes with the operating temperature and the applied strain rate. K_{IC} and G_{IC} are related as follows:

$$\frac{(1-v)K_{IC}^2}{E} = G_{IC} \tag{1-6}$$

According to the ASTM E399 standard, there are several types of specimens for measuring the fracture toughness, such as compact tension, indentation, bending, and tensile, or single-edge notched specimens [147]. In bending tests, it could be considered as an infinite plate subjected to remote tensile stress problem. In the current study, K_I and K_{II} are considered when examining Mode I and II crack propagation. The Mode I and mode II (in plane shear mode) stress intensity factors of a slanted crack, as shown in **Figure 1.16**, can be determined by the following equations [148]:

$$K_I = \sigma \sin^2\beta\sqrt{\pi a} \qquad\qquad (1-7)$$

$$K_{II} = \sigma \sin\beta \cos\beta\sqrt{\pi a} \qquad\qquad (1-8)$$

For the mixed mode of I-II loading, the combined K is given as

$$K = \sqrt{K_I^2 + K_{II}^2} \qquad\qquad (1-9)$$

where β is the angle between the crack and the tensile stress direction. Note that the length a is half the crack length of cracks lying inside the material and the full length of the crack that was initiated from the edge of the material. This is important when the crack propagation in thermal sprayed coatings are examined.
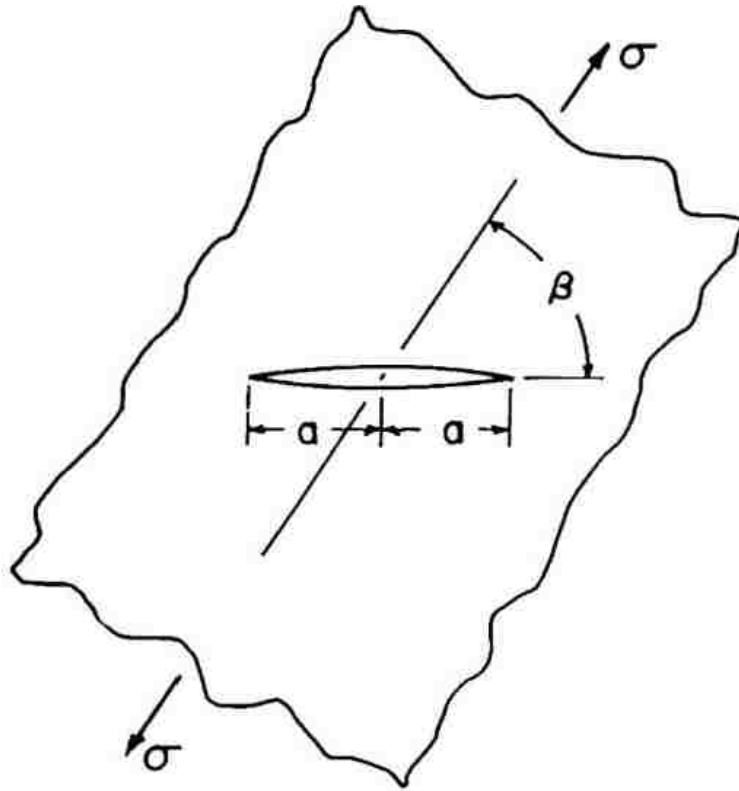
Figure 1.16 A slanted crack at an angle β in an infinite plate subjected to remote tensile stress [148].

The following sections will introduce bending and indentation tests in detail since fundamental concepts related to these two methods have been applied and further developed during the current research.

1.3.2 Bending Test for Evaluating Fracture Toughness

The geometry of bending test specimens has been standardized by ASTM standards [149]. The standard bend specimen is a single edge-notched beam (SENB) with a pre-existing crack. **Figure 1.17** shows the general principles of the four-point bending test fixture, in which W stands for the thickness of the specimen, S_0 is the outer span, and S_i is the inner span of the four-point bending fixture. The fracture toughness K_{IC} can be calculated from the maximum load and the geometry of the specimen with a given crack length.
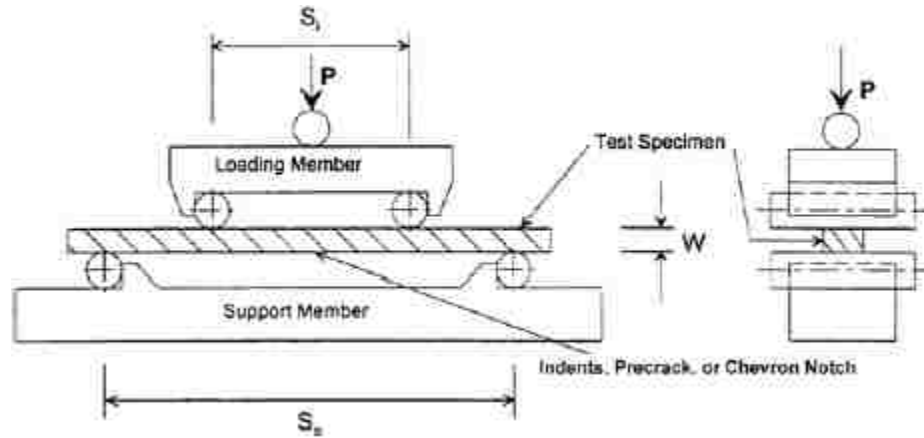
Figure 1.17 ASTM four-point bending test fixture design [149].

The ASTM design is used to determine the fracture toughness of homogenous materials. For measuring the fracture toughness of the coatings, the properties of the substrate, interface adhesion, and elastic mismatch should be considered. The fracture behaviour of coating/substrate system is affected by these factors, and fractures in either the coating or the delamination will lead to the failure of the system.

Oxide layers play an important role in the fracture behaviour of the PTWA thermal spray coatings. The fracture problems related to oxide have long been considered. Robertson and Manning [150] studied the adherence of oxide scales, namely Fe_3O_4, Cr_2O_3, Al_2O_3, SiO_2, and NiO on metal components exposed to tensile strain. They used fracture mechanics to establish a criterion for the failure of the oxide scales as a result of applied strain. Since the oxide scales they considered were brittle, they used Griffith's theory to determine the critical fracture strain ε for both tension and compression conditions:

$$\varepsilon = \left(\frac{2.5\gamma}{hE}\right)^{\frac{1}{2}} \qquad\qquad (1-10)$$

From the critical strain, the limit oxide scales thickness h was found. This critical oxide thickness could be used as a screen test or failure criterion for evaluating different materials.

31

Charalambides et al. [151] designed a bending test configuration for measuring the interface fracture resistance of a bi-material system consisting of polymethyl methacrylate (PMMA) and an Al substrate. The sample and the fixture are shown in **Figure 1.18**, and these researchers used a finite element approach to characterize the stress intensities, elastic properties, and crack length. The fracture resistance measurements accomplished by measuring the delamination crack length and finite element analysis could help the interpretation and prediction of decohesion phenomena. Evans et al. [152] used the same design to measure the fracture energy of the bi-material interfaces and found that the fracture energy Γ_i is much larger than the work of adhesion.
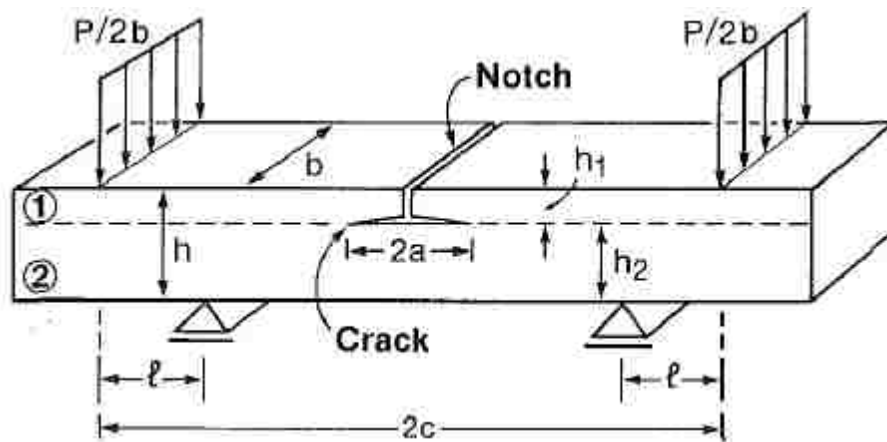
Figure 1.18 Schematic of a bi-material notched four-point bending specimen [151].

Ma [153] developed a method to measure the subcritical crack growth velocity of the CVD SiO_2 system by analyzing the load-displacement curve of a sandwich structured (SiO_2-TiN-SiO_2) four-point bending specimen. The crack growth velocity was obtained by observing that the compliance ($C=(D1+D2)/2P$, as shown in **Figure 1.19**) of the specimen was linearly proportional to the crack length at the interface. It was also found that the crack growth rate depends on the stress intensity factor exponentially. Dauskardt [154] used a similar four-point bending test to quantitatively measure the adhesion and interfacial fracture resistance of SiO_2/TiN thin film structures. Since there was no R-curve behaviour [155], the fracture toughness of the interface, G_C,

was determined from the horizontal plateau of the load-displacement curve, as shown in **Figure 1.20**. A power-law relationship was found between the debonded-crack-growth rate and strain energy release rate *G*. Based on this relationship, the lifetime of the sample under certain working conditions was predicted.
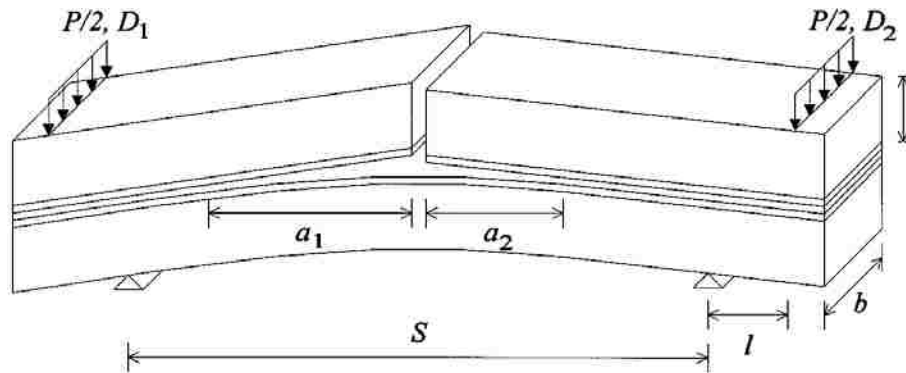
Figure 1.19 Schematic illustration of the 4-point bending configuration for sandwiched structure [153].
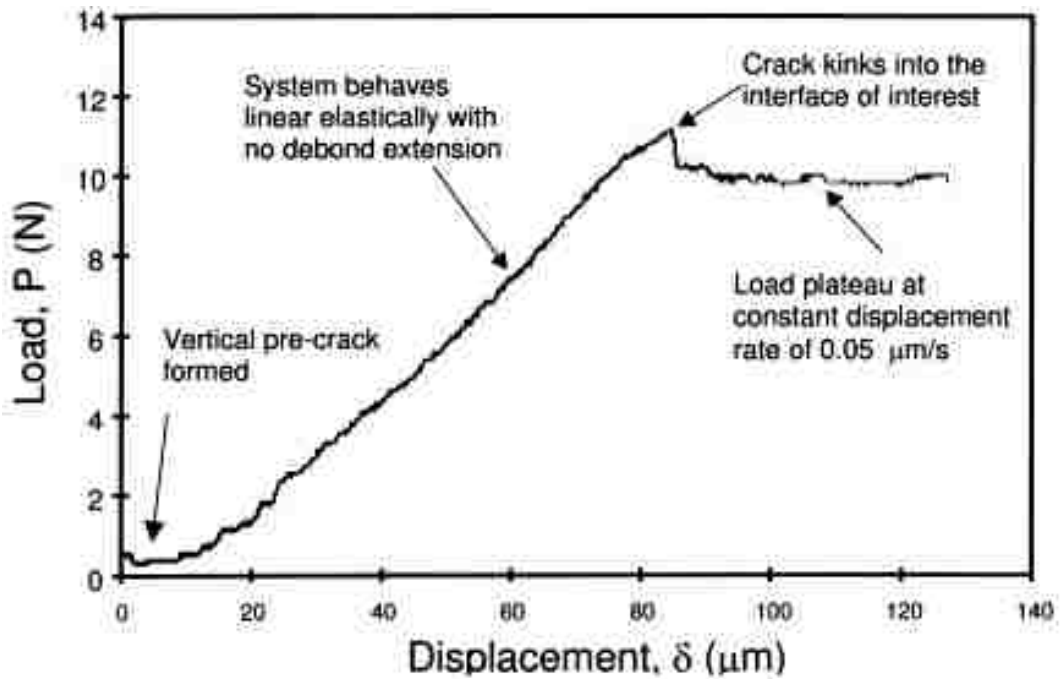
Figure 1.20 A typical load-displacement curve for debonding along a SiO_2/TiN interface [154].

Li et al. [156] applied this test method to the thermal sprayed hydroxyapatite coatings and found that the shape and sizes of the grains in the coating structure that adhered to the substrate affected the adhesion strength of the thermal spray coatings. The enlarged hexagonal grains would deteriorate the adhesion, while the granular nano-sized grains could improve the adhesion by means of an interlocking effect.

1.3.3 Indentation Fracture Toughness Test

When the indenter is pressed on the testing material surface, cracks may initiate and propagate at the impression site depending on the fracture toughness of the material. By measuring the crack length induced by the indentations, the Mode I critical stress intensity factor, K_{IC} could be calculated. Indentation tests are a rapid evaluation method for fracture toughness [157] for small specimens, which could be considered a non-destructive test method. Therefore, it could be used to determine the fracture toughness of thin coatings and different phases in inhomogeneous materials.

Hertz [158] analyzed the elastic contact between two curved bodies to determine the elastic stress field and define the point of maximum stress. The maximum contact pressure at the center of the circular contact area is:

$$P_{max} = \frac{3P}{2\pi a^2} \qquad (1-11)$$

where P is the load, and a is the contact area given by:

$$a = \sqrt[3]{\frac{3F\left[\frac{1-v_1^2}{E_1} + \frac{1-v_2^2}{E_2}\right]}{4\left(\frac{1}{R_1} + \frac{1}{R_2}\right)}} \qquad (1-12)$$

where E_1 and E_2 are the elastic moduli for spheres 1 and 2 and v_1 and v_2 are the Poisson's ratios, respectively. R_1 and R_2 stand for the radius of the curved bodies.

Indentation fracture toughness studies focused more on the application of a sharp indenter such as a cone or pyramid shaped indenters. The contact pressure is independent of the size of the indentation for these sharp shaped indenters [159]. **Figure 1.21** [160] shows the pressure distribution under different shapes of indenters and the corresponding stresses. Here a convenient scaling parameter, namely the mean contact pressure, is introduced:

$$p_0 = \frac{P}{\alpha \pi a^2} \qquad (1-13)$$

where P is the applied load and α is a dimensionless constant reflecting the indenter geometry. For symmetrical indenters, $\alpha=1$.

The linear elastic material stress distribution under normal point load P (**Figure 1.21**a&b) was first identified by Boussinesq [161], where v represents Poisson's ratio.
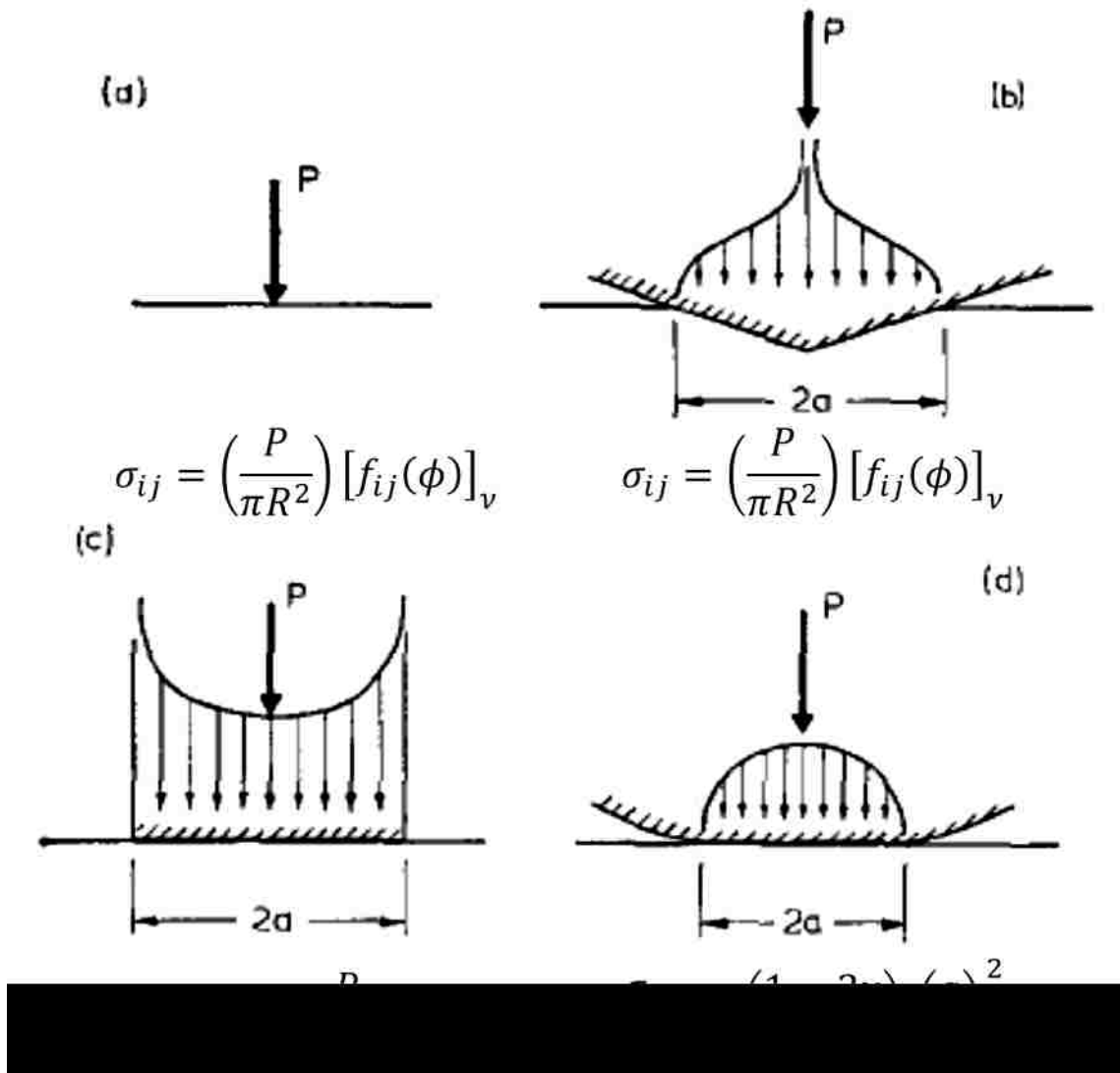
Figure 1.21 Elastic contact pressure distributions for different indenter shapes: (a) point, (b) sharp, (c) flat and (d) sphere [160].

A relationship was found between fracture toughness K_C and indentation crack length c as:

$K_C \propto P/c^{3/2}$ [162]. The general shape of this relationship was universally agreed upon by researchers working on indentation fracture toughness measurements. Many variations of this equation were introduced to determine the fracture toughness based on crack formation sequence, indenter shapes, and material type, whether brittle or ductile. Evans and Charles [163] created a

formula to describe the relationship between indentation crack length C and indentation impression radius a:

$$\frac{K_C \Phi}{H\sqrt{a}} = F_1\left(\frac{C}{a}\right) F_2\left(v, \mu, \frac{R_y}{a}\right) \qquad (1-14)$$

where K_C is fracture toughness, H is hardness, Φ is the constraint factor, v Poisson's ratio, μ is the COF between the indenter and the material, and R_y is the plastic zone radius.

Palmqvist [164] proposed another crack system called Palmqvist cracks (shown in **Figure 1.22**). The difference is that the half-penny cracks completely surround the indentation, while the Palmqvist cracks begin only at the end of the diagonals of the indentation (**Figure 1.22b**). In **Figure 1.22**, mc means median crack, lc stands for lateral crack and rc means radial crack.
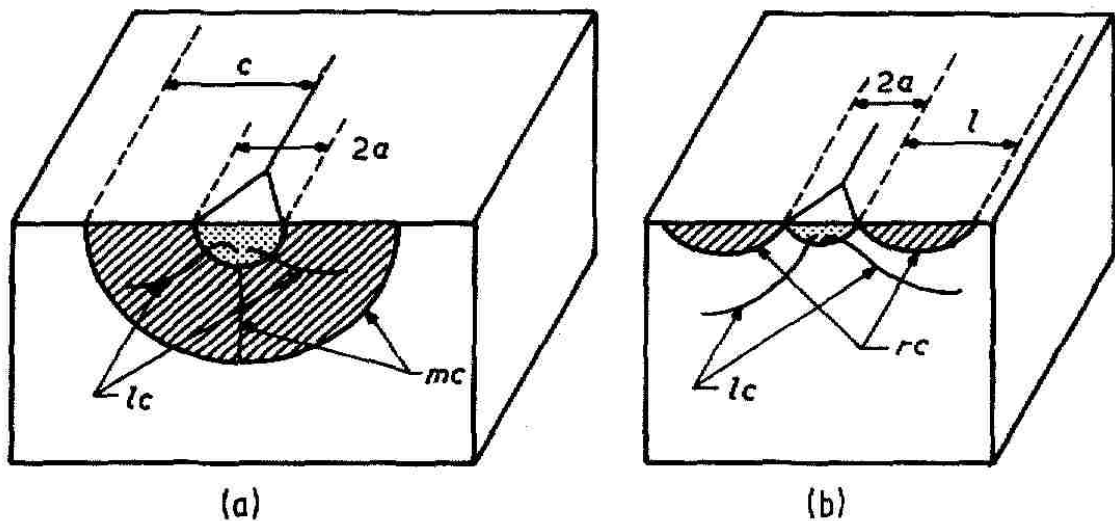
Figure 1.22 Half-penny and Palmqvist cracks in top and cross-sectional views by Vickers indentations [165].

Ponton and Rawlings [166, 167] summarized 19 equations (listed in **Table 1.2**) that determine the fracture toughness values for brittle materials by measuring the crack length induced by Vickers indentations. They applied them to a range of brittle materials: glass ceramic, alumina, zirconia and WC-Co cermet. By comparing the fracture toughness values derived from these

equations and conventional fracture toughness tests, they ranked these equations and gave their recommendations. They stated that Vickers indentation fracture toughness measurement has advantages for brittle materials when ranking fracture toughness and measuring the intrinsic fracture toughness with an experimental accuracy of about 30%.

Table 1.2 List of equation for determining fracture toughness by indentation cracks [166, 167].

Equation	Condition
Radial-median (halfpenny shaped) crack equations	
$K_c = 0.0101P/(ac^{1/2})$	
$K_c = 0.0515P/c^{3/2}$	
$K_c = 0.079(P/a^{3/2})\log(4.5a/c)$	*0.6≤c/a<4.5*
$K_c = 0.0824P/c^{3/2}$	
$K_c = 0.4636(P/a^{3/2})(E/H_V)^{2/5}$	
$K_c = 0.0141(P/a^{3/2})(E/H_V)^{2/5}\log(8.4a/c)$	
$K_c = 0.0134(P/c^{3/2})(E/H_V)^{1/2}$	
$K_c = 0.0154(P/c^{3/2})(E/H_V)^{1/2}$	
$K_c = 0.0330(P/c^{3/2})(E/H_V)^{2/5}$	*c/a≥2.5*
$K_c = 0.0363(P/a^{3/2})(E/H_V)^{2/5}(a/c)^{1.56}$	
$K_c = 0.0232(P/ac^{1/2})(f\,E/H_V)$	*c/a≤2.8*
$K_c = 0.0417(P/a^{0.42}c^{1.08})(f\,E/H_V)$	*c/a≥2.8*
$K_c = 0.0095(P/c^{3/2})(E/H_V)^{2/3}$	
$K_c = 0.022(P/c^{3/2})(E/H_V)^{2/5}$	
$K_c = 0.035(P/c^{3/2})(E/H_V)^{1/4}$	
Palmqvist crack equations	
$K_c = 0.0089(P/al^{1/2})(E/H_V)^{2/5}$	*0.25<l/a<2.5*
$K_c = 0.0122(P/al^{1/2})(E/H_V)^{2/5}$	*1≤l/a≤2.5*
$K_c = 0.0319P/al^{1/2}$	
$K_c = 0.0143(P/c^{3/2})(E/H_V)^{3/2}(a/l)^{1/2}$	

However, the equations mentioned here are all used for homogenous materials. For thermal spray coatings, especially thermal spray steel coatings, the crack paths and K_C values are influenced by microstructural elements such as pores, oxides and splats in the coating structure. New crack measurements and fracture toughness determination methods should be adjusted for these coatings, and a statistical analysis method (Weibull) is necessary to account for the variations in microstructures.

Lima et al. [168] used a non-linear regression analysis to predict the fracture toughness of WC-Co cermet high velocity oxy-fuel (HVOF) thermal spray coatings. They found that both half-penny cracks and Palmqvist cracks could be formed by Vickers indentation and that the crack's form depends on the load: Palmqvist cracks form at low indentation loads while half-penny cracks are found at higher loads.

Faisal et al. [82] considered radial, edge, and other cracks around the Vickers indentations. They measured all the cracks that could be observed near the indentations, and put them into different categories. **Figure 1.23** illustrates how the cracks were differentiated.
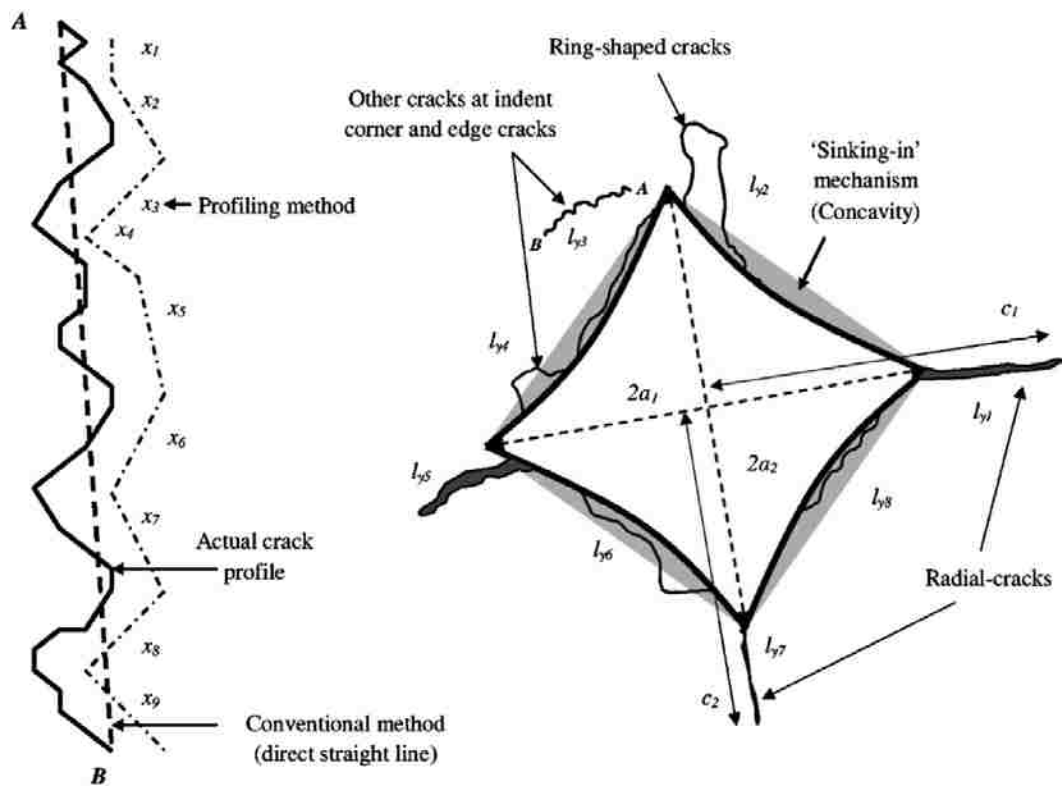
Figure 1.23 Scheme for measuring the total surface crack length using a profiling method. A. the profiling method for measuring a single crack; B. different types of cracks formed at the indentation [82].

Two crack length indicators were then used to take all cracks formed near indentations into account and evaluate the fracture toughness of the thermal sprayed coatings. The fracture toughness

values of several coatings were measured. The results were as follows: 4.3 ± 0.1 MPa·m$^{1/2}$ for HVOF Al$_2$O$_3$, 5.2 ± 0.3 MPa·m$^{1/2}$ for HVOF WC-12%Co, and 7.4 ± 0.2 MPa·m$^{1/2}$ for HIPed HVOF WC-12Co. These measurements were consistent with published values.

Wang et al. [101] used a bending test configuration to measure the mechanical properties of DLC films on steel substrates (**Figure 1.24**). By observing the crack pattern formed on the film, the fracture toughness of DLC films have been measured (~2 MPa·m$^{1/2}$). The substrate properties' effect was also considered.
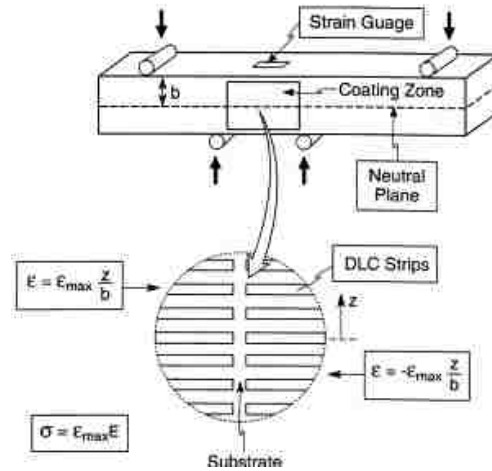
Figure 1.24 (a) The multistrain specimen and test configuration [101].

1.3.4   Weibull Distribution Function and Analysis Methods

The Weibull distribution is a continuous probability distribution named after Swedish mathematician Waloddi Weibull. It describes a "weakest link" model: the strength of a piece of material is the strength of its weakest link, and the fracture strength depends on what happens at the weakest place.

Consider a tensile stress applied to a set of identical specimens with volume V_0, and the fraction of specimens that survive the loading are σ:

$$P_s(V_0) = exp\left\{-\left(\frac{\sigma}{\sigma_0}\right)^m\right\} \qquad\qquad (1-15)$$

where $P_s(V_0)$ is the survival probability, and m is the Weibull Modulus. This measures the spread in strength values: the lower m is, the higher the variability of strength. For brick, cement, and pottery, m is around 5, whereas for metallic materials, m is around 100.

The microstructure of thermal spray ferrous coatings is complex, which results in the relative large variety of their mechanical properties, namely hardness and fracture toughness. Lima and Marple [169] evaluated the Weibull Modulus values of the TiO_2 HVOF coating's hardness and found the largest Weibull Modulus of 29 at the indentation load of 1000 gf. They attributed the low Weibull Modulus at low indentation loads to the small test volume.
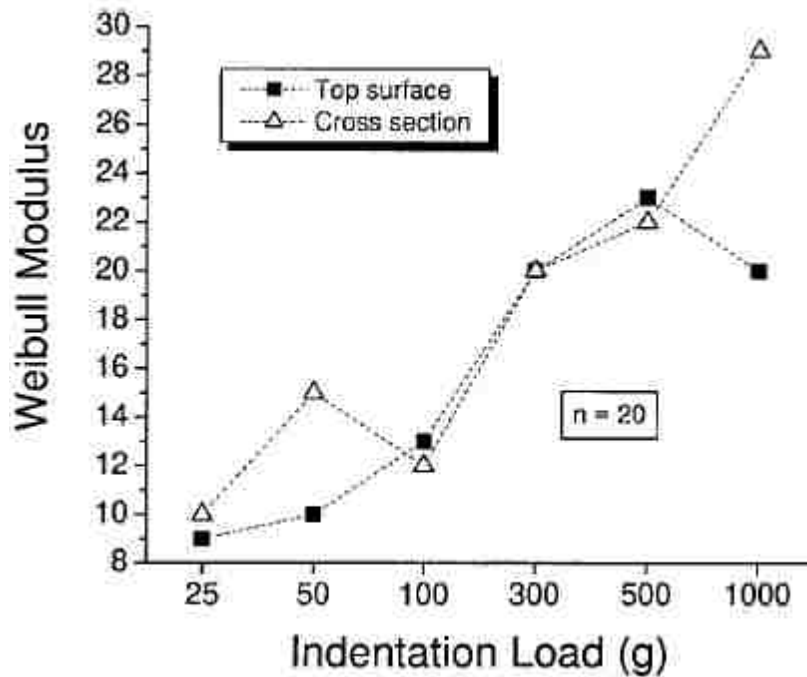
Figure 1.25 Weibull modulus of hardness of the top surface and cross-section of HVOF TiO_2 coatings at different indentation loads [169].

Lin and Berndt [170] performed microhardness measurements on thermal spray NiCoCrAlY coating. They used a Weibull distribution to assess the engineering reliability of the coating system. The aging time at higher temperatures resulted in the highest Weibull Modulus of 12.5. Their work proved that the Weibull analysis is an accurate tool for evaluating the reliability of thermal spray coatings. In this dissertation, Weibull analysis will be conducted to the fracture behaviour study of thermal spray coatings.

1.4   Lithium Ion Batteries with C- Based Electrodes

The methods summarized for tribological coatings can also be applied to the determination of mechanical properties of Li ion battery electrodes. Lithium ion batteries with high electrochemical energy efficiency are good candidates for replacing/compementing current internal combustion engines for better energy conservation and less polluting gas emission. The C-based electrodes have been widely applied in lithium batteries as electrodes (anode). The high energy capacity, chemical inertness and good conductivity make them work well in corrosive electrolyte in lithium batteries. However, all batteries suffer from a capacity fading problem. Utilizing fracture mechanics and corresponding test methods could help determine the capacity fading mechanisms in C- based electrodes.

Raman spectroscopy is a fast and useful technique to identify C-C bonding in various structures of graphite, such as single crystal and polycrystalline [171]. The typical Raman spectra peaks are shown in **Figure 1.26** [172]. Graphite has a fundamental characteristic Raman peak near 1581 cm^{-1}, denoted as the G-peak. Another characteristic Raman peak is located near 1350 cm^{-1}, which is denoted as D-peak derived from the disorder in the graphite lattice. The changes in the structure of carbon will result in different values of the D and G-peak intensities and peak positions.

Graphite is a good anode material for lithium batteries because of the excellent electronic and ionic conductivities and chemical inertness [173]. Though graphite works as an anode,

42

intercalation in graphite will occur. It is the phenomena where different chemical species inset into graphite layers resulting in a volume change to the graphite. Although the intercalation process is reversible, the atomic arrangement within the graphite layer remains unchanged [174]. Because the weak Van der Waals forces are between the graphite layers, during lithium intercalation, the lithium ions will go into the gap between two graphite layers, as shown in **Figure 1.27** [175].
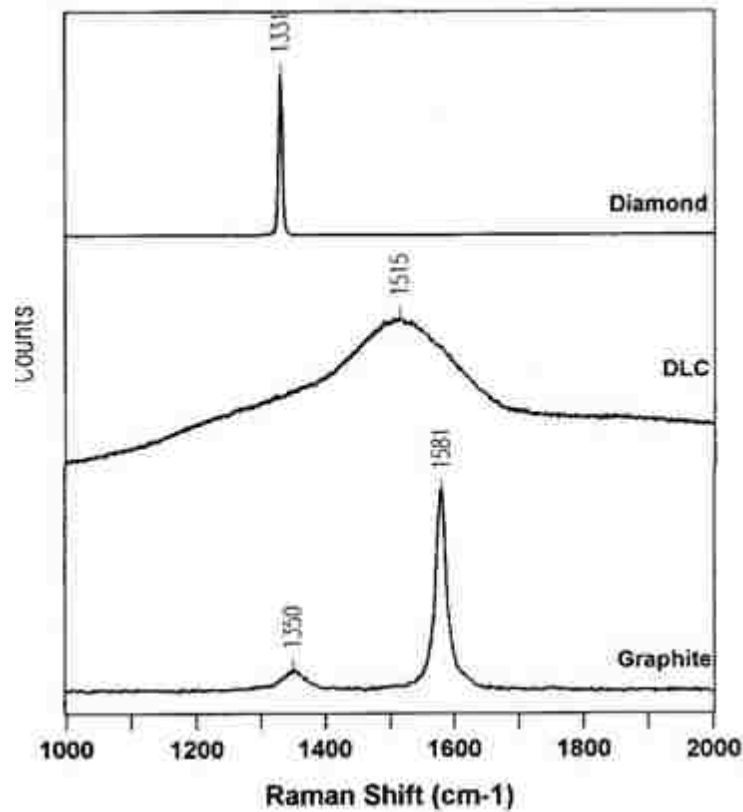
Figure 1.26 Raman spectra of graphite, DLC coatings and diamond [172].

The lithium ions only intercalate into distant graphite layers before the neighboring graphite layers are occupied. These phenomena could be described into several intercalation stages. **Figure 1.28** shows a schematic of the intercalation process stages. As the lithium ions come into the graphite, the hexagonal ABAB structure could be changed to an AAAA stacking structure [176-178]. The structural change has been studied by Boehm theoretically [179]. The intercalation

process weakens the Van der Waals forces between carbon layers and increases the number of Li-

C bonds.
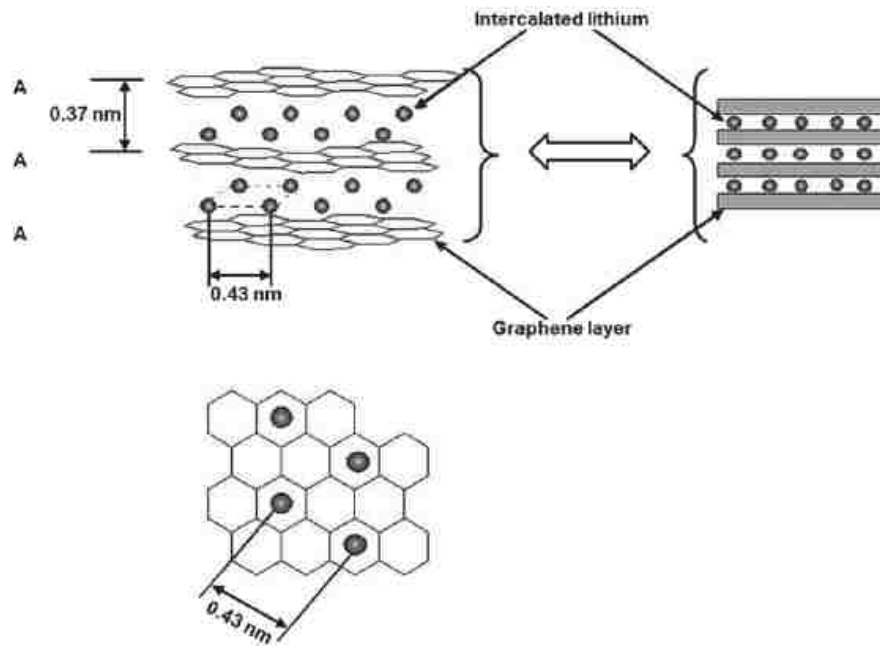
Figure 1.27 Schematic of lithium intercalation into graphite [175].
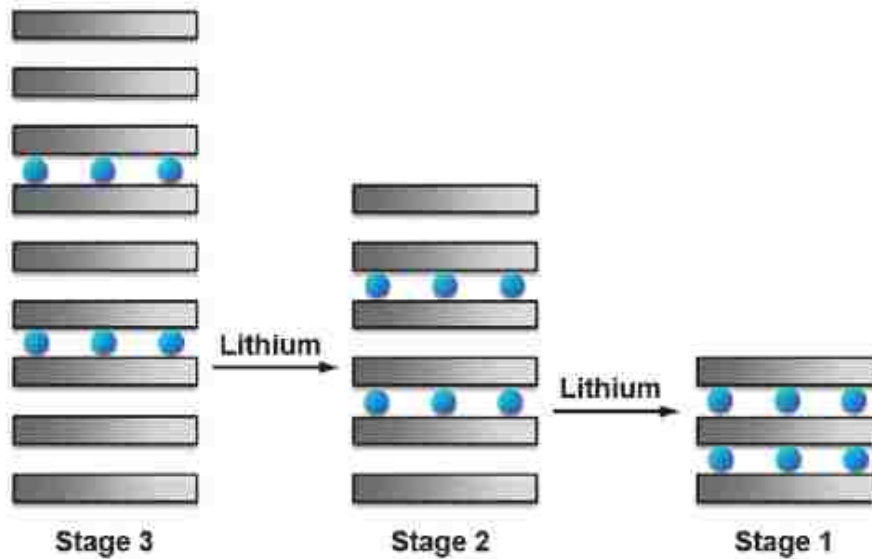
Figure 1.28 Schematic illustration of the intercalation stages [180].

The cyclic lithium intercalation and de-lithiation cycles could induce cyclic strains to the graphite. The strain will result in the shifting of the Raman peaks. The shift of G-band is related to the uniaxial and shear strains. The relationship between Raman shift and the strain could be determined as [181, 182]:

$$\frac{\Delta\omega}{\omega_o} = \gamma(\varepsilon_{xx} + \varepsilon_{yy}) \qquad (1-16)$$

where ω_o is the G-band frequency, $\Delta\omega$ is the shift in the frequency (from 1581 cm^{-1}), and γ=1.59 is the Gruneisen parameter for graphite [181].

During the charge/discharge process of the lithium battery, a layer of solid electrolyte interphase (SEI) consisting of Li_2CO_3 and lithium alkylcarbonate will be formed by electrolytic decomposition on the graphite anodes, resulting in a reduction of battery capacity [183-185]. Combined with SEI and the exfoliated graphite, the solid electrolyte reduction products could be formed at the crack tip in the graphite resulting in closure of these cracks. This phenomenon provides the self-healing property of graphite in lithium batteries [39, 186, 187].

The strain induced by intercalation generates a cyclical stress intensity factor of $\Delta K = K_{max} - K_{min}$. Accordingly, an existing crack would open during the lithiation stage reaching the highest stress intensity (K_{max}) before closing (K_{min}) during de-lithiation. The formation of SEI deposits may reduce the effective ΔK value by preventing physical contact with the crack's flanks and cause crack closure [188]. This results in reduced crack growth rate. The degradation of graphite electrode is responsible for the capacity loss of lithium battery. The understanding of crack growth behaviour of graphite will help reduce capacity loss in batteries. Further tests are needed to directly measure the crack growth rate of graphite. The corrosive electrolyte and static stress condition present a stress-corrosion problem. This dissertation will present the results of stress-corrosion tests on graphite electrodes to evaluate their performance.

1.5   Stress-Corrosion Cracking

Stress-corrosion cracking (SCC) is the growth of crack in the material under sustained load with the assistance of corrosive environment. SCC can produce brittle fractures in a simple tensile test at stresses that are far below the strength of the materials [189]. Therefore, SCC testing has been developed with the use of static stress. Tests for predicting the stress-corrosion performance of the material in a particular application should be conducted in a controlled environment equipped with a stress applying system (tensile or bending).

Figure 1.29 shows three stages of crack growth, which occur depending on the magnitude of the stress intensity factor K. In the first stage, da/dt depends strongly on the K level. The K_{ISCC} stands for the crack initiation threshold. When the K level is below the K_{ISCC}, the crack growth rate is negligible. In stage II, the crack growth rate is relatively independent of the K level. As K increases, it reaches to stage III, where da/dt increases quickly with K leading to the sudden fracture of the material, at this point K reaches its limit, K_{IC} [190].
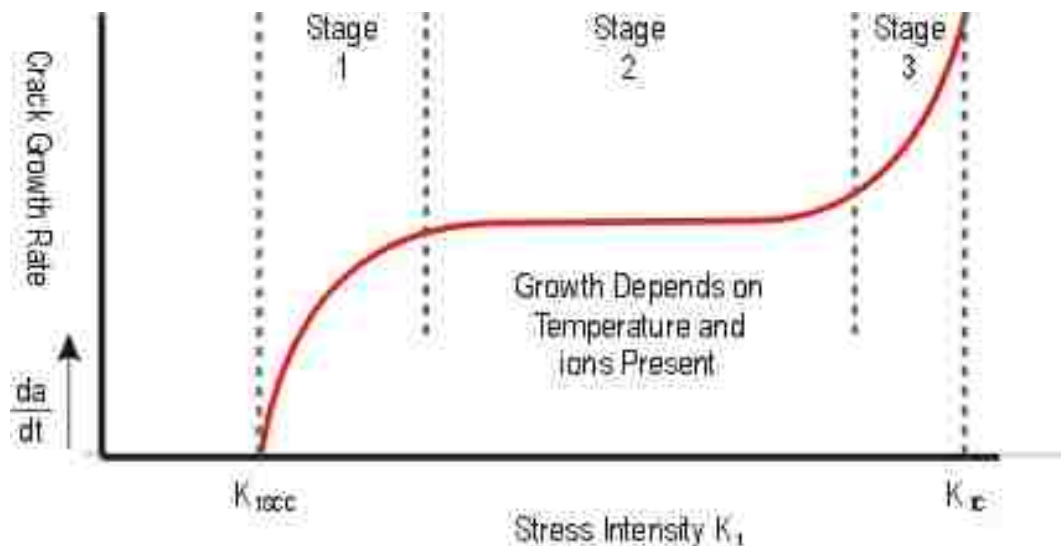
Figure 1.29 Effect of stress intensity on the kinetics of SCC [190].

Graphite is normally considered as inert to environmental attacks. However, it was found that there was time-dependent failure for graphite when it was under low strain rate. Hodkinson [191] performed slow crack growth tests on isotropic graphite and pyrolytic graphite. The crack growth rate of different types of graphite were measured at both room temperature and 500 ℃, and the K_I-V curves were plotted. He concluded that the microstructural features in the material determine mechanical failure. Likewise, Hollenback [192] studied the subcritical crack growth of glassy carbon and measured the crack growth velocity. Glassy carbon resembles common silicate with chemical inertness, though it was assumed that the crack tip of glassy carbon material involves a reaction with the moisture in the air, which results a stress corrosion process. Minnear [193] extended the tests in water for glassy carbon.

Ritchie [194] used compacted tension samples. He first measured the fracture toughness of C-based materials (1.1-1.9 MPa·m$^{1/2}$), then examined the crack growth rate of graphite under cyclic loading conditions and stress-corrosion conditions. He found that, for both loading conditions, the crack growth rates showed a conventional Paris law dependence to either ΔK or static K_I [195]:

$$\frac{da}{dt} = A\Delta K^n \qquad\qquad (1-17)$$

$$\frac{da}{dt} = AK_I^n \qquad\qquad (1-18)$$

Figure 1.30 shows the crack growth rate as a function of the stress intensity factor K in stress-corrosion conditions for graphite tested in Ringer's lactate solution. Moreover, a relationship between *da/dt* and *K* was discovered: *da/dt*=8.93×10^{-19}*K*$^{74.4}$. With this equation, the life time of the graphite under certain stress and environmental conditions could be forecasted.
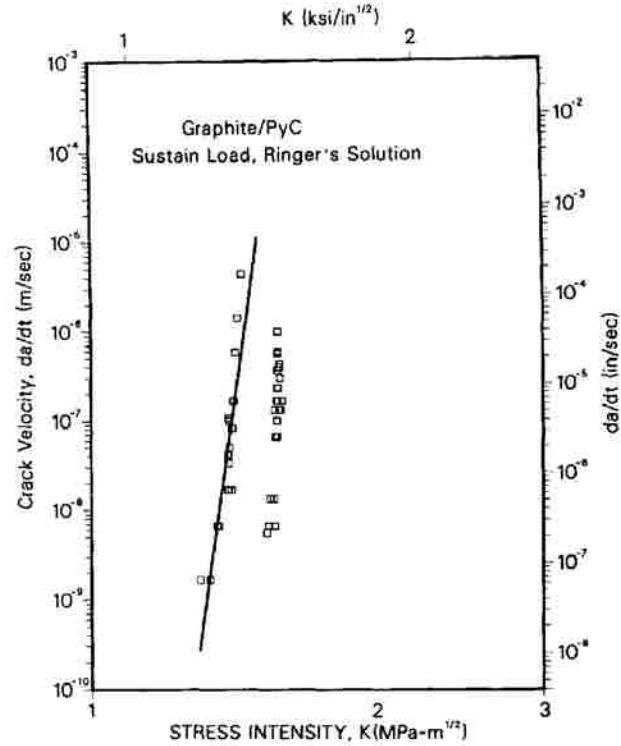
Figure 1.30 Experimental *da/dt vs. K* sustained-load (stress-corrosion) cracking data for graphite/pyrolytic carbon-coated composite tested in Ringer's lactate solution [194].

An SEI layer will be formed on the graphite surface when subjected to the charging process in the lithium battery cell. Bhattacharya et al. [186, 196] found that after the intercalation induced crack formation, 25-50 nm thick continuous layers were formed along the crack faces, as shown in **Figure 1.31**. The SEI layers formed at the crack tip reduced effective ΔK in equation 1-12; therefore, the crack growth rate was reduced.
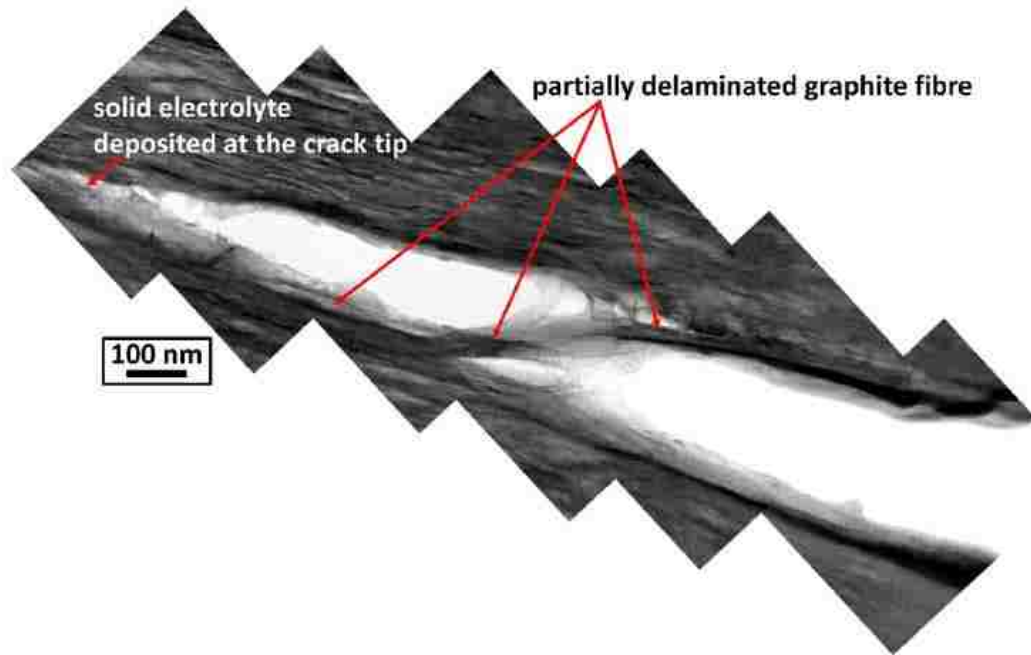
Figure 1.31 High magnification TEM image revealing the deposition of SEI layers at crack faces [196].

1.6   Scope and Organization of Dissertation

Exploiting novel tribological coatings with low friction and wear resistance is a sound approach to reducing frictional energy losses accompanied with prolonged life time of the automotive products. In particular, thermal spray coatings are ideal candidates as replacement to the traditional iron liners as they provide better tribological performance at a lighter weight. PVD coatings—namely C- and Mo-based Ti-MoS$_2$ and B$_4$C—are proposed for manufacturing processes of lightweight Ti and Al alloys. Successful application of these coatings in industry will effectively reduce energy consumption.

Tribological materials usually operate either under constant or cyclical stress conditions and are in contact with counterfaces. Under contact conditions, multiple physical, chemical, and environmental reactions occur at the material surfaces. The tribological materials often operate at elevated temperatures and environmental conditions. Therefore, it is necessary to study the

tribological and mechanical properties of new coatings under different environments and temperatures.

Hardness and fracture toughness are two main properties that should be considered for new coatings in tribological applications. Normally, increasing the hardness of the material will result in reduced wear rate [197, 198]. However, for solid lubricant materials such as graphite and MoS_2, the low hardness is not a disadvantage as the friction reduction and easy-shear of transfer layers typically formed on counter surfaces maintain low COF [52, 54, 56, 57, 113]. Materials with higher fracture toughness show higher wear resistance [199, 200]. However, the mechanism controlling the relationships between the wear rate and fracture toughness is complicated. Mechanical properties of surfaces in contact influence the formation of tribolayers. The COF, wear rate, and longevity are determined by these factors.

The efficiency of internal combustion engines will be improved by friction and weight reduction. From the energy generating point, replacing internal combustion engines with higher energy effective batteries will be another approach. Batteries are more energy efficient and create less pollution; therefore, electronic vehicles should gradually replace traditional internal combustion engine vehicles. C-based materials have high specific energy capacity, are highly resistant to chemical degradation by corrosive electrolytes, and are less likely to lead to mechanical damage and have good conductivity. Therefore, as a member of C-based materials, graphite is the preferred electrode candidate for lithium batteries.

When lithium batteries are being charged, the lithium ions diffuse into the spaces between graphite layers: this process is called intercalation. The intercalated graphite electrode suffers from strain-induced mechanical damage. This damage will cause the degradation of the lithium battery capacity as charge/discharge cycles increase. One of the most critical aspects of lithium battery design is its ability to reduce the strain-induced damage during the charging process. It has been

found that micro cracks are formed after one cycle of intercalation. Measurement of the crack growth rate of graphite electrodes under working conditions will help develop an understanding of the capacity degradation mechanisms. With the help of in-situ crack observation, in-situ Raman spectrometry, and SEM/EDS analysis, the factors controlling the lithium battery capacity fading phenomenon could be found. Understanding the degradation mechanisms will help select and design better lithium battery electrodes with higher capacity fading resistance and longer cycle life.

Four-point bending tests equipped with in-situ crack observation were performed on the thermal spray coatings to determine the coating's fracture behaviour, namely how the cracks initiate, propagate, and finally lead to the failure of the coating. The fracture mechanic analysis was applied to understand the influence of the oxide layer distribution on the fracture. This work provided designing methods for coating microstructure with higher fracture resistance and demonstrated the possibility of studying fracture behaviours with in-situ bending tests. Micro-indentations were likewise used to measure the hardness and fracture toughness of thermal spray steel coating. The tribolayer effect on the mechanical properties of the coating was examined. After studying the mechanical properties of thermal spray coatings and effect of tribolayer on these properties, the following chapters evaluated the effects of the tribolayer, environment, and temperature on the wear behaviour of tribological coatings. Moreover, studying the effect of environments on the wear behaviour of B_4C coatings against Ti-6Al-4V demonstrates how environmental factors shaped the wear behaviour of B_4C coating. In addition, an investigation of the tribological behaviour of Ti-MoS_2 coatings illustrated that MoS_2 has a similar layered structure with graphite. For the B_4C coating, water as oxygen provider increased the COF of Ti-MoS2 coating. The low COF of Ti-MoS_2 coating could be maintained up to 400 °C. With the experiences acquired from these studies in in-situ bending test and C- based coatings, the current study then investigated the fracture behaviour of graphite as anode in lithium battery using the in-situ bending set-up. This study proved that the bending-with-in-situ-observation method could be applied to the

research on tribology materials in selected environments. Furthermore, the measured-crack-growth rate could help design electrode materials for high efficiency and long cycle life batteries. Finally, the current study summarizes the research findings and addresses the relationships among stress, environment, and tribological behaviour for the materials investigated.

1.7 Bibliography

[1] V.J. Karplus, S. Paltsev, Proposed Vehicle Fuel Economy Standards in the United States for 2017 to 2025 Impacts on the Economy, Energy, and Greenhouse Gas Emissions, Transport Res Rec, (2012) 132-139.

[2] T. Klier, J. Linn, New-vehicle characteristics and the cost of the Corporate Average Fuel Economy standard, Rand J Econ, 43 (2012) 186-213.

[3] H.P. Jost, Lubrication (tribology) : education and research; a report on the present position and industry's needs, H.M.S.O, London, 1966.

[4] G.W. Stachowiak, A.W. Batchelor, Engineering tribology, 3rd ed., Elsevier Butterworth-Heinemann, Amsterdam ; Boston, 2005.

[5] B.S. Andersson, Company Perspectives in Vehicle Tribology - Volvo, in: D. Dowson, C.M. Taylor, M. Godet (Eds.) Tribology Series, Elsevier, Oxford, UK, 1991, pp. 503-506.

[6] M. Priest, C.M. Taylor, Automobile engine tribology - approaching the surface, Wear, 241 (2000) 193-203.

[7] S.C. Tung, M.L. McMillan, Automotive tribology overview of current advances and challenges for the future, Tribology International, 37 (2004) 517-536.

[8] E. Konca, Y.T. Cheng, A.T. Alpas, Sliding wear of non-hydrogenated diamond-like carbon coatings against magnesium, Surf Coat Tech, 201 (2006) 4352-4356.

[9] E. Konca, Y.T. Cheng, A.M. Weiner, J.M. Dasch, A. Alpas, Elevated temperature tribological behavior of non-hydrogenated diamond-like carbon coatings against 319 aluminum alloy, Surf Coat Tech, 200 (2006) 3996-4005.

[10] Y. Qi, E. Konca, A.T. Alpas, Atmospheric effects on the adhesion and friction between non-hydrogenated diamond-like carbon (DLC) coating and aluminum - A first principles investigation, Surface Science, 600 (2006) 2955-2965.

[11] A. Abou Gharam, M.J. Lukitsch, Y. Qi, A.T. Alpas, Role of oxygen and humidity on the tribo-chemical behaviour of non-hydrogenated diamond-like carbon coatings, Wear, 271 (2011) 2157-2163.

[12] A. Abou Gharam, M.J. Lukitsch, M.P. Balogh, N. Irish, A.T. Alpas, High temperature tribological behavior of W-DLC against aluminum, Surf Coat Tech, 206 (2011) 1905-1912.

[13] A. Banerji, A. Edrisy, V. Francis, A.T. Alpas, Effect of bio-fuel (E85) addition on lubricated sliding wear mechanisms of a eutectic Al-Si alloy, Wear, 311 (2014) 1-13.

[14] A. Banerji, M.J. Lukitsch, A.T. Alpas, Friction reduction mechanisms in cast iron sliding against DLC: Effect of biofuel (E85) diluted engine oil, Wear, 368 (2016) 196-209.

[15] A. Banerji, S. Bhowmick, A.T. Alpas, Role of temperature on tribological behaviour of Ti containing MoS2 coating against aluminum alloys, Surf Coat Tech, 314 (2017) 2-12.

[16] S. Wilson, A.R. Riahi, A.T. Alpas, Wear maps for manufacturing and automotive engineering applications, Environment Conscious Materials - Ecomaterials, (2000) 757-772.

[17] S. Wilson, A.T. Alpas, Wear mechanism maps for metal matrix composites, Wear, 212 (1997) 41-49.

[18] J. Zhang, A.T. Alpas, Wear Regimes and Transitions in Al2o3 Particulate-Reinforced Aluminum-Alloys, Mat Sci Eng a-Struct, 161 (1993) 273-284.

[19] J. Zhang, A.T. Alpas, Transition between mild and severe wear in aluminium alloys, Acta Mater, 45 (1997) 513-528.

[20] A. Edrisy, T. Perry, A.T. Alpas, Wear mechanism maps for thermal-spray steel coatings, Metallurgical and Materials Transactions a-Physical Metallurgy and Materials Science, 36A (2005) 2737-2750.

[21] M. Chen, T. Perry, A.T. Alpas, Ultra-mild wear in eutectic Al-Si alloys, Wear, 263 (2007) 552-561.

[22] M. Chen, A.T. Alpas, Ultra-mild wear of a hypereutectic Al-18.5 wt.% Si alloy, Wear, 265 (2008) 186-195.

[23] M. Chen, X. Meng-Burany, T.A. Perry, A.T. Alpas, Micromechanisms and mechanics of ultra-mild wear in Al-Si alloys, Acta Mater, 56 (2008) 5605-5616.

[24] T. Eckardt, K. Bewilogua, G. van der Kolk, T. Hurkmans, T. Trinh, W. Fleischer, Improving tribological properties of sputtered boron carbide coatings by process modifications, Surf Coat Tech, 126 (2000) 69-75.

[25] H.S. Ahn, P.D. Cuong, K.H. Shin, K.S. Lee, Tribological behavior of sputtered boron carbide coatings and the influence of processing gas, Wear, 259 (2005) 807-813.

[26] M.G.R. W. Cermignani, T. Hu, L. Stiehl, W. Rafaniello, T. Fawcett, P. Marshall, S. Rozeveld, Processing, properties and performance of high volume sputter deposited boron-carbon coatings, Proc. Annu. Tech. Conf. Soc. Vac. Coaters, (1998) 66-74.

[27] J.K.G. Panitz, L.E. Pope, J.E. Lyons, D.J. Staley, The Tribological Properties of Mos2 Coatings in Vacuum, Low Relative-Humidity, and High Relative-Humidity Environments, Journal of Vacuum Science & Technology a-Vacuum Surfaces and Films, 6 (1988) 1166-1170.

[28] J.M. Martin, C. Donnet, T. Lemogne, T. Epicier, Superlubricity of Molybdenum-Disulfide, Phys Rev B, 48 (1993) 10583-10586.

[29] D. Aurbach, E. Zinigrad, Y. Cohen, H. Teller, A short review of failure mechanisms of lithium metal and lithiated graphite anodes in liquid electrolyte solutions, Solid State Ionics, 148 (2002) 405-416.

[30] A. Mukhopadhyay, A. Tokranov, X.C. Xiao, B.W. Sheldon, Stress development due to surface processes in graphite electrodes for Li-ion batteries: A first report, Electrochim Acta, 66 (2012) 28-37.

[31] H.H. Zheng, L. Zhang, G. Liu, X.Y. Song, V.S. Battaglia, Correlationship between electrode mechanics and long-term cycling performance for graphite anode in lithium ion cells, J Power Sources, 217 (2012) 530-537.

[32] B.A. Boukamp, G.C. Lesh, R.A. Huggins, All-Solid Lithium Electrodes with Mixed-Conductor Matrix, J Electrochem Soc, 128 (1981) 725-729.

[33] T.D. Hatchard, J.R. Dahn, In situ XRD and electrochemical study of the reaction of lithium with amorphous silicon, J Electrochem Soc, 151 (2004) A838-A842.

[34] K.E. Aifantis, J.P. Dempsey, S.A. Hackney, Cracking in Si-based anodes for Li-ion batteries, Rev Adv Mater Sci, 10 (2005) 403-408.

[35] S. Bhattacharya, A.T. Alpas, Self-healing of cracks formed in Silicon-Aluminum anodes electrochemically cycled at high lithiation rates, J Power Sources, 328 (2016) 300-310.

[36] S. Bhattacharya, A.T. Alpas, Effects of Electrolyte Composition and Voltage Scan Rate on Cyclic Performance of Silicon-Aluminum Anodes for Lithium-Ion Cells, ECS Transactions, 75 (2017) 1-15.

[37] S. Bhattacharya, M. Shafiei, A.T. Alpas, Microstructural Characterization of Nanocrystalline Sn-Coated Carbon Fibre Electrodes Cycled in Li-Ion Cells, Metallurgical and Materials Transactions E-Materials for Energy Systems, 2 (2015) 208-219.

[38] S. Bhattacharya, A.R. Riahi, A.T. Alpas, Thermal cycling induced capacity enhancement of graphite anodes in lithium-ion cells, Carbon, 67 (2014) 592-606.

[39] S. Bhattacharya, A.R. Riahi, A.T. Alpas, Electrochemical cycling behaviour of lithium carbonate (Li_2CO_3) pre-treated graphite anodes - SEI formation and graphite damage mechanisms, Carbon, 77 (2014) 99-112.

[40] C. Donnet, A. Erdemir, Historical developments and new trends in tribological and solid lubricant coatings, Surf Coat Tech, 180 (2004) 76-84.

[41] S. Stewart, R. Ahmed, Rolling contact fatigue of surface coatings - a review, Wear, 253 (2002) 1132-1144.

[42] P. Fauchais, M. Vardelle, A. Vardelle, L. Bianchi, Plasma spray: Study of the coating generation, Ceram Int, 22 (1996) 295-303.

[43] K. Sarakinos, J. Alami, S. Konstantinidis, High power pulsed magnetron sputtering: A review on scientific and engineering state of the art, Surf Coat Tech, 204 (2010) 1661-1684.

[44] D.M. Mattox, Handbook of Physical Vapor Deposition (PVD) Processing, William Andrew.

[45] H.O. Pierson, Handbook of Chemical Vapor Deposition: Principles, Technology and Applications, Elsevier Science, 1999.

[46] S.J. Bull, TRIBOLOGY OF CARBON COATINGS - DLC, DIAMOND AND BEYOND, Diam Relat Mater, 4 (1995) 827-836.

[47] A. Grill, Diamond-like carbon: state of the art, Diam Relat Mater, 8 (1999) 428-434.

[48] A. Erdemir, The role of hydrogen in tribological properties of diamond-like carbon films, Surf Coat Tech, 146 (2001) 292-297.

[49] F.G. Sen, Y. Qi, A.T. Alpas, Surface stability and electronic structure of hydrogen- and fluorine-terminated diamond surfaces: A first principles investigation, J Mater Res, 24 (2009) 2461-2470.

[50] V.R. Johnson, G.W. Vaughn, Investigation of the Mechanism of MoS2 Lubrication in Vacuum, J Appl Phys, 27 (1956) 1173-1179.

[51] T. Spalvins, Lubrication with Sputtered Mos2 Films - Principles, Operation, and Limitations, J Mater Eng Perform, 1 (1992) 347-352.

[52] R.F. Deacon, J.F. Goodman, Lubrication by Lamellar Solids, Proceedings of the Royal Society of London. Series A, Mathematical and Physical Sciences, 243 (1958) 464-482.

[53] T. Endo, T. Iijima, Y. Kaneko, Y. Miyakawa, M. Nishimura, Tribological characteristics of bonded MoS2 films evaluated in rolling-sliding contact in a vacuum, Wear, 190 (1995) 219-225.

[54] C. Donnet, Advanced solid lubricant coatings for high vacuum environments, Surf Coat Tech, 80 (1996) 151-156.

[55] M.R. Hilton, P.D. Fleischauer, Applications of Solid Lubricant Films in Spacecraft, Surf Coat Tech, 55 (1992) 435-441.

[56] D.G. Teer, New solid lubricant coatings, Wear, 251 (2001) 1068-1074.

[57] T.W. Scharf, S.V. Prasad, Solid lubricants: a Review, J Mater Sci, 48 (2013) 511-531.

[58] F. Thevenot, A REVIEW ON BORON-CARBIDE, 1991.

[59] Y.G. Tkachenko, V.F. Britun, D.Z. Yurchenko, M.S. Kovalchenko, I.I. Timofeeva, L.P. Isaeva, Structure and Phase Formation in Boron Carbide and Aluminum Powder Mixtures during Hot Pressing, Powder Metall Met C+, 50 (2011) 202-211.

[60] S. Bhowmick, G. Sun, A.T. Alpas, Low friction behaviour of boron carbide coatings (B4C) sliding against Ti-6Al-4V, Surf Coat Tech, 308 (2016) 316-327.

[61] G. Pereira, A. Lachenwitzer, M. Kasrai, P.R. Norton, T.W. Capehart, T.A. Perry, Y.T. Cheng, B. Frazer, P. Gilbert, A multi-technique characterization of ZDDP antiwear films formed on Al (Si) alloy (A383) under various conditions, Tribol Lett, 26 (2007) 103-117.

[62] X. Meng-Burany, T.A. Perry, A.K. Sachdev, A.T. Alpas, Subsurface sliding wear damage characterization in Al-Si alloys using focused ion beam and cross-sectional TEM techniques, Wear, 270 (2011) 152-162.

[63] A. Edrisy, T. Perry, Y.T. Cheng, A.T. Alpas, Wear of thermal spray deposited low carbon steel coatings on aluminum alloys, Wear, 251 (2001) 1023-1033.

[64] A. Edrisy, T. Perry, Y.T. Cheng, A.T. Alpas, The effect of humidity on the sliding wear of plasma transfer wire arc thermal sprayed low carbon steel coatings, Surf Coat Tech, 146 (2001) 571-577.

[65] A. Edrisy, A.T. Alpas, Microstructures and sliding wear resistances of 0.2% carbon steel coatings deposited by HVOF and PTWA thermal spray processes, Thin Solid Films, 420 (2002) 338-344.

[66] A. Edrisy, T. Perry, A.T. Alpas, Investigation of scuffing damage in aluminum engines with thermal spray coatings, Wear, 259 (2005) 1056-1062.

[67] G. Barbezat, Advanced thermal spray technology and coating for lightweight engine blocks for the automotive industry, Surface and Coatings Technology, 200 (2005) 1990-1993.

[68] K. Alamara, S. Saber-Samandari, C.C. Berndt, Splat formation of polypropylene flame sprayed onto a flat surface, Surf Coat Tech, 205 (2010) 2518-2524.

[69] A.S.M. Ang, C.C. Berndt, M. Dunn, M.L. Sesso, S.Y. Kim, Modeling the Coverage of Splat Areas Arising from Thermal Spray Processes, J Am Ceram Soc, 95 (2012) 1572-1580.

[70] C.M. Taylor, Automobile engine tribology—design considerations for efficiency and durability, Wear, 221 (1998) 1-8.

[71] K. Bobzin, F. Ernst, J. Zwick, T. Schlaefer, D. Cook, K. Kowalsky, K. Bird, D.H. Gerke, R.E. Sharp, K.R. Raab, S. Lindon, Asme, Thermal spraying of cylinder bores with the PTWA internal coating system, 2008.

[72] T. Lampe, S. Eisenberg, E.R. Cabeo, Plasma surface engineering in the automotive industry - trends and future prospectives, Surf Coat Tech, 174 (2003) 1-7.

[73] Y. Wang, S. Jiang, M.D. Wang, S.H. Wang, T.D. Xiao, P.R. Strutt, Abrasive wear characteristics of plasma sprayed nanostructured alumina/titania coatings, Wear, 237 (2000) 176-185.

[74] H.C. Choe, Y.M. Ko, Interface activation and surface characteristics of Ti/TiN/HA coated sintered stainless steels, Met Mater-Int, 12 (2006) 31-37.

[75] R. Mcpherson, A Review of Microstructure and Properties of Plasma Sprayed Ceramic Coatings, Surf Coat Tech, 39 (1989) 173-181.

[76] H. Herman, S. Sampath, R. McCune, Thermal spray: Current status and future trends, Mrs Bull, 25 (2000) 17-25.

[77] A. Rabiei, D.R. Mumm, J.W. Hutchinson, R. Schweinfest, M. Ruhle, A.G. Evans, Microstructure, deformation and cracking characteristics of thermal spray ferrous coatings, Mat Sci Eng a-Struct, 269 (1999) 152-165.

[78] A. Rabiei, A.G. Evans, Failure mechanisms associated with the thermally grown oxide in plasma-sprayed thermal barrier coatings, Acta Mater, 48 (2000) 3963-3976.

[79] P.K. Wright, A.G. Evans, Mechanisms governing the performance of thermal barrier coatings, Current Opinion in Solid State & Materials Science, 4 (1999) 255-265.

[80] L. Pawlowski, P. Fauchais, Thermal Transport-Properties of Thermally Sprayed Coatings, Int Mater Rev, 37 (1992) 271-289.

[81] V.V. Sobolev, J.M. Guilemany, J. Nutting, J.R. Miquel, Development of substrate-coating adhesion in thermal spraying, Int Mater Rev, 42 (1997) 117-136.

[82] N.H. Faisal, R. Ahmed, A.K. Prathuru, S. Spence, M. Hossain, J.A. Steel, An improved Vickers indentation fracture toughness model to assess the quality of thermally sprayed coatings, Eng Fract Mech, 128 (2014) 189-204.

[83] C.K. Lin, C.C. Berndt, Measurement and Analysis of Adhesion Strength for Thermally Sprayed Coatings, J Therm Spray Techn, 3 (1994) 75-104.

[84] S.J. Howard, T.W. Clyne, INTERFACIAL FRACTURE-TOUGHNESS OF VACUUM-PLASMA-SPRAYED COATINGS, Surf Coat Tech, 45 (1991) 333-342.

[85] S. Kuroda, J. Kawakita, M. Watanabe, H. Katanoda, Warm spraying-a novel coating process based on high-velocity impact of solid particles, Sci Technol Adv Mat, 9 (2008).

[86] B.J. D., The structure of graphite, Proceedings of the Royal Society of London. Series A, 106 (1924) 749-773.

[87] I.C. Roselman, D. Tabor, The friction and wear of individual carbon fibres, Journal of Physics D: Applied Physics, 10 (1977) 1181.

[88] D.H. Buckley, Surface effects in adhesion, friction, wear, and lubrication, Elsevier Science, 1981.

[89] E.R. Braithwaite, Chapter V - Graphite and Molybdenum Disulphide, Solid Lubricants and Surfaces, Pergamon, 1964, pp. 120-169.

[90] J. Skinner, N. Gane, D. Tabor, Micro-Friction of Graphite, Nature-Phys Sci, 232 (1971) 195.

[91] A. Grill, Tribology of diamondlike carbon and related materials: an updated review, Surf Coat Tech, 94-5 (1997) 507-513.

[92] J. Robertson, Hard amorphous (diamond-like) carbons, Progress in Solid State Chemistry, 21 (1991) 199-333.

[93] J. Robertson, Diamond-like amorphous carbon, Mat Sci Eng R, 37 (2002) 129-281.

[94] A. Grill, Diamond-like carbon: state of the art, Diam Relat Mater, 8 (1999) 428-434.

[95] K. Bewilogua, G. Brauer, A. Dietz, J. Gabler, G. Goch, B. Karpuschewski, B. Szyszka, Surface technology for automotive engineering, Cirp Annals-Manufacturing Technology, 58 (2009) 608-627.

[96] A. Erdemir, C. Donnet, Tribology of diamond-like carbon films: recent progress and future prospects, J Phys D Appl Phys, 39 (2006) R311-R327.

[97] A. Erdemir, C. Donnet, Tribology of diamond-like carbon films: recent progress and future prospects, Journal of Physics D: Applied Physics, 39 (2006) R311-R327.

[98] M. Weiler, S. Sattel, K. Jung, H. Ehrhardt, V.S. Veerasamy, J. Robertson, Highly Tetrahedral, Diamond-Like Amorphous Hydrogenated Carbon Prepared from a Plasma Beam Source, Appl Phys Lett, 64 (1994) 2797-2799.

[99] D.R. McKenzie, Tetrahedral bonding in amorphous carbon, Reports on Progress in Physics, 59 (1996) 1611-1664.

[100] A. Ferrari, J. Robertson, Interpretation of Raman spectra of disordered and amorphous carbon, Phys Rev B, 61 (2000) 14095.

[101] J.S. Wang, Y. Sugimura, A.G. Evans, W.K. Tredway, The mechanical performance of DLC films on steel substrates, Thin Solid Films, 325 (1998) 163-174.

[102] J.G. Deng, M. Braun, DLC MULTILAYER COATINGS FOR WEAR PROTECTION, Diam Relat Mater, 4 (1995) 936-943.

[103] Y. Liu, A. Erdemir, E.I. Meletis, Influence of environmental parameters on the frictional behavior of DLC coatings, Surf Coat Tech, 94-5 (1997) 463-468.

[104] J. Andersson, R.A. Erck, A. Erdemir, Friction of diamond-like carbon films in different atmospheres, Wear, 254 (2003) 1070-1075.

[105] J. Andersson, R.A. Erck, A. Erdemir, Frictional behavior of diamondlike carbon films in vacuum and under varying water vapor pressure, Surf Coat Tech, 163 (2003) 535-540.

[106] A. Erdemir, O.L. Eryilmaz, G. Fenske, Synthesis of diamondlike carbon films with superlow friction and wear properties, Journal of Vacuum Science & Technology a-Vacuum Surfaces and Films, 18 (2000) 1987-1992.

[107] J.C. Sanchez-Lopez, A. Erdemir, C. Donnet, T.C. Rojas, Friction-induced structural transformations of diamondlike carbon coatings under various atmospheres, Surf Coat Tech, 163 (2003) 444-450.

[108] W. Tillmann, E. Vogli, F. Hoffmann, Wear-resistant and low-friction diamond-like-carbon (DLC)-layers for industrial tribological applications under humid conditions, Surf Coat Tech, 204 (2009) 1040-1045.

[109] A. Erdemir, G.R. Fenske, Tribological performance of diamond and diamondlike carbon films at elevated temperatures, Tribol T, 39 (1996) 787-794.

[110] A. Banerji, S. Bhowmick, A.T. Alpas, High temperature tribological behavior of W containing diamond-like carbon (DLC) coating against titanium alloys, Surf Coat Tech, 241 (2014) 93-104.

[111] S. Bhowmick, A. Banerji, M.J. Lukitsch, A.T. Alpas, The high temperature tribological behavior of Si, O containing hydrogenated diamond-like carbon (a-C:H/a-Si:O) coating against an aluminum alloy, Wear, 330 (2015) 261-271.

[112] F.G. Sen, Y. Qi, A.T. Alpas, Material transfer mechanisms between aluminum and fluorinated carbon interfaces, Acta Mater, 59 (2011) 2601-2614.

[113] S. Prasad, J. Zabinski, Lubricants - Super slippery solids, Nature, 387 (1997) 761-763.

[114] H.E. Sliney, Solid Lubricant Materials for High-Temperatures - a Review, Tribology International, 15 (1982) 303-315.

[115] C. Donnet, J.M. Martin, T. LeMogne, M. Belin, Super-low friction of MoS2 coatings in various environments, Tribology International, 29 (1996) 123-128.

[116] S.V. Prasad, J.S. Zabinski, Tribology of Tungsten Disulfide (Ws2) - Characterization of Wear-Induced Transfer Films, J Mater Sci Lett, 12 (1993) 1413-1415.

[117] J.F. Yang, B. Parakash, J. Hardell, Q.F. Fang, Tribological properties of transition metal di-chalcogenide based lubricant coatings, Front Mater Sci, 6 (2012) 116-127.

[118] H.S. Khare, D.L. Burris, The Effects of Environmental Water and Oxygen on the Temperature-Dependent Friction of Sputtered Molybdenum Disulfide, Tribol Lett, 52 (2013) 485-493.

[119] P.I. Sanin, G.N. Kuzmina, Y.A. Lozovoi, T.A. Zaimovskaya, Molybdenum Complexes as Synthetic Additives to Lubricating Oils, Petrol Chem+, 26 (1986) 252-257.

[120] Y. Yamamoto, S. Gondo, Friction and Wear Characteristics of Molybdenum Dithiocarbamate and Molybdenum Dithiophosphate, Tribol T, 32 (1989) 251-257.

[121] C. Grossiord, K. Varlot, J.M. Martin, T. Le Mogne, C. Esnouf, K. Inoue, MoS2, single sheet lubrication by molybdenum dithiocarbamate, Tribology International, 31 (1998) 737-743.

[122] Y.R. Jeng, S.J. Hwang, Z.G.H. Fong, J.A. Shieh, The effects of adding molybdenum dithiocarbamate additive to a sulfur-phosphorus gear oil on two roller apparatus performance, Lubr Eng, 58 (2002) 9-15.

[123] L.R. Rudnick, Lubricant Additives: Chemistry and Applications, CRC Press, Taylor & Francis Group, 2017.

[124] J. Graham, H. Spikes, S. Korcek, The friction reducing properties of molybdenum dialkyldithiocarbamate additives: Part I - Factors influencing friction reduction, Tribol T, 44 (2001) 626-636.

[125] M. Kasrai, J.N. Cutler, K. Gore, G. Canning, G.M. Bancroft, K.H. Tan, The chemistry of antiwear films generated by the combination of ZDDP and MoDTC examined by X-ray absorption spectroscopy, Tribol T, 41 (1998) 69-77.

[126] N.M. Renevier, V.C. Fox, D.G. Teer, J. Hampshire, Performance of low friction MoS2/titanium composite coatings used in forming applications, Mater Design, 21 (2000) 337-343.

[127] X.Z. Ding, X.T. Zeng, X.Y. He, Z. Chen, Tribological properties of Cr- and Ti-doped MoS2 composite coatings under different humidity atmosphere, Surf Coat Tech, 205 (2010) 224-231.

[128] X. Wang, Y.M. Xing, S.L. Ma, X.L. Zhang, K.W. Xu, D.G. Teer, Microstructure and mechanical properties of MOS2/titanium composite coatings with different titanium content, Surf Coat Tech, 201 (2007) 5290-5293.

[129] P. Stoyanov, R.R. Chromik, D. Goldbaum, J.R. Lince, X.L. Zhang, Microtribological Performance of Au-MoS2 and Ti-MoS2 Coatings with Varying Contact Pressure, Tribol Lett, 40 (2010) 199-211.

[130] T. Kubart, T. Polcar, L. Kopecky, R. Novak, D. Novakova, Temperature dependence of tribological properties of MoS(2) and MoSe(2) coatings, Surf Coat Tech, 193 (2005) 230-233.

[131] E. Arslan, Y. Totik, O. Bayrak, I. Efeoglu, A. Celik, High temperature friction and wear behavior of MoS(2)/Nb coating in ambient air, J Coat Technol Res, 7 (2010) 131-137.

[132] K.C. Wong, X. Lu, J. Cotter, D.T. Eadie, P.C. Wong, K.A.R. Mitchell, Surface and friction characterization of MoS2 and WS2 third body thin films under simulated wheel/rail rolling-sliding contact, Wear, 264 (2008) 526-534.

[133] A. Erdemir, C. Bindal, C. Zuiker, E. Savrun, Tribology of naturally occurring boric acid films on boron carbide, Surf Coat Tech, 86-7 (1996) 507-510.

[134] F. Thevenot, Laboratory methods for the preparation of boron carbides, Nato Adv Sci I E-App, 185 (1990) 87-96.

[135] F. Thevenot, A Review on Boron-Carbide, Advanced Ceramics, 56 (1991) 59-88.

[136] Z.Y. Wang, K.P. Rajurkar, Cryogenic machining of hard-to-cut materials, Wear, 239 (2000) 168-175.

[137] E.O. Ezugwu, J. Bonney, Y. Yamane, An overview of the machinability of aeroengine alloys, J Mater Process Tech, 134 (2003) 233-253.

[138] A. Erdemir, G.R. Fenske, R.A. Erck, A Study of the Formation and Self-Lubrication Mechanisms of Boric-Acid Films on Boric Oxide Coatings, Surf Coat Tech, 43-4 (1990) 588-596.

[139] A. Abou Gharam, M.J. Lukitsch, M.P. Balogh, A.T. Alpas, High temperature tribological behaviour of carbon based (B4C and DLC) coatings in sliding contact with aluminum, Thin Solid Films, 519 (2010) 1611-1617.

[140] Z.D. Kovziridze, Z. Mestvirishvili, G. Tabatadze, N.S. Nizharadze, M. Mshvildadze, E. Nikoleishvili, Improvement of Boron Carbide Mechanical Properties in B_4C-TiB_2 and B_4C-ZrB_2 Systems, Journal of Electronics Cooling and Thermal Control, Vol.03No.02 (2013) 6.

[141] T.L. Anderson, Fracture Mechanics: Fundamentals and Applications, Fourth Edition, CRC Press, 2017.

[142] T.E. Tay, Characterization and analysis of delamination fracture in composites: An overview of developments from 1990 to 2001, Applied Mechanics Reviews, 56 (2003) 1-32.

[143] A.A. Griffith, The Phenomena of Rupture and Flow in Solids, Philosophical Transactions of the Royal Society of London. Series A, Containing Papers of a Mathematical or Physical Character, 221 (1921) 163-198.

[144] E. Orowan, Fracture and strength of solids, Reports on Progress in Physics, 12 (1949) 185.

[145] S.Y. Yarema, On the contribution of G. R. Irwin to fracture mechanics, Materials Science, 31 (1996) 617-623.

[146] S.Y. Hobbs, Fracture Toughness of Polycarbonate Structural Foams, J Appl Phys, 48 (1977) 4052-4057.

[147] ASTM Standard E399, Standard Test Method for Linear-Elastic Plane-Strain Fracture Toughness KIc of Metallic Materials, ASTM International, West Conshohocken, PA, 2017.

[148] G.C. Sih, P.C. Paris, F. Erdogan, Crack-Tip, Stress-Intensity Factors for Plane Extension and Plate Bending Problems, Journal of Applied Mechanics, 29 (1962) 306-312.

[149] ASTM Standard E1820, Standard Test Method for Measurement of Fracture Toughness, ASTM International, West Conshohocken, PA, 2015.

[150] J. Robertson, M.I. Manning, Limits to Adherence of Oxide Scales, Mater Sci Tech Ser, 6 (1990) 81-91.

[151] P.G. Charalambides, J. Lund, A.G. Evans, R.M. McMeeking, A test specimen for determining the fracture resistarim of bimaterial interfaces, J Appl Mech-T Asme, 56 (1989) 77-82.

[152] A.G. Evans, M. Ruhle, B.J. Dalgleish, P.G. Charalambides, The Fracture Energy of Bimaterial Interfaces, Metall Trans A, 21 (1990) 2419-2429.

[153] Q. Ma, A four-point bending technique for studying subcritical crack growth in thin films and at interfaces, J Mater Res, 12 (1997) 840-845.

[154] R. Dauskardt, M. Lane, Q. Ma, N. Krishna, Adhesion and debonding of multi-layer thin film structures, Eng Fract Mech, 61 (1998) 141-162.

[155] Z.H. Jin, R.C. Batra, Some basic fracture mechanics concepts in functionally graded materials, J Mech Phys Solids, 44 (1996) 1221-1235.

[156] H. Li, K.A. Khor, P. Cheang, Adhesive and bending failure of thermal sprayed hydroxyapatite coatings: Effect of nanostructures at interface and crack propagation phenomenon during bending, Eng Fract Mech, 74 (2007) 1894-1903.

[157] S.M. Wiederhorn, Prevention of Failure in Glass by Proof-Testing, J Am Ceram Soc, 56 (1973) 227-228.

[158] H.R. Hertz, Über die Berührung fester elastischer Körper und über die Härte, Verhandlungen des Vereins zur Beförderung des Gewerbfleißes, Berlin : Verein zur Beförderung des Gewerbefleisses, 1882 (2006) 449-463.

[159] D. Tabor, The Hardness of Metals, OUP Oxford, 2000.

[160] K.L. Johnson, The correlation of indentation experiments, J Mech Phys Solids, 18 (1970) 115-126.

[161] S. Timoshenko, J.N. Goodier, Theory of Elasticity, McGraw-Hill, New York, 1951.

[162] B.R. Lawn, D.B. Marshall, Hardness, Toughness, and Brittleness - Indentation Analysis, J Am Ceram Soc, 62 (1979) 347-350.

[163] A.G. Evans, E.A. Charles, Fracture Toughness Determinations by Indentation, J Am Ceram Soc, 59 (1976) 371-372.

[164] S. Palmqvist, A method to determine the toughness of brittle materials, especially hard materials, Jernkontorets Ann, 141 (1957) 303-307.

[165] K. Niihara, R. Morena, D.P.H. Hasselman, Evaluation of Klc of Brittle Solids by the Indentation Method with Low Crack-to-Indent Ratios, J Mater Sci Lett, 1 (1982) 13-16.

[166] C.B. Ponton, R.D. Rawlings, Vickers Indentation Fracture-Toughness Test .1. Review of Literature and Formulation of Standardized Indentation Toughness Equations, Mater Sci Tech Ser, 5 (1989) 865-872.

[167] C.B. Ponton, R.D. Rawlings, Vickers Indentation Fracture-Toughness Test .2. Application and Critical-Evaluation of Standardized Indentation Toughness Equations, Mater Sci Tech Ser, 5 (1989) 961-976.

[168] M.M. Lima, C. Godoy, J.C. Avelar-Batista, P.J. Modenesi, Toughness evaluation of HVOF WC–Co coatings using non-linear regression analysis, Materials Science and Engineering: A, 357 (2003) 337-345.

[169] R.S. Lima, B.R. Marple, High Weibull modulus HVOF Titania coatings, J Therm Spray Techn, 12 (2003) 240-249.

[170] C.K. Lin, C.C. Berndt, Statistical-Analysis of Microhardness Variations in Thermal Spray Coatings, J Mater Sci, 30 (1995) 111-117.

[171] J. Robertson, Amorphous carbon, Advances in Physics, 35 (1986) 317-374.

[172] D.R. Tallant, J.E. Parmeter, M.P. Siegal, R.L. Simpson, The Thermal-Stability of Diamond-Like Carbon, Diam Relat Mater, 4 (1995) 191-199.

[173] G. Pistoia, Lithium batteries: new materials, developments, and perspectives, Elsevier, Amsterdam, 1994.

[174] J.O. Besenhard, H.P. Fritz, The Electrochemistry of Black Carbons, Angewandte Chemie International Edition in English, 22 (1983) 950-975.

[175] M. Winter, J.O. Besenhard, M.E. Spahr, P. Novak, Insertion electrode materials for rechargeable lithium batteries, Adv Mater, 10 (1998) 725-763.

[176] D.P. Divincenzo, C.D. Fuerst, J.E. Fischer, (P,T) Phase-Boundary in Li-Intercalated Graphite - Theory and Experiment, Phys Rev B, 29 (1984) 1115-1117.

[177] S.A. Solin, The Nature and Structural-Properties of Graphite-Intercalation Compounds, Adv Chem Phys, 49 (1982) 455-532.

[178] Y. Imai, A. Watanabe, Energetic evaluation of possible stacking structures of Li-intercalation in graphite using a first-principle pseudopotential calculation, J Alloy Compd, 439 (2007) 258-267.

[179] R.C. Boehm, A. Banerjee, Theoretical-Study of Lithium Intercalated Graphite, J Chem Phys, 96 (1992) 1150-1157.

[180] N.A. Kaskhedikar, J. Maier, Lithium Storage in Carbon Nanostructures, Adv Mater, 21 (2009) 2664-2680.

[181] S. Reich, H. Jantoljak, C. Thomsen, Shear strain in carbon nanotubes under hydrostatic pressure, Phys Rev B, 61 (2000) 13389-13392.

[182] C. Thomsen, S. Reich, P. Ordejon, Ab initio determination of the phonon deformation potentials of graphene, Phys Rev B, 65 (2002) 073403.

[183] M. Winter, P. Novak, A. Monnier, Graphites for lithium-ion cells: The correlation of the first-cycle charge loss with the Brunauer-Emmett-Teller surface area, J Electrochem Soc, 145 (1998) 428-436.

[184] P. Novak, F. Joho, M. Lanz, B. Rykart, J.C. Panitz, D. Alliata, R. Kotz, O. Haas, The complex electrochemistry of graphite electrodes in lithium-ion batteries, J Power Sources, 97-8 (2001) 39-46.

[185] D. Aurbach, B. Markovsky, A. Shechter, Y. EinEli, H. Cohen, A comparative study of synthetic graphite and Li electrodes in electrolyte solutions based on ethylene carbonate dimethyl carbonate mixtures, J Electrochem Soc, 143 (1996) 3809-3820.

[186] S. Bhattacharya, A.T. Alpas, Micromechanisms of solid electrolyte interphase formation on electrochemically cycled graphite electrodes in lithium-ion cells, Carbon, 50 (2012) 5359-5371.

[187] G.C. Chung, H.J. Kim, S.I. Yu, S.H. Jun, J.W. Choi, M.H. Kim, Origin of graphite exfoliation - An investigation of the important role of solvent cointercalation, J Electrochem Soc, 147 (2000) 4391-4398.

[188] S. Suresh, G.F. Zamiski, R.O. Ritchie, Oxide-Induced Crack Closure - an Explanation for near-Threshold Corrosion Fatigue Crack Growth-Behavior, Metall Trans A, 12 (1981) 1435-1443.

[189] B.F. Brown, U.S.N.B.o. Standards, U.S.A.R.P. Agency, Stress Corrosion Cracking Control Measures, U.S. Department of Commerce, National Bureau of Standards, 1977.

[190] R.W. Hertzberg, Deformation and fracture mechanics of engineering materials, Wiley, 1989.

[191] P.H. Hodkinson, J.S. Nadeau, Slow Crack Growth in Graphite, J Mater Sci, 10 (1975) 846-856.

[192] T.M. Hollenback, W.P. Minnear, R.C. Bradt, P.L. Walker, Subcritical Crack-Propagation in Glassy Carbon, Carbon, 13 (1975) 550-550.

[193] W.P. Minnear, T.M. Hollenbeck, R.C. Bradt, P.L. Walker, Subcritical Crack Growth of Glassy Carbon in Water, J Non-Cryst Solids, 21 (1976) 107-115.

[194] R.O. Ritchie, R.H. Dauskardt, W.K. Yu, A.M. Brendzel, Cyclic Fatigue-Crack Propagation, Stress-Corrosion, and Fracture-Toughness Behavior in Pyrolytic Carbon-Coated Graphite for Prosthetic Heart-Valve Applications, Journal of biomedical materials research, 24 (1990) 189-206.

[195] P. Paris, F. Erdogan, A Critical Analysis of Crack Propagation Laws, Journal of Basic Engineering, 85 (1963) 528-533.

[196] S. Bhattacharya, A.R. Riahi, A.T. Alpas, A transmission electron microscopy study of crack formation and propagation in electrochemically cycled graphite electrode in lithium-ion cells, J Power Sources, 196 (2011) 8719-8727.

[197] H. Torabian, J.P. Patak, S.N. Tiwari, Effect of hardness on wear rates of Al-Si alloys, J Mater Sci Lett, 14 (1995) 1631-1632.

[198] S. Wada, Effects of hardness and fracture toughness of target ceramics and abrasive particles on wear rate by abrasive water jet, Journal of the Ceramic Society of Japan, 104 (1996) 247-252.

[199] S.F. Scieszka, Wear transition as a means of fracture toughness evaluation of hardmetals, Tribol Lett, 11 (2001) 185-194.

[200] S.F. Scieszka, The wear transition as means for hardmetal fracture toughness evaluation, Int J Refract Met H, 19 (2001) 101-108.

CHAPTER 2

FRACTURE BEHAVIOUR AND TOUGHNESS MEASUREMENT OF THERMAL SPRAY COATINGS BY IN-SITU OBSERVATION OF BENDING TESTS

2.1   Introduction

Thermal spray steel coatings are good candidates for replacing the cast iron liners for Al alloy engines. [1, 2] The engine blocks made of Al-Si alloy can be protected by depositing thermal spray coatings on the sliding surfaces. Thermal spray low carbon steel coatings can reduce more weight and cost than cast iron liners.

Plasma Transferred Wire Arc (PTWA) process is a common spray deposition technique and uses a spray jet in rotational motion that goes up and down inside a cylinder bore. The feed stock materials are usually in a wire form [3]. The spray coatings deposited using PTWA technique have a lamellar structure consisting of iron splats, resulting from flattening of molten metal droplets as they hit the surface, separated by iron oxide (FeO) stringers [4]. Few studies in the past have investigated the failure mechanisms of the PTWA deposited ferrous based coatings. Wedge impression tests [4-6] have been used to investigate failure mechanisms of thermal spray thermal barrier coatings. It was suggested that the low fracture toughness of the interfacial oxide could cause splat delamination.

Evaluation of the mechanical properties, especially fracture mechanism, of thermal spray low carbon coating are important for their application in automotive parts. However, the thermal spray coating has unique lamellar microstructure and during thermal spray process, oxide layers formed in the coating [7, 8]. When the thermal spray coating under certain stress, these oxide layers act both as crack propagation path and crack barriers. The fracture mechanism of the coating is therefore unique by these oxide layers.

71

Faisal et al. [9] performed Vickers indentations on five different thermal spray coatings, and measured surface crack length and characterized them into three types (radial, edge and other cracks). Accordingly, the authors proposed a model based on different types of cracks to determine fracture toughness of thermal spray coatings. Lin and Berndt [10] have summarized different methods that have been used to measure adhesion of thermal spray coatings—namely, the tensile adhesion test, scratch test, indentation test and the bending test. Both three point and four point bending tests were performed, however, the four point bending test had more uniform stress distribution than three point bending test and the sample was loaded with the coating in tension. Howard and Clyne [11] measured interfacial fracture toughness of thermal spray titanium coatings by using a notched four point bending specimen. An artificially introduced crack at the interface was caused to propagate under the four-point bending arrangement, then interfacial fracture energy and critical stress intensity factor were evaluated. Rabiei [4] performed wedge impression tests on thermal spray ferrous coatings with a WC wedge indenter. K_I fracture toughness < 1 MPa·m$^{1/2}$ was measured indicating a weak interface between oxides and α-Fe in the coating.

In this work, in-situ observation with an optical microscope has been performed to investigate and record crack initiation and coating failure behaviour while conducting four-point bending tests on thermal spray coatings. Using the results from the bending tests fracture mechanics analyses were applied to the cracks and the effect of crack tip stress field was discussed.

2.2   Experimental Details

2.2.1   Thermal Spray Coatings

The surfaces of the Al 380 (Al-9.0% Si) bores, used as substrates for the thermal spray coatings, were mechanically roughened to provide two shapes of mechanical interlocking for the coatings to adhere to the substrate. The steel coatings were deposited on the inner walls of Al 380

linerless cylinder bores using rotating single wire (RSW) technology. The wire feed stock for the RSW gun was steel with nominal AISI 5130 composition. PTWA technique was sued to deposit 1010 steel coating using wire feed stock with AISI 1010 composition. The RSW 5130 steel based coatings also consisted of 0.1-0.3 at.% Al and 0.02 at.% Ti addition, which was introduced to reduce the oxide content of the coating and will be further designated as 5130M (modified) steel coatings. The 1010 steel coating deposited on an engine bore was sectioned and provided by GM for investigation.

Figure 2.1 is a composite secondary electron (SE)-SEM image of the as-received 1010 low carbon thermal-spray coating showing the top surface (plane-view) and the cross-sectional view, which is in the direction parallel to the piston movement. During thermal spray deposition, coatings are formed by stacking of flattened α-Fe splats [12] and the oxides (FeO) formed at the splat boundaries. In addition, in certain regions FeO aggregates could be observed. The total fraction of the oxide aggregates and oxide stringers was determined to be 22±2 % by quantitative metallography. The detailed parameters of two kinds of coatings are listed in Table 2.1. Although the size of the oxide aggregates on the top surface were about 2.4 times higher than those observed in the coating cross-section, the inter-stringer distances in both the faces were comparable.
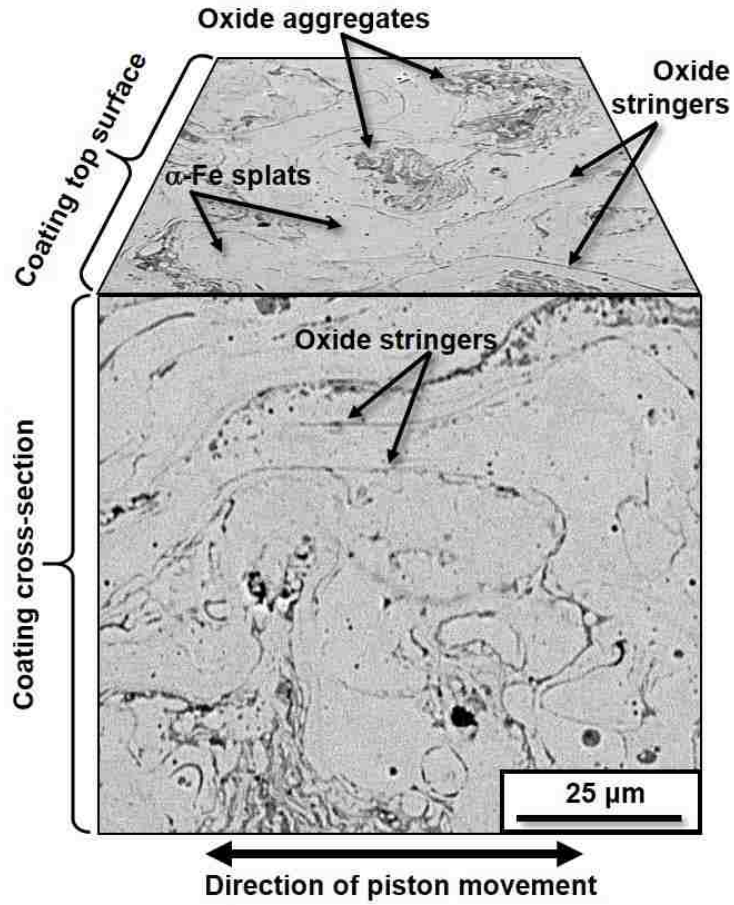
Figure 2.1 Composite secondary electron SEM micrograph of the as-deposited low carbon spray coating, showing the microstructure of the top surface placed in contact with the counterface for wear experiments, and the cross-section on which indentation experiments were performed.

Table 2.1 Structural parameters measured for two kinds of steel coatings.

	5130M	1010
Coating thickness (µm)	350±50	250±50
Volume fraction of pores	0.034±0.001	0.062±0.001
Volume fraction of FeO	0.15±0.02	0.22±0.02

2.2.2 Four Point Bending Tests

A four point bending test was used for observing the microstructural aspects of the fracture behaviour of 5130M coatings. The fracture events and crack length were observed and measured during loading of the sample using an optical microscope with large depth of focus as shown in **Figure 2.2**.
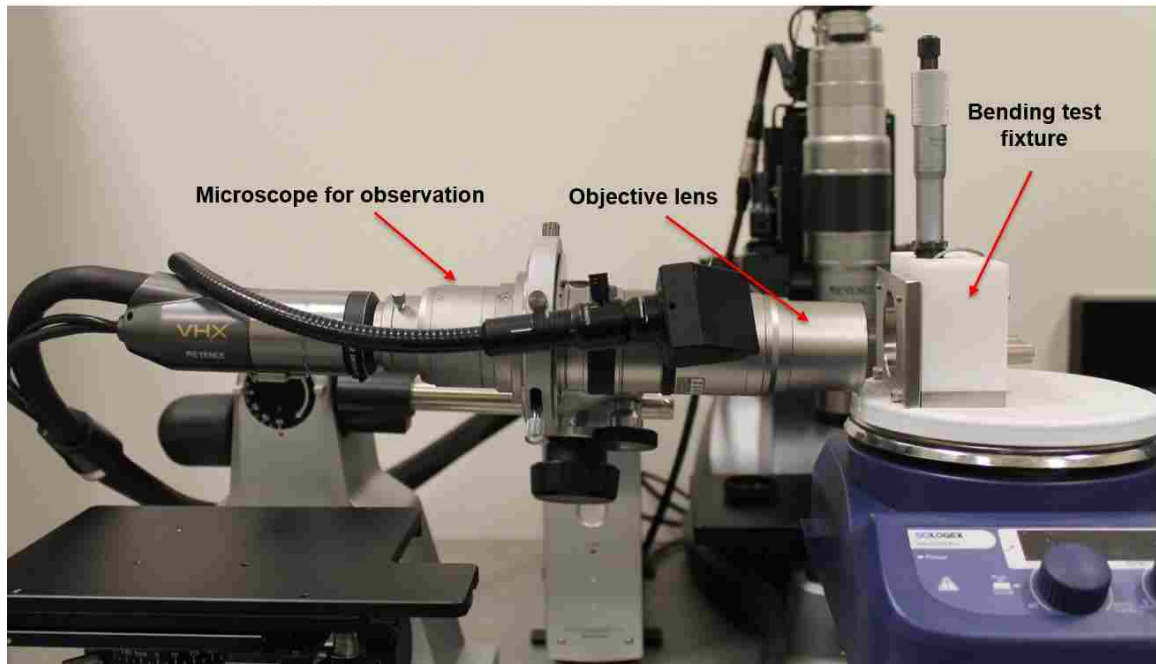
Figure 2.2 Setup for in-situ fracture behaviour observation. Four points bending fixture with coating samples is placed. Keyence optical microscope is placed horizontally for observing and recording fracture behaviour of coatings in bending tests.

The crack initiation, growth and delamination events were identified by observing polished sections of the sample in the plane of bending axis using a digital optical microscope with a large depth of focus during gradual loading of the sample These samples were cut from the cylinder bore into rectangular strips. The samples were placed in the four-point bending fixture fitted with a load cell to measure the applied load. **Figure 2.3** shows the schematic of four point bending test configuration and **Figure 2.3**b is an optical image of coating showing the interlocked morphology of coating-substrate interface before the start of the bending test. The bending load was applied in

a direction normal to this face. During the test, as the applied normal load was increased gradually a bending stress was developed on the plane shown in **Figure 2.3** with the tensile component above the neutral axis increasing with distance d. Thus, the maximum tensile component acted at the surface of the coating. Optical images of the coating were taken using a magnification of 200x and 300x at several stages of the loading process until the sample fractured. The lengths and location of the cracks in the coating were then determined. By determining the crack lengths and orientations with respect to the direction of the tensile stress at each applied load, the stress intensity factors K_I and K_{II} at crack tip of cracks formed in the oxide layers were determined. This fracture mechanics analysis helped to recognize the progress of crack propagation within the coating and at the interface with the aluminum engine bore.
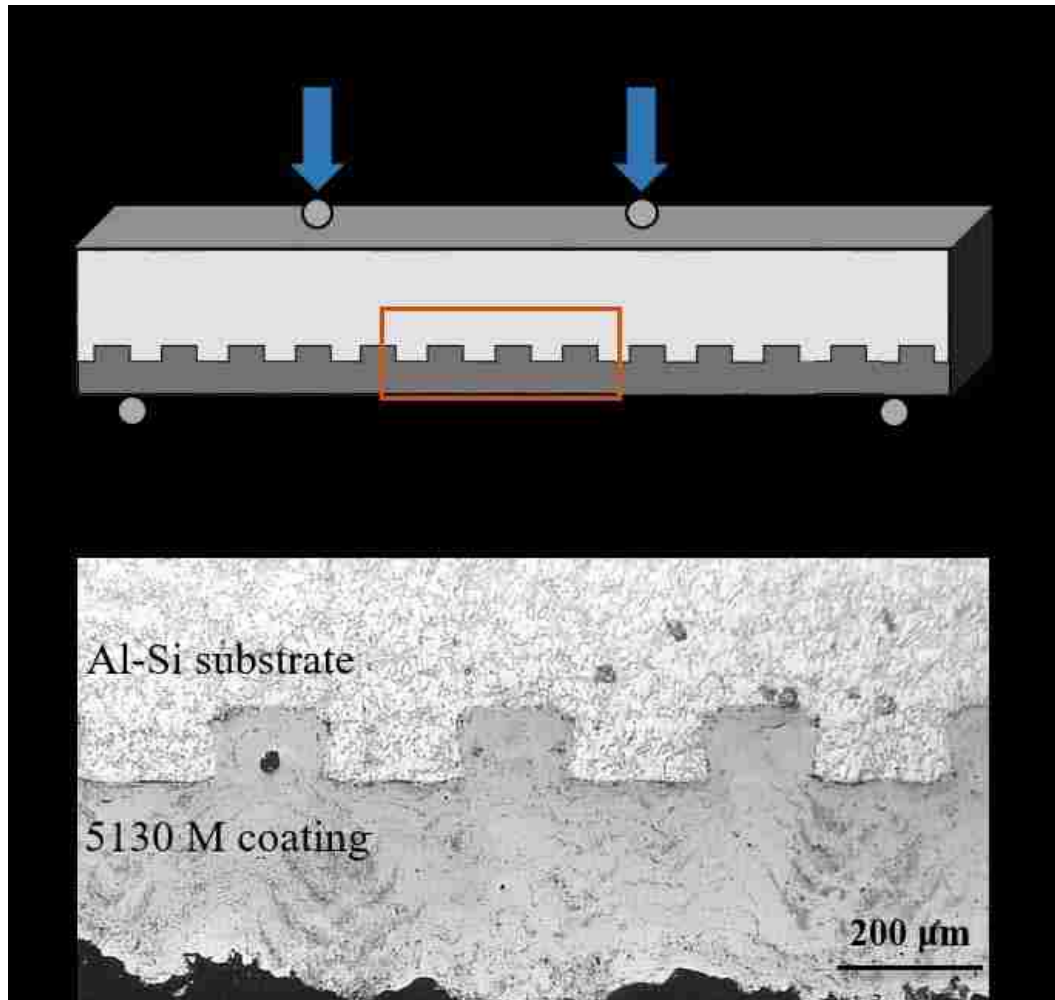
Figure 2.3 Schematic of four-point bending test fixture and image showing coating under test in tensile stress condition. (a) four-point bending fixture and dimensions (the span of lower support is L=16 mm and upper is L_i=6 mm, b=2 mm and d=1.8 mm); (b) cross section showing the coating, and the coating-A380 interface.

Two kinds of samples were prepared, with the coating on top of the interlocks on transverse side (**Figure 2.4a**) and the other was sectioned on longitudinal side with interlock shape could be seen (**Figure 2.4b**). The stress conditions on the coatings during bending tests on the transverse section was regarded as representative of the working condition of cylinder bore when the coating is under hoop expansion stress. Crack propagation process in bending tests was observed and recorded by an optical microscope.
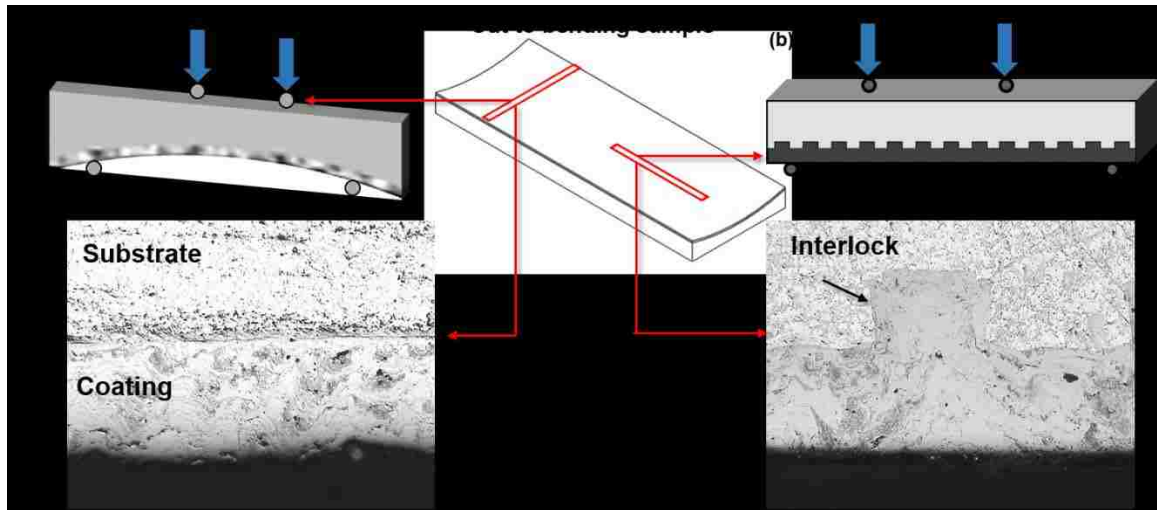
Figure 2.4 Cross-sectional images showing coatings on (a) transverse side coating on the top of interlocks (T) and (b) longitudinal side with interlocks (L).

2.2.3   Examination of Fracture Surfaces

Crack propagation process in bending tests was observed and recorded by an optical microscope. The details of the worn surface morphologies and tribolayers that form during sliding were studied using a FEI Quanta 200 FEG scanning electron microscope (SEM) equipped with an energy-dispersive X-ray EDAX (SiLi Detector) spectrometer. The SEM/EDS technique enabled the accurate detection of formation of an oil degraded tribolayer on the 5130M coating surface after the first stage of sliding of the two-stage sliding lubricated-unlubricated test.

The different oxide phases in the thermal sprayed coatings were identified using a Horiba Raman micro-spectrometer with a 50 mW Nd–YAG laser (532 nm excitation line) equipped with 50× objective lens having a laser spot diameter of 1 μm.

2.3   Results and Discussion

2.3.1   Fracture Mechanisms Operating in Thermal Spray Coatings

Figure 2.5 shows typical cracks formed in the 5130M coatings on samples taken from longitudinal L (a) and transvers T (b) direction (as identified in **Figure 2.4**). The propensity of crack formation in longitudinal direction appears to be higher compared to the transverse direction. Also, after coating failure, delamination on the longitudinal side was localized at two neighboring interlocks close to the long crack. All cracks were initiated from coating surface and propagated towards the interface as expected.
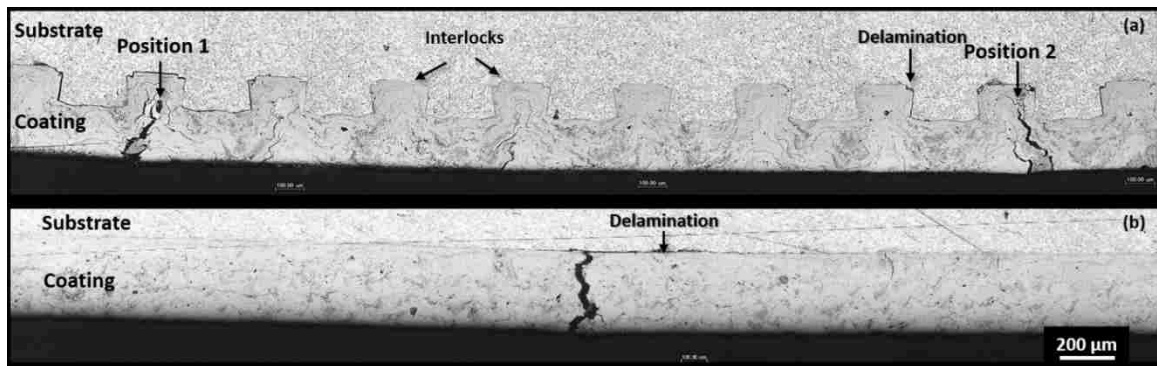
Figure 2.5 Coating failure after bending tests: (a) in longitudinal direction (L2), interlocks could be seen on this side; (b) in transverse direction (T2), coating is on the bottom of interlocks.

Figure 2.6(a) shows a horizontal pre-existing crack. The pre-existing crack parallel to the coating surface did not propagate during the bending test. On the other hand, a crack was formed vertically along oxide layer as shown in **Figure 2.6(b)**. As the load increased, this crack propagated towards the substrate and finally led to coating failure.
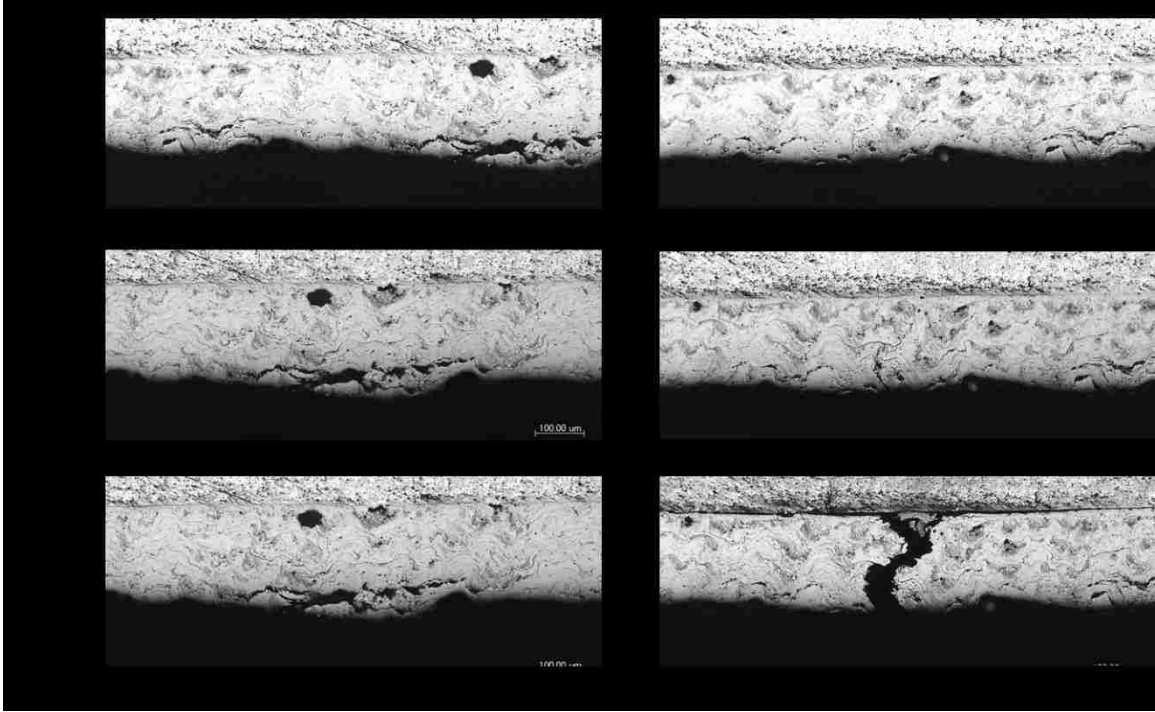
Figure 2.6 Transvers side bending test (T1) showing horizontal (parallel to surface of the coating) and vertical (perpendicular to surface of the coating) defects change during bending test on 5130M coating: (a) no crack propagation along horizontal defect during bending test; (b) crack propagated along vertical defect towards substrate.

To check the fracture behaviour of the coating, a step-by-step detailed four-point bending test was conducted on 5130M coatings. During the test, at each incrementally applied normal load, cross-sectional images of coating were taken as shown in **Figure 2.7**. Optical microscopy images that show the process of crack initiation, propagation and coalescence are presented in **Figure 2.7**. The remote tensile stress generated at the coating surface could be determined for the four-point bending test geometry shown in **Figure 2.3** as:

$$\sigma = \frac{3F(L-L_i)}{2bd^2} \tag{1}$$

where F is load applied, b is the width of sample (1.60 mm), d is thickness of sample (2.72 mm), L is length of bottom support span (16 mm) and L is the length of top loading span (6 mm), see Figure 4a. Accordingly in **Figure 2.7**, the tensile stress generated at coating surface can be

calculated as 275 MPa. It was assumed the tensile stress in the coating decreases linearly along the coating depth. Therefore, the tensile stress at each the tip of crack could be determined as follows:

$$\sigma = \frac{\sigma_{max}\left(\frac{d}{2}-h\right)}{\frac{d}{2}} \tag{2}$$

where h is the depth of each crack tip from the coating surface.
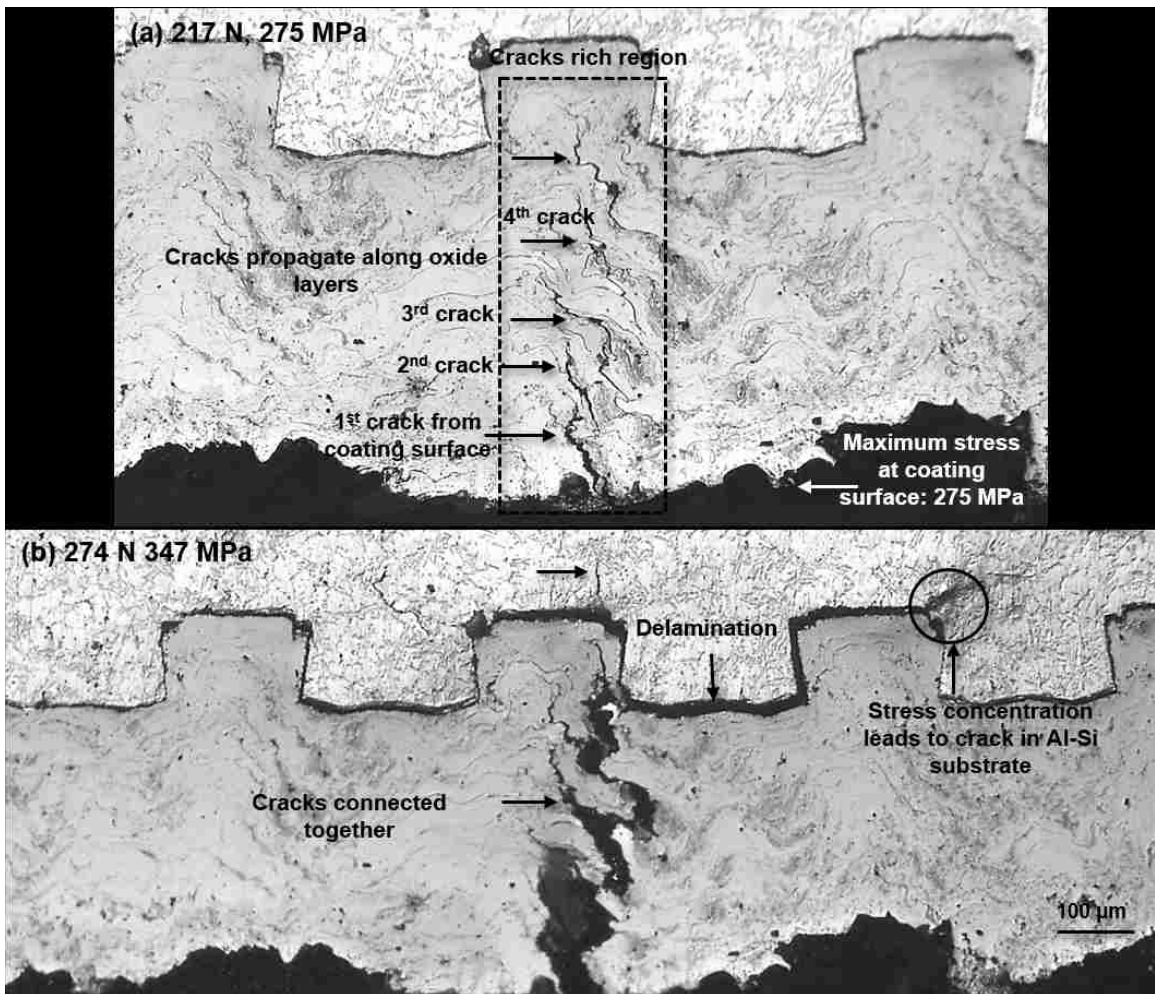
Figure 2.7 5130M coating fracture behaviour under four points bending test. (a) at 217 N load; (b) at 274 N load.

Figure 2.7 shows the changes in the 5130M coating's morphology during the bending test at two applied normal loads namely (a) at 217 N corresponding to a tensile stress of 275 MPa at the coating surface according to Equation 1, and (b) at 274 N corresponding to a tensile stress of 347 MPa at the coating. It is observed the first crack was initiated near the location of the maximum tensile stress adjacent to the coating surface. Then new cracks were formed at the interface between the oxide layers and ferrite matrix by delaminating the interface in a narrow region of 300-400 μm above the initial crack and the sequence by which these cracks were formed is shown in **Figure 2.7a**. At the tip of the cracks formed within the oxide layers, stress intensity exceeded the fracture toughness of ferrite, and the cracks propagated into the ferrite matrix and connected the oxide cracks together forming a single crack with rather torturous path. The stress concentration at the corner of the interlock geometry of the interface appears to have caused a new crack to initiate in substrate.

Based on the observations made on the coating cross-sections during different stages of the bending test, the progress of crack propagation in the 5130M coating could be summarized as shown in **Figure 2.8**. Initially, when coating surface is under a tensile stress of 215 MPa, a crack appears to have formed at an oxide layer near the coating surface possibly as a result of separation of the oxide/iron interface (**Figure 2.8(1)**). This crack propagated along the oxide layer in a slanted angle and possibly as K decreased when the oxide orientation changes the crack propagation stopped at the oxide-ferrite interface. The typical length of an oxide crack is about 140 microns (**Figure 2.8(2)**). However, the new crack formed at the oxide layers acted as an internal flaw; at the tip of the oxide crack the local stresses were intensified. The stress state at the crack tip can be better described using the intensity factor K at the crack tip. As the local K value exceeded fracture toughness of the ferritic matrix as shown in **Figure 2.8(3)** the cracks propagated within the ferrite layers between the oxide layers. Eventually, the oxide cracks were bridged by means of the cracks propagating in the ferritic matrix and complete failure of the coating occurred when these cracks

coalesced to form a single crack across the entire thickness of the 5130M coating. The stress

concentration at the sharp corner of the interlock at the interface is shown **Figure 2.8(4)** in which

initiates a new crack in the Al 380 the substrate. The delamination of the 5130M–A380 interface is

also marked on this figure.
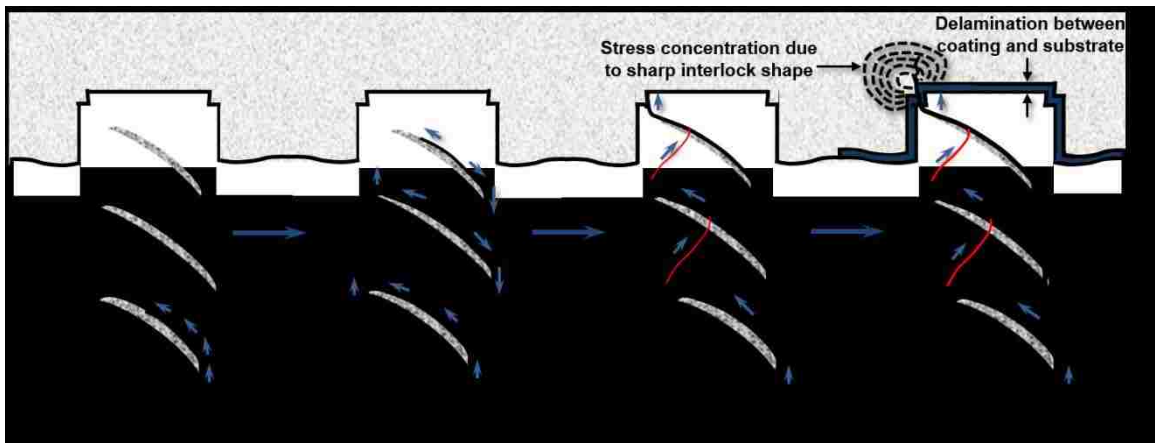
Figure 2.8 Schematic showing the four steps of the fracture of 5130M coating and: 1) Cracks initiate at an oxide layer; 2) Cracks propagate along the oxide layers; 3) Cracks in oxide layers coalesce by fracture of ferrite layers between them; 4) Delamination occurs at the interface between coating and substrate, and stress concentrates at the corner of interlocks on the substrate. The load and corresponding maximum surface tensile stress are given for each step.

As stated previously, the failure process of the thermal sprayed coatings consists of several

stages namely: 1. Cracks initiate at an oxide layer at or near the coating surface; 2. The mode I

crack (opening mode) propagates along the oxide layer and the cracks reaching the α-Fe matrix; 3.

The stress intensified at the crack tip initiates another crack on the oxide layer close to the crack

tip; 4. The new crack propagates along oxide and activates more cracks towards substrate; 5. When

the stress intensity factor is high enough to cause crack propagation into α-Fe matrix, these cracks

coalesce together and the coating failure follows.

Interestingly, oxide layers not only provide crack propagation paths, they can also stop crack

growth if were distributed in a correct direction (perpendicular to the propagation direction of the

main crack). **Figure 2.9** shows a vertical crack propagation process observed in 1010 coating

bending test. The crack was stopped by oxide layers perpendicular to the crack on top of the crack tip. Also as the cracks were formed from these oxide layers, the strain energy of provided to the coating during application of bending stresses was absorbed during formation of new free surfaces at these layers. These perpendicularly distributed oxide layers may therefore be desirable microstructural features as they act as toughening barriers increasing the fracture toughness of the coating.
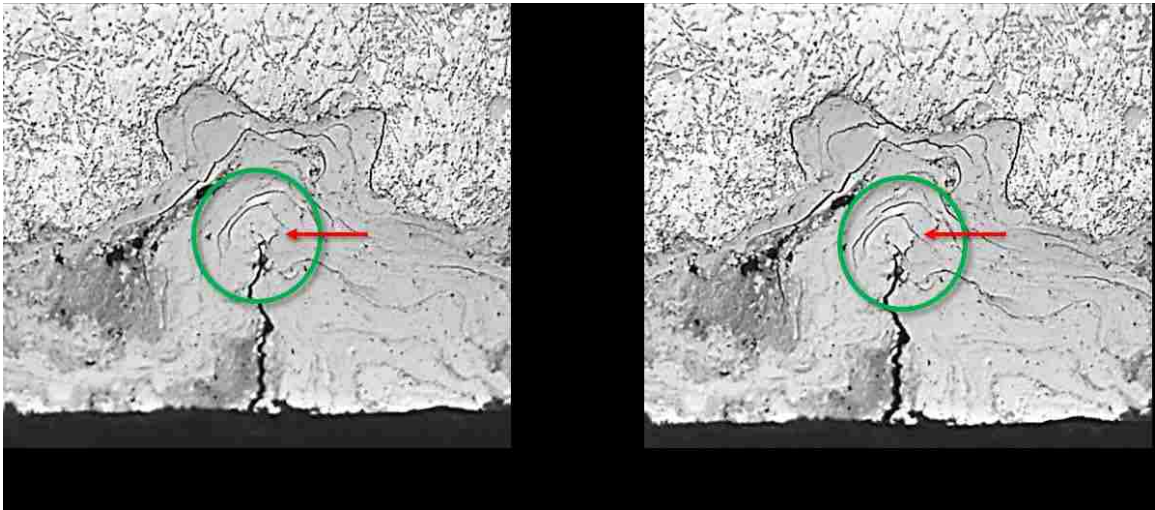
Figure 2.9 1010 bending on longitudinal side with interlocks. The horizontal cracks around vertical crack tip absorbed strain energy when their crack surfaces were formed. These cracks enhanced toughness of 1010 coating by releasing strain energy on themselves.

2.3.2 Fracture Mechanic Analysis of Coating Fracture

With remote tensile stress at a depth corresponding to crack tip position (h) inside the coating obtained from Equation (2), mode I (opening mode), mode II (in plane shear mode) stress intensity factors that occur at the tip of an oxide cracks formed in Figure 7a could be determined by following equations.

$$K_I = \sigma sin^2 \beta \sqrt{\pi a} \tag{3}$$

$$K_{II} = \sigma sin\beta cos\beta \sqrt{\pi a} \tag{4}$$

84

and combined K is given as

$$K = \sqrt{K_I^2 + K_{II}^2} \tag{5}$$

where β is the angle between the crack length orientation and the horizontal axis, which is parallel to the surface of the coating (shown in **Figure 2.10**). Note that the length a is half the crack length of cracks lying inside the coating and the full length of the crack that initiated from the coating surface.
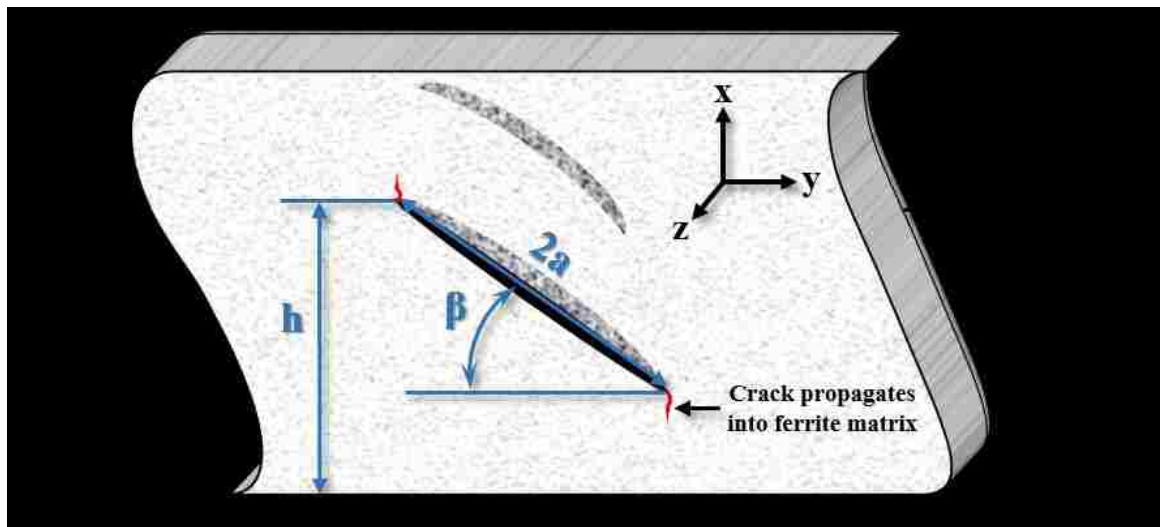
Figure 2.10 Schematic showing the crack tip in an oxide crack and propagation of cracks under the influence of stress intensity fields of K_I and K_{II} in the ferrite layers. $2a$ is the crack length, h is the depth of crack tip inside the coating and β is the angle between oxide and coating surface. The combined stress intensity factor K is the driving force for cracks propagation into ferrite matrix. All the notations and numbers are listed in **Table 2.2**.

Equation 5 shows the combined stress intensity value K and this K is the driving force for crack propagation into the ferritic matrix. It is clear from Equations 3 and 4 that mode I dominates when $\beta > 60\,°$.

The calculation results are listed in **Table 2.2**. Mode I, mode II and combined stress intensity factors at each crack tip were calculated. It can be observed that the stress intensity factors at oxide crack tips are 1.65-3.28 MPa·m$^{1/2}$ for mode I, 0.05-2.30 MPa·m$^{1/2}$ for mode II resulting in a

combined K of 2.52-4.01 MPa·m$^{1/2}$. As the oxide crack angles $\beta > 45°$ for most of the cracks (eg., crack 1, crack 2 and crack 4), $K_I > K_{II}$, which means that the cracks in the ferrite phase propagate under the influence of K_I, namely perpendicular to the remote tensile stress direction. The propagation direction of the cracks in ferrite is shown in **Figure 2.10** which is consistent with the observed crack propagation direction shown in **Figure 2.7**. If the angle β is decreased to 0°, the through coating thickness crack within the ferrite matrix would be much harder to form, and a coating with oxide layers parallel to the coating surface would have higher resistance to fracture.

Table 2.2 Parameters used to calculate stress intensity factors in equations (1-5). β is the angle between the crack and horizontal axis (y axis), σ is the remote tensile stress introduced by bending of the coating, r is the distance between the oxide crack tip and the closest oxide layer, a is the half crack length of an internal crack, K_I is the stress intensity factor applied to the crack opening mode, K_{II} applies to crack sliding mode, K is the combined stress intensity factor.

Crack Geometries and Stress Intensity Factors								
	Crack length (a μm)	Angle β	Remote tensile stress σ (MPa)	Distance from crack tip r (μm)	Intensified stress σ_y (MPa)	K_I (MPa·m$^{1/2}$)	K_{II} (MPa·m$^{1/2}$)	K (MPa·m$^{1/2}$)
Crack 1	120.5	55	251.7	15.4	271.7	3.28	2.30	4.01
Crack 2	50.5	89	236.7	27.2	240.6	2.98	0.05	2.98
Crack 3	81.4	41	240.0	39	69.0	1.65	1.90	2.52
Crack 4	77.4	64	205.2	30.2	166.7	2.59	1.26	2.88

As shown in **Figure 2.8** once oxide cracks form the new cracks emanating from the tip of these cracks tend to propagate vertically into ferrite matrix, which is consistent with the fact that the opening crack mode is the driving force. **Figure 2.7a** shows that cracks are still located at

oxide/ferrite interface, so that the new cracks have not started propagating through the ferrite matrix. Accordingly, it can be suggested that the combined K must be higher than 4.01 MPa·m$^{1/2}$ for crack propagate ion in the ferrite matrix. In other words, the fracture toughness (K_c) of ferrite matrix > 4.01 MPa·m$^{1/2}$.

Table 2.3 lists bending tests results for samples tested in two different directions. The stress intensity factor values were calculated at the highest load applied and the crack length was measured before the coating failure. These K values could be considered as fracture toughness of the coatings with different oxide distributions. The oxide distribution parameters, namely distribution angle, oxide layer length and the distance between oxide layers would control the fracture toughness of the thermal sprayed coatings. The stresses at crack tips are also listed in Table 2.3. It should be noted that the high stress field around the crack tip is the reason for crack initiation on an adjacent oxide layer whereas the stress intensity factors provide the driving force for crack propagation.

On transverse direction, the maximum K value (1.92 MPa·m$^{1/2}$) observed was less than that in the longitudinal direction (4.01 MPa·m$^{1/2}$ for L1 and 4.09 MPa·m$^{1/2}$ for L2) due to the shorter distance between the oxide layers. The oxide layers around vertical crack tip coating provided the highest fracture toughness (6.11 MPa·m$^{1/2}$) to the 10101 coating because of the toughening effect of perpendicularly distributed oxides.

2.3.3 Possible Improvements in the Oxide Morphologies to Increase Thermal Spray Coatings' Fracture Resistance

Based on the calculations, it can be suggested that if the microstructure of the coating could be modified, the fracture resistance of the 5130 M coatings can be improved. Figure 2.11 shows three potentially useful methods to improve spray deposited coatings' fracture performance. These consist of the following:

Table 2.3 Fracture toughness of 5130M coatings on different samples. σ is remote tensile stress introduced by bending of the coating, β is the angle between the crack and the horizontal axis, a is the half crack length of an internal crack, K is fracture toughness measured at maximum load before coating fracture in crack opening mode.

Crack Geometries and Stress Intensity Factors								
	Crack Length ($2a$ μm)	Angle β	Remote tensile stress σ (MPa)	Distance from crack tip r (μm)	Intensified stress σ_y (MPa)	K_I (MPa·m$^{1/2}$)	K_{II} (MPa·m$^{1/2}$)	K (MPa·m$^{1/2}$)
5130M L1	120.5	55	251.7	15.4	271.7	3.28	2.30	4.01
5130M L2 position 1	102.3	89	283.2	12.1	433.2	3.59	0.09	3.59
5130M L2 position 2	138.3	73	278.3	18.37	316.9	3.75	1.62	4.09
5130M T Vertical crack	175.8	83	115.3	5.48	321.4	1.89	0.33	1.92
5130M T Horizontal crack	194.1	7.5	115.3	8.8	-12.65	0.03	0.37	0.37
1010 Crack 187 N	510	90	227.8	57	363.2	6.12	0	6.12

1. Decreasing the angle β between the oxide layers and coating surface. Cracks are harder to propagate along the horizontal direction. For example, according to Equations 3 and 4 if angle β decreases from 60° to 30°, the combined stress intensity factor K would decrease by 42%. As mentioned earlier, if β were decreased to 0°, cracks would be forced to propagate in a sliding mode which would make crack propagation in the ferrite matrix harder, increasing the fracture toughness of the coating;
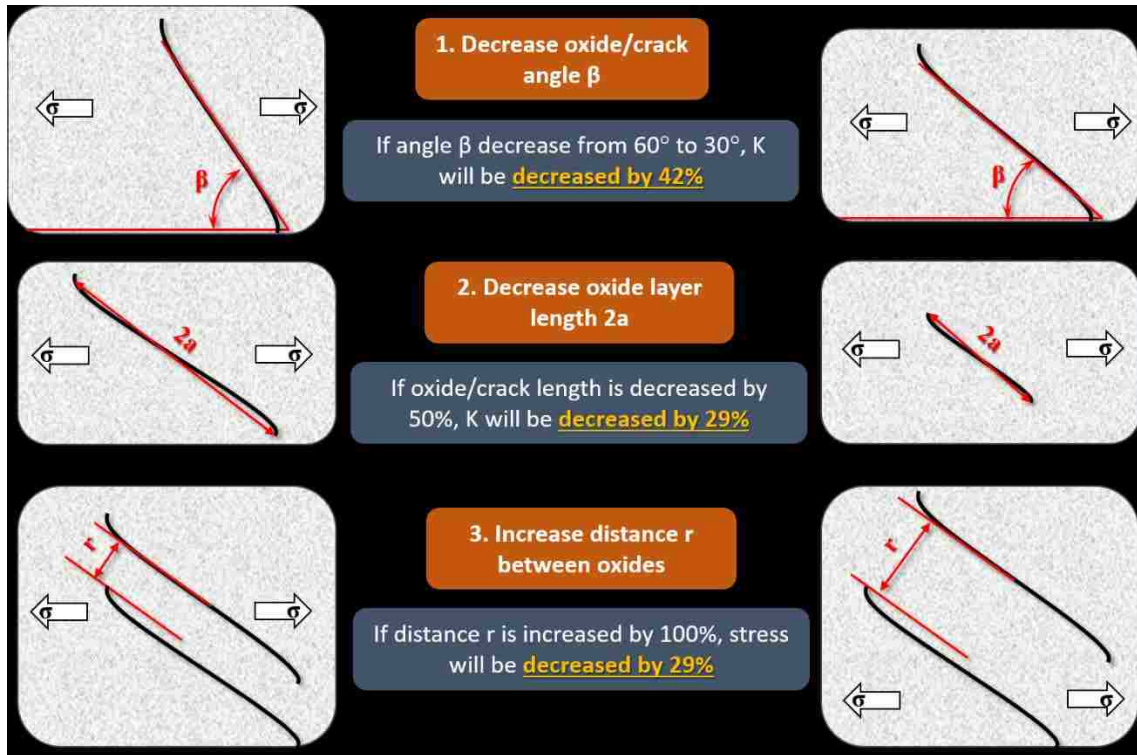
Figure 2.11 Proposed microstructural optimization methods for improving fracture toughness of the thermal spray coatings: 1.Decreasing the angle that the oxide layer makes with coating surface; 2. Decreasing average oxide layer length; 3. Increasing the distance between the oxide layers.

2. Decreasing oxide layer length 2a. Cracks were initially formed at the oxide layers and the crack length would be expected to be limited to the oxide layer length. For example, for a crack to propagate at a constant angle, if oxide length is decreased by 50%, based on equations 3-5, K would be decreased by 30 %;

3. Increasing the distance between the oxide layers. If the distance is increased to twice the original one, the stress intensity factor would need to be 29% higher to initiate cracks on nearby oxides, which makes it harder to generate cracks at neighbouring oxide sites.

2.4   Conclusions

Four-point bending tests were performed on a low carbon steel (AISI 1010 and 5130) with a thermal spray coating to understand the coating's fracture behaviour. A fracture mechanics analysis was used to understand the influence of the oxide layer distribution. The main conclusions can be summarized as follows:

1. Four-point bending tests were performed on both longitudinal and transverse directions to study the fracture behaviors of the coatings. K_I values were measured to be from 3.28 to 3.75 MPa·m$^{1/2}$ with the presence of interlocks, influenced by the distribution factors (angle, length and distance between) of oxide layers. Without interlock, the K_I was decreased to 1.89 MPa·m$^{1/2}$;

2. Oxide layers not only act as crack propagation paths, they could also stop crack growth if they are distributed perpendicular to each other. It was found that the perpendicular distributed oxide layers could increase the K_I to 6.12 MPa·m$^{1/2}$;

3. Crack coalescence and delamination occurred leading to the fracture of 5130M coating during the bending tests. It was observed that the cracks propagated along the oxide veins that were oriented >45 degrees to the direction of maximum tensile stress and cracks in the ferrite layers propagated at the tip of oxide cracks under the influence of mode I type stress intensity factor. A fracture mechanics analysis of coating fracture was presented leading to recommendation on microstructural design of the coatings.

Based on the fracture mechanics analysis, the coating microstructure optimization methods are proposed: 1. decrease the oxide layer angle; 2. decrease the length of oxide layers; 3. increase the distance between oxide layers.

2.5   Bibliography

[1] A. Edrisy, T. Perry, Y.T. Cheng, A.T. Alpas, The effect of humidity on the sliding wear of plasma transfer wire arc thermal sprayed low carbon steel coatings, Surf Coat Tech, 146 (2001) 571-577.

[2] A. Edrisy, T. Perry, Y.T. Cheng, A.T. Alpas, Wear of thermal spray deposited low carbon steel coatings on aluminum alloys, Wear, 251 (2001) 1023-1033.

[3] H. Herman, S. Sampath, R. McCune, Thermal spray: Current status and future trends, Mrs Bull, 25 (2000) 17-25.

[4] A. Rabiei, D.R. Mumm, J.W. Hutchinson, R. Schweinfest, M. Ruhle, A.G. Evans, Microstructure, deformation and cracking characteristics of thermal spray ferrous coatings, Mat Sci Eng a-Struct, 269 (1999) 152-165.

[5] A. Rabiei, A.G. Evans, Failure mechanisms associated with the thermally grown oxide in plasma-sprayed thermal barrier coatings, Acta Mater, 48 (2000) 3963-3976.

[6] P.K. Wright, A.G. Evans, Mechanisms governing the performance of thermal barrier coatings, Current Opinion in Solid State & Materials Science, 4 (1999) 255-265.

[7] L. Pawlowski, P. Fauchais, Thermal Transport-Properties of Thermally Sprayed Coatings, Int Mater Rev, 37 (1992) 271-289.

[8] V.V. Sobolev, J.M. Guilemany, J. Nutting, J.R. Miquel, Development of substrate-coating adhesion in thermal spraying, Int Mater Rev, 42 (1997) 117-136.

[9] N.H. Faisal, R. Ahmed, A.K. Prathuru, S. Spence, M. Hossain, J.A. Steel, An improved Vickers indentation fracture toughness model to assess the quality of thermally sprayed coatings, Eng Fract Mech, 128 (2014) 189-204.

[10] C.K. Lin, C.C. Berndt, Measurement and Analysis of Adhesion Strength for Thermally Sprayed Coatings, J Therm Spray Techn, 3 (1994) 75-104.

[11] S.J. Howard, T.W. Clyne, INTERFACIAL FRACTURE-TOUGHNESS OF VACUUM-PLASMA-SPRAYED COATINGS, Surf Coat Tech, 45 (1991) 333-342.

[12] A.S.M. Ang, C.C. Berndt, A review of testing methods for thermal spray coatings, Int Mater Rev, 59 (2014) 179-223.

CHAPTER 3

INDENTATION FRACTURE BEHAVIOUR OF LOW CARBON THERMAL SPRAY COATINGS: ROLE OF DRY SLIDING-INDUCED TRIBOLAYER

3.1   Introduction

Due to their high strength-to-weight ratios, lightweight Al-Si alloys are widely used for automotive applications for reducing carbon footprint. However, the major drawbacks of Al-Si alloys are poor wear resistance and unprotected surfaces that would suffer from cold-scuff failure [1-3]. Owing to the superior wear resistance of thermal spray coatings, these coatings have been used as substitutes for iron liners in cylinder bore for reducing weight, lowering cost and reducing emissions. Wear experiments performed with the coated samples showed that the wear rates decreased at high loads and sliding velocities due to the formation of a thick protective oxide film accompanied by hardening of the sliding surface [4-6].

Thermal spray coatings are formed by rapid solidification and stacking of molten source material splats by multiple passes of a spray torch. The spreading of the molten particles during splat formation, along with other important artefacts such as oxides, cracks and porosities construct the unique microstructure of thermal spray coatings [7-9]. Conventional Vickers indentation experiments as well as nano-indentation tests were used to investigate the mechanical properties of coated systems. Korsunsky et al. performed indentations using loads ranging from 0.5 gf to 3.0×10^4 gf to study the differences in coating- or substrate-dominated responses in the measured hardness values. The hardness of the coating itself could be calculated by plotting hardness as a function of the ratio of normalized indentation depth to coating thickness. With this method, the hardness of PVD coatings including TiN (32 GPa), NbN (40.5 GPa) and CrN (31.4 GPa) deposited on steel substrates were measured [10]. Evans et al. [11] proposed relationships between K_{1c},

hardness, radius and crack length of residual indents by analysing the data obtained after performing indentations on ceramic materials like WC-12Co, Si_3N_4, SiC, BC and sapphire. Using the same technique, Lima et al. [12] calculated K_{1c} of thermal sprayed WC-12%Co coatings (K_{1c} = 1.6 ± 0.9 MPa·m$^{1/2}$) on AISI 1020 steel substrate by measuring the interlamellar crack length described in the equation proposed by Niihara [13]. Using nano-indentation techniques, Bhattacharya and Alpas [14] measured the mechanical properties (hardness = 3.45 ± 0.17 GPa and elastic modulus = 116.30 ± 6.64 GPa) of the tribofilms that formed on the silicon particles in Al-Si alloys and stated that the tribofilm reduced the probability of fracture during sliding contact. In absence of the tribofilm, cross-sectional FIB/SEM showed that surface and subsurface lateral cracks were formed that led to chipping fracture in the silicon particles [14, 15]. For a thermal spray coating manufactured by HVOF, Rabiei et al. [16] measured the coating's elastic modulus as 200 GPa and hardness as 3 GPa using nanoindentation experiments. The fracture toughness (K_{1c}) was measured in the range of 0.6-1.5 MPa·m$^{1/2}$ using cracks located near the Fe/FeO interface. It was suggested that the low K_{1c} of the interfacial oxide may act as crack initiation sites and lead to splat delamination during frictional contact of thermal spray ferrous coatings. Deformation and cracking in thermal spray coatings were found to be related more to the morphology of the coatings than their mechanical properties. Therefore, there is a need to study the mechanical properties of thermal spray coatings considering the effect of the distribution of the oxide layers within the coating.

The objective of this work is to study the fracture behaviour of an AISI 1010 (0.1%wt. C steel) coating thermally sprayed on an Al-Si substrate. The paper is organized in two sections: first, by examining the pattern of cracks formed during micro-indentation experiments, the different types of coating damage were distinguished and characterized in terms of fracture of the oxides and separation of oxide layers causing chipping. Then dry sliding reciprocating wear tests were conducted where tribolayers were generated on the wear track. The mechanical properties of the tribolayers were investigated. Thereafter the effect of the tribolayer on the crack formation

mechanisms were studied. Weibull statistical distribution was used to calculate the probability of chipping fracture in the coating with and without the sliding-induced tribolayer. The effect of crack growth and instability conditions were discussed using the *R*-curve behaviour of the coating with and without the tribolayer.

3.2   Experimental

3.2.1   Description of the thermal spray coating properties and indentation experiments

The ferrous thermal spray coating was deposited on the surfaces of substrates made from an Al-9wt.%Si cylinder bore and had a thickness of 240 μm **Figure 3.1** is a composite secondary electron (SE)-SEM image of the as-received low carbon thermal-spray coating showing the top surface (plane-view) and the cross-sectional view, which is in the direction parallel to the piston movement. During thermal spray deposition, coatings are formed by stacking of flattened α-Fe splats [17] and the oxides (FeO) formed at the splat boundaries. In addition, in certain regions FeO aggregates could be observed. The total fraction of the oxide aggregates and oxide stringers was determined to be 22.3±1.4 % by quantitative metallography. On the other hand, the cross-section primarily consisted of oxide stringers formed along the α-Fe splats. The splats consisted of flattened α-Fe grains and the length, width and aspect ratio of the splats can be seen in **Table 3.1**. The honed top surface with 51.2±6.7-μm-long and 29.5±7.2-μm-wide splats was removed by metallographic polishing. The distance between the oxide stringers along with the diameter of the oxide aggregates measured from both the top surface and cross-section has also been listed in Table 1. Although the size of the oxide aggregates on the top surface were about 2.4 times higher than those observed in the coating cross-section, the inter-stringer distances in both the faces were comparable.
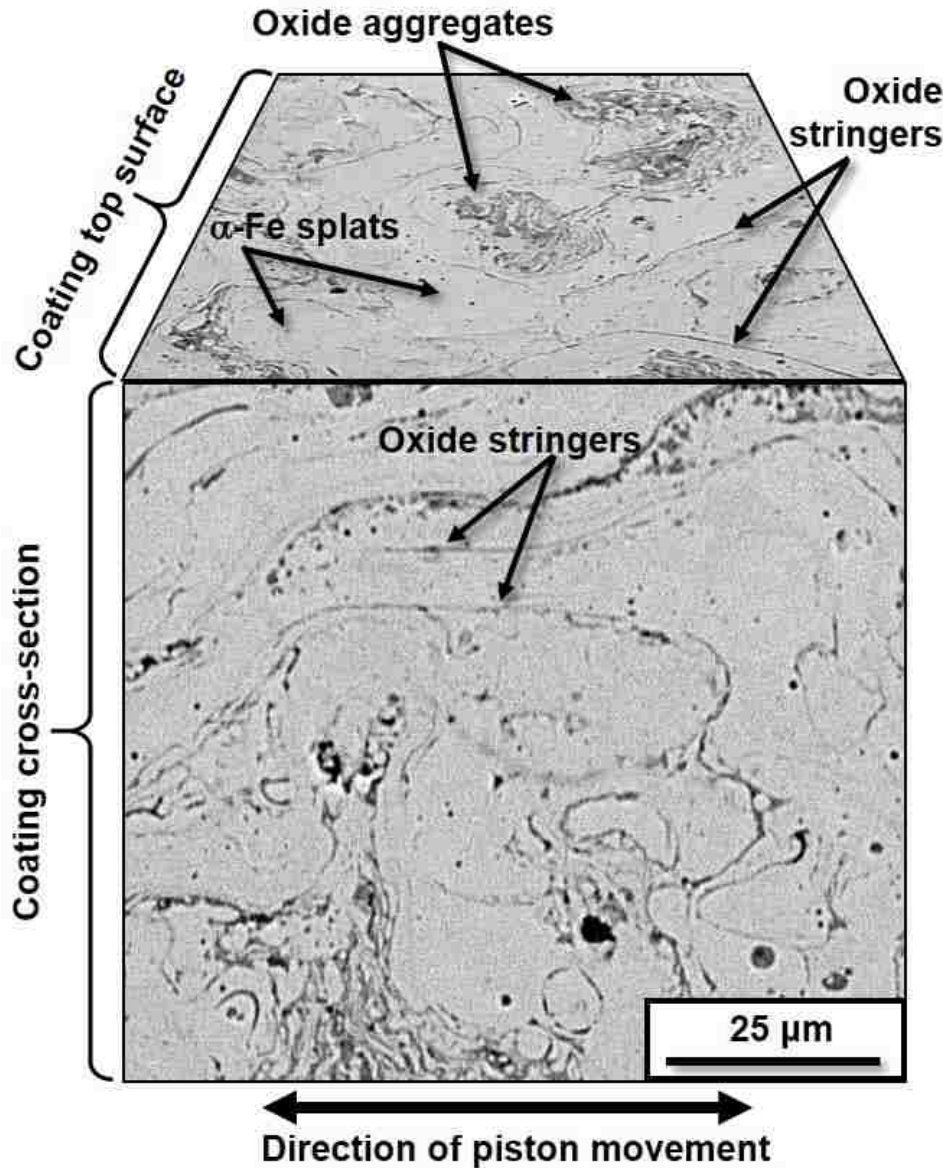
Figure 3.1 Composite secondary electron SEM micrograph of the as-deposited low carbon spray coating, showing the microstructure of the top surface placed in contact with the counterface for wear experiments, and the cross-section on which indentation experiments were performed.

Micro-indentations were performed on the low carbon spray coating for investigating the deformation, fracture and damage accumulation in the coating as a function of the indentation load. Nano-indentation tests were performed using the Nano Indenter XP from MTS and Hysitron TI 900 TriboIndenter™ using a Berkovich indenter on different locations of the top surface of the

coating. Both the nanohardness and the elastic modulus of the coating before and after generation of the sliding-induced tribolayer (see section 2.2) were measured.

Table 3.1 Parameters measured on each face of the low carbon spray coating.

Low carbon spray coating surface	Diameter of oxide aggregates (μm)	Distance between oxide stringers (μm)	Dimensions of α-Fe splats		
			Length (μm)	Width (μm)	Aspect ratio
Top	203.2±28.2	22.8±2.0	51.2±6.7	29.5±7.2	1.8±0.4
Cross-sectional	84.0±9.8	20.2±3.0	57.7±7.0	6.3±1.8	9.7±2.9

3.2.2 Description of reciprocating wear tests

Dry sliding tests were conducted using a reciprocating (CSM) tribometer at room temperature. The surface area of the rectangular low carbon spray coatings prepared for the sliding tests were 20.5×2.3 mm^2 and the sample thickness was 1.2 mm. Prior to the sliding tests, the coated specimens were polished with progressively smaller diamond polishing abrasives available in 3.0, 1.0 and 0.1 μm sizes in liquid suspensions. The samples were cleaned ultrasonically. The average surface roughness of the sample obtained after fine polishing was R_a = 31.4±6.5 nm according to white-light interferometry measurements. 10.1-mm-long segments of rings coated with CrN (a common top compression ring (TCR) coating [18, 19]), with a width of 2.7 mm and a height of 1.2 mm, were used as the counterface. The R_a of the ring was measured as 203.6±27.4 nm. During the reciprocating sliding, the stroke length was maintained at 10 mm and a normal load of 5 N was used that corresponded to a Hertzian contact pressure of 52.4 MPa. A schematic diagram of the experimental setup is shown in **Figure 3.2**. Dry sliding tests were conducted for 2×10^4 cycles. The COF measured during the experiments is shown in **Figure 3.3**. It can be seen that the friction curve had a running-in COF of 0.25. The average steady state COF was 0.14±0.05.
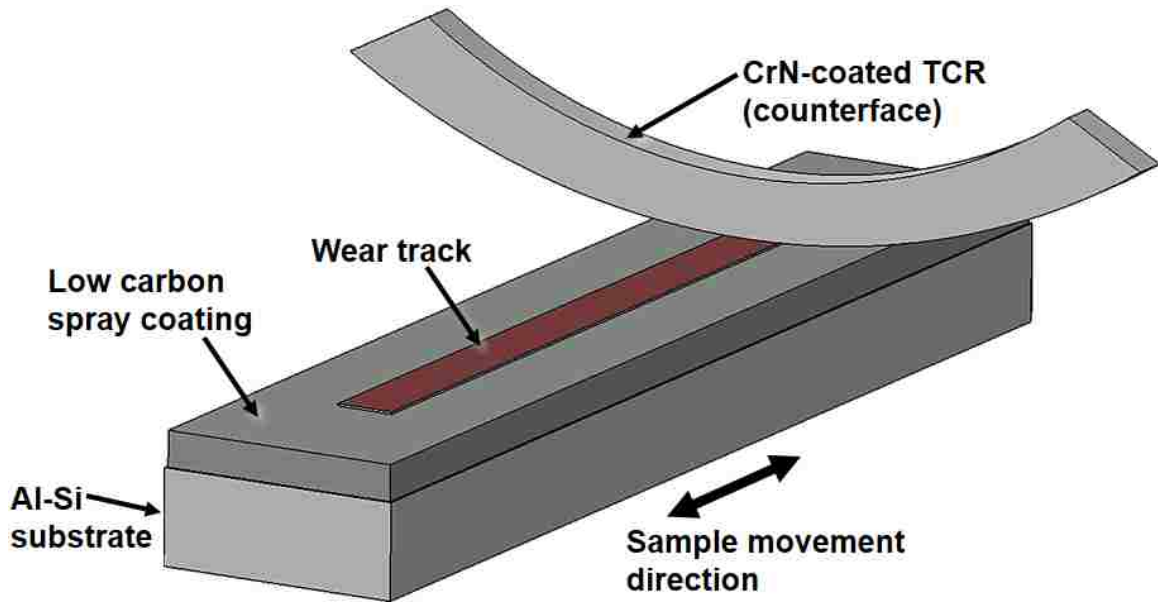
Figure 3.2 Schematic diagram of the experimental setup for reciprocating wear tests.
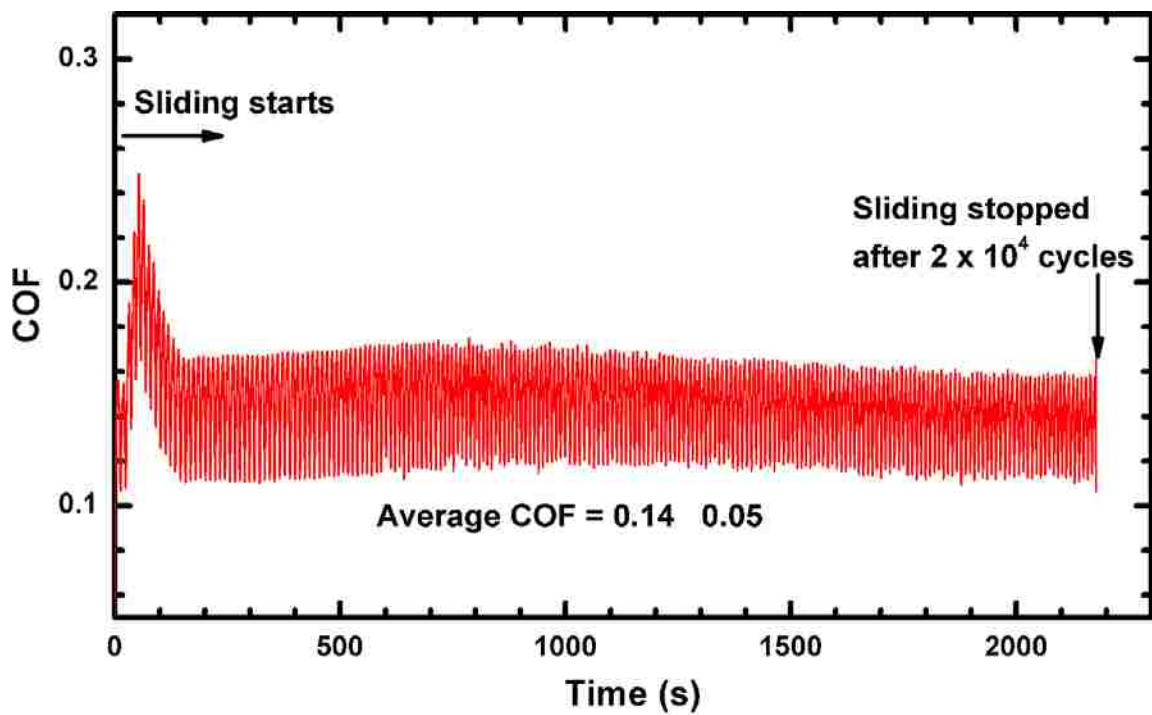
Figure 3.3 COF data obtained during dry sliding reciprocating wear experiments with low carbon spray coating samples for 2×10^4 cycles.

3.2.3 Description of tribolayers formed during dry sliding reciprocating wear tests

An optical microstructure of the wear track formed on the low carbon coating surface after reciprocating wear experiments is shown in **Figure 3.4(a)**. It can be seen that a layer of dark contrast was formed at the centre of the wear track along the sliding direction. In addition, optically transparent layers were observed to form at both the edges of the wear track. The surface profile of the wear track showing the topographical variations of the central tribolayer and the edge layers are shown in a 3-dimensional optical profilometry image shown in **Figure 3.4(b)**. The layers formed at the edges were, in fact, compacted wear debris that were pushed to the edges during the reciprocating action of the counterface. The thicknesses of the edge debris and the tribolayer was calculated from the two-dimensional contour plot of the cross-section obtained along a horizontal line, A-B, across the wear track in **Figure 3.4(b)** and shown in **Figure 3.4(c)**. The edge debris had a thickness of 4.1±0.6 μm and the thickness of the tribolayer was measured as 770±261 nm. The composition of the tribolayer was analyzed as described in section 2.2.4 and results are given in section 2.3.2.
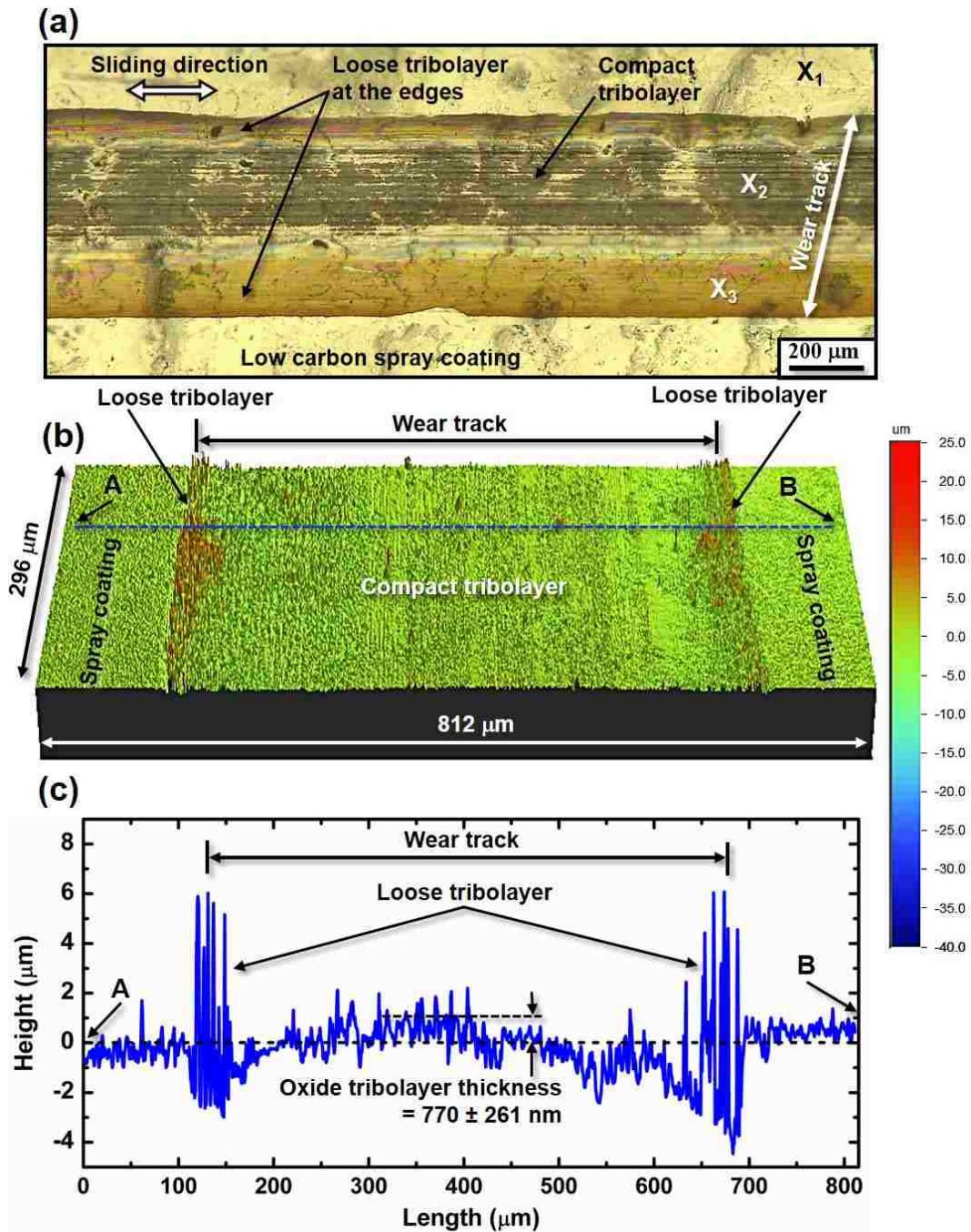
Figure 3.4 (a) Optical microstructure of the wear track formed on the surface of the low carbon spray coating. Thick oxides could be seen to be formed at both the edges of the wear track. (b) A 3-dimensional surface profilometry image of the wear track showing the elevated topography of the debris at the edges and (c) a 2-dimensional cross-sectional profile scanned along a horizontal direction A-B marked in (b) showing the thickness of the oxide tribolayer at the centre of the wear track.

3.2.4 SEM, Raman spectroscopy and optical profilometry

The low carbon spray coating, residual indents and the features of the worn surfaces on the coated samples were observed using an FEI Quanta 200 FEG scanning electron microscope (SEM). The morphologies of the wear tracks and the tribolayers were also examined using an optical surface profilometer (WYKO NT1100) in the vertical-scanning interferometry (VSI) measurement mode.

Raman spectroscopy was used to analyze the composition of the oxides in the coating and on the tribolayers. A 50 mW Nd-YAG solid-state laser diode, emitting a continuous wave laser at the 532 nm excitation line, was used for generating Raman signals. The resulting Raman spectra were recorded using a Horiba spectrometer equipped with a CCD detector. The diameter of the laser spot focused on the specimen surface using a 50× objective was 1 μm.

3.3   Results and Discussion

3.3.1 Indentation morphology and phenomenological description of coating fracture

Microindentation experiments were performed on the cross-sections of the coatings to observe their indentation-induced deformation and fracture behaviour. Typical damage features are shown in Figure 5. An SE-SEM image of a micro-indentation performed at 10 gf (**Figure 3.5(a)**) shows the indenter was placed on an oxide-rich region. The FeO aggregates fractured even at this low load. The cracks initiated in the oxide propagated between adjacent α-Fe splats but were then arrested by other oxide layers with orientations that were perpendicular to the direction of the crack propagation. The oxide fragmentation, propagation and arrest of cracks are also schematically shown in **Figure 3.5(b)**. **Figure 3.5(c)** shows an SE-SEM image of an indentation performed at 25 gf primarily on the ductile α-Fe. Thus, no oxide fragmentation occurred but the oxide stringers

101

within the plastic zone around the indentation were separated. The separation of oxide stringers led to crack propagation between the adjacent α-Fe splats. These processes are depicted in the schematic of **Figure 3.5(d)**. At higher loads (e.g., 50 gf), the crack propagation due to oxide stringer separation typically led to occurrence of chipping-type fracture as can be seen in **Figure 3.5(e)**. **Figure 3.5(f)** shows the schematic description of chipping where plastic deformation of the α-Fe matrix caused volume expansion and subsequently separation of oxide occurred between the adjacent α-Fe splats.
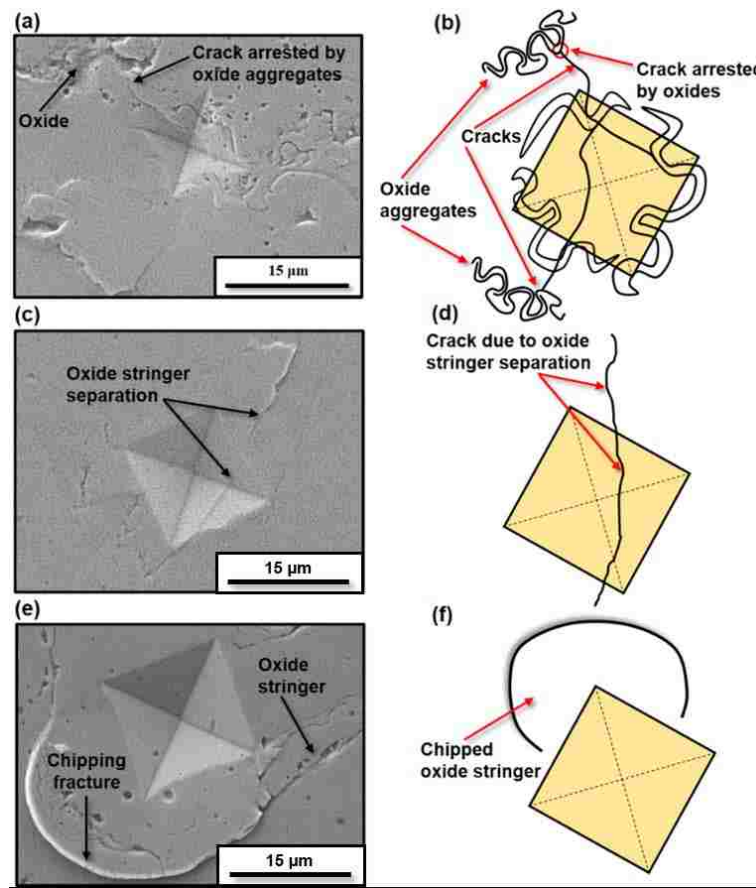
Figure 3.5 (a) SE-SEM image of an indentation performed on the low carbon spray coating at 10 gf. (b) Schematic illustration of fragmentation of oxide aggregates and arresting of cracks by neighbouring oxide aggregates. (c) SE-SEM image of an indentation performed at 25 gf; (d) Schematic illustration of crack arising out of stringer separation. (e) SE-SEM image of an indentation performed at 50 gf; and (f) Schematic illustration showing chipping fracture due to separation of oxide stringer from the matrix.

Figure 3.6(a) shows a cross-sectional SE-SEM image of an indentation placed on the Fe-matrix at 100 gf that caused chipping by separation of the oxide stringers in the near-surface region. The oxide stringers that were fractured leading to crack formation in the subsurface region is marked. Giannakopoulos and Suresh [20] suggested that the radius (R_p) of the indentation-induced plastic deformation zone can be expressed in terms of applied indentation load, L, and the yield strength Y, as $R_p = \sqrt{0.3L/Y}$. Considering Y of 1010 steel as 330 MPa [21], R_p was 29.8 μm when a 100 gf load was applied. This is consistent with the observation in **Figure 3.6(a)** where the separated oxide stringers were within plastic zone caused due to indentation with a 100 gf load. The crack formed due to stringer separation reached the surface and caused chipping at the vicinity of the indentation (**Figure 3.6(b)**). The cross-sectional view of an indentation impression formed at 300 gf on an oxide aggregate can be seen in **Figure 3.6(c)**. In this case, R_p was calculated as 51.7 μm. Within the plastic zone, fracture of the oxide particles located below the indenter can be seen. Fractured and fragmented oxide particles is also observed in the plane-view image of the indentation in **Figure 3.6(d)**.
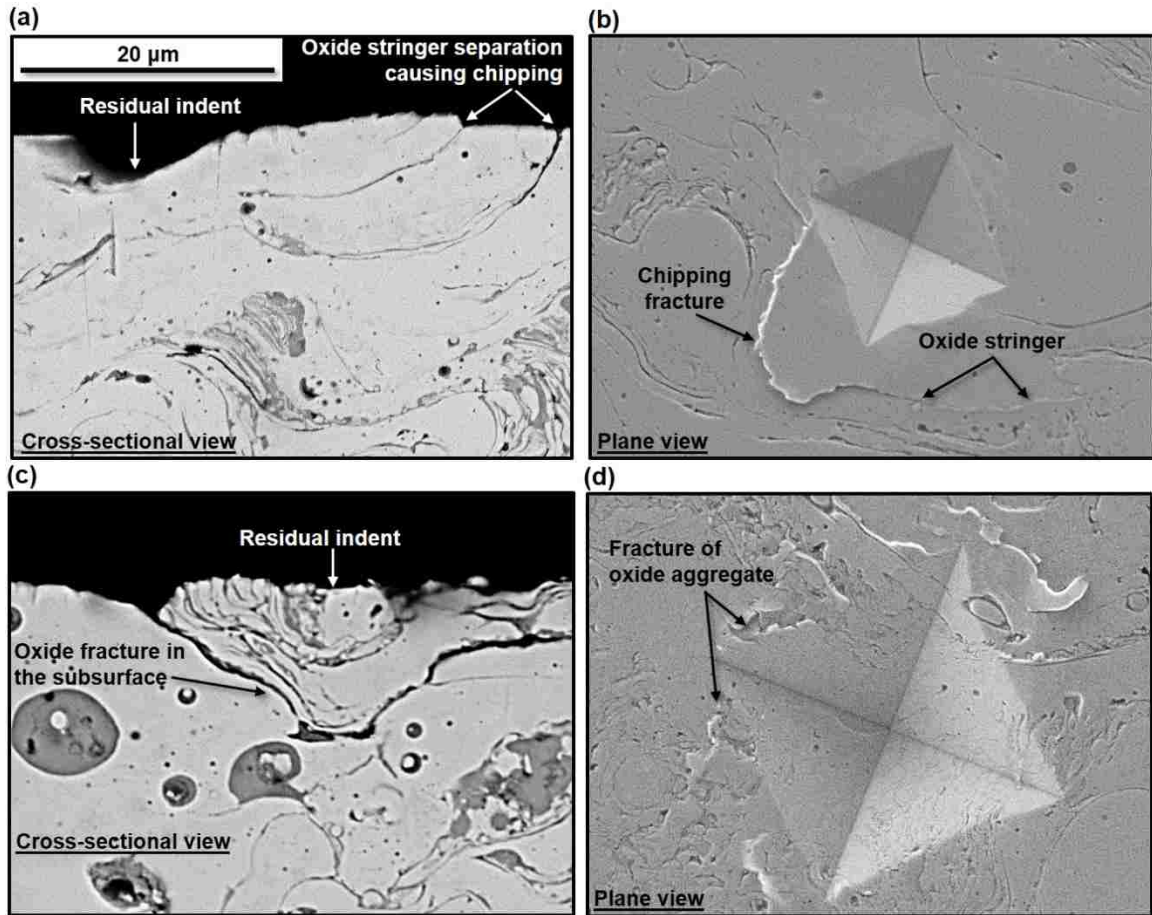
Figure 3.6 Plane-view SEM images of indentations performed on the low carbon spray coating at (a) 100 gf load showing chipping fracture, and (b) 300 gf load showing fracture of oxides within the residual indent. Cross-sectional SEM images of indentations performed at (c) 100 gf showing separation of oxide splats in the subsurface leading to chipping fracture, and (d) 300 gf showing fractured oxides in the subsurface.

Figure 3.7(a) shows the load-displacement curve obtained after nanoindentation of the matrix. The nanohardness of the matrix was 4.7±0.2 GPa whereas the elastic modulus was measured as 190.8±1.1 GPa. The optical microstructure of the corresponding nano-indentation on the steel matrix is shown in **Figure 3.7(b)**. A typical load-displacement curve obtained after nanoindentation of the oxide-rich regions is shown in **Figure 3.7(c)**. The nanohardness of the oxide-rich regions was 3.0±0.8 GPa, their elastic modulus was 93.9±17.9 GPa. During the indenter loading stage, multiple 'pop-in's were observed as shown in the inset of **Figure 3.7(c)**. The occurrence of the 'pop-in's in the loading curve possibly indicated oxide particle fracture events

104

within the FeO agglomerate even at a load as low as 600 mN. The energy expended for oxide fracture, obtained by calculating the work done during the loading stage of the nano-indentation tests (from the initiation of loading to the point of pop-in) shown in **Figure 3.7(c)**, was 272±31 nJ. Microstructure of the corresponding nano-indent on the oxides is shown in **Figure 3.7(d)** that provide evidence of fracture of oxides.
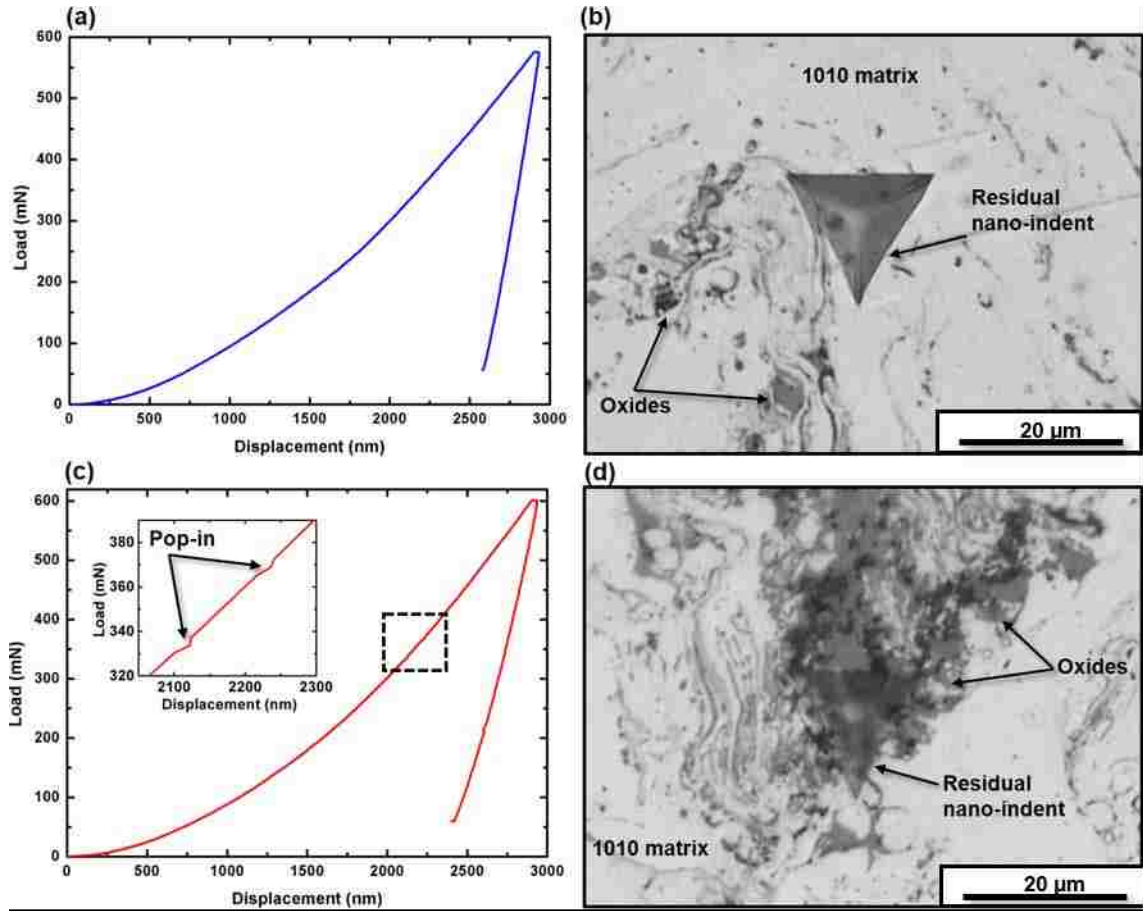
Figure 3.7 (a) Load-displacement curve obtained during nano-indentation on the matrix of the as-received low carbon spray coating; (b) optical microstructure of the residual Berkovich indent on the coating matrix; (c) load-displacement curve obtained during nano-indentation on an oxide-rich region of the as-received coating. Inset showing 'pop-in's observed during the loading stage possibly occurring due to crack propagation along the oxide/matrix interface; (d) optical microstructure of the residual Berkovich indent on an oxide aggregate.

In summary, indentations on the matrix would lead to separation between Fe-splats by means of crack propagation at the FeO stringers located within the indentation plastic zone. Splat

separation led to their chipping. Particles within the oxide aggregates would fracture at the lowest load but the probability of chipping-type fracture would depend on the load applied and presence of tribolayers generated during sliding experiments.

3.3.2 Chemical and mechanical characterization of the tribolayer generated on the low carbon spray coating

It is assumed that the tribolayer formed on the low carbon spray coating during sliding contact could have an influence on reducing chipping fracture due to separation of oxide stringers. Compositional analyses of the compact tribolayer at the centre of the wear track and the loose tribolayer at the edge (**Figure 3.4(a)**) was performed by Raman spectroscopy, in comparison to that performed with the coating outside the wear track. **Figure 3.8** shows the Raman spectra obtained from regions marked as X1 (located outside the wear track in **Figure 3.4(a)**), X2 (tribolayer at the centre of the wear track) and X3 (tribolayer at the edge). Raman spectrum obtained from a location outside the wear track (X1 in **Figure 3.4(a)**) consisted of a prominent peak at 660 cm^{-1} that corresponded to FeO [22] in the as-received coating. A sharp peak at 667 cm^{-1} observed in the spectrum obtained from X2 in **Figure 3.4(a)** indicated that the tribolayer at the centre of the wear track was rich in Fe$_3$O$_4$ (magnetite) [22, 23]. Other smaller peaks located at 245, 299, 410 and 1321 cm^{-1} in this spectrum revealed the presence of α-Fe$_2$O$_3$ (hematite) on the wear track. In contrast, sharps peaks were observed at 245, 299, 410 and 1321 cm^{-1} in the spectrum obtained from the strips of the tribolayers at the edge of the wear track (X3 in **Figure 3.4(a)**) indicating that the material at the edges of the wear track was rich in α-Fe$_2$O$_3$. The Raman spectrum also depicted a small peak at 667 cm^{-1} due to the presence of Fe$_3$O$_4$. The spinel-type Fe$_3$O$_4$ is known to be adherent to steel surface [24,25] and hence acted as a protective layer and a solid lubricant [24]. α-Fe$_2$O$_3$ which is thought to be less adherent was pushed to the edges of the wear track. Similar observations were

reported by Clark et al [25]. The mechanical properties of the oxide tribolayer was determined and discussed in the following paragraphs.
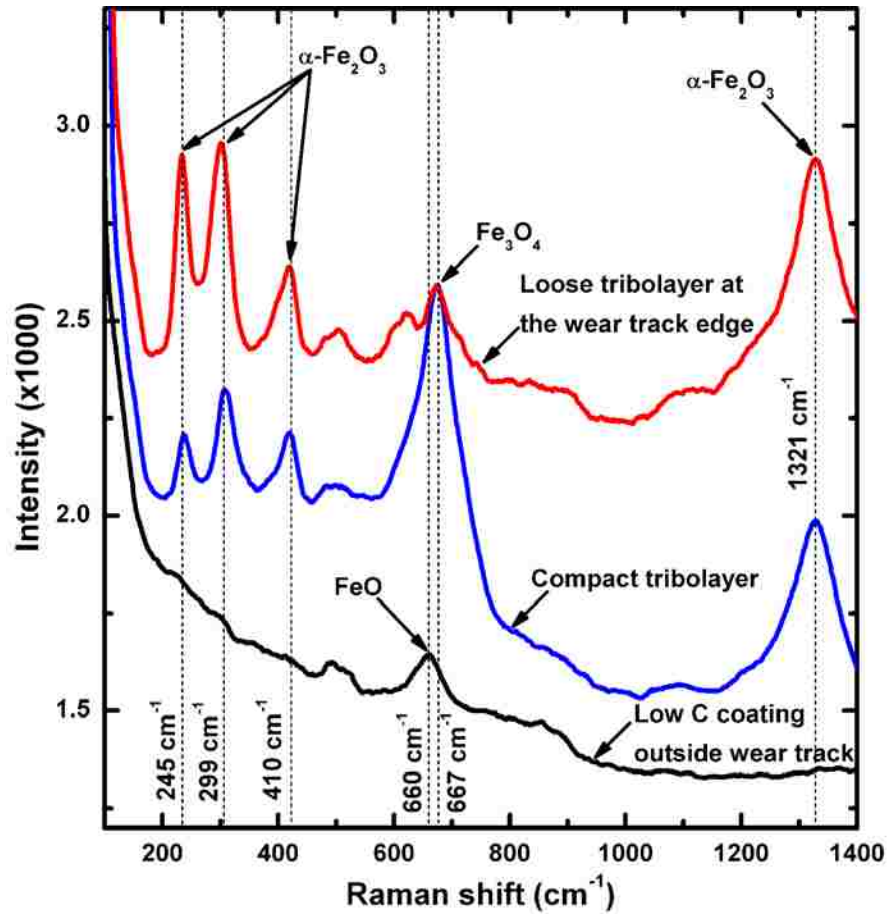
Figure 3.8 Raman spectra obtained from the low carbon spray coating, the compact tribolayer generated at the centre of the wear track and the loose tribolayer at the wear track edge.

Incremental multi-cycle nanoindentation experiments were performed on the Fe_3O_4-rich tribolayers to assess the variation in hardness with the relative indentation depth. The relative indentation depth (RID), has been defined as [10]: RID = h/t, where h is the penetration depth during the loading stage of the indentation and t is the tribolayer thickness. According to **Figure 3.9(a)**, the hardness values can be classified into two regimes within a depth that was approximately equal to the tribolayer thickness (~770 nm). At $h/t \leq 0.68$, higher hardness values were indicative of an elastic-only deformation response from the tribolayer. The decrease in the hardness values

with load was attributed to indentation-size effect [26.27]. At $h/t > 0.68$, a gradual increase in the hardness values indicated a response dominated by the substrate, low carbon coating. Thus, the hardness and elastic modulus of tribolayer, determined at a penetration depths of 523.6 nm (for $h/t \leq 0.68$), was devoid of any influence of the substrate. Accordingly, nanoindentation experiments were performed on the tribolayer at $h/t \sim 0.68$, and typical load-displacement curves thus obtained is shown in **Figure 3.9(b)**. Analyzing the load-displacement data of four measurements using Oliver-Pharr method [24], the hardness of the tribolayer was measured as 0.36 ± 0.10 GPa, its elastic modulus was 38.4 ± 5.3 GPa. The low hardness of the Fe_3O_4-rich tribolayer was consistent with previously reported data by Takeda et al. [25] who performed indentation experiments on the iron oxide scales formed at high temperature (1000 °C) on steels and obtained a hardness of 0.08 GPa for Fe_3O_4, and 0.53 GPa for Fe_2O_3.
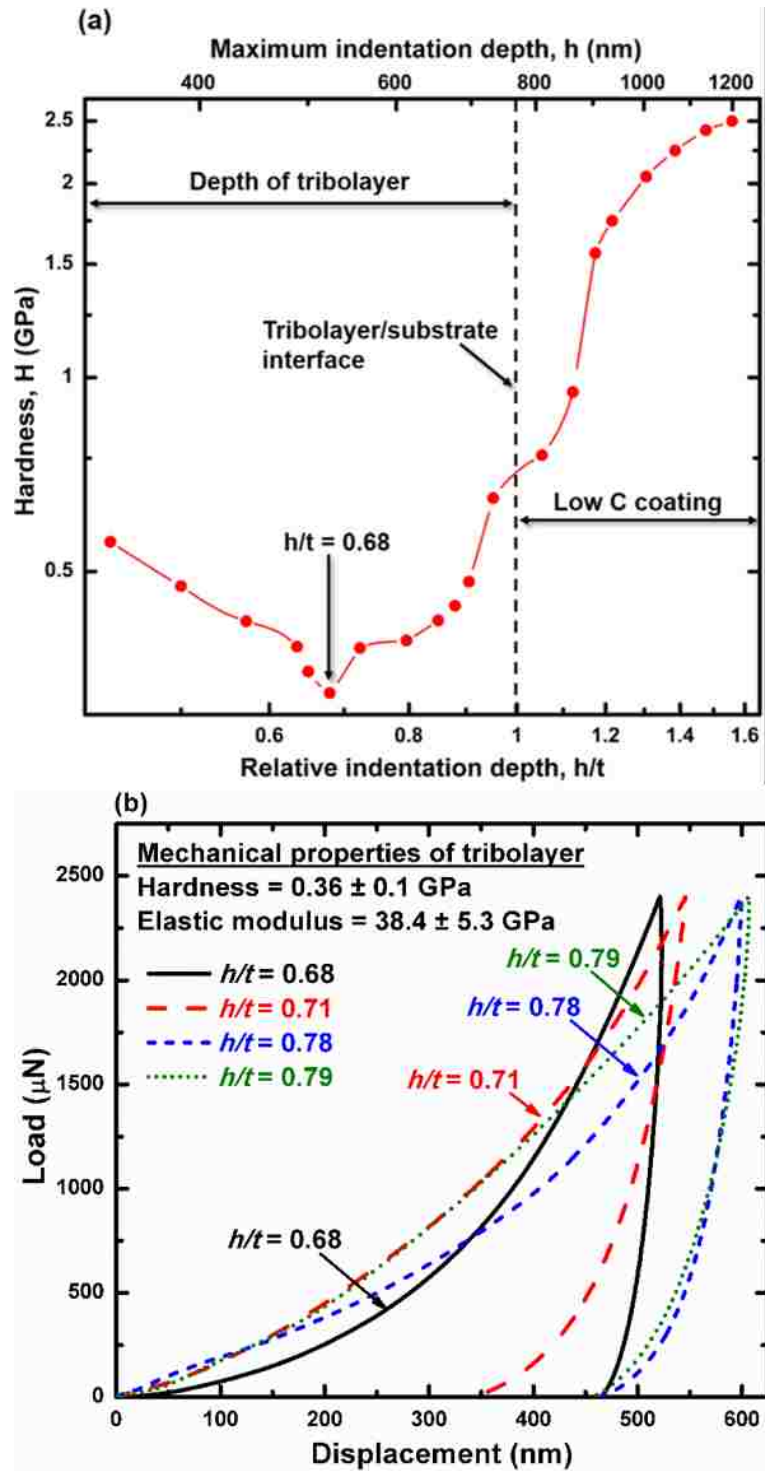
Figure 3.9 (a) Change in hardness of the tribolayer, generated during reciprocating sliding on the low carbon spray coating, measured with respect to the relative and maximum indentation depths. Hardness measurements were performed using incremental multi-cycle indentation experiments using a Berkovich tip. (b) Load-displacement curves of nanohardness measurements performed on the tribolayer.

Radial cracks emanating from the corners of the residual microindents were used to measure the indentation K_{1c} of the low carbon coating and also K_{1c} was measured using the K_{1c} on the wear track to determine the effect of the tribolayer on K_{1c}. Ponton and Rawlings [26, 27] proposed the following relationship for calculating K_{1c}:

$$K_{IC} = 0.0363 \left(\frac{E}{H}\right)^{\frac{2}{5}} \frac{L}{a^{\frac{3}{2}}} \left(\frac{a}{c}\right)^{1.56} \qquad (3-1)$$

where E is the elastic modulus of the coating, H is the coating hardness, $L = 300$ gf, a is half of the diagonal length of the residual Vickers indent and c is radial crack length added to a. By measuring the crack length and indent size obtained in 5 experiments, the indentation K_{1c} of the as-received low carbon coating was determined as 1.41 ± 0.52 MPa·m$^{1/2}$. When a Fe_3O_4-rich tribolayer was formed, however, the K_{1c} was found to increase to 1.98 ± 0.65 MPa·m$^{1/2}$.

3.3.3 Statistical analysis of chipping fracture in the low carbon spray coating with and without the oxide tribolayer

Coating damage due to indentation in the low carbon coating with and without the tribolayer was modelled by determining the probability of chipping fracture of oxide stringers between α-Fe splats. For probability calculations, results of 20 individual tests, performed on different locations at loads starting from 10-500 gf, were analyzed using optical and SEM images of the indentation impressions. **Figure 3.10(a)** shows the change in the probability of coating failure by chipping ($P_f(L)$) as a function of L. It was observed that $P_f(L)$ increased with L thus enhancing the probability of chipping fracture of the coating. For all values of L, the calculated $P_f(L)$ measured from indentations performed inside the Fe_3O_4-rich tribolayer covered wear track were less than those measured for the low carbon coating outside the wear track. Subsequently, the values of P_f were fitted with a Weibull exponential function. Survival probability values, $P_s(L)$ (= 1- $P_f(L)$), are plotted in **Figure 3.10(b)** that shows the resistance to occurrence of chipping fracture. In presence

of the tribolayer on the wear track, the Weibull parameter, L_o (for $P_s(L) = 37\%$) was calculated as 500 gf, whereas for the low carbon coating, $L_o = 242$ gf. Thus, the Weibull distribution function could be expressed as,

$$lnln\left(\frac{1}{P_s(L)}\right) = mln\left(\frac{L}{L_0}\right) \qquad (3-2)$$

The logarithmic scale plots of the Weibull distribution function are presented in **Figure 3.10(c)**. The slope of the fitted linear function provided the Weibull modulus, m. The calculated Weibull parameters (L_o and m) with the resulting equation is:

$$P_S = \exp\left(-\frac{L}{242}\right)^{0.84} : Low\ carbon\ spray\ coating$$

$$P_S = \exp\left(-\frac{L}{500}\right)^{1.51} : Tribolayer \qquad (3-3)$$

which depicts the survival probabilities of the coating and the wear track to chipping fracture at a given indentation load. A higher value for m, 1.51, for the Fe_3O_4-rich tribolayer implied less variability in stringer separation-induced chipping, compared to that for the low carbon coating ($m = 0.84$). The tribolayer could have acted as an energy absorbing entity and reduced the probability of chipping investigated in this indentation-load range.
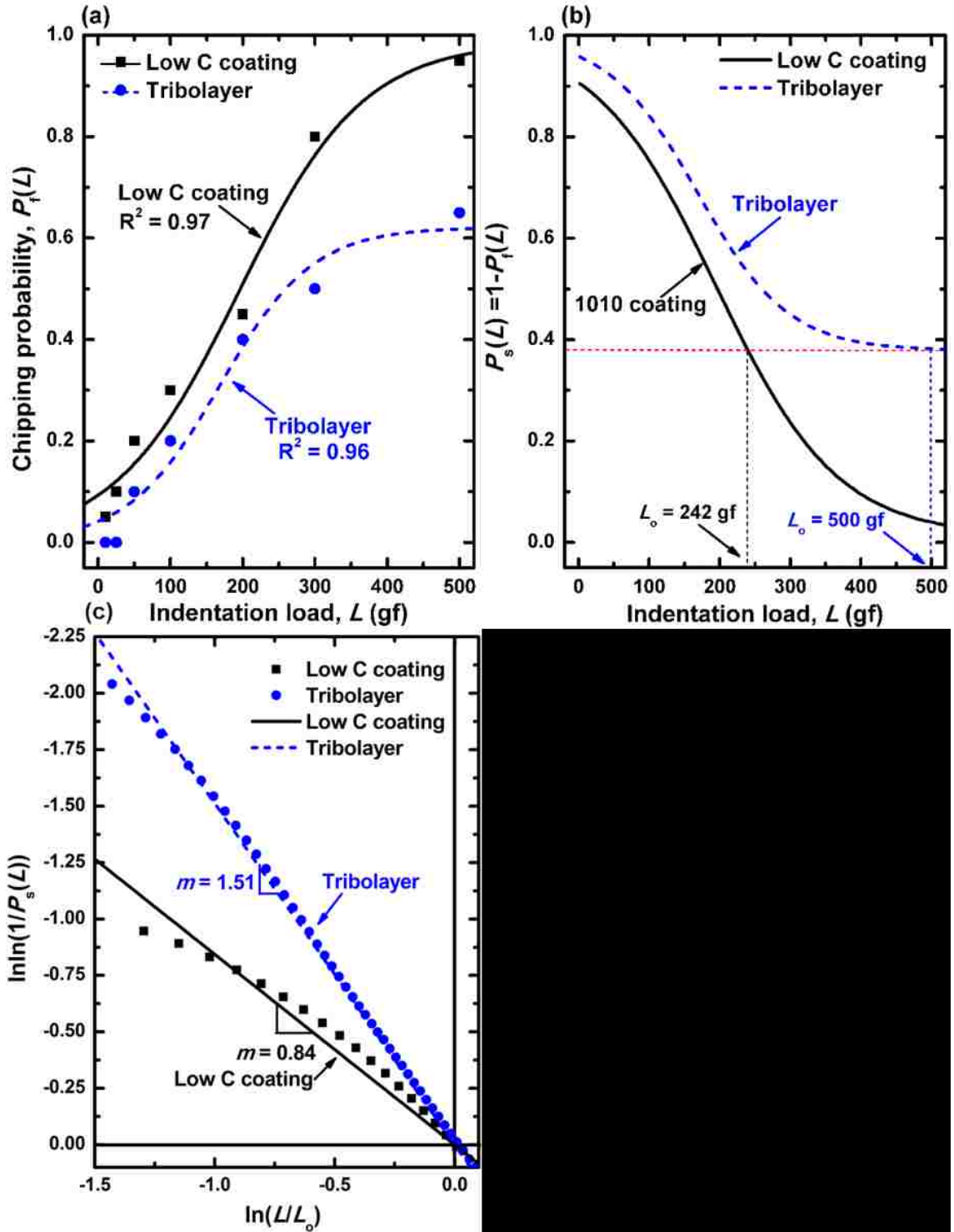
Figure 3.10 (a): Probability of chipping fracture due to separation of oxide stringer in the low carbon coating and the tribolayer generated in the wear track plotted as a function of the indentation load (L); (b) Weibull distribution functions plotted using the experimental data in (a); (c) logarithmic scale plots of Weibull distribution functions.

3.3.4 Fracture and R-curve behaviour of the low carbon coating in presence of tribolayers

The morphology of the microindentation impressions performed at the same load inside and outside the wear track were observed by means of SE-SEM images. **Figure 3.11(a)** shows an SEM image of a 300 gf indentation impression on an as-received low carbon spray coating. Cracks formed due to oxide stringer separation and initiation of chipping can be seen in this image. An SEM image of a residual indent formed on the tribolayer-covered coating at the same load (300 gf) can be seen in **Figure 3.11(b)**. In contrast to the observations in **Figure 3.11(a)**, chipping due to stringer separation was not observed. Therefore, the tribolayer played a role in absorbing the energy during indentation that delayed crack formation.

(a)

Low carbon coating outside wear track

Separation of oxide stringers from matrix

(b)

Fe_3O_4-rich tribolayer

No chipping observed due to indentation in the tribolayer

10 µm
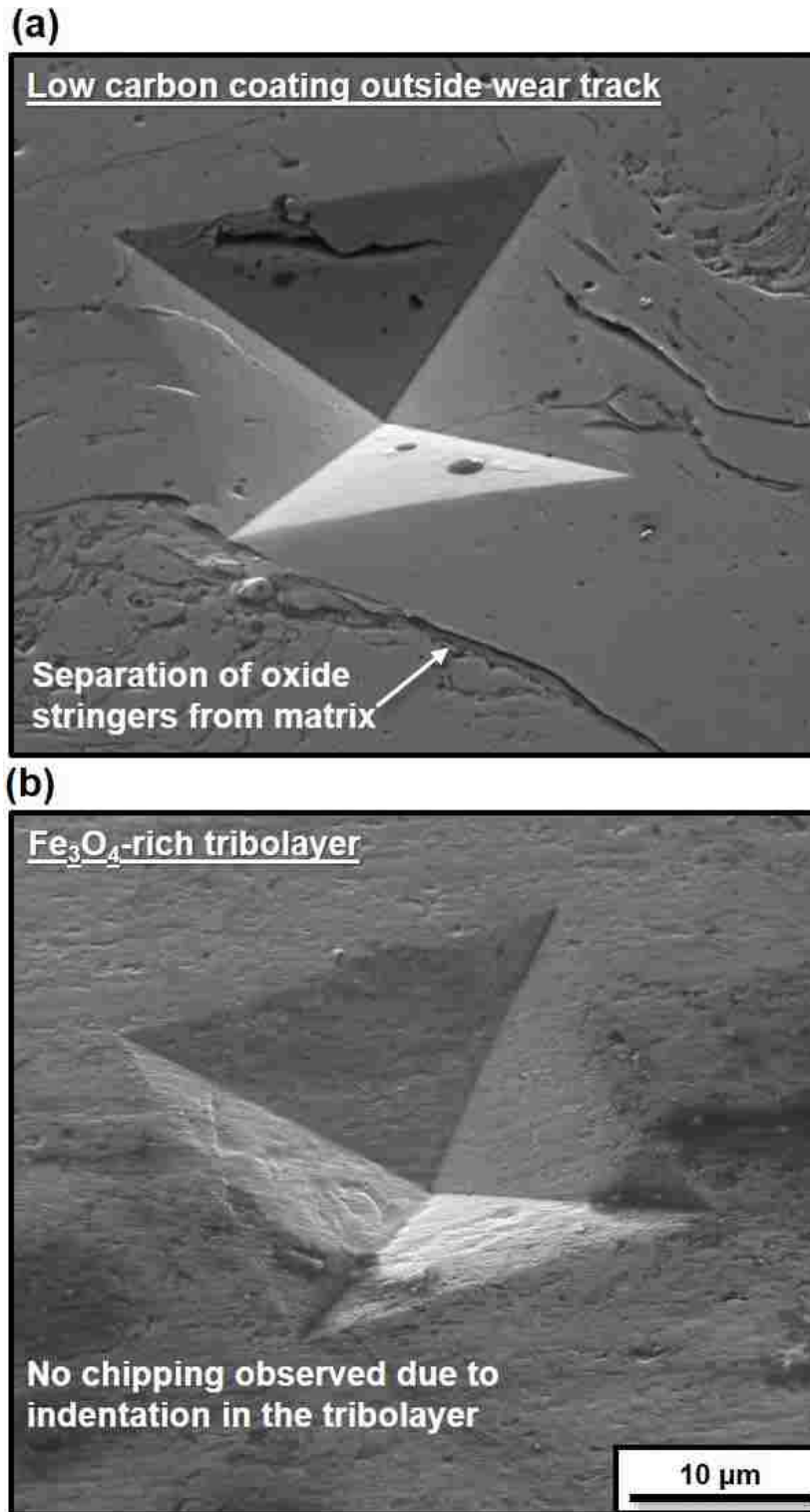
Figure 3.11 SEM images of micro-indentations performed using a load of 300 gf on (a) the as-received low carbon coating showing cracks inside the residual indent, and (b) the wear track on the low carbon spray coating, where only shear deformation could be identified inside the residual indent.

114

When micro-indentations were performed, separation of the oxide stringers occurred leading to crack formation, and the cracks grew at a certain rate subcritically (**Figure 3.6(a)**). When the crack instability conditions were reached, catastrophic fracture occurred. This is because the work of indentation was expended in plastic deformation of the low carbon spray coating. A fracture mechanics argument can be developed to account for the crack growth and instability conditions for the coating covered by the tribolayer and the as-received low carbon coating. The strain energy release rate (G) due to crack extension in plane-strain condition (sample thickness was 1.2 mm for indentations performed on the wear track and 2.3 mm for indentations performed on the coating cross-section) could be determined by following relation between G and K_{1c} measured in section 3.3 [28]:

$$G = \frac{K_{1c}^2 \left(1 - v^2\right)}{E}$$
(4)

where v is Poisson's ratio of the coating, 0.3 [29]. Based on Eq.4, $G_1 = 15.07 \pm 3.19$ J/m^2 for the coating and $G_2 = 31.00 \pm 3.30$ J/m^2 for the wear track. The energy balance suggested by Broek [30] states that the driving force for crack growth (G) should exceed the resistance to crack growth (R). The driving force, G, is provided by the elastic energy release rate and defined as, $G = d/dc(W_f - S_\gamma)$, where dW_f/dc is the rate of work done to extend a lateral crack of length, c. The resistance to crack growth, R, is provided by the surface energy of the newly provided crack surfaces, dS_γ/dc, and the energy required for the formation of a new plastic zone at the tip of the crack. Thus, the fracture condition for crack propagation in the low carbon spray coating follows construction as in **Figure 3.12**, where R increases with c, and G should exceed R for the final fracture to occur at point A when $c = c_{1010}$;

$$\frac{dG}{dc} = \frac{dR}{dc}; \ G = R$$
(5)
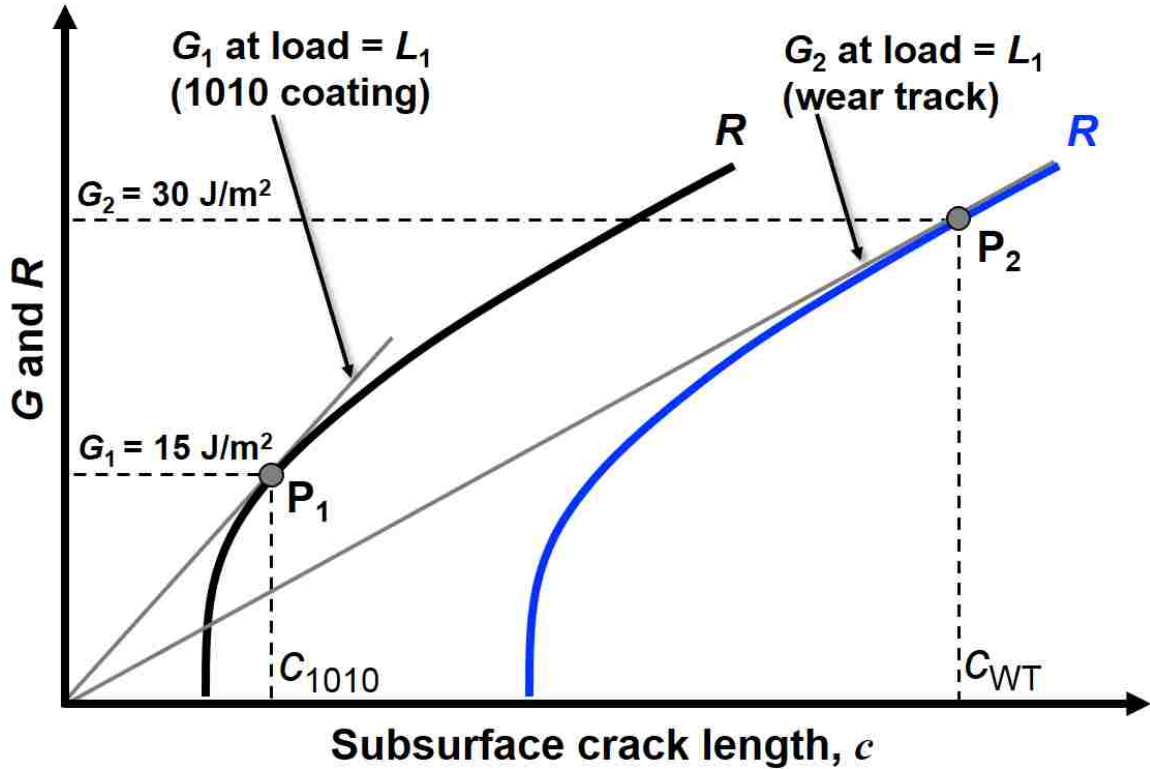
Figure 3.12 Fracture mechanics representation of the rising R-curve behaviour of low carbon spray coating in presence of the tribolayer.

Thus, in absence of the tribolayer, conditions of unstable crack growth led to chipping fracture of the low carbon coating (also schematically shown in **Figure 3.13(a)** at any particular indentation load, L_1. It has also been shown in **Figure 3.12** that at the same indentation load, there is stable crack growth only at a higher G value ($G_2 > G_1$). Reaching the point of instability is delayed from P_1 to P_2 since a fraction of the energy is expended to deform the oxide tribolayer and, hence, the driving force is insufficient for unstable crack growth. The energy expended to deform the tribolayer was calculated as 349.7 pJ, obtained by estimating the work done during the loading stage of the nano-indentation experiments reported in Section 2.2 (the depth of penetration during the loading was 523.6 nm). The construction in **Figure 1.14** can be used to interpret the role of the tribolayer acting as an energy-absorbing entity. At a given load, the work done by the indenter is constant, hence, the driving force that is necessary for crack growth in the low carbon coating would

decrease due to the presence of the tribolayer (**Figure 3.13(b)**) as a certain fraction of the work done by the indenter will be expended in the deformation of the surface layer; therefore, less energy would be available for driving a crack. Ultimately, the critical crack size for unstable crack growth in presence of the tribolayer is increased from c_{1010} to c_{WT}.
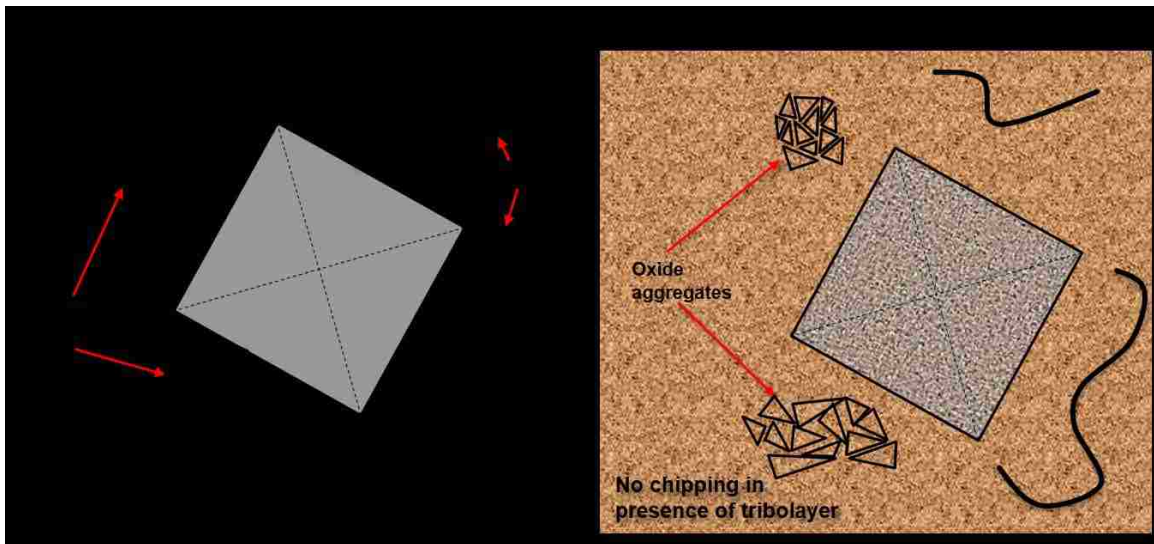
Figure 3.13 Schematic representation depicting the difference in damage in the low carbon spray coating (a) without and (b) with the tribolayer. The tribolayer acted as an energy-absorbing entity that reduced the driving force necessary for oxide stringer separation in the low carbon coating.

In summary, the fracture mechanics approach serves to rationalize the delay in crack formation in presence of the tribolayer. Once formed on the coating surface during sliding, the tribolayer consisting of Fe_3O_4–rich oxides, could prevent chipping fracture and enhance the wear behaviour and durability of low carbon spray-coated surfaces during engine running conditions.

3.4 Conclusions

Vickers micro-indentations were performed on a low carbon (AISI 1010) thermal spray coating to understand the coating's fracture behaviour. Reciprocating dry sliding tests conducted with the coated samples generated an approximately 770-nm-thick tribolayer. A fracture mechanics

approach was used to rationalize the crack growth and instability conditions in the coating with and without the tribolayer. The main conclusions can be summarized as follows:

1. Micro-indentations caused fracture of particles within the FeO aggregates at loads as low as 10 gf, and separation of the FeO stringers within the indentation plastic zone that led to chipping-type fracture in the coating.

2. The sliding-induced tribolayer formed during dry sliding tests on the coating were rich in Fe_3O_4 and had a hardness of 0.36 ± 0.1 GPa with an elastic modulus of 38.4 ± 5.3 GPa.

3. In presence of the oxide tribolayer, resistance to oxide stringer separation was improved as the Weibull modulus, m, increased from 0.84 (for the low carbon coating) to 1.51 (due to presence of the tribolayer).

4. The tribolayer acted as an energy-absorbing entity and reduced the driving force that is necessary for FeO stringer separation in the low carbon coating. Hence, chipping fracture in presence of the tribolayer occurred only at higher loads.

3.5   Bibliography

[1] S. Wilson, A.T. Alpas, Wear mechanism maps for metal matrix composites, Wear, 212 (1997) 41-49.

[2] G. Pereira, A. Lachenwitzer, M. Kasrai, P.R. Norton, T.W. Capehart, T.A. Perry, Y.T. Cheng, B. Frazer, P. Gilbert, A multi-technique characterization of ZDDP antiwear films formed on Al (Si) alloy (A383) under various conditions, Tribol Lett, 26 (2007) 103-117.

[3] X. Meng-Burany, T.A. Perry, A.K. Sachdev, A.T. Alpas, Subsurface sliding wear damage characterization in Al-Si alloys using focused ion beam and cross-sectional TEM techniques, Wear, 270 (2011) 152-162.

[4] A. Edrisy, T. Perry, Y.T. Cheng, A.T. Alpas, Wear of thermal spray deposited low carbon steel coatings on aluminum alloys, Wear, 251 (2001) 1023-1033.

[5] A. Edrisy, T. Perry, Y.T. Cheng, A.T. Alpas, The effect of humidity on the sliding wear of plasma transfer wire arc thermal sprayed low carbon steel coatings, Surf Coat Tech, 146 (2001) 571-577.

[6] G. Barbezat, Advanced thermal spray technology and coating for lightweight engine blocks for the automotive industry, Surface and Coatings Technology, 200 (2005) 1990-1993.

[7] J.R. Davis, A.S.M.I.T.S.S.T. Committee, Handbook of Thermal Spray Technology, ASM International, 2004.

[8] K. Alamara, S. Saber-Samandari, C.C. Berndt, Splat formation of polypropylene flame sprayed onto a flat surface, Surf Coat Tech, 205 (2010) 2518-2524.

[9] A.S.M. Ang, C.C. Berndt, M. Dunn, M.L. Sesso, S.Y. Kim, Modeling the Coverage of Splat Areas Arising from Thermal Spray Processes, J Am Ceram Soc, 95 (2012) 1572-1580.

[10] A.M. Korsunsky, M.R. McGurk, S.J. Bull, T.F. Page, On the hardness of coated systems, Surf Coat Tech, 99 (1998) 171-183.

[11] A.G. Evans, E.A. Charles, Fracture Toughness Determinations by Indentation, J Am Ceram Soc, 59 (1976) 371-372.

[12] M.M. Lima, C. Godoy, P.J. Modenesi, J.C. Avelar-Batista, A. Davison, A. Matthews, Coating fracture toughness determined by Vickers indentation: an important parameter in cavitation erosion resistance of WC-Co thermally sprayed coatings, Surf Coat Tech, 177 (2004) 489-496.

[13] K. Niihara, R. Morena, D.P.H. Hasselman, Evaluation of Klc of Brittle Solids by the Indentation Method with Low Crack-to-Indent Ratios, J Mater Sci Lett, 1 (1982) 13-16.

[14] S. Bhattacharya, A.T. Alpas, Role of sliding-induced tribofilms on fracture of particles in aluminium–silicon alloys, Wear, 301 (2013) 707-716.

[15] S. Bhattacharya, A.R. Riahi, A.T. Alpas, Indentation-induced subsurface damage in silicon particles of Al-Si alloys, Mat Sci Eng a-Struct, 527 (2009) 387-396.

[16] A. Rabiei, D.R. Mumm, J.W. Hutchinson, R. Schweinfest, M. Ruhle, A.G. Evans, Microstructure, deformation and cracking characteristics of thermal spray ferrous coatings, Mat Sci Eng a-Struct, 269 (1999) 152-165.

[17] A.S.M. Ang, C.C. Berndt, A review of testing methods for thermal spray coatings, Int Mater Rev, 59 (2014) 179-223.

[18] S.C. Tung, H. Gao, Tribological characteristics and surface interaction between piston ring coatings and a blend of energy-con serving oils and ethanol fuels, Wear, 255 (2003) 1276-1285.

[19] S.C. Tung, H. Gao, Tribological investigation of piston ring coatings operating in an alternative fuel and engine oil blend, Tribol T, 45 (2002) 381-389.

[20] A.E. Giannakopoulos, S. Suresh, Determination of elastoplastic properties by instrumented sharp indentation, Scripta Mater, 40 (1999) 1191-1198.

[21] H. Imrek, M. Bagci, O.M. Khalfan, Solid Particle Erosion as Influenced by Tensile Axial Loads, Tribol T, 54 (2011) 779-783.

[22] D.L.A. de Faria, S. Venâncio Silva, M.T. de Oliveira, Raman microspectroscopy of some iron oxides and oxyhydroxides, Journal of Raman Spectroscopy, 28 (1997) 873-878.

[23] M.F.B. Abdollah, Y. Yamaguchi, T. Akao, N. Inayoshi, N. Umehara, T. Tokoroyama, Phase transformation studies on the a-C coating under repetitive impacts, Surface and Coatings Technology, 205 (2010) 625-631.

[24] W.C. Oliver, G.M. Pharr, An Improved Technique for Determining Hardness and Elastic-Modulus Using Load and Displacement Sensing Indentation Experiments, J Mater Res, 7 (1992) 1564-1583.

[25] M. Takeda, T. Onishi, S. Nakakubo, S. Fujimoto, Physical Properties of Iron-Oxide Scales on Si-Containing Steels at High Temperature, Mater Trans, 50 (2009) 2242-2246.

[26] C.B. Ponton, R.D. Rawlings, Vickers Indentation Fracture-Toughness Test .1. Review of Literature and Formulation of Standardized Indentation Toughness Equations, Mater Sci Tech Ser, 5 (1989) 865-872.

[27] C.B. Ponton, R.D. Rawlings, Vickers Indentation Fracture-Toughness Test .2. Application and Critical-Evaluation of Standardized Indentation Toughness Equations, Mater Sci Tech Ser, 5 (1989) 961-976.

[28] G.E. Dieter, Mechanical metallurgy, 3rd ed., McGraw-Hill, New York, 1986.

[29] A. Rabiei, A.G. Evans, Failure mechanisms associated with the thermally grown oxide in plasma-sprayed thermal barrier coatings, Acta Mater, 48 (2000) 3963-3976.

[30] D. Broek, Artificial slow crack growth under constant stress. The r-curve concept in plane stress, Eng Fract Mech, 5 (1973) 45-53.

CHAPTER 4

LOW FRICTION BEHAVIOUR OF BORON CARBIDE
COATINGS (B₄C) SLIDING AGAINST TI–6AL–4V

4.1   Introduction

Tool wear during machining of components made of titanium alloys could be intense because high cutting temperatures are generated due to the low thermal conductivity of Ti alloys [1-5]. The high chemical reactivity of titanium with tool coatings including TiN, TiAlN, TiCN and WC results in adhesion of the workpiece to the tool surface leading to premature tool failure [6-8]. This type of wear is considered as the diffusive wear [9]. Thus, effective tool coatings should have sufficiently high hot hardness, and also good thermal stability.

Polycrystalline diamond (PCD) coatings are among the candidate coatings that were studied. Rahman et al. [10] compared the performance of polycrystalline diamond (PCD) tools in cutting of Ti–6Al–4V with the uncoated carbide (WC-Co) tools. Machining tests (end-milling) with high pressure coolant were carried out and a cutting distance of 11 m was achieved using PCD tools without titanium adhesion while uncoated tools could only last for 2 m and titanium adhesion was observed. Oosthuizen et al. [11] studied the performance of PCD tools in high-speed milling of Ti–6Al–4V. The PCD tool yielded longer tool life than a WC-Co tool at cutting speeds above 100 m/min. A slower wear progression was found with an increase in cutting speed for the PCD tool because of elevated cutting temperature leading to phase transformation of Ti–6Al–4V (from HCP α to BCC β at about 950 °C). Adhesion of titanium was once more observed during cutting with the carbide tools that caused higher surface roughness compared to the PCD tools that exhibited less adhesion. Nabhani [12] studied the wear of uncoated WC-Co and PCD tools as well as cubic boron nitride (CBN) coated carbide inserts in turning of Ti–4/Al–8Si alloy. Crater wear and adhesion of workpiece material to the tools were indicated to be responsible for the high surface

122

roughness observed for the uncoated carbide (Ra = 10 μm) and CBN (Ra = 8 μm) compared to PCD tools (1 μm). Ezugwu et al. [13] investigated the performance of CBN tool in machining of Ti–6Al–4V with high pressure coolant supplies of 11–20 MPa. The tool life of CBN tool was lower than the uncoated carbide tool, due to the rapid notching and chipping of the cutting edge. Nevertheless, high pressure coolant could help removing clips adhered on PCD tools, which was denoted as the main reason for the damage, and consequently an increase in coolant pressure tended to improve tool life of PCD [14]. In summary, PCD tools showed better cutting performance than the uncoated and CBN coated WC–Co tools. However, the PCD tools that are currently used in industry are expensive ($3000 per drill) and their replacement with a more economical coating is desirable. Boron carbide (B_4C) tool coatings can be considered as potential candidates for titanium machining because of the high hardness of B_4C (25–29 GPa) [15] only lower than those of the diamond and CBN, and most importantly, low adhesion to titanium because of the passivation of carbon. According to B–C phase diagram, the B_4C phase consists of 9–20 at.% carbon with melting point of 2490–2375 °C [15]. B_4C retains most of its hardness up to 1000 °C [16]. The coefficient of friction (COF) of 0.4 B_4C sliding against B_4C remains constant up to 1000 °C in vacuum. At 800 °C, a lower COF of 0.20 was observed [17, 18] because of formation of hybrid sp^3 bonds at elevated temperature. In ambient air, the COF of B_4C was determined as 0.21 according to tests done at room temperature and decreased to 0.11 at 800 °C [17]. The low COF of 0.11 observed in air was accompanied by the formation of boron oxide and hydroxide films on the surface above 527 °C. At 827 °C, a continuous film of boron hydroxide covered the B_4C surface. Similar behaviour was observed for B_4C sliding against ZrO_2 under an ambient atmosphere, where a COF of 0.3 was measured. After annealing B_4C at 800 °C for one hour, the room temperature COF of B_4C showed a significant drop to 0.05 [17, 19]. The observed very low COF was attributed to the presence of lubricious boron hydroxide film at the sliding interface. Meanwhile, Erdemir et al. [19] obtained low COF of 0.05 for the annealed B_4C at 800 °C against zirconia. They found the low COF could be attributed to the formation of layered structured boric acid during annealing.

In order to improve the tribological performance of B_4C coatings, Eckardt et al. [20] considered the effect of C_2H_2 addition to the deposition gas and studied the friction of deposited coating in dry sliding against AISI 52100 steel. The B_4C coating without C_2H_2addition exhibited a high COF value of 0.90 while the lowest value of 0.15 was observed for the coating deposited with 4 sccm C_2H_2 flow. A similar reduction in the COF of B_4C coating deposited by the blending of CH_4 into Ar sputtering gas was observed when the coating was tested in dry sliding against the steel by Ahn et al. [21]. The COF was reduced approximately from 0.40 to 0.11. Results indicated that organic gas enhanced the passivation of carbon surface by H, by developing C–H which helped to reduce the COF, a mechanism that similar to that observed in hydrogenated diamond-like carbon (H-DLC).

B_4C coatings have been applied to tools for machining of aluminum alloys [22]. Studies have shown that a tap coated with B_4C lasted for 2000 taps, while the same tap coated with TiN lasted only 20 taps when tapping a hypereutectic aluminum silicon alloy. Similarly, drill life improved to 5000 holes using the same coating from 500 holes using a uncoated HSS tool indicating high wear resistance of B_4C against primary silicon present in aluminum-silicon alloys [23]. Reports on the machining of titanium alloys by B_4C coated tools are not readily available in the open literature, and the tribological behaviour of B_4C coating dry sliding against titanium alloys in different atmospheres and liquids environments have yet to be studied. The aim of this study is to investigate the lubrication mechanisms of B_4C coatings under different atmospheres. The tribological behaviour of B_4C coatings deposited on M2 steel substrates subjected to dry sliding against a Ti–6Al–4V alloy in various humidity levels and inert atmospheres were studied. The effects of ethanol (C_2H_5OH) and iso-propyl alcohol (C_3H_7OH) on the friction of the B_4C were studied as it was hypothesized that tests in ethanol and iso-propyl alcohol could reduce COF of B_4C. Worn surfaces were examined by scanning electron microscopy (SEM) and energy-dispersive X-ray spectroscopy (EDS). X-ray photoelectron spectroscopy (XPS), Fourier transform infrared spectroscopy (FTIR)

and Raman spectroscopy were performed to study the passivation mechanism of boron carbide coatings. It was found that carbon rather than boron played an important role in reducing the COF while sliding against Ti–6Al–4V in passivating environments.

4.2   Experimental

4.2.1   Coating: deposition and properties

Substrates for coating deposition were machined from an annealed AISI type M2 tool steel bar of 2.54 cm in diameter. The M2 steel bar was first cut into 1.00 cm thick disks which were then subjected to a heat treatment procedure that consisted of austenizing at 1200 °C for 3–4 min followed by air cooling to 25 °C and then tempering at 560 °C for 120 min. The final hardness of the M2 steel disks was $63 \pm 2R_c$. The purpose of the heat treatment was to increase the hardness of the substrates to provide better support to the coatings.

Coarse grinding of the hardened M2 steel disks was conducted to remove the burr marks from previous cutting, followed by fine grinding in running water using SiC emery papers (120, 240, 400 and 600 grit). Water-based diamond suspensions of 3 and 1 μm were used to polish the disk surfaces. The final surface roughness of the polished M2 steel disks as measured by the optical surface profilometer was 9.5 ± 4.1 nm (R_a). The coating was deposited by the planar magnetron sputtering of a B_4C target using Ar as the sputtering gas. Cross-sections obtained by focused ion beam (FIB) milling (Carl Zeiss NVision 40 CrossBeam) were examined using SEM. The details of the FIB technique can be found in [23]. Energy-dispersive X-ray spectroscopy (EDS) spectra were recorded using an FEI Quanta 200 FEG scanning electron microscope equipped with an EDAX SiLi detector spectrometer. **Figure 4.1**(a) shows the cross-sectional SEM microstructure of the B_4C coating with about 0.41 μm thick Cr interlayer. The figure shows the columnar structure of B_4C coating. The thickness of the B_4C coating was 3.0 μm. The EDS map in **Figure 4.1**(b, c), show the

distributions of C and B across the thickness of the coating. The average surface roughness (R_a) of the B_4C coating was measured as 10.8 ± 1.2 nm.
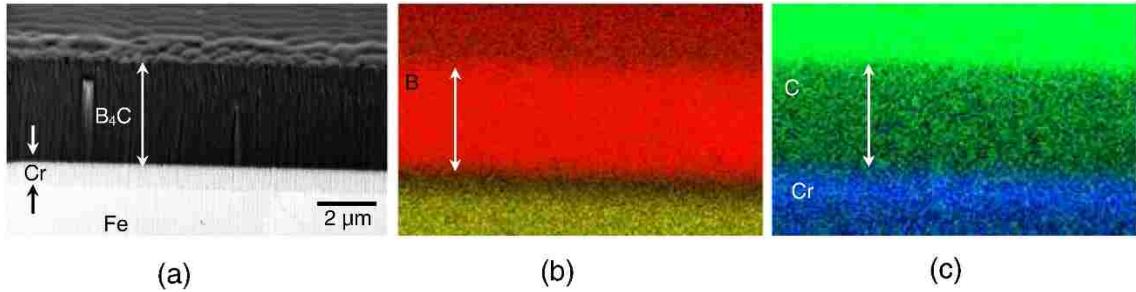
Figure 4.1 (a) Focused ion beam (FIB) cross-sectional image of B_4C coating showing B_4C coatings with Cr interlayer. EDS maps showing (b) the distribution of B in coating and Fe in the substrate; (c) the distribution of C in coating and Cr in interlayer.

The hardness and elastic modulus of the coatings were measured by a Hysitron TI 900 Triboindenter equipped with a Berkovich nanoindenter. The indentation depth was limited to < 300 nm, which was less than 10% of the total thickness of the coating. The hardness of the B_4C coating was 19.5 ± 4.5 GPa and the elastic modulus was 264.5 ± 31.5 GPa.

Ti–6Al–4V balls of 4.0 mm in diameter were used in the tribological tests as a counterface sliding against the B_4C coating surface. Ti–6Al–4V had the following composition (in wt.%): 5.50–6.75% Al, < 0.08% C, < 0.4% Fe, < 0.03% N, < 0.2% O, < 0.02% H, 3.50–4.50% V and the balance Ti. The microhardness of the alloy was 380.00 ± 3.01 HV (3.72 GPa).

4.2.2 Ball-on-disk testing conditions and wear rate calculations

A tribometer with environmental chamber was used in the ball-on-disk configuration under different testing conditions. All tests were performed at a constant load of 2.00 N corresponding to an initial Hertzian stress of 0.60 GPa. A linear sliding speed of 0.02 m/s was used. The effect of relative humidity (RH) was evaluated using four humidity levels, namely at 25%, 52%, 70% and 85% RH. The tests were initially conducted in air with 52% RH. An aqueous KCl solution was

then placed in the test chamber to create testing atmospheres with 70% and 85% RH [24]. For 25% RH tests, dry argon gas was purged to the testing chamber to eliminate moisture as determined by a hygrometer with ± 0.1 sensitivity. In order to conduct tests under dry nitrogen, Ar and air atmosphere, each gas was introduced into the test chamber at a rate of 1 l/s. The moisture content ($< 0.5\%$ RH) of the chamber was confirmed by the hygrometer. The tests were also conducted while the samples were immersed in liquids, namely in water, ethanol and iso-propyl alcohol.

Sliding tests in water, ethanol and iso-propyl alcohol were conducted under the boundary lubrication regime conditions as determined from the ratio (λ) of the minimum lubricant thickness (h_{min}) to the root mean square (r.m.s.) roughness (r*) of the surfaces in contact [25]. The r* value of B_4C coating and Ti-6Al-4 V at the start of the wear tests was 0.45 μm. The value of λ at 25 °C was 1.07×10^{-3} in the case of tests in water, 1.14×10^{-3} for ethanol and 1.89×10^{-3} for iso-propyl alcohol at the beginning of the tests. The parameters used to calculate λ for tests in water and, ethanol and isopropyl alcohol are summarized in **Table 4.1**. As the $\lambda < 1$, boundary lubrication conditions were satisfied for the tests.

Tests were run for 10^3 cycles. During early stages of sliding (running-in period), when contact surfaces start to adapt to each other and a tribolayer was yet to be formed, a relatively high running-in COF was observed. Whenever a steady state COF was attained the average COF of the steady-state stage of the friction curve was calculated from the arithmetic mean of the COF values, typically after 5.00×10^2 cycles using three tests conducted under the same condition. For tests in which no steady state COF was observed, the mean of the fluctuating COF curves were reported.

Table 4.1 Parameters used to calculate the lubrication conditions (λ=hmin/r*) values for tests in water, ethanol and iso-propyl alcohol. R is the radius of the Ti–6Al–4V ball in m, V is the sliding velocity in m/s, P is the normal load in N, E* is the composite elastic modulus in GPa could be calculated by equation 1, $\eta 0$ is the viscosity constant of lubricants, α is the lubricant pressure viscosity coefficient, and r* is the r.m.s. surface roughness of the contacting surfaces. The minimum lubrication thickness hmin and r* of Ti-6Al-4V in contact with B_4C coating were calculated using equations 2 and 3, respectively [25]:

$$\frac{1}{E^*} = \frac{1 - v_{B_4C}^2}{E_{B_4C}} + \frac{1 - v_{Ti-6Al-4V}^2}{E_{Ti-6Al-4V}} \tag{1}$$

where E_{B_4C} is 264 GPa and $E_{Ti-6Al-4V}$ is 114 GPa, the poisson's ratio v_{B_4C} is 0.34 and

$v_{Ti-6Al-4V}$ is 0.2.

$$h_{min} = 1.79 R^{0.47} \alpha^{0.49} \eta_0^{0.68} V^{0.68} (E^*)^{-0.12} P^{-0.07} \tag{2}$$

$$r^* = \sqrt{r_{B_4C}^2 + r_{Ti-6Al-4V}^2} \tag{3}$$

R (m)	V (m/s)	P (N)	E* (GPa)	r* (μm)	η0 (mPa.s)		
0.002	0.02	2	87.6	0.45	water	ethanol	Isopropyl alcohol
α (×10⁻⁸)			λ (×10⁻³)				
water	ethanol	Isopropyl alcohol	water		ethanol		Isopropyl alcohol
2.34	2.30	1.93	1.07		1.14		1.89

The wear losses of the B_4C coatings were calculated from the volume of the material removed which was measured from the area of the wear track at eight different locations taken

along a circular sliding track with radius of 1.25 mm. A white light interferometry technique – using a Wyko NT 1100 optical surface profilometer – was used for this purpose in a way similar to that described in [7]. When material transfer (from Ti–6Al–4V) occurred to the coating surface the adhered material was removed by boiling in HNO_3 prior to conducting the surface profilometry on the sliding track. The reported wear rates were the average values (with the corresponding standard deviations) obtained from three tests at each test condition.

4.2.3 Surface characteristic analysis methods

Following the sliding tests, the Ti–6Al–4V ball contact surfaces were examined by SEM and the compositions of the contact areas were analyzed using EDS, FTIR and micro-Raman spectroscopy. The EDS spectra were recorded using an FEI Quanta 200 FEG SEM equipped with an EDAX SiLi detector spectrometer. FTIR analyses were conducted using a Thermoelectron Nicolet 760 spectroscope in reflectance mode at two different spots using a $100\ \mu m \times 100\ \mu m$ aperture. The chemical composition of the transfer layers was determined using an XPS system (Kratos Axis Ultra) and the charge correction was carried out using a carbon reference. The survey scans of the samples were conducted using a pass energy of 160 eV. High resolution XPS analyses were conducted on the same area using a pass energy of 20 eV. The Raman spectra of the transfer layers were obtained using a 50 mW Nd-YAG solid state laser (532.00 nm excitation line) through the $50 \times$ objective lens of a Horiba Raman micro-spectrometer.

4.3 Experimental results

4.3.1 Tribological behaviour of B₄C in dry atmosphere

B₄C coatings were tested against Ti–6Al–4V in order to evaluate the friction and wear behaviour of the coating in dry atmospheres ($< 0.5\%$ RH). In all dry test atmospheres used, B₄C exhibited high COFs and large fluctuations in COF. Typical friction curves obtained in dry N_2, dry

Ar and dry air, showing the variations of COF with the number of revolutions are presented in **Figure 4.2**. The COF values for the sliding periods of 500–1000 cycles obtained from these tests were 0.65 ± 0.06 in dry N_2, 0.59 ± 0.06 in dry Ar and 0.59 ± 0.06 in dry air. Average steady state COF values obtained from each of the three tests were listed in **Table 4.2**.
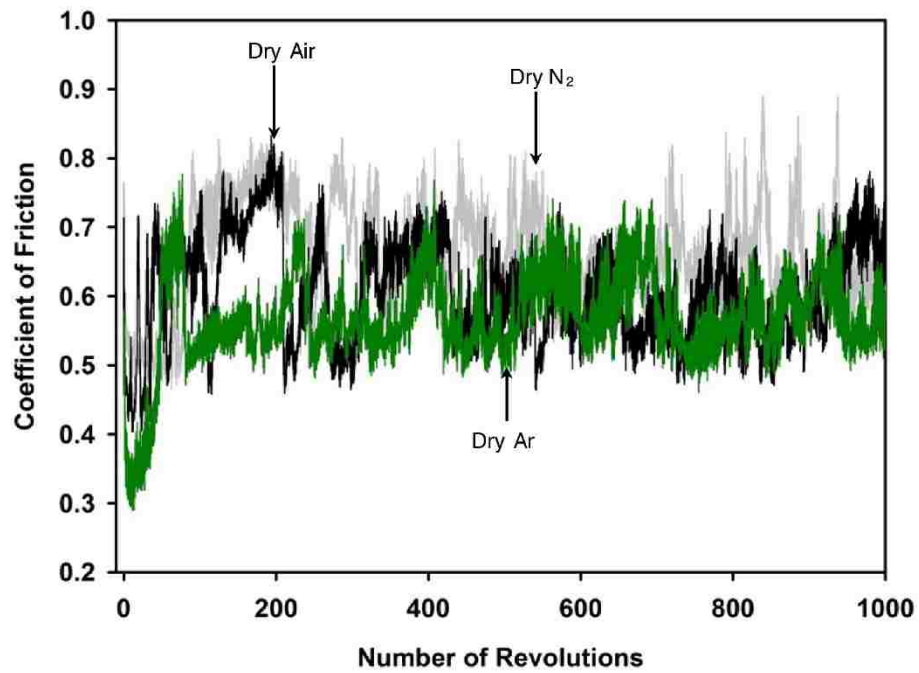
Figure 4.2 Variations of the COF with the number of revolutions for B_4C tested against Ti–6Al–4V in dry air, dry N_2 and dry Ar atmosphere.

Table 4.2 Coefficient of friction values of B_4C coatings tested against Ti–6Al–4V at different environmental conditions. The standard deviation of an individual COF curve was calculated by determining the fluctuations from the average COF value for each test. The last row shows the averages of the mean values of three COF curves and their standard deviations under each test condition.

Test No.	Dry N_2	Dry Ar	Dry Air	25% RH	52% RH
1	0.66 ± 0.07	0.61 ± 0.06	0.59 ± 0.06	0.49 ± 0.03	0.43 ± 0.03
2	0.67 ± 0.08	0.58 ± 0.08	0.60 ± 0.05	0.53 ± 0.01	0.45 ± 0.04
3	0.64 ± 0.06	0.59 ± 0.04	0.58 ± 0.07	0.51 ± 0.01	0.44 ± 0.03
Average	0.65 ± 0.06	0.59 ± 0.06	0.59 ± 0.05	0.51 ± 0.02	0.44 ± 0.03
Test No.	70% RH	85% RH	Water	Ethanol	Iso-propyl
1	0.24 ± 0.01	0.18 ± 0.02	0.17 ± 0.01	0.11 ± 0.02	0.07 ± 0.01
2	0.24 ± 0.02	0.18 ± 0.01	0.16 ± 0.02	0.12 ± 0.01	0.07 ± 0.01
3	0.25 ± 0.01	0.19 ± 0.01	0.16 ± 0.01	0.11 ± 0.01	0.06 ± 0.01
Average	0.24 ± 0.01	0.18 ± 0.01	0.16 ± 0.01	0.12 ± 0.01	0.07 ± 0.01

The wear tracks formed on the B_4C surfaces were examined by SEM and the representative secondary electron images (SEIs) are shown in **Figure 4.3**(a, b). According to these images, material transfer from Ti–6Al–4V occurred to the B_4C surface during sliding both in dry N_2 and dry Ar, and the wear tracks were almost entirely covered by the adhered titanium layers. The wear track of B_4C tested in dry air was also covered by the transferred titanium (not shown as it was almost identical to the dry N_2 and Ar atmospheres). The average widths of wear tracks were 958 ± 10, 955 ± 8 and 961 ± 11 μm for samples tested in dry N_2, dry Ar and dry air. For tests conducted in dry N_2, a wear crater of about 600 μm in diameter was formed on the contact surface of the Ti–6Al–4V ball (**Figure 4.3**c). The corresponding EDS map for elements of interests namely for Ti, O, Fe and C are shown in **Figure 4.3**(d-g). The Ti–6Al–4V contact surface subjected to wear had no evidence of C transfer from B_4C (**Figure 4.3**g). The presence of Fe (**Figure 4.3**f) detected on

the contact surface revealed that the B_4C coating was worn out and removed from the sliding track and the substrate was exposed. SEM and EDS investigations conducted on Ti-6Al-4V tested in dry Ar and dry air had wear track diameter of were 722 ± 0.10 and 726 ± 0.11 µm, with compositions similar to those in **Figure 4.3**(d–g). In summary, tests conducted in dry atmospheres showed high and unsteady COF and B_4C coatings were severely worn and the exposed surfaces were covered with material transferred from Ti–6Al–4V.
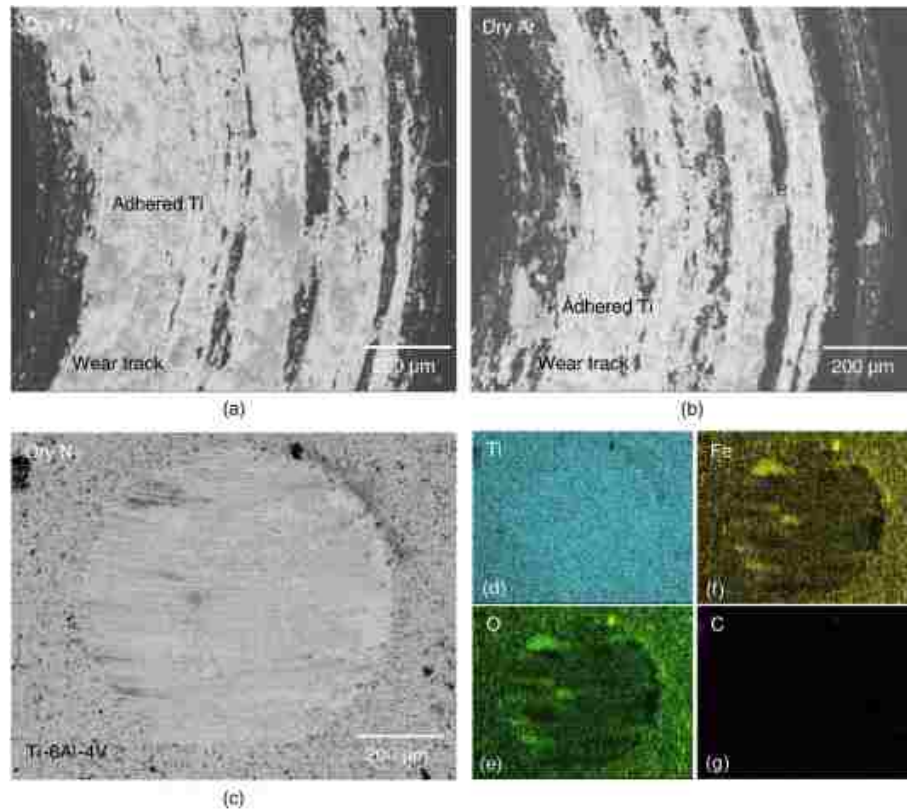
Figure 4.3 Typical secondary electron images of wear tracks formed on the B_4C surface when tested against Ti–6Al–4V at (a) dry N_2 and (b) dry Ar. (c) Secondary electron image of the Ti–6Al–4V ball surface taken after sliding against B_4C coating at dry N_2 atmosphere. The elemental EDS maps taken from the whole area shown in (c) are for (d) Ti, (e) O, (f) Fe and (g) C.

4.3.2   Changes in tribological behaviour of B_4C at different humidity levels

It has been shown that the B_4C exhibited a low and steady state COF when sliding against steel used the environments with high humidity [17, 19]. In this work, the effect of humidity on the

COF values of B_4C tested against Ti–6Al–4V where measured in air atmospheres with 25% RH, 52% RH, 70% RH and 85% RH. The typical COF curves recorded during the course of sliding contact between the Ti–6Al–4V balls and B_4C samples at different humidity levels are presented in **Figure 4.4**(a). At 25% and 52% RH the COF curves are characterized by high fluctuations and high mean COF values throughout the duration of the test. The COF curves obtained during tests at 70% and 85% RH are different as they show low COF values and small fluctuations. The average steady state COF values (see **Table 4.2**) of three tests obtained under the same conditions are plotted against RH % in **Figure 4.4**(b). In comparison with the experiments conducted in air with $< 0.5\%$ RH (**Figure 4.2**), a slight drop in the average COF can be observed when the tests were conducted at 25% (0.51 ± 0.02) and 52% RH (0.44 ± 0.03). These results indicate that in test environment with up to about 52% RH COF was still high as discussed in Section 7.4. A 45% drop of average steady state COF was observed at 70% RH and this low value was further reduced at 85% RH. The average values were (**Figure 4.4** (b)) 0.24 ± 0.01 at 70% RH, 0.18 ± 0.01 at 85% RH and 0.16 ± 0.01 at 100% RH. For tests at 70% RH, the COF initially increased and peaked at 0.43 and then dropped to 0.21 immediately and rose to 0.43, fluctuated around this value for about 1.10×10^2 revolutions and then decreased gradually to a low steady state for the rest of the test (**Figure 4.4**a). A similar friction behaviour but with an even lower steady state COF was observed when the test was conducted at 85% RH. The COF initially increased to 0.30 and then dropped to 0.22. Following the running in period, the COF became relatively stable at 0.18 ± 0.01 for the rest of the test.
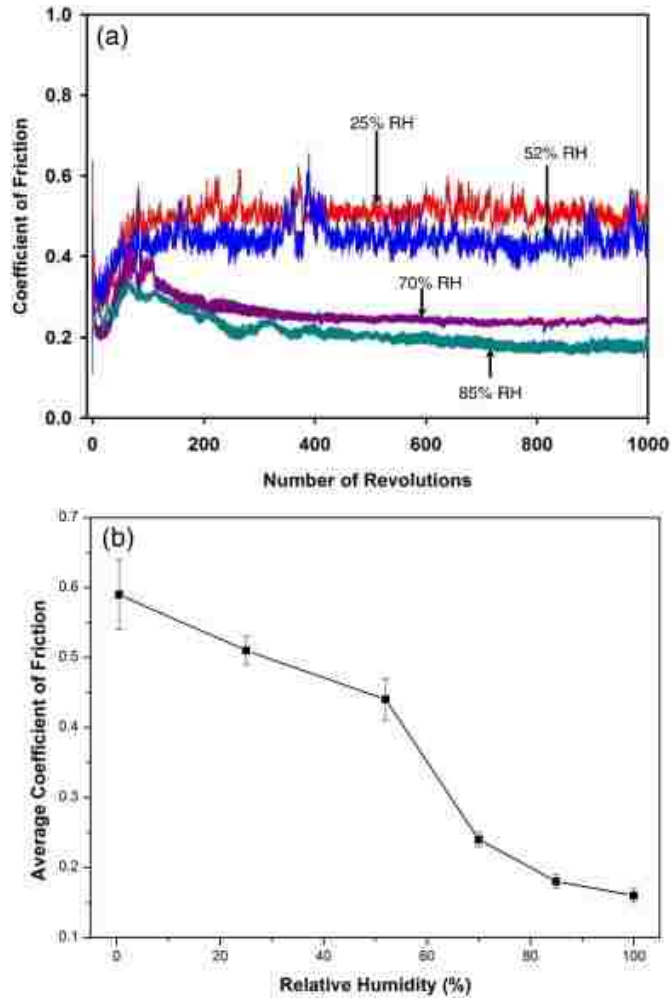
Figure 4.4 (a) variations of the COF with the number of revolutions for B$_4$C tested against Ti–6Al–4V at 25% RH, 52% RH, 70% RH and 85% RH; (b) variations of average steady-state COF with relative humidity.

SEM images of B$_4$C wear tracks (**Figure 4.5**[a–d]) showed that as the RH increased, the amount of material transferred from Ti–6Al–4V decreased. A considerable amount of material transfer occurred on the B$_4$C surface at both 25% RH and 52% RH. The wear tracks were covered by material layers (**Figure 4.5**[a, b]) but not as exclusively as, the wear tracks observed under dry atmospheres (see **Figure 4.3**). No significant transfer of material from Ti–6Al–4V to the B$_4$C could be detected when the tests were performed at 70% RH as well as at 85% RH (**Figure 4.5**[c, d]). Some debris of transferred material could be found along the wear tracks for the test performed at 70% RH as marked on the image (**Figure 4.5**c). No evidence of transferred Ti–6Al–4V, neither in

the form of adhered layer or wear tracks or chips along it could be observed for the tests done at

85% RH (**Figure 4.5**d). The widths of wear tracks were smaller at high humidity tests with 70%

RH and 85% RH (~ 250 μm) compared to the wear track generated during 25% and 52% RH.
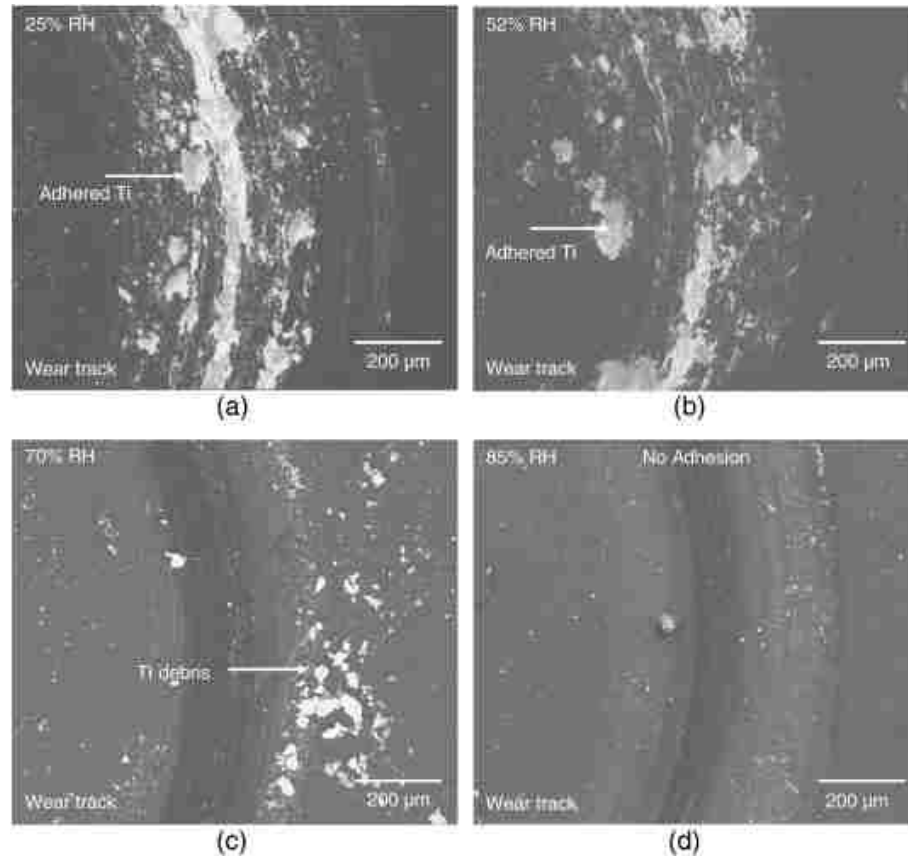
Figure 4.5 Typical secondary electron images of wear tracks formed on the B$_4$C surface when tested against Ti–6Al–4V at (a) 25% RH, (b) 52% RH, (c) 70% RH and (b) 85% RH.

The Ti–6Al–4V ball contact surfaces were examined by SEM to reveal the morphological

features of the worn area after the tests conducted at 52% RH and 85% RH. Tests conducted at

52% RH showed that almost no carbon transfer occurred to the contact surface of the Ti–6Al–4V.

The morphology of contact area and the corresponding EDS maps for Ti, O, Fe and C, are shown

in **Figure 4.6**(b–e). The Ti–6Al–4V contact surface was subjected to wear and had the same wear

contact diameter of 600 μm as in dry wear (**Figure 4.3**(c)). The B$_4$C coating was partially removed

from the wear track and Fe from the substrate transferred to the ball surface. The test performed at

85% RH revealed that the contact surfaces of Ti–6Al–4V were partially covered with patches of carbon transferred from the B_4C. The corresponding EDS elemental maps show C transfer from the coating and O due to oxidation (**Figure 4.6**[g-j]). The formation of carbonaceous transfer layers on Ti–6Al–4V was consistent with the low COF recorded during sliding under an atmosphere with 85% RH (**Figure 4.4**). As the wear track on the coating exhibited a smooth surface morphology without adhesion (**Figure 4.5**d). No evidence of Fe transfer (**Figure 4.6**i) was found on the counterface as the B_4C coating remained intact with only slight wear.
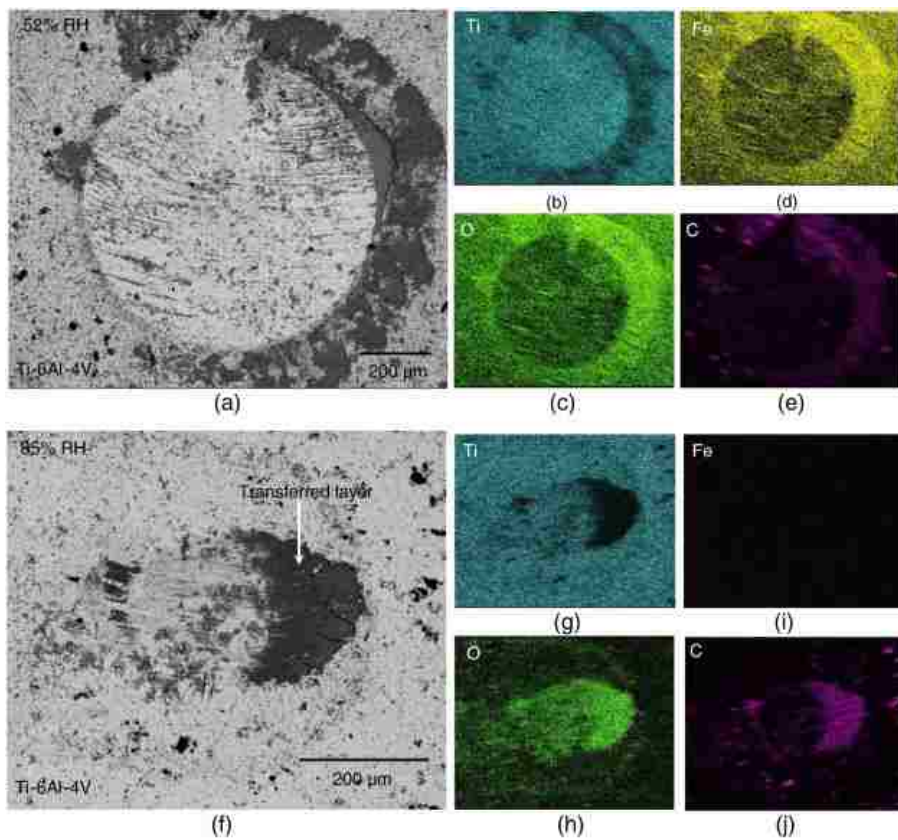
Figure 4.6 (a) Secondary electron image of the Ti–6Al–4V ball surface taken after sliding against B_4C coating at 52% RH. The elemental EDS maps taken from the area shown in (a) are for (b) Ti, (c) O, (d) Fe and (e) C. (f) Secondary electron image of the Ti–6Al–4V ball surface taken after sliding against B_4C coating at 85% RH. The elemental EDS maps taken from the area shown in (f) are for (g) Ti, (h) O, (i) Fe and (j) C.

4.3.3 Changes in tribological behaviour of B$_4$C immersed in: water, ethanol and iso-propyl alcohol

When the tests were conducted while the B$_4$C was immersed in water, where the sliding occurred under the boundary lubricated condition, a maximum COF of 0.32 was recorded during the running-in period, which lasted for 20 cycles followed by a decrease to 0.20 then to 0.16 ± 0.01 as shown in **Figure 4.7**. Both running-in and steady state COF were lower for tests conducted in ethanol; with running-in COF of 0.22 followed by a steady state COF of 0.12 ± 0.01. Even lower running-in and steady state COFs were observed during tests conducted in ethanol. The lowest running-in and steady state COF were obtained in iso-propyl alcohol, as 0.16 for the running in COF and 0.07 ± 0.01 for the steady state COF. The average values of the COF by three tests in each liquid are shown in **Table 4.2**.
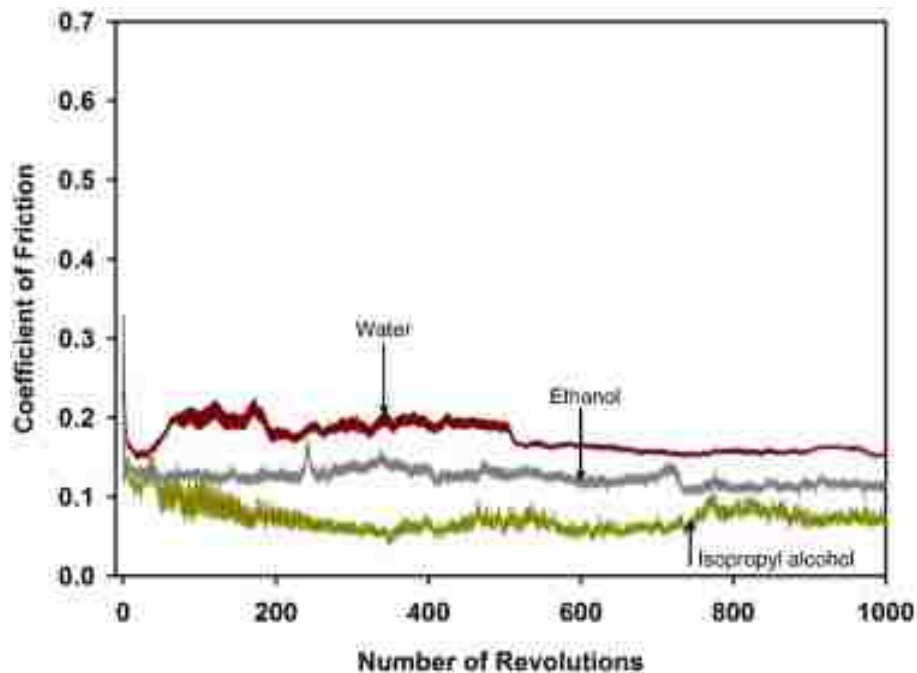
Figure 4.7 Variations of the COF with the number of revolutions for B$_4$C tested against Ti–6Al–4V in water, ethanol and iso-propyl alcohol environments.

Consistent with the decrease in the COF values, notable reductions in the amount of material transfer from the counterface (Ti–6Al–4V) to B_4C coating's wear track occurred during tests conducted in ethanol and in iso-propyl alcohol (**Figure 4.8**a and b). When B_4C as tested in iso-propyl alcohol, a transfer layer covered the contact surface of the Ti–6Al–4V ball, as shown in **Figure 4.8**(c). Note that the contact area became smaller compared to tests conducted in air (**Figure 4.6**), indicating that the minimum amount wear occurred under this condition. The well-developed carbon transfer layer that was formed on the contact surface of Ti–6Al–4V is shown in **Figure 4.8**(c and d). Ti debris could be seen ahead of the transfer layer (**Figure 4.8**e). The oxidation of the contact area was indicated by the high O concentration in **Figure 4.8**(f).
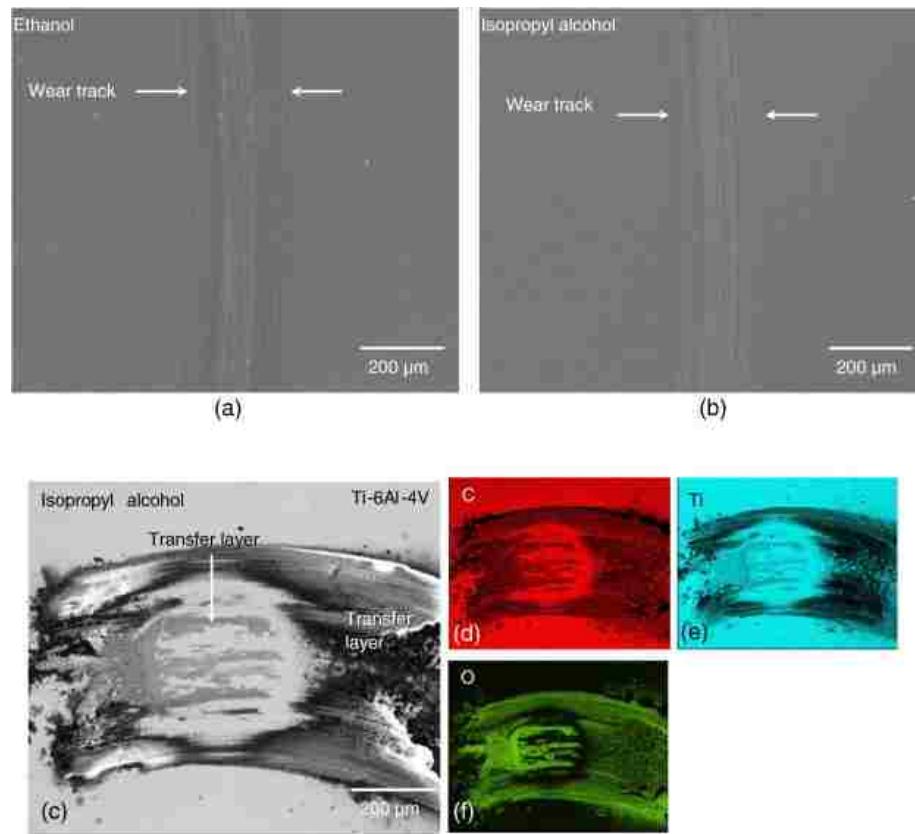

Figure 4.8 Typical secondary electron images of wear tracks formed on the B_4C surface when tested against Ti–6Al–4V in (a) ethanol and (b) iso-propyl alcohol environments. (c) Secondary electron image of the Ti–6Al–4V ball surface taken after sliding against B_4C coating in iso-propyl alcohol. The elemental EDS maps taken from the whole area shown in (c) are for (d) C, (e) Ti and (f) O.

4.3.4 Relationship between COF and wear rate

The wear test results indicated that the COFs and wear rates of B_4C decreased with the increase of humidity in the test atmosphere. Immersion into water, ethanol and iso-propyl alcohol further reduced COFs and wear rates. The highest wear rate and COF were obtained in dry N_2 with a wear rate of 160.6×10^{-5} mm^3/Nm and a COF of 0.65 ± 0.06, while the lowest wear rate of 1.18×10^{-5} mm^3/Nm and COF of 0.07 ± 0.01 obtained in iso-propyl alcohol. Furthermore, it was found that the wear rates and COFs were interdependent. **Figure 4.9** shows the linear relationship between natural logarithm wear rate (ln(wear rate)) and COF. The following equations describe the relationship between COF and wear rate for tests conducted in different atmospheres:

$$W = \exp(a\mu + b) \qquad\qquad (4-1)$$

$$W_I = 3.87 \times 10^{-5} \exp(5.89\mu) \qquad\qquad (4-2)$$

where μ is COF, W is wear rate, a and b are obtained from linear fitting curve in **Figure 4.9**. When B_4C immersed in lubricants, the equation is as follows:

$$W_{II} = 4.33 \times 10^{-6} \exp(13.83\mu) \qquad\qquad (4-3)$$

The wear rate and COF in boundary lubrication regimes are controlled by the passivation of transfer layers.
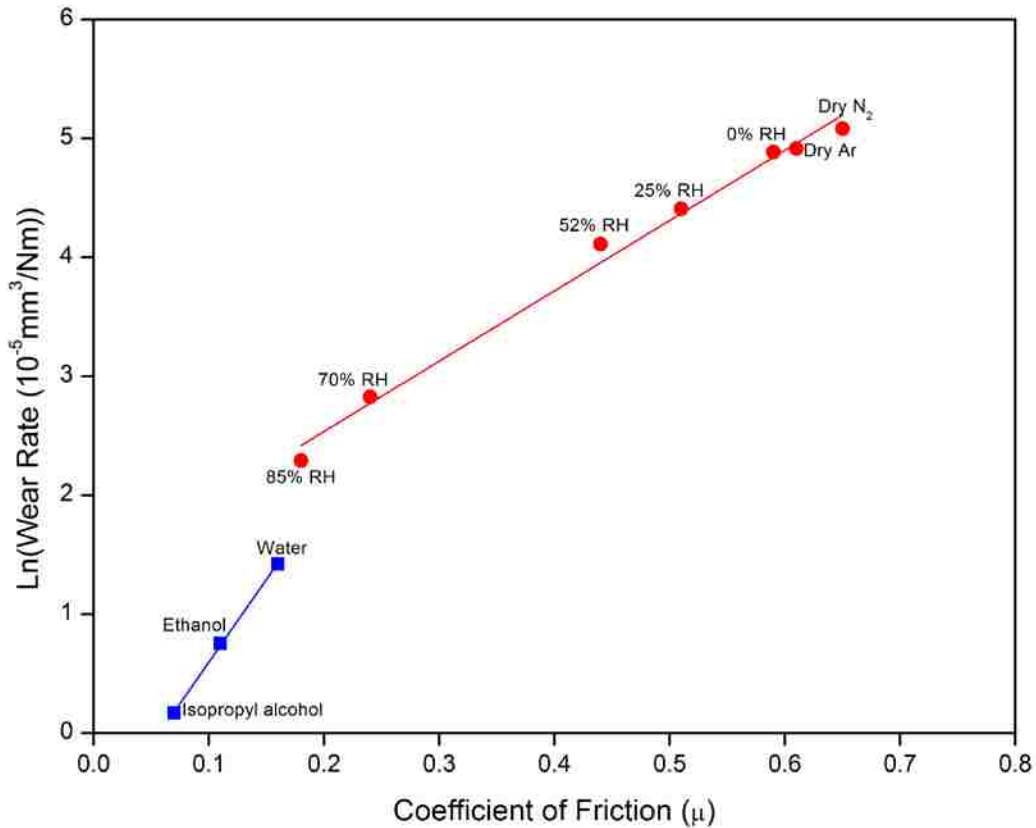
Figure 4.9 The average steady state coefficient of friction (COF) and natural logarithm of the wear rate of the B$_4$C coating sliding against Ti–6Al–4V under various test atmospheres and environments.

4.3.5 Characterization of wear tracks and transfer layers by micro-Raman analyses

The micro-Raman spectra that were obtained from the wear tracks of B$_4$C coatings together with the spectra of the corresponding Ti–6Al–4V counterface surfaces under different testing conditions are presented in **Figure 4.10**(a–d). The Raman spectra of the worn B$_4$C coating in an atmosphere of 70% RH showed peaks centered at 1388 cm^{-1} and 1583 cm^{-1} namely D and G peaks [26], where the G peak can be assigned to graphitized carbon (**Figure 4.10**a). The surface of the counterface was covered with a transfer layer and the Raman spectra indicated peaks at 1388 cm^{-1} and 1583 cm^{-1} (**Figure 4.10**b). These results indicate that the graphitized C in B$_4$C coating was transferred to the Ti–6Al–4V. The distinct D and G bands observed on the wear tracks

of B_4C and transfer layers formed on the Ti–6Al–4V during the tests conducted in ethanol and iso-propyl alcohol indicated sliding induced graphitization occurred under these test conditions as well. In addition to the D and G bands, distinct peaks were also observed at 480 cm^{-1} and 2950 cm^{-1} on both wear tracks and transfer layers in ethanol (**Figure 4.10**c) and iso-propyl alcohol (**Figure 4.10**d). The formation of these peaks may be attributed to the adsorption of ethanol and isopropyl alcohol molecules [26], and possibly responsible for passivating the graphitized carbon transferred to the Ti–6Al–4V surface.
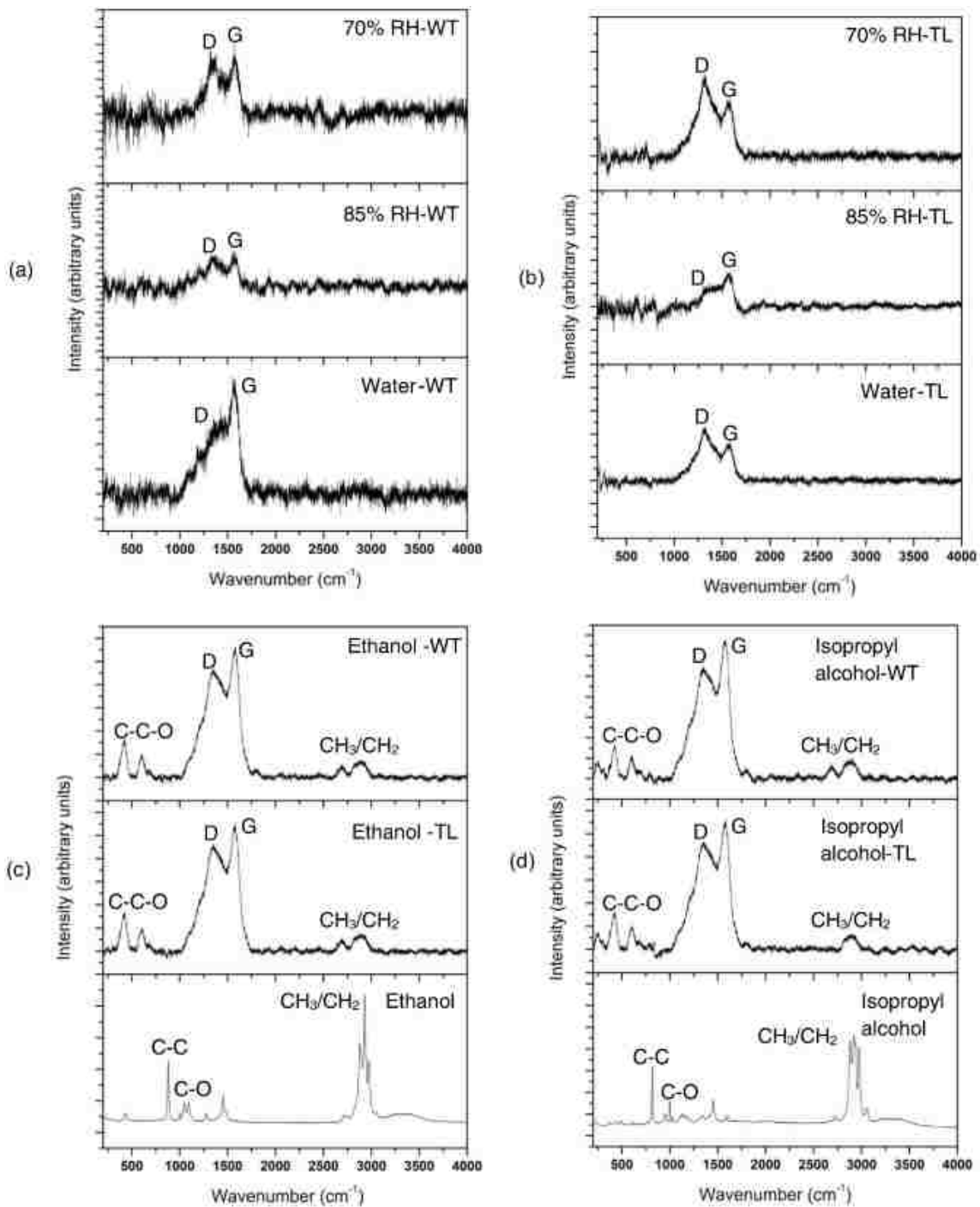
Figure 4.10 Micro-Raman spectra of (a) the wear track (WT) formed on B$_4$C surface, and (b) the transfer layer (TL) formed on Ti–6Al–4V counterface in water, 85% RH and 70% RH. Micro-Raman spectra of the WT formed on B$_4$C surface and the TL formed on the Ti–6Al–4V counterface when the test conducted in (c) ethanol and (d) iso-propyl alcohol environments. The Raman spectra of ethanol and iso-propyl alcohol were also given for comparison.

4.3.6 Characterization of wear tracks by FTIR

Fourier transform infrared spectroscopy, FTIR, analyses conducted on the wear tracks of B$_4$C showed that for experiments conducted in 85% RH, a peak at 1480 cm^{-1} was observed and attributed to the stretching associated with C–H group (**Figure 4.11**a). The carbonaceous material formed on the B$_4$C coating may passivate the surface. It was suggested that H and OH formation due to dissociation of water during sliding of other carbon based materials, such as DLC [25] could cause COF reduction. A broad band observed at 3458 cm^{-1} could be attributed to vibrations of hydroxyl (O–H) groups [27, 28]. According to the FTIR spectra shown in **Figure 4.10**(b), the wear track of B$_4$C formed during tests conducted in ethanol consisted of hydrocarbon compounds; where bands associated with to C–H groups were identified at 1480 cm^{-1}. Similar to the wear track formed in 85% RH, a broad band was observed at 3458 cm^{-1} that was likely due to the stretching of hydroxyl (O–H) groups. In addition to the C–H and O–H, a prominent peak at 1305 cm^{-1} was observed on the wear track, and may be attributed to B$_2$O$_3$ [17, 19]. The formation of this peak indicates that the B in B$_4$C coating was oxidized during the sliding contact and friction. Similar observations were made on the wear tracks generated when the tests were conducted in iso-propyl alcohol; C–H, O–H and B$_2$O$_3$ groups were identified at 1480 cm^{-1}, 3458 cm^{-1} and 1305 cm^{-1}.
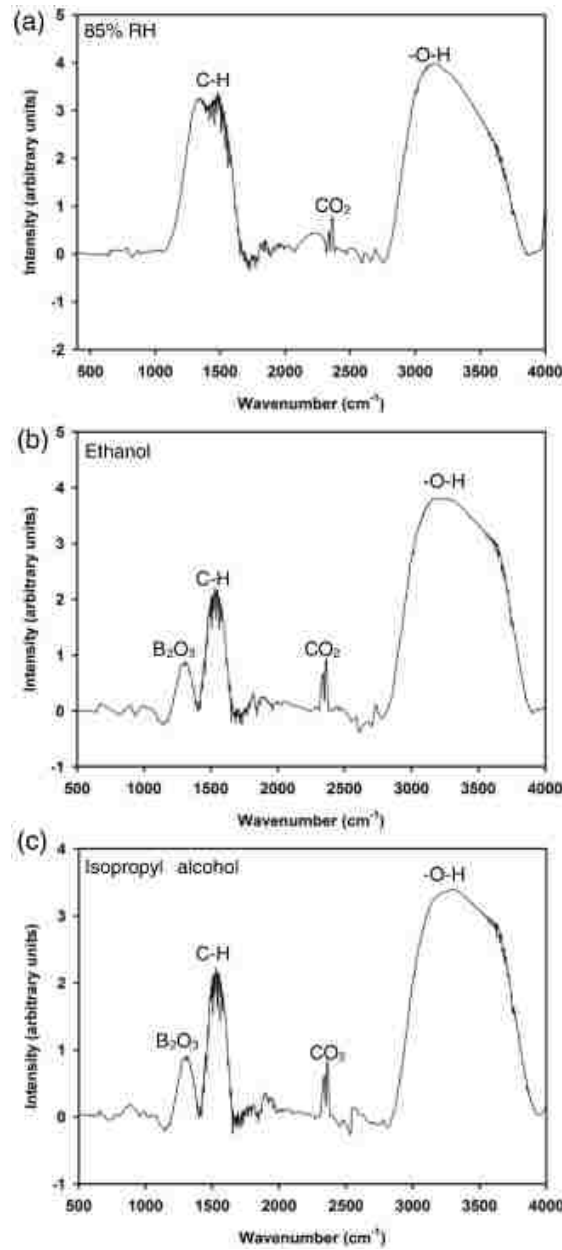
Figure 4.11 FTIR spectra of the B_4C (wear track) tested against Ti–6Al–4V at (a) 85% RH, (b) ethanol and (c) iso-propyl alcohol. (The CO_2 peaks at 2350 cm^{-1} observed in all testing environments may be due to contamination from the surrounding atmosphere [26]).

Consequently, ethanol and iso-propyl alcohol were more effective oxidizing agents for boron, as indicated by the prominent B_2O_3 peak (**Figure 4.11**[b, c]), as compared to tests conducted in 85% RH (**Figure 4.11**a). The decreases in running-in and steady state COF values are in agreement with the previously suggested surface passivation mechanism of graphitic carbon bonds by H and OH

144

molecules dissociated from the moisture during sliding contact [29-32]. More direct evidence for passivation was provided by the XPS data.

PS analyses of C 1s, O 1s, Ti 2p and B 1s of the transfer layers (see **Figure 4.8**) that were formed during the test conducted in iso-propyl alcohol are shown in [**Figure 4.12**(a–d)]. The C 1s binding energies of 284.80 and 286.30 (**Figure 4.12**a) can be assigned to the –C–C/− C–H and –C–OH/− C–O–C bonding states, respectively [33, 34]. The H_2O, OH and oxide peaks observed at 532.78 eV and 531.61 eV are shown in **Figure 4.12**(b). These results suggested that the carbon atoms in the graphitized transfer layers were terminated by –OH, − H, and –O.
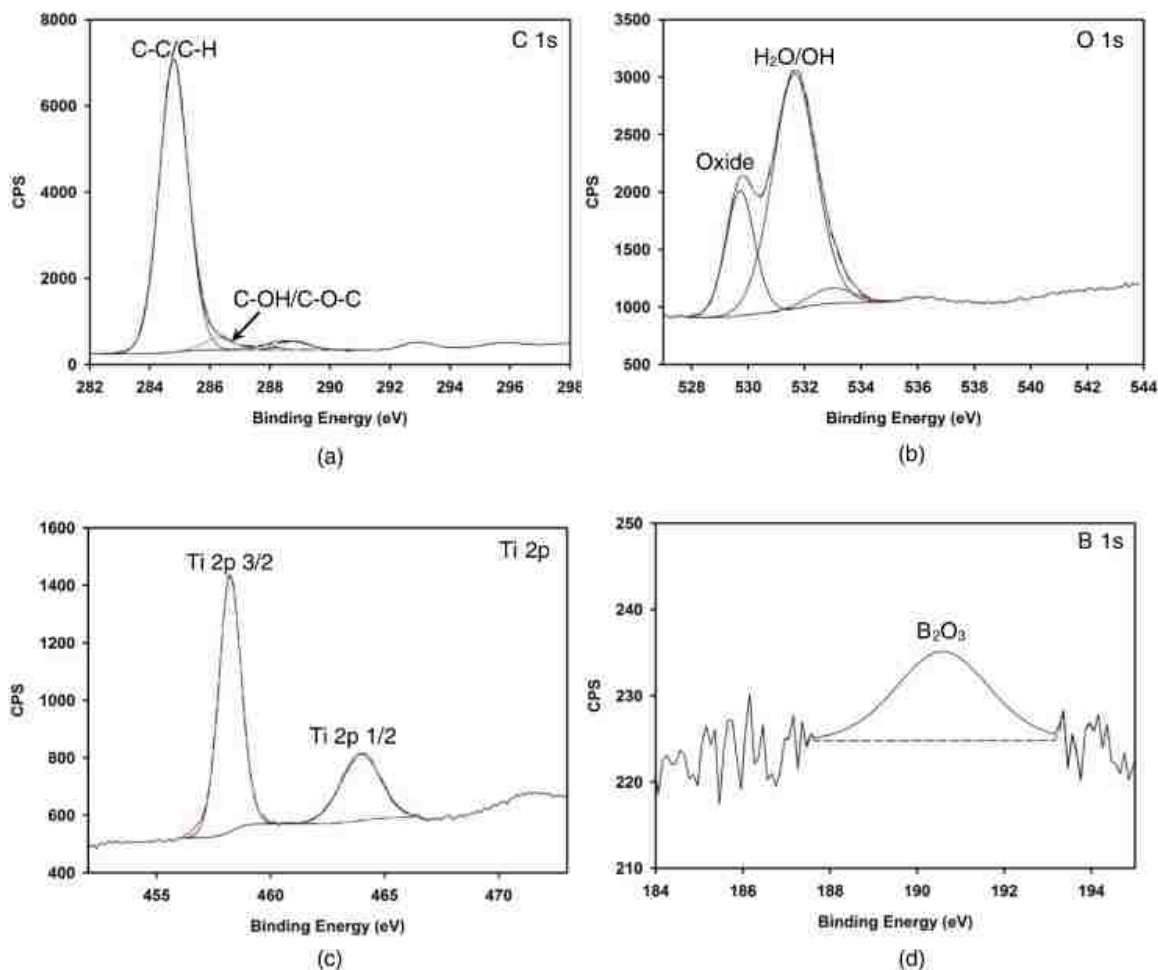
Figure 4.12 X-ray photoelectron spectroscopy (XPS) spectra of transfer layers that formed on Ti–6Al–4V counterface during sliding against B_4C in iso-propyl alcohol environment for (a) C 1s, (b) O 1s, c) Ti 2p and d) B 1s.

4.4   Discussion

In previous studies, the COFs of B_4C coatings were reported to be in the range of 0.10-0.20 [16-20], which were attributed to the formation of boric acid. Because the boric acid has a layered structure similar to that of graphite, the weak van der Waals forces between layered crystal structures of boric acid can result in low COF [19, 20]. The boron carbide can react chemically with oxygen and water according to

$$B_4C + O_2 \rightarrow B_2O_3 + C + CO(g)\uparrow + CO_2(g)\uparrow$$

$$\frac{1}{2}B_2O_3 + \frac{3}{2}H_2O \rightarrow H_3BO_3 \text{, } \Delta H_{298} = \text{-45.1 kJ/mol}$$
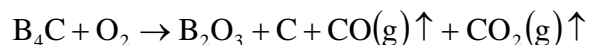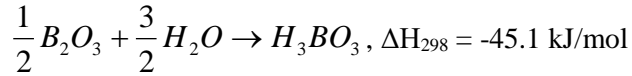
In current study, the formation of B_2O_3 was observed in both transfer layer and on the wear track as confirmed by the FTIR (**Figure 4.11**) and XPS (**Figure 4.12**) studies. The B_2O_3 can react with OH provided by the water, ethanol and iso-propyl alcohol and form boric acid at the sliding interfaces. However, micro-Raman spectra did not support the formation of boric acid, because there were no characteristic peaks that belonged to boric acid (**Figure 4.13**). The OH dissociated from water and alcohol was more likely consumed in the passivation of carbon as carbon has high chemical affinity to both H and OH compared to boron. Although no evidence was found for the formation of boric acid at the sliding interface in the current tests conducted at room temperature, H_3BO_3 formation at the sliding interface was observed when B_4C samples were annealed at 600 °C for 60 min and cooled in the air. Sliding tests were conducted against Ti–6Al–4V, while the counterface and B_4C were submerged in water. The variation of COF with number of revolutions is shown in **Figure 4.13**(a) for tests carried out under the same loading conditions as the samples that were not subjected to the annealing treatment. It can be seen that a low and stable COF of 0.23 was observed after ~ 60 revolutions. Micro-Raman spectra of the transfer layer formed on the contact surface of Ti–6Al–4V revealed a peak at 802 cm^{-1}, which is associated with H_3BO_3 in **Figure 4.13**b. This result indicated that the formation of boric acid in sample tested after annealing at 600 °C was possible and played a role in obtaining a low and stable COF.
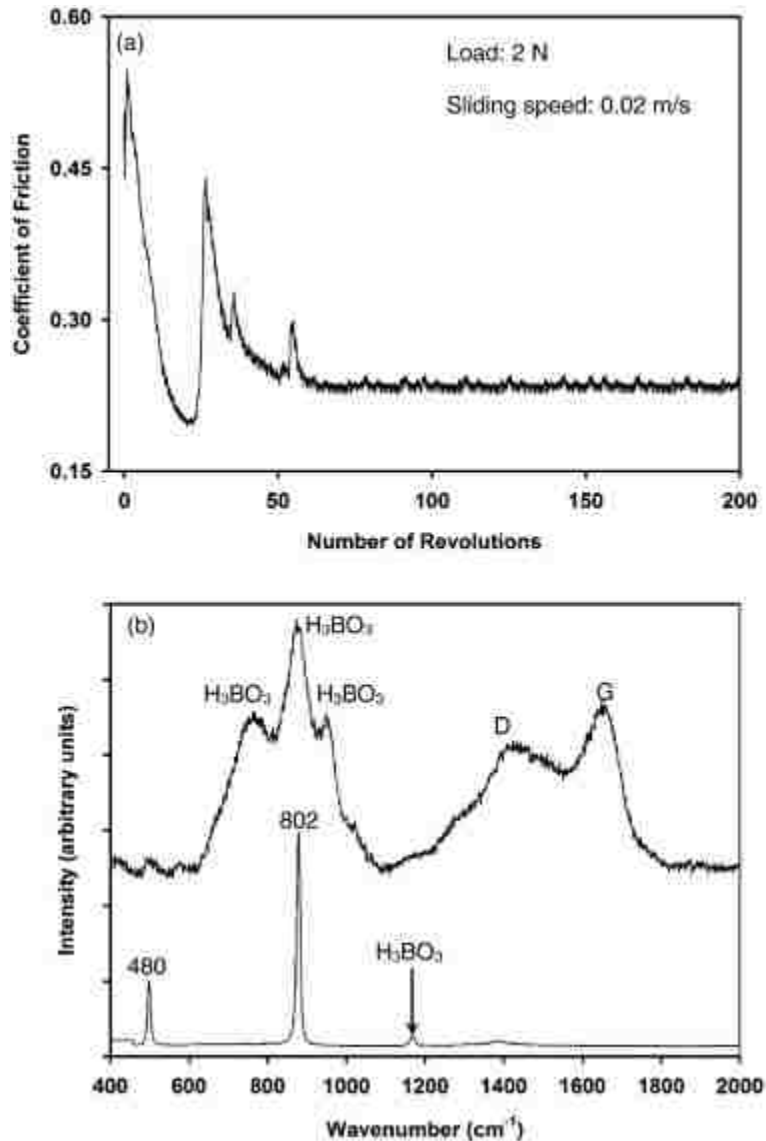
Figure 4.13 a) variations of the COF with the number of revolutions tested against heat treated B₄C in water environment; (b) the micro-Raman spectra of boric acid and the transfer layer formed at the sliding surface.

In the present study, B$_4$C exhibited high COFs and high wear rates in dry N$_2$, Ar and air atmospheres with $< 0.5\%$ RH, which indicated that moisture in atmosphere was needed for low COF. In dry atmospheres, the surface carbon atoms tend to interact with the atoms of the counterface material. The degree of these interactions is expected to increase with increasing the chemical affinity of the counterface material towards C in the B$_4$C coating. Ti has high driving

force for compound formation with C. The standard Gibbs free energy of formation (ΔG_f^o) of TiC is $-$ 180.0 kJ/mol at 300 K [25]. The high chemical affinity of Ti towards C would likely to promote adhesion of Ti to the B_4C surface resulting in high COF values and high wear rates in dry atmospheres.

The COF started to decrease when the tests were conducted in 25% RH and 52% RH. However, these tests did not show a considerable decrease in COF and Ti transfer was not prevented. A significant decrease in COF was observed at > 70% RH and was further reduced with increasing RH revealing that the graphitic carbon formed as a result of sliding contact at the B_4C surface and the transferred to the counterface may be passivated by H and OH. Adsorption and dissociation processes of H_2O on C surfaces and formation of C-OH and C-H bonds have been previously described [30, 35-38]. Carbon atoms and the mechanism of OH passivation has been studied by first principles calculations and dissociation energies of water molecules on diamond surfaces were computed [30]. At the present time similar calculations for B_4C are lacking. However, the presence of OH groups at the contact surfaces was confirmed by the FTIR analyses. FTIR spectra shown in **Figure 4.10**(b) and (c) indicated that an atmospheric humidity > 85% RH would lead to a low COF and wear rate due to the passivation of carbon by H and OH. These observations were also supported by XPS results.

OH passivation of the carbonaceous surfaces may also be responsible for further reduction in the COF when the tests were conducted under boundary lubrication condition (in ethanol and iso-propyl alcohol). The appearance of micro-Raman peaks (**Figure 4.11**c) corresponding to CH_3 stretching and bending observed in tests conducted in ethanol should be noted. The dissociation of a methanol molecule and the formation of OH groups have been previously studied [39-43] using a model that considered a methanol molecule sandwiched between two carbon surfaces. Quantum dynamics studies showed that the methanol molecule could dissociate and produce OH groups, which terminate the surface carbon atoms. Some details of carbon

passivation by water and ethanol can be found in [25]. A further reduction in COF was observed while the sliding tests were conducted in iso-propyl alcohol (C_3H_7OH). The passivating ability of water, ethanol and isopropyl alcohol may be related to their propensity to dissociate to OH and H^+, $C_2H_5^+$ and $C_3H_7^+$. Accordingly, the isopropyl alcohol has the highest propensity to dissociate as the resultant isopropyl carbocation is the most stable due to charge delocalization via resonance [39-43]. It is expected that the isopropyl alcohol will readily passivate the carbon surfaces. Further theoretical calculations are needed to delineate the details of dissociation and passivation mechanisms and kinetics.

4.5   Conclusions

1. When B_4C was tested in dry atmospheres with < 0.5% RH, high COF values of 0.59–0.65 and high wear rates were observed against Ti-6Al-4 V. The increase in humidity between 25% and 85% RH resulted in a decrease in COF from 0.51 to 0.18. The lowest COF values were obtained in water (0.16), ethanol (0.11) and iso-propyl alcohol (0.07).

2. A linear relationship between the natural logarithm wear rate (ln (wear rate)) and the COF was found. When initial wear rate was high, the COF was also high.

3. In high humidity atmospheres where sliding induced graphitization occurred as observed by Raman, FTIR and XPS, the passivation of graphite layers controlled COF.

4.6   Acknowledgement

4.7 Bibliography

[1] R.R. Boyer, An overview on the use of titanium in the aerospace industry, Mat Sci Eng a-Struct, 213 (1996) 103-114.

[2] A. Molinari, C. Musquar, G. Sutter, Adiabatic shear banding in high speed machining of Ti-6Al-4V: experiments and modeling, Int J Plasticity, 18 (2002) 443-459.

[3] L.N. Lopez de lacalle, J. Perez, J.I. Llorente, J.A. Sanchez, Advanced cutting conditions for the milling of aeronautical alloys, J Mater Process Tech, 100 (2000) 1-11.

[4] J.L. Cantero, M.M. Tardio, J.A. Canteli, M. Marcos, M.H. Miguelez, Dry drilling of alloy Ti-6Al-4V, International Journal of Machine Tools & Manufacture, 45 (2005) 1246-1255.

[5] A.K.M.N. Amin, A.F. Ismail, M.K.N. Khairusshima, Effectiveness of uncoated WC-Co and PCD inserts in end milling of titanium alloy-Ti-6Al-4V, J Mater Process Tech, 192 (2007) 147-158.

[6] S. Bhowmick, A.T. Alpas, The Performance of Diamond-Like Carbon Coated Drills in Thermally Assisted Drilling of Ti-6Al-4V, Journal of Manufacturing Science and Engineering-Transactions of the Asme, 135 (2013).

[7] A. Banerji, S. Bhowmick, A.T. Alpas, High temperature tribological behavior of W containing diamond-like carbon (DLC) coating against titanium alloys, Surf Coat Tech, 241 (2014) 93-104.

[8] X.D. Wu, D.P. Wang, S.R. Yang, Q.J. Xue, Tribochemical investigation of tungsten carbide/titanium alloy tribo-couples under aqueous lubrication, Wear, 237 (2000) 28-32.

[9] N.P. Suh, Tribophysics, Prentice-Hall, 1986.

[10] M. Rahman, Y.S. Wong, A.R. Zareena, Machinability of titanium alloys, Jsme International Journal Series C-Mechanical Systems Machine Elements and Manufacturing, 46 (2003) 107-115.

[11] G.A. Oosthuizen, G. Akdogan, N. Treurnicht, The performance of PCD tools in high-speed milling of Ti6Al4V, Int J Adv Manuf Tech, 52 (2011) 929-935.

[12] F. Nabhani, Machining of aerospace titanium alloys, Robot Cim-Int Manuf, 17 (2001) 99-106.

[13] E.O. Ezugwu, R.B. Da Silva, J. Bonney, A.R. Machado, Evaluation of the performance of CBN tools when turning Ti-6Al-4V alloy with high pressure coolant supplies, International Journal of Machine Tools & Manufacture, 45 (2005) 1009-1014.

[14] F. Thévenot, Boron carbide—A comprehensive review, Journal of the European Ceramic Society, 6 (1990) 205-225.

[15] Y.G. Tkachenko, V.F. Britun, D.Z. Yurchenko, M.S. Kovalchenko, I.I. Timofeeva, L.P. Isaeva, Structure and Phase Formation in Boron Carbide and Aluminum Powder Mixtures during Hot Pressing, Powder Metall Met C+, 50 (2011) 202-211.

[16] G.T. G.V. Samsonov, A.G. Yu, Dobrovol'skii, Temperature dependence of the coefficients of friction of boron and silicon carbides in a vacuum, Sov. Powder Metall. Met. Ceram., 9 (1970) 587-589.

[17] A. Erdemir, G.R. Fenske, R.A. Erck, A Study of the Formation and Self-Lubrication Mechanisms of Boric-Acid Films on Boric Oxide Coatings, Surf Coat Tech, 43-4 (1990) 588-596.

[18] B.G. Y.G. Tkachenko, N. Bodnaruk, V. Sychev, Friction and wear of boron carbide at temperatures in the range 20–1500 °C, Sov. Powder Metall. Met. Ceram., 16 (1977) 541-543.

[19] A. Erdemir, C. Bindal, C. Zuiker, E. Savrun, Tribology of naturally occurring boric acid films on boron carbide, Surf Coat Tech, 86-7 (1996) 507-510.

[20] T. Eckardt, K. Bewilogua, G. van der Kolk, T. Hurkmans, T. Trinh, W. Fleischer, Improving tribological properties of sputtered boron carbide coatings by process modifications, Surf Coat Tech, 126 (2000) 69-75.

[21] H.S. Ahn, P.D. Cuong, K.H. Shin, K.S. Lee, Tribological behavior of sputtered boron carbide coatings and the influence of processing gas, Wear, 259 (2005) 807-813.

[22] M.G.R. W. Cermignani, T. Hu, L. Stiehl, W. Rafaniello, T. Fawcett, P. Marshall, S. Rozeveld, Processing, properties and performance of high volume sputter deposited boron-carbon coatings, Proc. Annu. Tech. Conf. Soc. Vac. Coaters, (1998) 66-74.

[23] X. Meng-Burany, A.T. Alpas, FIB and TEM studies of damage mechanisms in DLC coatings sliding against aluminum, Thin Solid Films, 516 (2007) 325-335.

[24] E. Konca, Y.T. Cheng, A.M. Weiner, J.M. Dasch, A.T. Alpas, Effect of test atmosphere on the tribological behaviour of the non-hydrogenated diamond-like carbon coatings against 319 aluminum alloy and tungsten carbide, Surf Coat Tech, 200 (2005) 1783-1791.

[25] S. Bhowmick, A. Banerji, A.T. Alpas, Tribological behavior and machining performance of non-hydrogenated diamond-like carbon coating tested against Ti-6Al-4V: Effect of surface passivation by ethanol, Surf Coat Tech, 260 (2014) 290-302.

[26] A. Abou Gharam, M.J. Lukitsch, M.P. Balogh, A.T. Alpas, High temperature tribological behaviour of carbon based (B4C and DLC) coatings in sliding contact with aluminum, Thin Solid Films, 519 (2010) 1611-1617.

[27] I. Caretti, I. Jimenez, Composition and bonding structure of boron nitride B1-xNx thin films grown by ion-beam assisted evaporation, Chem Phys Lett, 511 (2011) 235-240.

[28] A. Abou Gharam, M.J. Lukitsch, Y. Qi, A.T. Alpas, Role of oxygen and humidity on the tribo-chemical behaviour of non-hydrogenated diamond-like carbon coatings, Wear, 271 (2011) 2157-2163.

[29] A. Erdemir, The role of hydrogen in tribological properties of diamond-like carbon films, Surf Coat Tech, 146 (2001) 292-297.

[30] Y. Qi, E. Konca, A.T. Alpas, Atmospheric effects on the adhesion and friction between non-hydrogenated diamond-like carbon (DLC) coating and aluminum - A first principles investigation, Surface Science, 600 (2006) 2955-2965.

[31] S. Bhowmick, A.T. Alpas, The role of diamond-like carbon coated drills on minimum quantity lubrication drilling of magnesium alloys, Surf Coat Tech, 205 (2011) 5302-5311.

[32] S. Bhowmick, A.T. Alpas, Minimum quantity lubrication drilling of aluminium-silicon alloys in water using diamond-like carbon coated drills, International Journal of Machine Tools & Manufacture, 48 (2008) 1429-1443.

[33] F.G. Sen, X. Meng-Burany, M.J. Lukitsch, Y. Qi, A.T. Alpas, Low friction and environmentally stable diamond-like carbon (DLC) coatings incorporating silicon, oxygen and fluorine sliding against aluminum, Surf Coat Tech, 215 (2013) 340-349.

[34] S. Bhowmick, F.G. Sen, A. Banerji, A.T. Alpas, Friction and adhesion of fluorine containing hydrophobic hydrogenated diamond-like carbon (F-H-DLC) coating against magnesium alloy AZ91, Surf Coat Tech, 267 (2015) 21-31.

[35] J.F. Mammone, S.K. Sharma, M. Nicol, Raman-spectra of methanol and etthanol at pressures up to 100 kbar, Journal of Physical Chemistry, 84 (1980) 3130-3134.

[36] S. Bhowmick, A. Banerji, A.T. Alpas, Role of humidity in reducing sliding friction of multilayered graphene, Carbon, 87 (2015) 374-384.

[37] J. Spreadborough, The frictional behaviour of graphite, Wear, 5 (1962) 18-30.

[38] B.K. Yen, Influence of water vapor and oxygen on the tribology of carbon materials with sp(2) valence configuration, Wear, 192 (1996) 208-215.

[39] N.A. Lange, J.A. Dean, Lange's Handbook of Chemistry, McGraw-Hill, 1973.

[40] K. Hayashi, S. Sato, S. Bai, Y. Higuchi, N. Ozawa, T. Shimazaki, K. Adachi, J.-M. Martin, M. Kubo, Fate of methanol molecule sandwiched between hydrogen-terminated diamond-like carbon films by tribochemical reactions: tight-binding quantum chemical molecular dynamics study, Faraday Discussions, 156 (2012) 137-146.

[41] J. McMurry, Organic Chemistry, Brooks/Cole Cengage Learning, 2011.

[42] M. Saunders, E.L. Hagen, Rosenfel.J, Rearrangement reactions of secondary carbonium ions . protonated cyclopropane intermediates formed from sec-butyl cation, J Am Chem Soc, 90 (1968) 6882-&.

[43] M. Saunders, P. Vogel, E.L. Hagen, Rosenfel.J, Evidence for protonated cyclopropane intermediates from studies of stable solutions of carbonium-ions, Accounts of Chemical Research, 6 (1973) 53-59.

CHAPTER 5

EFFECT OF ATMOSPHERE AND TEMPERATURE ON THE TRIBOLOGICAL BEHAVIOR OF THE TI CONTAINING MOS$_2$ COATINGS AGAINST ALUMINUM

5.1   Introduction

Transition metal dichalcogenides (TMD) such as WS$_2$ and MoS$_2$ are well known for their favorable tribological behavior as they act as solid lubricants under certain environmental conditions [1]. MoS$_2$ has a lamellar structure with a layer of Mo atoms being sandwiched between two layers of S atoms [2]. Covalent bonding occurs within the S–Mo–S sandwich layers, while Van der Waals forces are formed between the sandwich layers. There are three known structures of MoS$_2$; the 2H structure consists of two layers per unit cell stacked in hexagonal symmetry, while the 3R structure has three layers in rhombohedral symmetry [3]. Both 2H and 3R structures are relatively stable with trigonal prismatic coordination, while the 1T structure with Mo atoms coordinated in an octahedral manner is metastable [4]. The 1T phase can be transformed into the 2H phase by heating or aging [5]. The different phases of MoS$_2$ could be identified by Raman spectroscopy [6]. The basal planes of MoS$_2$ are easily sheared leading to the formation of transfer layers on the counterface and result in a low coefficient of friction (COF). Martin et al. [7] reported that the low friction (COF < 0.005) of MoS$_2$ coatings under the ultra-high vacuum could be attributed to the easy shear of the basal planes of the MoS$_2$ crystal structure oriented parallel to the contact surface. Other studies [8, 9] have also reported that MoS$_2$ coatings tested in vacuum had low COF values between 0.01 and 0.04. The COF of MoS$_2$ is not an intrinsic property, but depends on environmental conditions. These coatings exhibit low COF and long wear life in dry air, in inert gases in addition to vacuum testing conditions [7-12]. When tested in humid air, however, moisture could induce higher COF by reacting with dangling bonds on the edge of basal planes [13, 14].

Donnet et al. [15] measured a COF of 0.15 under ambient air (40% RH) when the MoS2 coatings were tested against SAE 52100 steel, whereas in ultra-high vacuum (5×10^{-8} Pa) low COF of 0.003 was obtained. It was suggested that in humid atmospheres, the vapor molecules would diffuse into the interlamellar gap and restrain the shear of basal planes [16]. Khare et al. [17] also observed that the COF values increased with increased moisture when MoS_2 coatings slid against 440C steel at temperatures below 100 °C. Deacon and Goodman [18] proposed that the increase in COF could be attributed to the bonding between water and edge sites of MoS_2 layers which restrains the shear movement.

It was found that the addition of Ti in MoS_2 (Ti–MoS_2) coatings reduced the sensitivity of the COF to the humidity [19]. Ti–MoS_2 maintained a low COF of 0.07 when tested against WC–Co counterface at 50% RH. It was shown that when 9.5 at% Ti was added to MoS_2, and the coating maintained low COF values of 0.03–0.08 during test in environments with RH between 25 and 75%, whereas higher COF values were observed for monolithic MoS_2 coating under the same test conditions using an Al_2O_3 counterface [20]. It was suggested that the presence of Ti atoms in MoS_2 coatings may reduce the propensity of water vapor entering interlamellar spaces [20]. Wang et al. [21] found that MoS2 tested against Si_3N_4 counterfaces at room temperature with 38% humidity showed a high COF of 0.82, whereas when 15.3 at% Ti was added to MoS_2, the COF was reduced to 0.16 under the same test conditions.

Mechanical properties of the MoS_2 coatings were also found to improve with the addition of Ti [22]. An hardness increase from 4.9 GPa for MoS_2 to 8.3 GPa for Ti–MoS_2 with 15.3 at% Ti was recorded and the hardness increased further to 10.35 GPa for Ti–MoS_2 with the addition of 19.5 at% Ti [21].

Although frictional properties of MoS_2 against steel- or ceramic-based counterfaces in air and under a vacuum atmosphere are widely studied, only few studies have considered the high

temperature friction and wear behavior of MoS$_2$ coatings. Kubart et al. [23] found that the COF values of MoS$_2$ coatings sliding against 52100 steel decreased from 0.14 at 28 °C (50% RH) to 0.04 at 100 °C. Arslan et al. [24] showed that the COF values of MoS2 coatings tested against Al2O3 counterfaces decreased from 0.07 at 25 °C to 0.03 at 300 °C, although they increased abruptly to above 0.45 at 500 °C. Wong et al. [25] found that MoS$_2$ coatings against sliding against A2 steel tested at 35% RH had a low COF of $\leqslant$ 0.11 at temperatures up to 320 °C which was attributed to the formation of a sulfur-rich transfer layer on the counterface. At temperatures higher than 400 °C, the MoS$_2$ layers oxidized completely to MoO$_3$ due to combined effects of high temperatures and sliding induced shear deformation resulting in the increase in COF values to above 0.35. A recent study showed that at temperatures between 25 and 200 °C Ti–MoS$_2$ coatings showed low COF values of 0.05–0.11 against Al-6.5% Si (Al 319) [26]. However, the COF (0.11–0.15) increased at the temperature range of 250–350 °C due to the formation of MoO$_3$ on the contact surfaces. At above 400 °C, the Ti–MoS$_2$ coatings began to disintegrate and the adhesion of 319 Al to the coating surface occurred. Consequently, elimination of O$_2$ from the test atmosphere is expected to stabilize the friction in the temperature range of 250–350 °C. Accordingly, in this study, friction and adhesion mechanisms of Ti–MoS$_2$ coatings tested against Al-6.5% Si alloys were investigated in the temperatures range between 25 and 400 °C in a N$_2$ atmosphere. SEM, Energy-dispersive X-ray spectroscopy (EDS) and micro-Raman analyses of the pristine coating and worn surfaces have been performed to delineate the friction mechanisms of Ti–MoS$_2$ coatings tested under a N$_2$ atmosphere at different temperatures.

5.2 Experimental Procedure

5.2.1 Materials

The Ti containing MoS$_2$ composite coatings designated as Ti–MoS$_2$ were produced by Miba (Teer) Coatings Group (Worcestershire, UK) using a d. c. magnetron sputtering technique. Three

MoS$_2$ targets and one Ti target were used during the deposition with the substrates continuously rotating between the targets [19, 27]. An argon sputtering pressure of 0.4 Pa was applied, and the substrate temperature was maintained at < 200 °C. The steel coupons of 2.54 cm in diameter and with a hardness of 64 ± 3 HRC were used as the substrate. The hardness of the coatings was measured using a Hysitron TI 900 TriboIndenter equipped with a Berkovich nano-indenter tip with an indenter contact depth of 150 nm. Accordingly, the Ti–MoS$_2$ had a hardness of 3.51 ± 0.10 GPa (harder than conventional MoS$_2$ coating with a hardness of 1.20 GPa [1]). The microstructure of Ti–MoS$_2$ was characterized by transmission electron microscopy (TEM) by observing cross-sections excised using focused ion beam (FIB) milling. Carl Zeiss NVision 40 Cross-Beam instrument was used for the preparation of FIB lift-out samples [28, 29, 30] which were subsequently analyzed using high-resolution TEM (FEI Titan 80–300). The bright-field TEM image of the as-deposited Ti–MoS$_2$ showing the layer structure of the coating is presented in **Figure 5.1**a. The average thickness of MoS2-rich layers was 2.3 and 1.9 nm for Ti-rich layers. EDS spectra were recorded using an FEI Quanta 200 FEG scanning electron microscope equipped with an EDAX SiLi detector spectrometer. The spectra revealed the distributions of Mo, S and Ti across the thickness of the coating. **Figure 5.1**b shows the elemental distribution of Ti, S and Mo along the thickness of the coating.
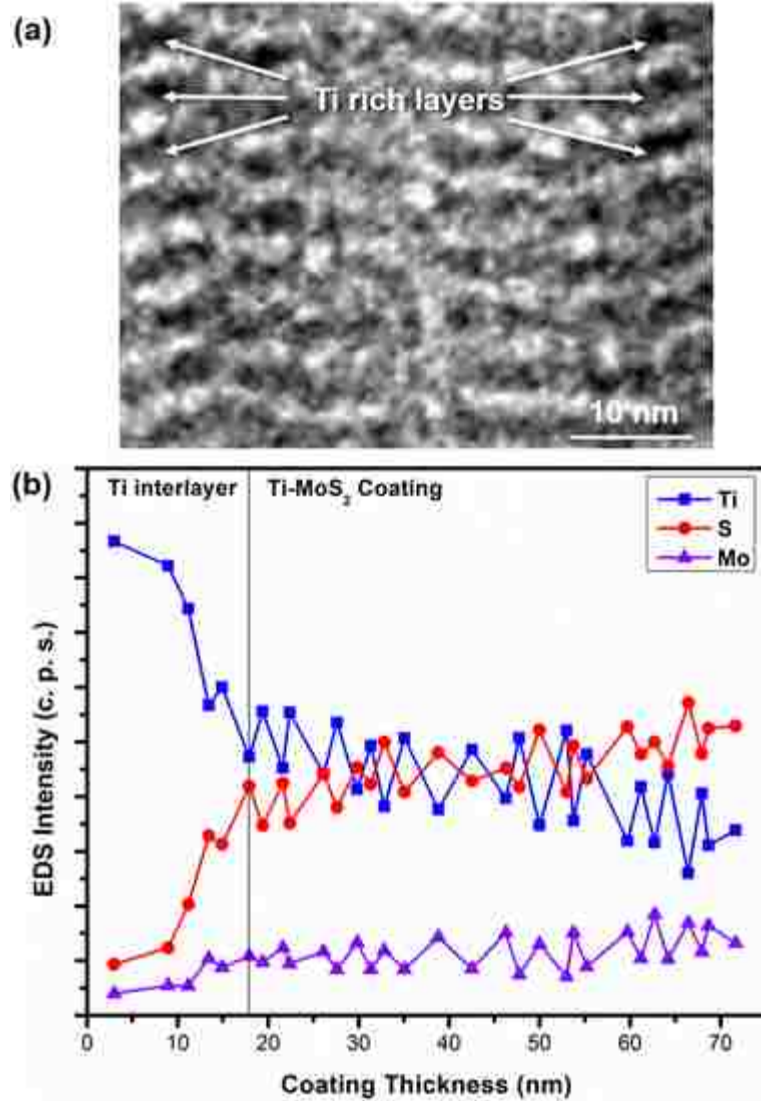
Figure 5.1 TEM cross-sectional image and elemental distribution along the thickness of Ti–MoS$_2$ coating. **a** A TEM bright-field image showing the microstructure of the Ti–MoS$_2$ coating Ti layer thickness: 1.9 ± 0.4 nm MoS$_2$ layer thickness: 2.3 ± 0.4 nm, **b** elemental composition variation along the thickness of the coating.

The counterfaces used for friction and wear tests were 15 mm long 319 Al alloy pins with one end machined into a hemisphere with the diameter of 4.05 mm. 319 Al had the following composition (in wt%): 5.5–6.5% Si, 3.0–4.0% Cu, 1.0% Fe, 0.10% Mg, 0.5% Mn, 0.35% Ni, 1.0% Zn, 0.25% Ti and the balance Al. The bulk hardness of 319 Al was 72.40 HR-15 T, measured as Rockwell superficial hardness using a 1/16 in (1.59 mm) diameter ball.

5.2.2 Pin-on-Disk Tests: COF Calculations

A high temperature pin-on-disk tribometer was used to measure the COF values and the volumetric wear rates of Ti–MoS$_2$ coatings against aluminum. A constant speed of 0.12 m/s and a normal load of 5.0 N were used for 2000 revolutions. Tests were performed in ambient air (58% RH), dry air (2% RH, 21.3 kPa O$_2$ partial pressure), dry O$_2$ (2% RH, 101.3 kPa O$_2$ partial pressure) and dry N$_2$ (2% RH). The COF was measured continuously during the sliding test. The COF values plotted as a function of sliding distance (number of revolutions) are reported. Whenever steady-state COF (μ_S) regime was attained, the average μ_S was taken typically after 1500 revolutions for the tests conducted in different atmospheres and after 1000 revolutions for the tests conducted at high temperatures in a dry N$_2$ atmosphere. For tests with no steady-state COF, the mean value of the entire curve (typically with high fluctuations) was reported. The Ti–MoS$_2$ coatings were subjected to high temperature tests at 100, 200, 300, 400 and 500 °C. Three tests were conducted at each test temperature.

5.2.3 Wear Rate Calculations

The volume of material transferred was determined by observing the Ti–MoS$_2$ coating wear tracks and 319 Al contact surfaces using an SEM operated at 15 kV. The areal distribution of aluminum transferred to the sliding track of the coating and coating transfer to the counterface were determined using an energy-dispersive spectroscopy (EDS) technique. The wear track was re-examined after dissolving the transferred material (in 10% NaOH) to calculate the volumetric wear loss from the Ti–MoS$_2$ contact surfaces using 2D depth profiles of the wear track generated by Wyko surface profilometer [31-33]. The average wear loss of the Ti–MoS$_2$ coating was calculated from the volumetric loss measured from three wear tracks at each temperature and six different locations from each wear track (18 measurements).

Micro-Raman spectra on the transfer layers were obtained using a 50 mW Nd–YAG laser (532 nm excitation line) through the 50× objective lens (diameter of the laser spot for Raman on the specimen surface was 1 µm) of a Horiba Raman micro-spectrometer.

5.3 Results and Discussion

5.3.1 Change in Tribological Behavior of Ti-MoS$_2$ with Test Atmosphere

Figure 5.2 shows the variation of the COF of Ti–MoS$_2$ coatings with the number of revolutions for the tests conducted in ambient, dry air, dry O$_2$ and dry N$_2$ atmospheres. Under these conditions, the Ti–MoS$_2$ coatings initially exhibited a high running-in COF (μ_R) value then a low steady-state COF (μ_S) value was reached in dry N$_2$ and under ambient air. All μ_R and μ_S values obtained from tests are listed in **Table 5.1**. Under ambient air, the μ_R and μ_S of Ti–MoS$_2$ were 0.18 and 0.14 with low fluctuation, the transition occurred at 1100 cycles. Under dry O$_2$, the μ_R and μ_S of Ti–MoS$_2$ were 0.13 and 0.145. The steady-state COF was maintained between 1550 and 2000 cycles. Similar μ_R (0.13) and μ_S (0.12) values were found under dry air. Under the later two conditions, the COF first dropped at around 140 cycles following the running-in then increased to steady-state COF with high fluctuations. Contrary to dry O$_2$, dry air and ambient conditions, a low and more stable COF was observed in a dry N$_2$ atmosphere: The μ_R and μ_S values were 0.12 and 0.074 with lower fluctuations.
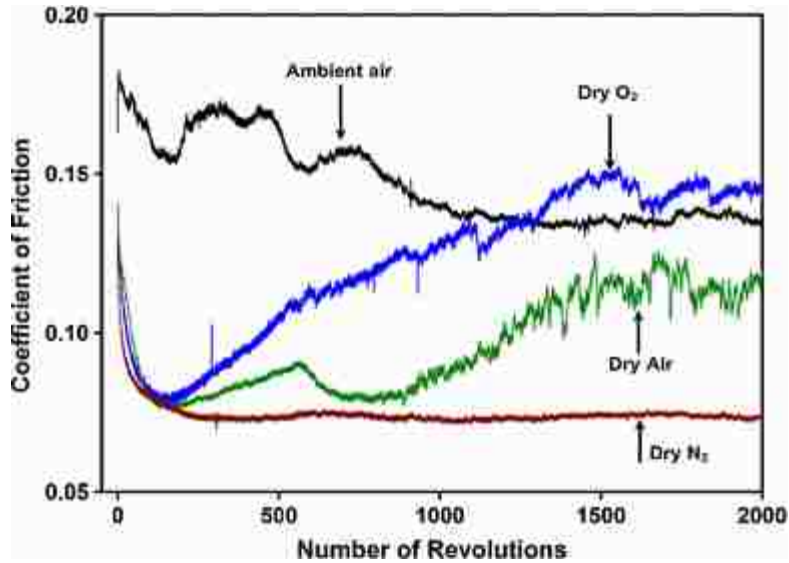
Figure 5.2 Variation of the COF with the number of revolutions when the Ti–MoS2 coating was tested against the 319 Al pin in an ambient air (58% RH), dry O2, dry air and dry N2 atmospheres.

Table 5.1 Summary of running-in (μ_r) and steady state coefficient of friction (μ_s) values of Ti-MoS$_2$ coating tested against 319 Al at ambient, dry O$_2$, dry air and dry N$_2$ atmospheres. The numbers in parenthesis indicate fluctuations in each curve. The standard deviations at the bottom row are the averages of mean values of 3 tests.

Test No.	Ambient		Dry O$_2$	
	μ_r	μ_s	μ_r	μ_s
Test 1	0.18	0.136 ± (0.002)	0.13	0.145 ± (0.003)
Test 2	0.16	0.127 ± (0.001)	0.12	0.130 ± (0.002)
Test 3	0.19	0.145 ± (0.003)	0.14	0.151 ± (0.003)
Average	**0.18 ± 0.02**	**0.136 ± 0.002**	**0.13 ± 0.01**	**0.142 ± 0.003**
Test No.	Dry Air		Dry N$_2$	
	μ_r	μ_s	μ_r	μ_s
Test 1	0.13	0.115 ± (0.003)	0.12	0.074 ± (0.001)
Test 2	0.12	0.125 ± (0.003)	0.11	0.074 ± (0.002)
Test 3	0.14	0.105 ± (0.004)	0.13	0.073 ± (0.001)
Average	**0.13 ± 0.01**	**0.115 ± 0.004**	**0.12 ± 0.01**	**0.074 ± 0.001**

A diagram showing COF values of Ti–MoS$_2$ coatings plotted together with the wear rates obtained in different environments at room temperature is constructed in **Figure 5.3**. The normalized wear rate was 11.69×10^{-5} mm^3/Nm in ambient air, and an increase in wear rate to 16.93×10^{-5} mm^3/Nm was observed in a dry O$_2$ atmosphere. The wear rate decreased to 9.25×10^{-5} mm^3/Nm in a dry air atmosphere. The lowest wear rate of 3.25×10^{-5} mm^3/Nm was observed in dry N$_2$. Optical surface profilometry measurements performed on the Ti–MoS$_2$coatings wear tracks determined a maximum wear depth of 0.79 µm in an ambient air, 0.95 µm in dry O$_2$, 0.90 µm in dry air and 0.74 µm in dry N$_2$ confirming that the coatings (with an initial thickness of 1.20 µm) were still intact. The Wyko profilometer images are inserted in **Figure 5.3**, and it could be easily seen that dry N$_2$ the coating had the lowest wear damage, whereas in dry O$_2$the coating damage was the highest.
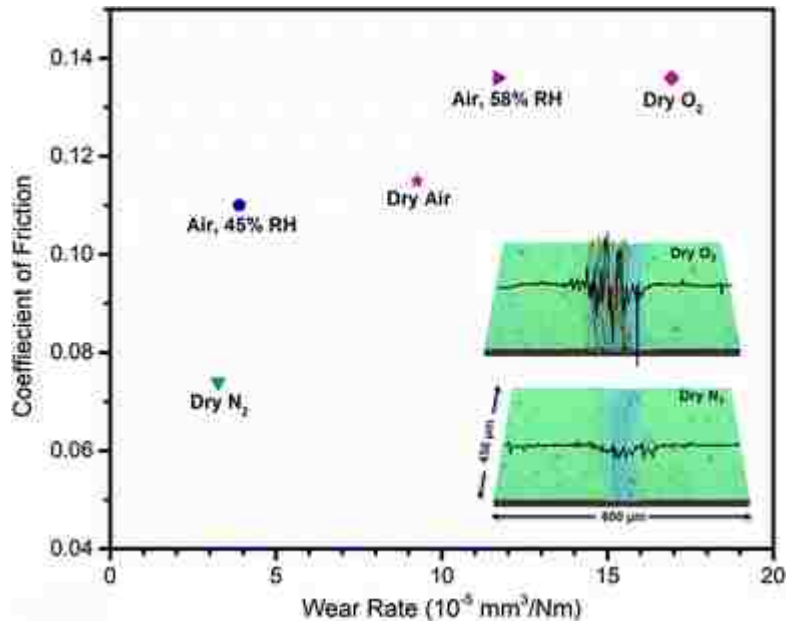
Figure 5.3 Wear rate and COF for Ti–MoS$_2$ coatings tested under different environments at room temperature and 3D optical surface profile wear track images in O$_2$ and N$_2$environments. Each data point corresponds to an average value determined from three friction and wear tests performed on Ti–MoS$_2$ coatings at a given atmosphere.

5.3.2 Transfer Layer Formation on 319 Al Counterfaces under Different Atmospheric Conditions

The 319 Al pin contact surfaces were examined by SEM after wear tests to reveal the morphological features of the worn area, and the elemental composition of this area was determined by EDS. During tests conducted in a dry O_2 atmosphere transfer layers were formed on the contact surface of the 319 Al pin (**Figure 5.4**a). EDS maps of the relevant elements Al, O, Mo and S are shown in **Figure 5.4**b–e. The 319 Al contact surfaces were subjected to wear and had Mo and S incorporated in the transfer layer compositions (**Figure 5.4**a, d). The O content of the transfer layer (**Figure 5.4**c) was high; the entire contact surface was oxidized during sliding in a dry O_2 atmosphere. The formation of oxygen rich transfer layer was also observed on the top surface of pin during the tests conducted in ambient air and dry air. The oxidation of Ti–$MoS_2$was the responsible for the increase in the COF values in ambient air, dry air and dry O_2conditions compared to the COF in dry N_2.
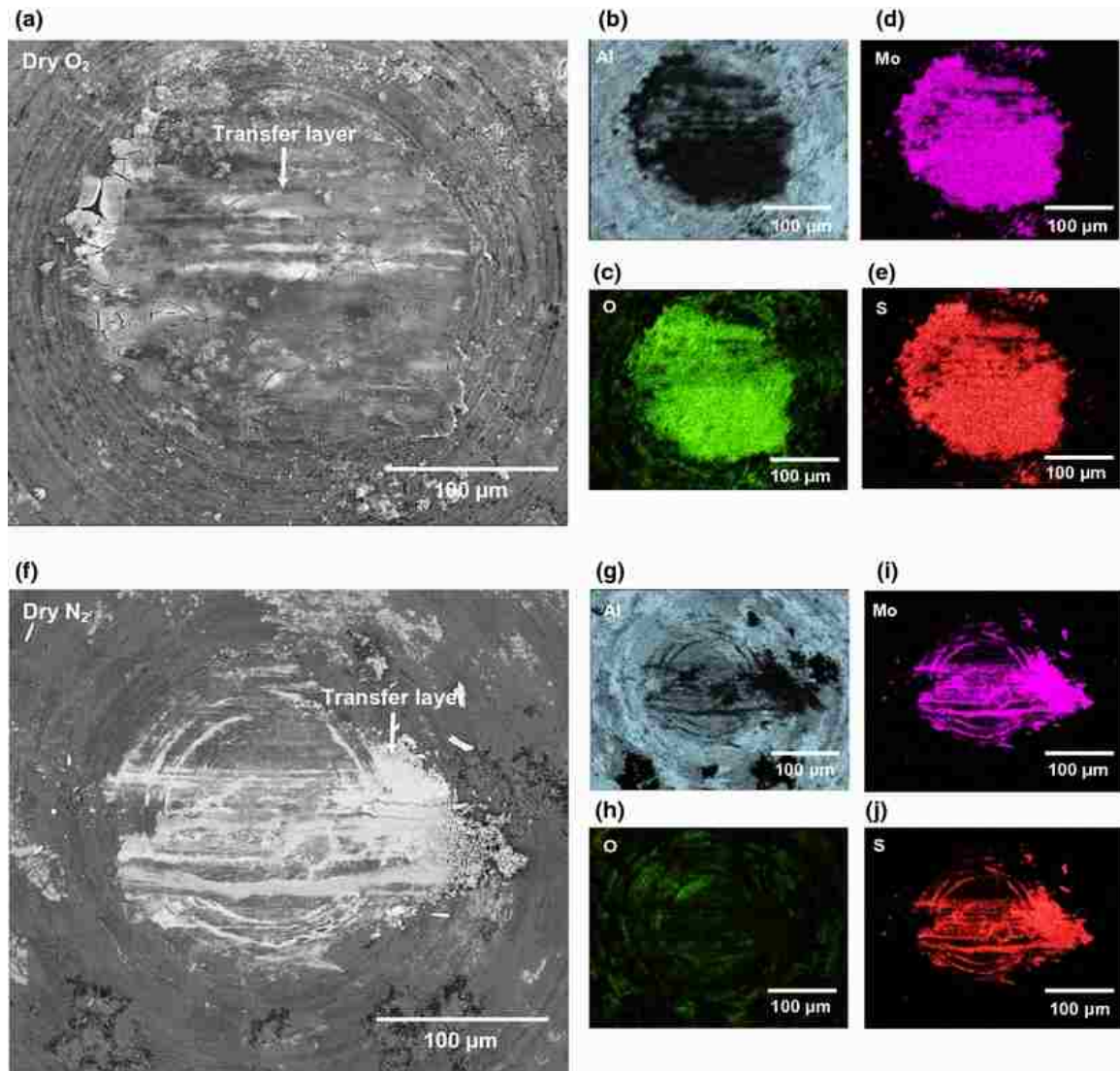
Figure 5.4 a Secondary electron image of the 319 Al pin surface taken after sliding against Ti–MoS$_2$coating in a dry O$_2$ atmosphere. The elemental EDS maps taken from the area shown in (**a**) are for **b** Al, **c** O, **d** Mo and **e** S. **f** Secondary electron image of 319 Al pin surface after the sliding against Ti–MoS$_2$ coating in dry N$_2$ atmosphere. The elemental EDS maps taken from the area shown in (**f**) are for **g** Al, **h** O, **i** Mo and **j** S.

During tests conducted in a dry N$_2$ atmosphere, the contact surfaces of the 319 Al pin were covered with patches of materials transferred from the Ti–MoS$_2$. An example is given in **Figure 5.4**f that shows the contact surface of the 319 Al pin after the test conducted in dry N$_2$ and reveals that the tip was covered by a different type of transfer layer, which could be responsible for the low steady-state COF (**Figure 5.2**). The corresponding EDS elemental maps (**Figure 5.4**g–j) show

165

the distributions of the elements that belong to the 319 Al namely Al (**Figure 5.4**g) as well as Mo (**Figure 5.4**i) and S (**Figure 5.4**j) transferred from the coating. It can be seen that the contact area was devoid of Al but a Mo- and S-rich transfer layer was formed. It should be noted that the concentration of oxygen in the transfer layer was negligible compared to the layer formed under the dry O_2 atmosphere. The prevention of Ti–MoS_2 oxidation of the transfer layers on 319 Al pin correlated well with the fact that steady-state COF occurred at dry N_2 atmosphere (**Figure 5.2**). The wear track on the coating surface was also smooth which indicated that the Ti–MoS_2 remained intact with only slight wear.

The wear tracks formed on the Ti–MoS_2 surfaces were examined using SEM, and the representative secondary electron images (SEIs) are shown in **Figure 5.5**. No significant transfer of material from 319 Al to the Ti–MoS_2 could be detected for the tests performed under an ambient air atmosphere (**Figure 5.5**a). On the other hand, a considerable amount of Al transfer occurred to the Ti–MoS_2 surface in dry O_2 (**Figure 5.5**b). Similar to the ambient air condition, there was no transferred Al that could be observed in the wear track for the tests conducted in dry air condition (**Figure 5.5**c). Traces of titanium could be found occasionally along the wear tracks as marked on these images obtained after tests in a dry N_2 atmosphere. As previously described, the wear track was examined by dissolving the transferred material which revealed that the coating was still intact on the steel substrate.
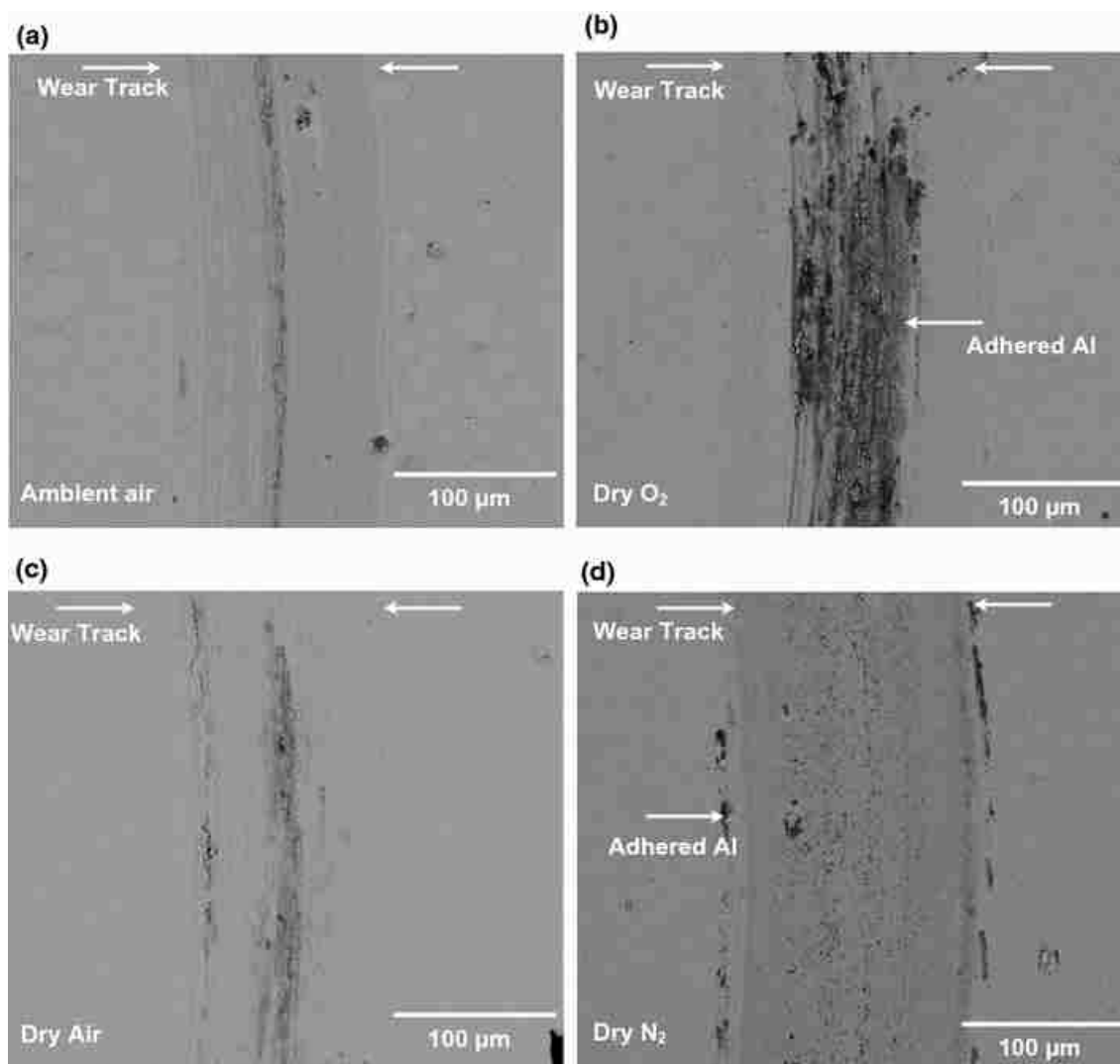
Figure 5.5 Typical secondary electron images of wear tracks formed on the Ti–MoS$_2$ surface when tested against 319 Al in **a** ambient air, **b** dry O$_2$, **c** dry air and **d** dry N$_2$.

The results show that the prevention of oxygen by dry N$_2$ resulted in low COF value and wear rate, therefore, the elevated temperatures tests were conducted in dry N$_2$ in order to understand the friction and wear behavior of Ti–MoS$_2$ coating in high temperature oxygen-free environments.

5.3.3 Change in Tribological Behavior of Ti-MoS$_2$ with Test Temperature in Dry N$_2$

The COF values of the Ti–MoS$_2$ coating plotted as a function of the number of revolutions at different testing temperatures between 25 and 400 °C in dry N$_2$ are presented in **Figure 5.6**a.

The μ_R and μ_S values obtained at constant temperature tests are listed in **Table 5.2**. The COF was initially 0.12 and then decreased to a low μ_s value of 0.07 at 25 °C. Both the μ_R and μ_s decreased with the increase in temperature. The μ_R was 0.08 at 100 °C, 0.09 at 200 °C, 0.10 at 300 °C and 0.06 at 400 °C. The μ_s values remained almost constant for all the tests conducted between 25 and 400 °C. The μ_s was 0.07 at 100 °C, 0.07 at 200 °C, 0.06 at 300 °C and 0.06 at 400 °C.

The average COF values of Ti–MoS$_2$ are presented as a function of testing temperature in **Figure 5.6**b. In ambient air condition, the COF's decreased from 25 to 200 °C but a slightly increase in COF values was observed at 225 °C and remained stable in the temperature range of 225–350 °C. An increase in the average COF values was observed when the temperatures were higher than 350 °C. However, in dry N$_2$ tests, the low steady-state COF values were maintained at all temperatures in the temperature range 25 and 400 °C.
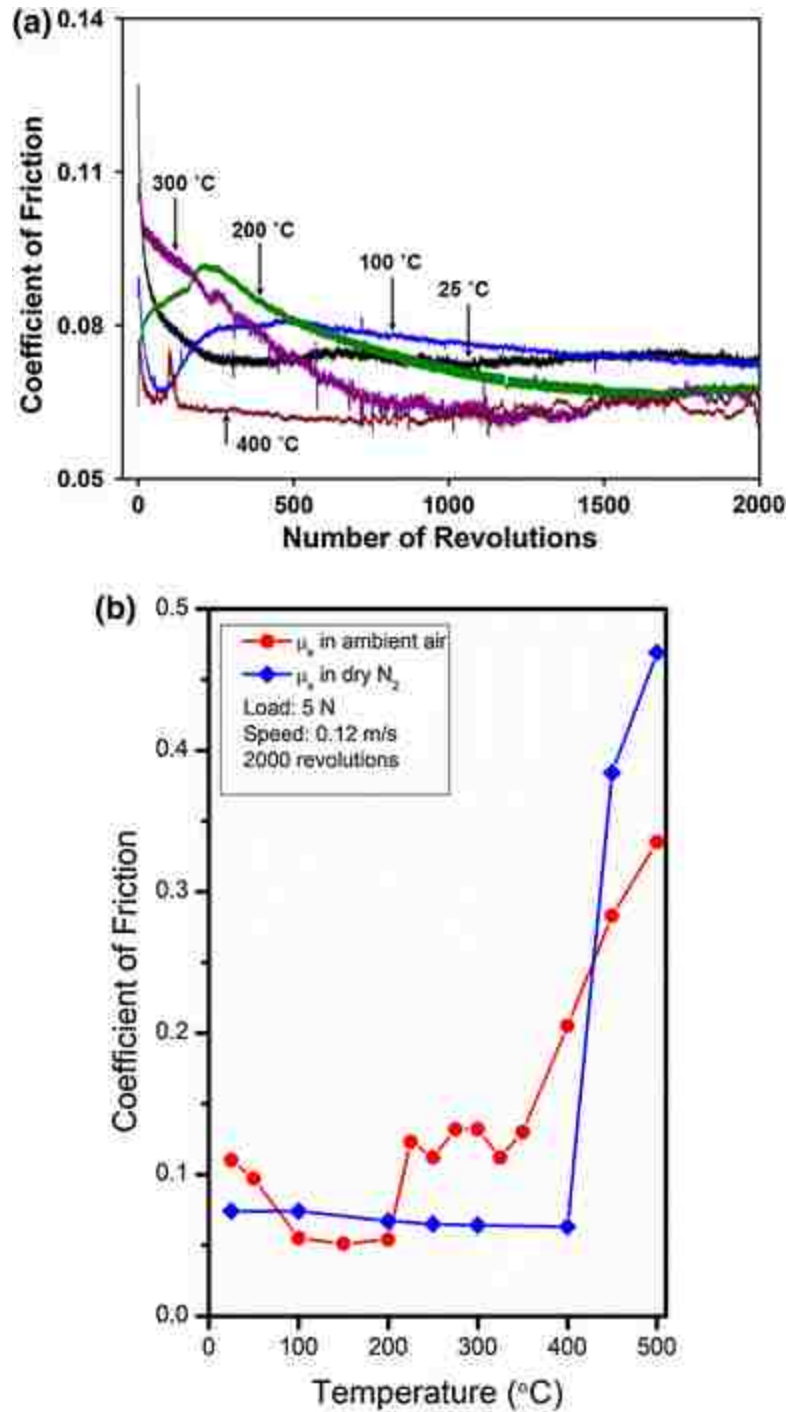
Figure 5.6 a Variation of the COF with the number of revolutions when the Ti–MoS$_2$ coating was tested in a dry N$_2$ against the 319 Al pin at 25, 100, 200, 300 and 400 °C. **b** Variations of the average COF of Ti–MoS$_2$ coating at different testing temperatures in ambient air and dry N$_2$. Each data point corresponds to an average value determined from friction results of three tests performed on Ti–MoS$_2$ coating at a given temperature. The COF data for ambient air conditions are re-produced from [22].

Table 5.2 Summary of running-in (μ_r) and steady-state coefficient of friction (μ_s) values of Ti–MoS$_2$ coating tested against 319 Al in dry N$_2$ atmospheres at 100, 200, 250, 300, 350, 400, 450 and 500 °C.

Test No.	100 ˚C		200 ˚C		250 ˚C	
	μ_r	μ_s	μ_r	μ_s	μ_r	μ_s
Test 1	0.06	0.074 ± (0.001)	0.08	0.067 ± (0.001)	0.08	0.066 ± (0.001)
Test 2	0.08	0.074 ± (0.002)	0.10	0.068 ± (0.001)	0.09	0.064 ± (0.001)
Test 3	0.10	0.073 ± (0.001)	0.09	0.067 ± (0.002)	0.07	0.065 ± (0.002)
Average	**0.08 ± 0.02**	**0.074 ± 0.001**	**0.09 ± 0.01**	**0.067 ± 0.001**	**0.08±0.01**	**0.065 ± 0.001**
Test No.	**350 ˚C**		**350 ˚C**		**400 ˚C**	
	μ_r	μ_s	μ_r	μ_s	μ_r	μ_s
Test 1	0.10	0.064 ± (0.004)	0.08	0.062 ± (0.002)	0.07	0.062 ± (0.002)
Test 2	0.11	0.066 ± (0.001)	0.07	0.063 ± (0.001)	0.09	0.063 ± (0.001)
Test 3	0.09	0.063 ± (0.001)	0.07	0.061 ± (0.001)	0.06	0.064 ± (0.001)
Average	**0.10 ± 0.01**	**0.064 ± 0.001**	**0.08 ± 0.01**	**0.062 ±0.001**	**0.07±0.02**	**0.063 ± 0.001**
Test No.	**450 ˚C**		**500 ˚C**			
	μ_r	μ_s	μ_r	μ_s		
Test 1	0.20	0.386 ± (0.013)	0.35	0.469 ± (0.042)		
Test 2	0.21	0.382 ± (0.015)	0.34	0.462 ± (0.044)		
Test 3	0.19	0.385 ± (0.014)	0.33	0.476 ± (0.040)		
Average	**0.20 ± 0.01**	**0.384 ± 0.014**	**0.34 ± 0.01**	**0.469 ± 0.042**		

The wear rates of Ti–MoS$_2$ coatings at different temperatures are shown in **Figure 5.7**. The normalized wear rate was 3.25×10^{-5} mm^3/Nm at 25 °C, and increased to 4.60×10^{-5} mm^3/Nm at 100 °C and remained at around 5.19×10^{-5} mm^3/Nm at 200 and 300 °C (5.08×10^{-5} mm^3/Nm). A slight increase to 7.08×10^{-5} mm^3/Nm was observed for the test conducted at 400 °C. A rapid increase in wear rates were observed at temperatures above 400 °C. The wear rates were 56.89×10^{-5} and 84.23×10^{-5} mm^3/Nm at 450 and 500 °C. It should be noted that optical surface profilometry measurements performed on the Ti–MoS$_2$wear tracks determined a maximum wear depth of 0.95 μm at 500 °C, confirming that the coatings on the substrate were not entirely worn after sliding tests at 500 °C; however, the COF and wear rate increased due to the adhesion of aluminum to the coatings surface. Contrary to the tests conducted in ambient air, the wear rates were almost constant between 25 and 400 °C when the tests were conducted in dry N$_2$.
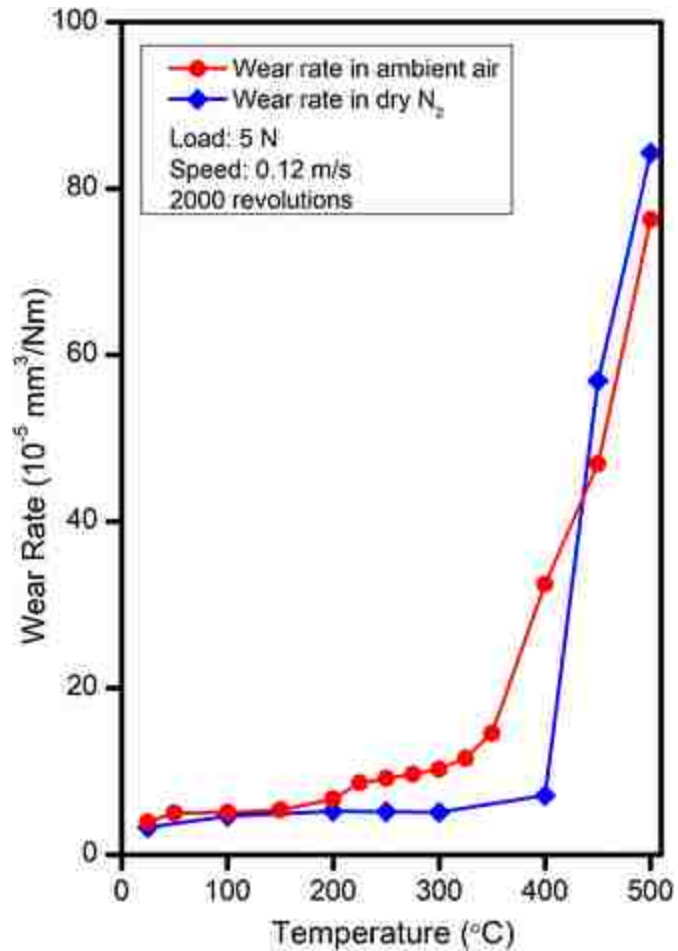
Figure 5.7 Variation of the wear rate of Ti–MoS$_2$ coating with the testing temperature in ambient air and dry N$_2$. The wear rates in ambient air are re-produced from [22].

Both the μ_R and μ_s values increased when the tests were conducted at 450 and 500 °C (in dry N$_2$). Tests conducted at 450 °C showed an unstable COF up to 675 revolutions, and then remained somewhat stable between 675 and 1340 revolutions; however, a high COF value of 0.38 with large fluctuations was recorded. At 500 °C, no steady-state COF could be achieved and high fluctuations were observed during the entire tests (**Figure 5.8**). Ti–MoS$_2$ tested at 450 °C exhibited extensive aluminum transfer to the coating surface (**Figure 5.9**a). The adhesion of aluminum and small amount of oxygen was observed in **Figure 5.9**b, c. Compositional analyses showed that less Mo

and S exsited at the wear track (**Figure 5.9**d, e) compared to the unworn surface. A considerable

amount of Al transfer occurred to the Ti–MoS$_2$ surface at 500 °C, and the wear tracks were entirely

covered by the adhered aluminum layers as reveled by the compositional analyses (**Figure 5.9**f–j).
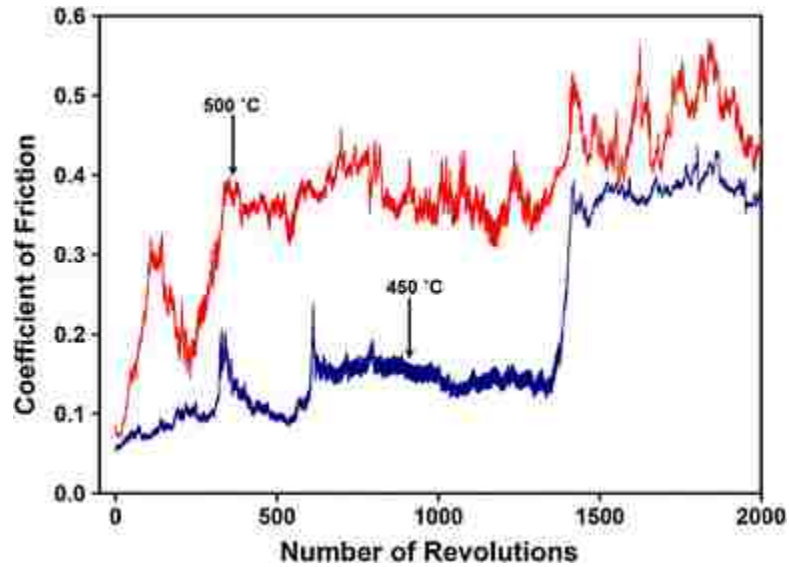
**Figure 5.8** Variation of the COF with the number of revolutions when the Ti–MoS$_2$ coating was tested in dry N$_2$ against the 319 Al pin at 450 and 500 °C.
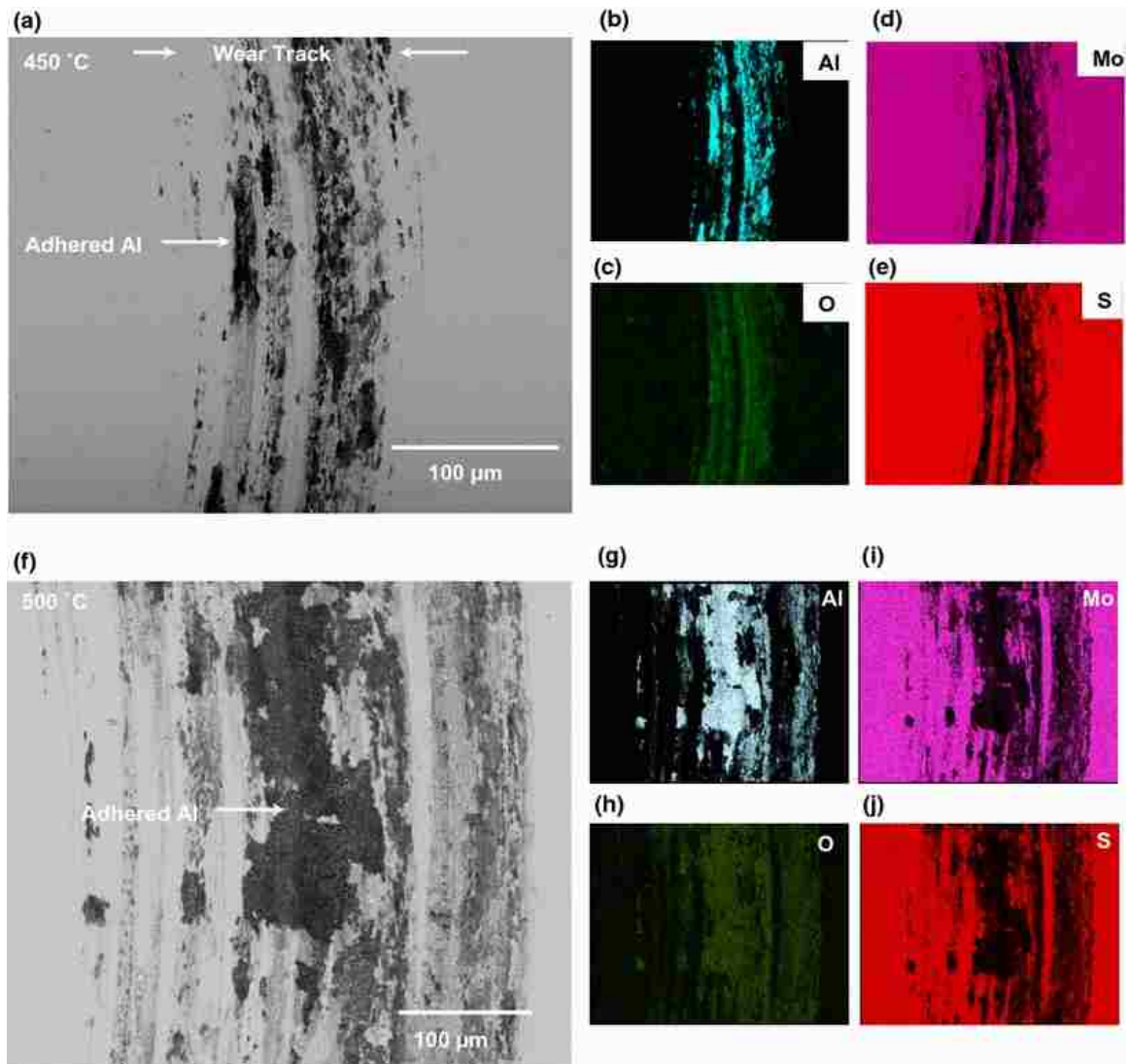
Figure 5.9 a Typical secondary electron images of wear tracks formed on the Ti–MoS$_2$ surface when tested against 319 Al at 450 °C in dry N$_2$. The elemental EDS maps taken from the area shown in (**a**) are for **b** Al, **c** O, **d** Mo and **e** S. **f** Typical secondary electron images of wear tracks formed on the Ti–MoS$_2$ surface when tested against 319 Al at 500 °C. The elemental EDS maps taken from the area shown in (**f**) are for **g** Al, **h** O, **i** Mo and **j** S.

5.3.4 Transfer Layer Formation on 319 Al Contact Surfaces Sliding against Ti-MoS$_2$ in Dry N$_2$

For tests conducted between 25 and 400 °C, the contact surfaces of the 319 Al pins were covered with patches of materials transferred from the Ti–MoS$_2$. Examples are given in **Figure**

174

5.10a–e that shows the contact surface of the 319 Al pin after the test conducted at 400 °C and reveals that the tip was entirely covered by a transfer layer. The corresponding EDS elemental maps show the distributions of the elements that belong to the coatings namely Mo, S and O. The formation of transfer layers on 319 maintained the low COF values recorded during sliding tests (Figure 5.2).
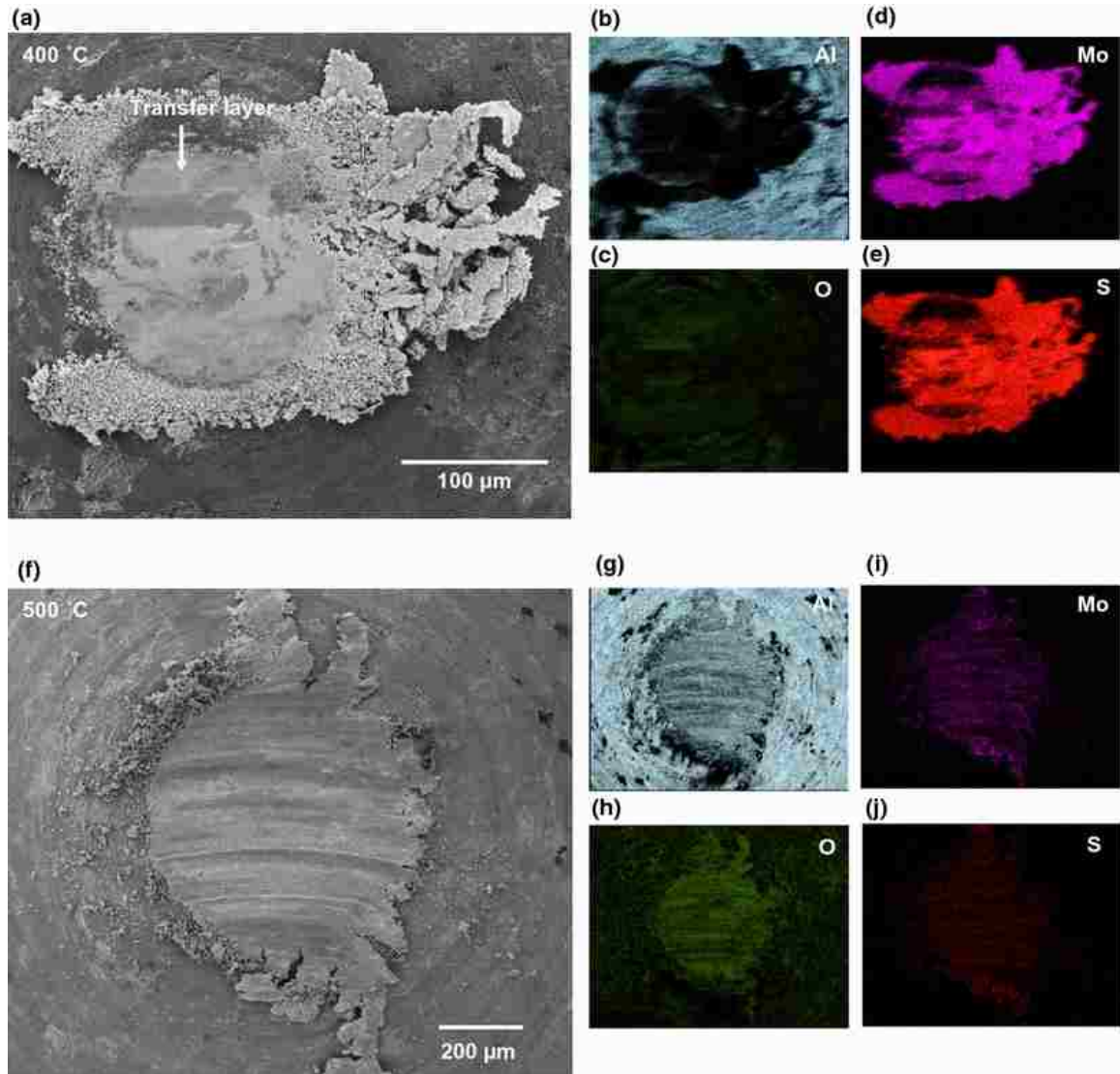
Figure 5.10 **a** Secondary electron image of the 319 Al pin surface taken after sliding against Ti–MoS$_2$coating in dry N$_2$ atmosphere at 400 °C. The elemental EDS maps taken from the area shown in (**a**) are for **b** Al, **c** O, **d** Mo and **e** S. **f** Secondary electron image of 319 Al pin surface after the sliding against Ti–MoS$_2$ coating in dry N$_2$ atmosphere at 500 °C. The elemental EDS maps taken from the area shown in (**f**) are for **g** Al, **h** O, **i** Mo and **j** S.

For tests conducted at 500 °C, no transfer layer was formed on the contact surface of the 319 Al pin. The secondary electron image of the tip of the 319 Al pin tested at 500 °C and the corresponding EDS maps of the relevant elements, Al, O, Mo and S, are shown in **Figure 5.10**f–j. The presence of Mo and S can be seen in the contact surface, but their concentrations appear to be low.

5.3.5   Characterization of Transfer Layers Formed Under Different Atmospheres and Different Temperatures (in Dry N$_2$)

Micro-Raman spectra obtained from the transfer layer on the counter face and that of the Ti–MoS$_2$ are shown in **Figure 5.11**a. The Raman spectrum of the as-deposited Ti–MoS$_2$ coating showed typical peaks at 375 and 410 cm^{-1}, which were interpreted as the E$_{2g}$ and A$_{1g}$ bands arising from the vibrational modes within the S–Mo–S layer [34, 35]. The Raman spectrum acquired from the transfer layer generated in dry O$_2$ showed a different set of peaks appearing at 115 (B$_{1g}$), 815 (A$_g$, B$_{1g}$) and 990 cm^{-1} (A$_g$, B$_{1g}$), which suggested the formation of MoO$_3$ [35] via oxidation of MoS$_2$. Formation of MoO$_3$ was prevented during the experiments conducted in a dry N$_2$atmosphere. The transfer layer formed on the 319 Al pin tested in a dry N$_2$ had similar composition to the as-deposited coating.
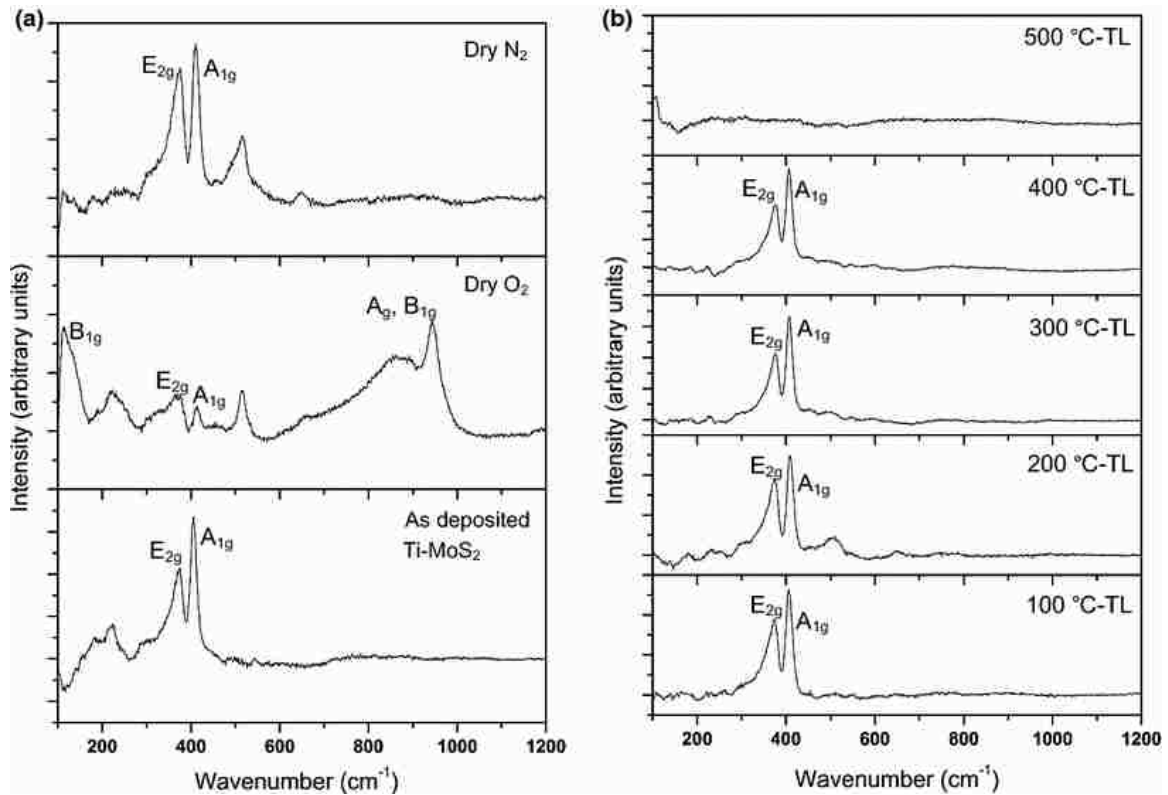
Figure 5.11 a Raman spectra of transfer layer (TL) formed on 319 Al surface tested against Ti–MoS$_2$ in dry O$_2$ and dry N$_2$ atmospheres at 25 °C. The Raman spectrum of unworn Ti–MoS$_2$ is given for comparison. **b** Raman spectra of TL formed on 319 Al surface tested against Ti–MoS$_2$ in dry N$_2$ atmospheres at 100, 200, 300, 400, 500 °C.

The micro-Raman spectra acquired from the transfer layer formed at different test temperatures are shown in **Figure 5.11**b. The Raman spectra did not change with the increase in temperature when the tests conducted in a dry N$_2$ atmosphere. No peaks corresponding to MoO$_3$ were detected in the transfer layers formed on the 319 Al surface in the temperature range of 25–400 °C implying that the Ti–MoS$_2$ was stable throughout this temperature range when tested in dry N$_2$. There was no Raman peaks found in the spectra obtained from the counter faces when the tests were conducted at 500 °C as there was no transfer layer formed on the top of 319 Al surface.

The micromechanisms controlling the tribological behavior of the Ti–MoS$_2$ coatings under different environments and at elevated temperatures can be discussed by referring to a COF versus

wear rate wear map. **Figure 5.12** shows the tribo-chemical mechanisms operating at different temperatures and environments using axes of COF and wear rate. The lowest COF and wear rates were found when the Ti-MoS$_2$ were tested in oxygen-free environments under 400 °C. According to **Figure 5.12**, three types of tribolayer formation occur and lead to three wear regimes with different COF and wear rate values. These three regimes consist of: (1) oxygen/moisture free range where MoS$_2$ transfer layers formed on the counterface provide low friction; (2) oxidation below 400 °C: in this regime, both MoS$_2$ and MoO$_3$ co-exist on the contact surfaces and control friction and wear; and (3) above 400 °C Al adhesion to the Ti–MoS$_2$ coatings occurs and leads to high COF values and wear rates.
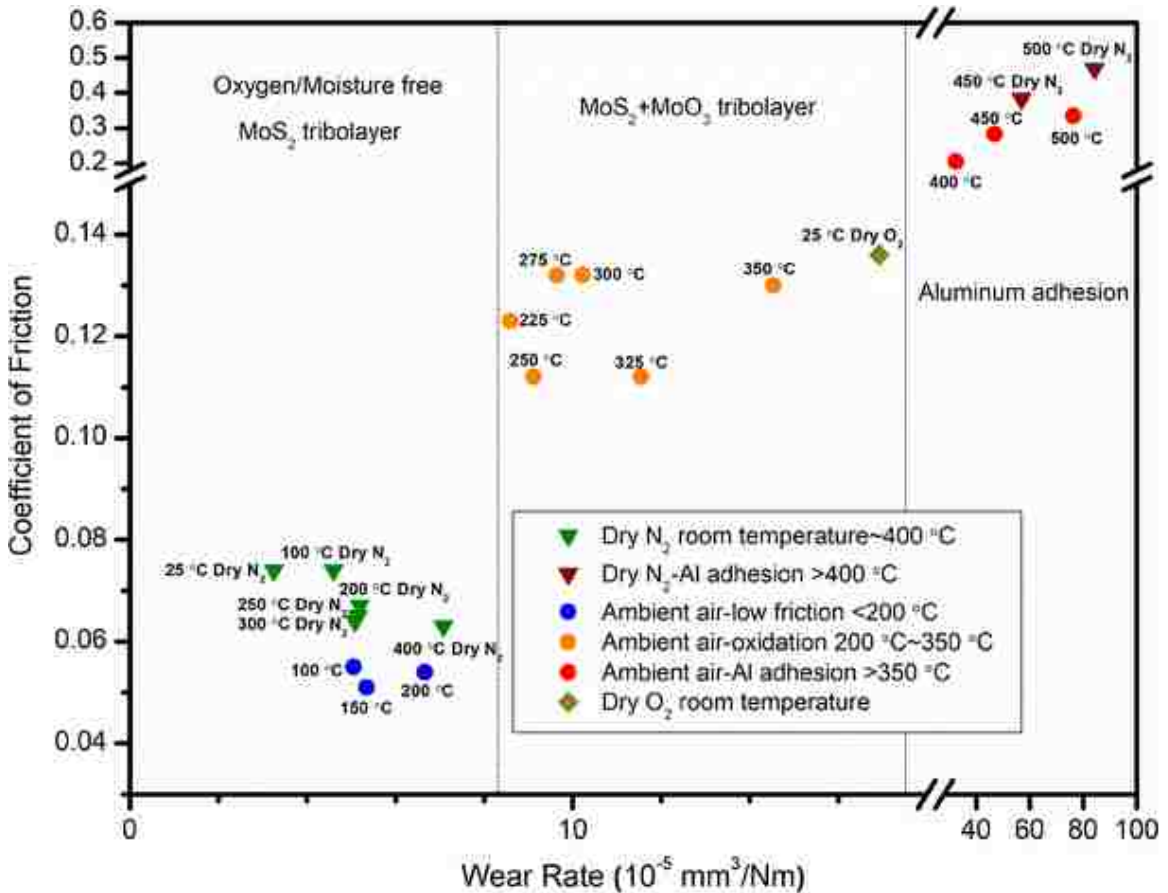
Figure 5.12 COF versus wear rate map for Ti–MoS$_2$ tested against 319 Al at different atmosphere and temperatures. The lowest COF and wear rates were found when tested in oxygen-free environments under 400 °C. The higher COF values in higher temperatures are attributed to the formation of MoO$_3$. At above 400 °C, Al–Si adhesion led to high COF and wear rates.

In summary, the COF vs wear rate map in **Figure 5.12** is a useful way to present the effects of temperature and environment on the tribological behavior of Ti–MoS$_2$ coatings sliding against Al–Si alloys. The map illustrates that under an oxygen-free atmosphere Ti–MoS$_2$ coating could be used in tribological applications up to 400 °C.

5.4   Conclusions

The main conclusions arising from this work can be summarized as follows:

1. Ti–MoS$_2$ tested in a dry N$_2$ showed a COF value of 0.074 against Al–Si (319 Al) which was lower compared to the COF values obtained in tests conducted in ambient air (0.136), dry O$_2$ (0.145) and dry air (0.115). The low COF in N$_2$ was attributed to the MoS$_2$ transfer layer formation on the counterfaces. Higher COF values observed in ambient air, dry O$_2$ and dry air were attributed to the formation of MoO$_3$ on sliding surfaces.

2. Ti–MoS$_2$ showed low wear rate in addition to low COF throughout the temperature range from 25 to 400 °C when tested in a N$_2$ atmosphere. Dry N$_2$ prevented the oxidation of Ti–MoS$_2$ coatings in entire temperature range. Accordingly, Ti–MoS$_2$offers strong prospect for elevated temperatures up to 400 °C for sliding applications that preclude oxidizing atmospheres such as in space tribology.

5.5   Acknowledgements

5.6   Bibliography

[1] T.W. Scharf, S.V. Prasad, Solid lubricants: a Review, J Mater Sci, 48 (2013) 511-531.

[2] S. Prasad, J. Zabinski, Lubricants - Super slippery solids, Nature, 387 (1997) 761-763.

[3] J.M. Martin, C. Donnet, T. Lemogne, T. Epicier, Superlubricity of Molybdenum-Disulfide, Phys Rev B, 48 (1993) 10583-10586.

[4] T. Spalvins, Lubrication with Sputtered Mos2 Films - Principles, Operation, and Limitations, J Mater Eng Perform, 1 (1992) 347-352.

[5] V.R. Johnson, G.W. Vaughn, Investigation of the Mechanism of MoS2 Lubrication in Vacuum, J Appl Phys, 27 (1956) 1173-1179.

[6] H.E. Sliney, Solid Lubricant Materials for High-Temperatures - a Review, Tribology International, 15 (1982) 303-315.

[7] J.K.G. Panitz, L.E. Pope, J.E. Lyons, D.J. Staley, The Tribological Properties of Mos2 Coatings in Vacuum, Low Relative-Humidity, and High Relative-Humidity Environments, Journal of Vacuum Science & Technology a-Vacuum Surfaces and Films, 6 (1988) 1166-1170.

[8] C. Donnet, J.M. Martin, T. LeMogne, M. Belin, Super-low friction of MoS2 coatings in various environments, Tribology International, 29 (1996) 123-128.

[9] J. Skinner, N. Gane, D. Tabor, Micro-Friction of Graphite, Nature-Phys Sci, 232 (1971) 195.

[10] S.V. Prasad, J.S. Zabinski, Tribology of Tungsten Disulfide (Ws2) - Characterization of Wear-Induced Transfer Films, J Mater Sci Lett, 12 (1993) 1413-1415.

[11] C. Donnet, Advanced solid lubricant coatings for high vacuum environments, Surf Coat Tech, 80 (1996) 151-156.

[12] J.F. Yang, B. Parakash, J. Hardell, Q.F. Fang, Tribological properties of transition metal di-chalcogenide based lubricant coatings, Front Mater Sci, 6 (2012) 116-127.

[13] H.S. Khare, D.L. Burris, The Effects of Environmental Water and Oxygen on the Temperature-Dependent Friction of Sputtered Molybdenum Disulfide, Tribol Lett, 52 (2013) 485-493.

[14] R.F. Deacon, J.F. Goodman, Lubrication by Lamellar Solids, Proceedings of the Royal Society of London. Series A, Mathematical and Physical Sciences, 243 (1958) 464-482.

[15] N.M. Renevier, V.C. Fox, D.G. Teer, J. Hampshire, Performance of low friction MoS2/titanium composite coatings used in forming applications, Mater Design, 21 (2000) 337-343.

[16] X.Z. Ding, X.T. Zeng, X.Y. He, Z. Chen, Tribological properties of Cr- and Ti-doped MoS2 composite coatings under different humidity atmosphere, Surf Coat Tech, 205 (2010) 224-231.

[17] X. Wang, Y.M. Xing, S.L. Ma, X.L. Zhang, K.W. Xu, D.G. Teer, Microstructure and mechanical properties of MOS2/titanium composite coatings with different titanium content, Surf Coat Tech, 201 (2007) 5290-5293.

[18] P. Stoyanov, R.R. Chromik, D. Goldbaum, J.R. Lince, X.L. Zhang, Microtribological Performance of Au-MoS2 and Ti-MoS2 Coatings with Varying Contact Pressure, Tribol Lett, 40 (2010) 199-211.

[19] T. Kubart, T. Polcar, L. Kopecky, R. Novak, D. Novakova, Temperature dependence of tribological properties of MoS(2) and MoSe(2) coatings, Surf Coat Tech, 193 (2005) 230-233.

[20] E. Arslan, Y. Totik, O. Bayrak, I. Efeoglu, A. Celik, High temperature friction and wear behavior of MoS(2)/Nb coating in ambient air, J Coat Technol Res, 7 (2010) 131-137.

[21] K.C. Wong, X. Lu, J. Cotter, D.T. Eadie, P.C. Wong, K.A.R. Mitchell, Surface and friction characterization of MoS2 and WS2 third body thin films under simulated wheel/rail rolling-sliding contact, Wear, 264 (2008) 526-534.

[22] A. Banerji, S. Bhowmick, A.T. Alpas, Role of temperature on tribological behaviour of Ti containing MoS2 coating against aluminum alloys, Surf Coat Tech, 314 (2017) 2-12.

[23] S. Bhowmick, A. Banerji, M.Z.U. Khan, M.J. Lukitsch, A.T. Alpas, High temperature tribological behavior of tetrahedral amorphous carbon (ta-C) and fluorinated ta-C coatings against aluminum alloys, Surf Coat Tech, 284 (2015) 14-25.

[24] S. Bhowmick, A. Banerji, M.J. Lukitsch, A.T. Alpas, The high temperature tribological behavior of Si, O containing hydrogenated diamond-like carbon (a-C:H/a-Si:O) coating against an aluminum alloy, Wear, 330 (2015) 261-271.

[25] H. Li, Q. Zhang, C.C.R. Yap, B.K. Tay, T.H.T. Edwin, A. Olivier, D. Baillargeat, From Bulk to Monolayer MoS2: Evolution of Raman Scattering, Adv Funct Mater, 22 (2012) 1385-1390.

[26] B.C. Windom, W.G. Sawyer, D.W. Hahn, A Raman Spectroscopic Study of MoS2 and MoO3: Applications to Tribological Systems, Tribol Lett, 42 (2011) 301-310.

CHAPTER 6

BOUNDARY LUBRICATED SLIDING BEHAVIOUR OF TI CONTAINING MOS₂ COATINGS AGAINST AN ALUMINUM ALLOY

6.1 Introduction

Molybdenum disulphide (MoS_2) has a lamellar-type structure with a layer of Mo atoms being sandwiched between two layers of S atoms connected by covalently bonding in a trigonal prismatic co-ordination, while the layers are held together by weak van der Waals interactions between sulphur atoms [1-5]. Therefore, MoS_2 has been extensively used as a solid lubricant coating in high vacuum systems or space technologies [6, 7]. Meanwhile, transition metal dichalcogenides are also widely used as additives in lubricant for low COF and wear rate [1, 3]. Tribological tests performed on MoS_2 coatings against SAE 52100 grade steel under ultra-high vacuum (5×10^{-8} Pa) resulted in a very low coefficient of friction, COF, of 0.003 [8]. Low COF values ranging between 0.01 and 0.04 were also reported under high vacuum conditions in other studies [9, 10]. Although MoS_2 coatings exhibit low friction and wear in dry atmosphere, their excellent tribological properties are sensitive to moisture. It was found that addition of Ti in MoS_2 (Ti-MoS_2) using magnetron sputtering reduced the sensitivity of the coating to test environment [11]. Ti-MoS_2 when tested against WC-Co counterface at 50% RH maintained a low COF of 0.07. Ding et al. [12] showed that Ti- and Cr-MoS_2 were promising coatings when tested against Al_2O_3 counterfaces under high humidity environments. It was shown that an optimum 9.5 at.% of Ti added to MoS_2 would maintain a low COF of 0.03-0.08 between 25% RH and 75% RH whereas a relatively high COF of 0.07-0.14 was observed for pure MoS_2 coating under the same test conditions. It was suggested that the presence of Ti atoms in MoS_2 coatings could reduce the propensity for water vapour entering interlamellar spaces in order to decrease oxidation rate. Ti also could increase the hardness of the

coatings [11]. Wang et al. [13] found that pure MoS_2 tested against Si_3N_4 counterfaces at room temperature and 38% RH showed a high COF of about 0.82 which was reduced to 0.16 under the same test conditions when 15.3 at.% Ti was added to MoS_2. Mechanical properties were also found to improve upon addition of Ti to the MoS_2 coating [14] — hardness increased from 4.9 GPa for MoS_2 to 8.3 GPa for Ti-MoS_2 with 15.3 at.% Ti and 10.35 GPa for Ti-MoS_2 with 19.5 at.% Ti [13]. The addition of Ti in the MoS_2 coating improved coating adhesion to the substrate — 25%Ti containing MoS_2 coated on Ti-6Al-4V showed lowest mass loss and COF when tested against 52100 steel compared to the uncoated Ti-6Al-4V blocks as well as diamond-like carbon (DLC) coated Ti-6Al-4V blocks under the same conditions [15]. Sun et al. [16] studied the tribological properties of Ti containing MoS_2 coating (Ti–MoS_2) tested against aluminum alloy (Al-6.5% Si) in ambient air (58% relative humidity, RH), dry oxygen, dry air and dry N_2 atmospheres (< 4% RH). The Ti–MoS_2 coating exhibited similar COF values under ambient (0.14), dry oxygen (0.15) and dry air (0.16) atmosphere conditions. It was found that oxidation of MoS_2 to MoO_3 was responsible for high COF under all testing conditions.

When used as additives in lubricant oil, MoS_2 can help form an effective surface-lubricating film under boundary-lubricating conditions. MoS_2 plays an important role in engine lubricants. As a decomposition product of MoDTC [17, 18], MoS_2 could be formed as tribolayers to contact surfaces to maintain low friction and wear [19-22]. MoDTC decomposes to from MoS_2 at 300 °C under thermal conditions only, while under tribological conditions MoS_2 could be formed at 100 °C [23]. The high contact temperature is necessary for the formation of MoS_2. It is also reported that the oxide MoO_3 and residual MoDTC could be detected in the tribofilms [24].

Although either MoS_2 coatings as solid lubrication films or MoDTC additives for engine oil are widely studied, few studies considered Ti-MoS_2 coatings used in MoDTC added lubricated conditions. In this condition, the mechanisms dominate the wear behaviour: MoS_2 transfer, MoDTC decomposition and the oxidation of MoS_2 should be identified. This study performed wear tests of

184

Ti-MoS$_2$ coatings wear against 319 Al pins at room and 100 °C temperatures, for comparison, M2 steel against Al are also conducted at these two temperatures. The COF values of the tests were recorded, and worn surfaces were examined by SEM, EDS mapping and micro-Raman analyses to study the mechanisms of Ti-MoS$_2$ coatings in lubricated wear conditions.

6.2   Experimental Approach

6.2.1   Materials and Coatings

A typical engine block material-319 Al alloy of 15 mm long pins and 4.05 mm in diameter was used for the tribological tests. The chemical compositions of 319 Al had (in wt.%): 5.5–6.5% Si, 3.0–4.0% Cu, 1.0% Fe, 0.10% Mg, 0.5 Mn, 0.35% Ni, 1.0% Zn, 0.25% Ti and the balance Al.

Ti-MoS$_2$ coatings were supplied by Miba Coatings Ltd. (Worcestershire, UK) where they were deposited on polished M2 grade tool steel disks (R_a=11.31±4.50 nm) using an unbalanced magnetron sputtering system equipped with two titanium and two MoS$_2$ targets. A 1.20 μm thick Ti-MoS$_2$ coating was deposited on a Ti interlayer of 40 nm thickness that served to promote adhesion to the steel substrate. The details of coatings deposition technique can be found in [25]. The hardness of the coatings was calculated from the loading–unloading curves obtained by a Berkovich type nano-indenter that penetrated to a maximum depth of 150 nm below the surface. The average hardness of the Ti-MoS$_2$ coatings was 3.51 ± 0.10 GPa, and the surface roughness was measured as 17.5 ± 3.1 nm (R_a) using an optical surface profilometer.

6.2.2   Tribological Tests

Sliding wear tests were conducted using a unidirectional rotating pin-on-disk tribometer (CSM) on Ti-MoS$_2$ coated coupons against 4.01 mm diameter 319 Al pins. Lubricated sliding tests were performed on 319 Al/M2 steel and 319 Al/Ti-MoS$_2$ tribocouples in ambient air with relative

humidity (RH) varying between 51-57%. The lubricant used for lubricated tests was fully synthetic engine oil 5W30. The sliding velocity for the wear tests was 0.05 m/s while the normal load was 5.0 N. The test duration was 5×10^3 sliding cycles. For experiments performed at 100 °C, the samples were heated with the lubricating oil and the tests were started 20 min after the temperature reached the specified temperature. The volumetric wear loss measurements from different regions of the coating wear track was determined using optical profilometry measurements (Wyko NT1100) as described in [24-27]. For each test condition at least three tests were performed and the average friction value has been reported (with corresponding error). The steady state COF (μ_S) was measured after a constant friction stage on a COF vs. sliding distance (number of revolutions) curve was attained, which typically took about 200 revolutions. The maximum COF value during the initial running-in period of a friction curve was reported as μ_R.

The lubrication regime, determined from the ratio (λ) of minimum film thickness (h_{min}) to the r.m.s roughness (r^*) of the contacting surfaces. The minimum lubrication thickness h_{min} and the r.m.s surface roughness (r^*) of the contacting bodies were calculated using equations 1 and 2, respectively [28]:

$$h_{min} = 1.79 R^{0.47} \alpha^{0.49} {\eta_o}^{0.68} U^{0.68} (E*)^{-0.12} W^{-0.07} \tag{1}$$

$$\mathrm{r}^* = \sqrt{\left(r_{Ti-MoS_2}\right)^2 + (r_{319Al})^2} \tag{2}$$

where R is the radius of the counterface pin, U is the sliding speed, W is the applied normal load applied and α and η_o represent viscosity properties of the lubricating fluid. The $\lambda < 1$ (0.006 in case of tests in engine oil 5W30) at the beginning of the wear tests indicated boundary lubrication [28, 29].

6.2.3 Examination of worn surface

The details of surface damage on wear tracks and counterfaces were studied using FEI Quanta 200 FEG scanning electron microscopes (SEM) equipped with an energy-dispersive X-ray EDAX (SiLi Detector) spectrometer. The micro-Raman studies of the unworn coating and transfer layer formed on the top of 319 Al pin were carried out using a 50 mW Nd-YAG solid state laser (532.0 nm excitation line) through the 50× objective lens of a Horiba Raman spectrometer.

6.3 Results and Discussion

6.3.1 Changes in friction behaviour of M2 steel and Ti-MoS$_2$ with temperature

Figure 6.1 shows friction curves of 319 Al tested against the Ti-MoS$_2$ coatings and uncoated M2 steel under boundary lubricated sliding conditions both at 25 and 100 °C. As **Figure 6.1** indicates, an initial μ_R of 0.14 was obtained and the COF immediately decreased to a low μ_S value of 0.13 which was maintained for the rest of the test when the 319 Al was tested against uncoated M2 steel at 25 °C. Both μ_R and μ_s were decreased to 0.12 and 0.10 respectively when the temperature was increased to 100 ˚C.
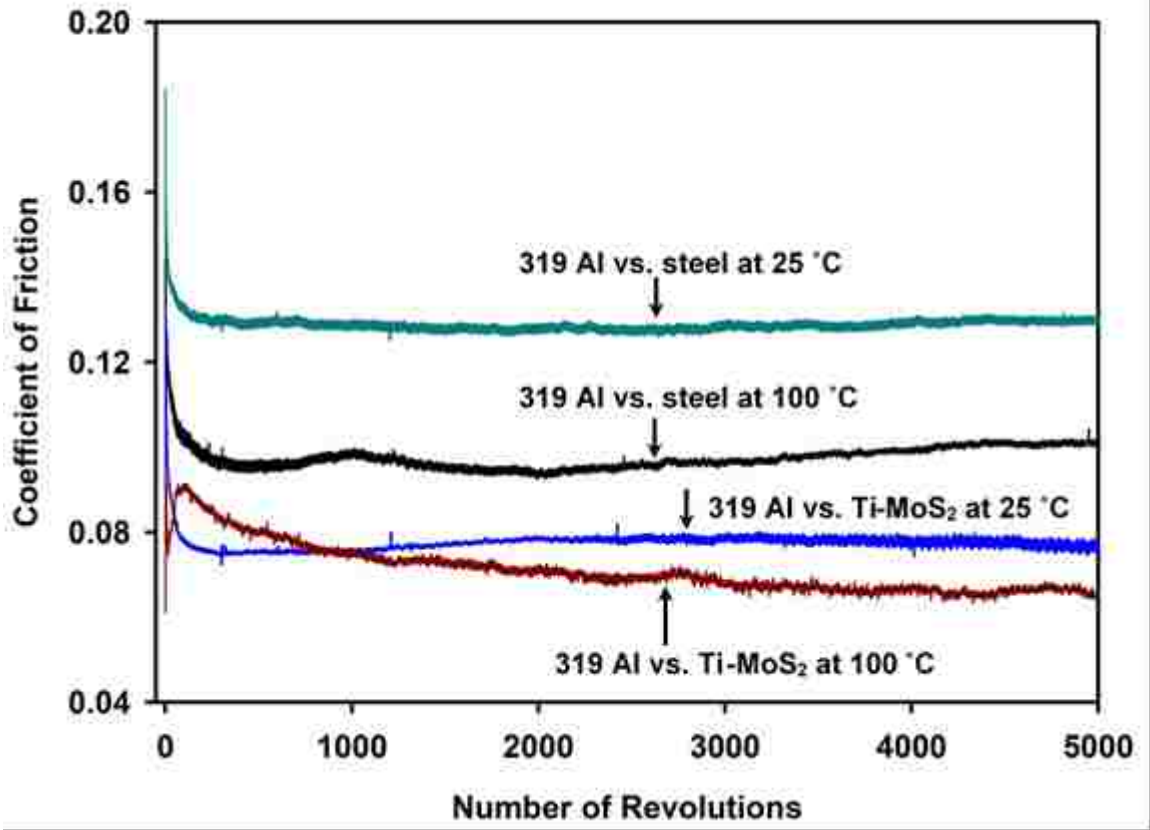
Figure 6.1 Variations of COF values with the number of revolutions for lubricated sliding tests performed on 319 Al against uncoated M2 and Ti-MoS$_2$ coated M2 steel at 25 ˚C and 100 ˚C. Load=5.0 N and sliding velocity=0.05 m/s were used for all tests

The use of Ti-MoS$_2$ coatings further reduced μ_R and μ_s at each test. The typical friction curve of the Ti-MoS$_2$ coating was characterized by a running in period (with μ_R of 0.11) followed by lower plateau (with μ_S of 0.08 for the tests shown in **Figure 6.1**) when the test was conducted at room temperature. The lowest μ_R (0.09) and μ_s (0.06) were recorded while the tests were conducted at 100 ˚C.

Three tests were conducted for each condition. The average values of μ_R and μ_S obtained are shown in **Figure 6.2**. The elevated temperatures reduced the COF values for both M2 steel and Ti-

MoS$_2$ coating. The underlying mechanisms for reduction of COF for both uncoated and Ti-MoS$_2$

coatings at 100 ˚C will be discussed in detail in the following sections.
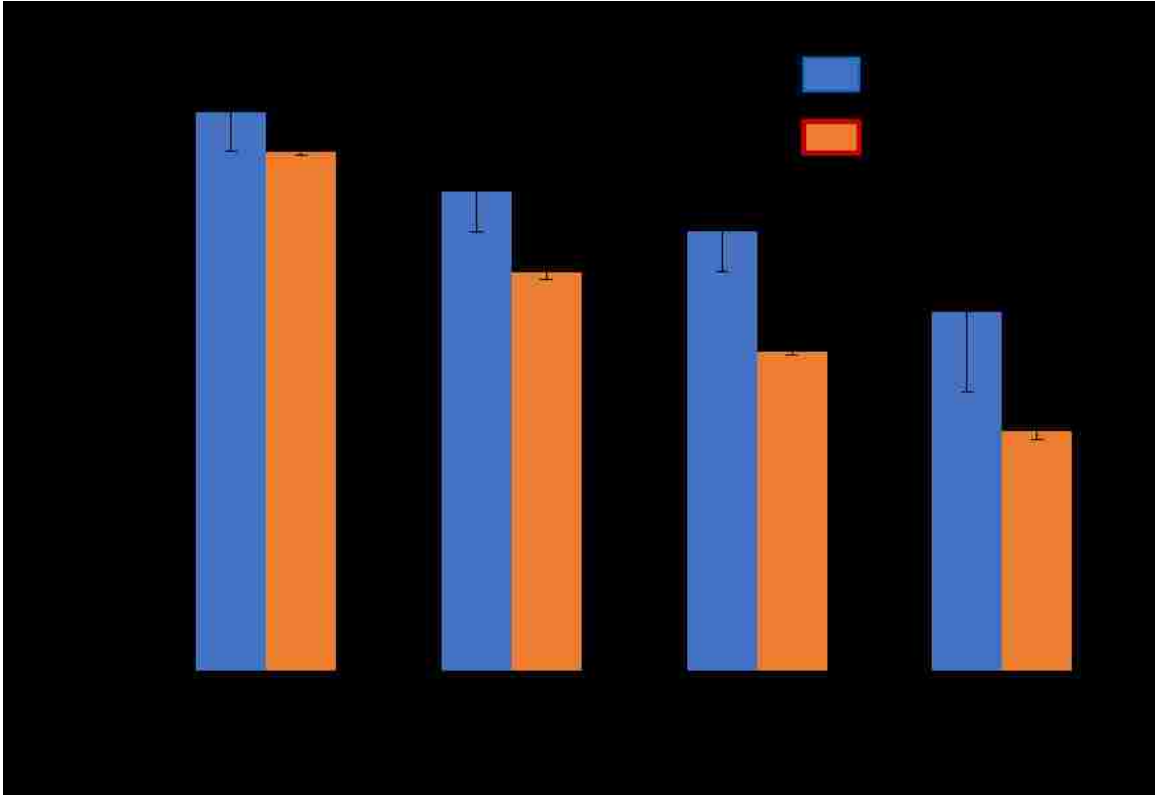
Figure 6.2 Comparisons of average running-in and steady state coefficient of friction (COF) for 319 Al vs. uncoated M2 steel and 319 Al vs. Ti-MoS$_2$ coated M2 steel while the lubricated tests were conducted at 25 ˚C and 100 ˚C. Each bar on this plot represents average COF value obtained from 3 tests performed on fresh samples.

The wear rate values are shown in **Figure 6.3**. The wear rate values at 100 °C are higher than

room temperature. However, all wear rate values are lower than 2.5×10^{-5} mm^3/Nm, which is lower

than the lowest wear rate value of Ti-MoS$_2$ wear against Al in dry N$_2$ environment. The higher wear

rate at 100 °C is caused by the deceased viscosity of the engine oil 5W30, which lead to more wear

contact between two wear surfaces.
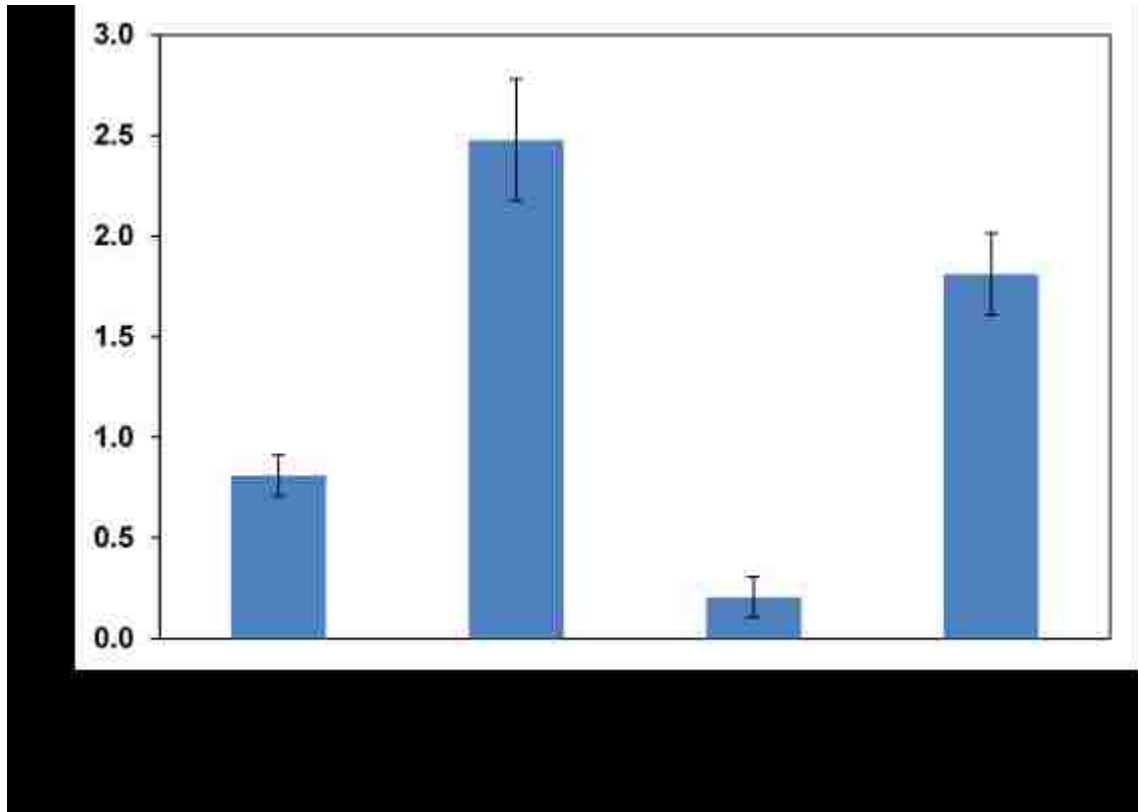
Figure 6.3 Wear rate of Ti-MoS$_2$ coatings and M2 steel tested at room temperature and 100 °C.

6.3.2 Tribolayers formation on Al counterfaces and wear tracks

Figure 6.4(a) shows backscattered SEM image of 319 Al worn surface after sliding against steel in oil at 100 °C. The dark regions around the worn surface are considered to be oil residue layers (ORL) formed during sliding, because the EDS map of C shown in **Figure 6.4(b)** indicates these regions are rich in C. Besides C, elements maps of O, Zn, S and P are shown in **Figure 6.4(c-f)**. The zinc dialkyldithio phosphate (ZDDP) tribolayer formation is confirmed by the presence of Zn, O, S and P on worn surface shown in the figure [1-3]. The ZDDP tribolayer helps reduce friction and protect the Al pin from wear loss. These ZDDP tribolayers were chemically composed of zinc phosphates, zinc sulphides and sulphates [30-32].
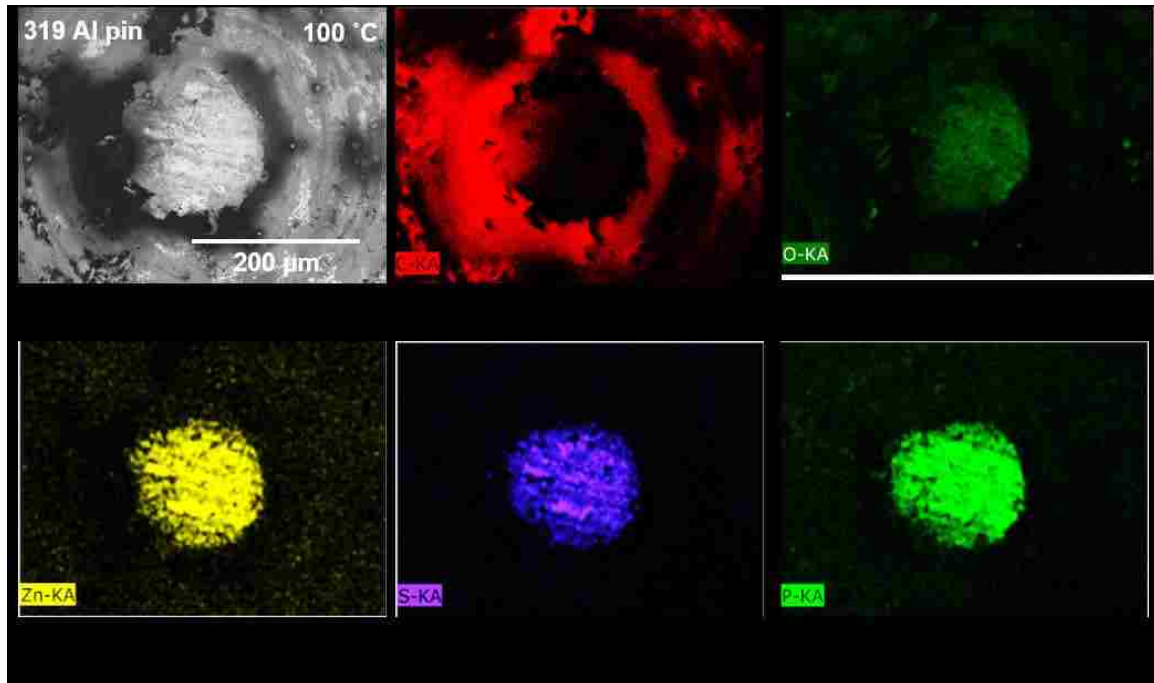
Figure 6.4 (a) Backscattered SEM image of 319 Al worn surface after sliding against uncoated steel in oil for 5 × 103 revolutions at 100 ˚C; (b) Elemental EDS maps taken from (a) showing the distributions of (b) C, (c) O, (d) Zn, (e) S and (f) P.

Figure 6.5 shows the SEM images and EDS maps of the wear track of the M2 steel after the wear test conducted at 100 °C in oil. **Figure 6.4(a)** shows the ORL formed on the wear track, which are confirmed by the EDS C map shown in **Figure 6.5(c)** results. Similar to the EDS results of the Al pin, the wear track is rich in O, Zn and P, which means ZDDP tribolayer is also formed on the wear track. For formation ORL on two contact surfaces are account for the low frication and wear rate.
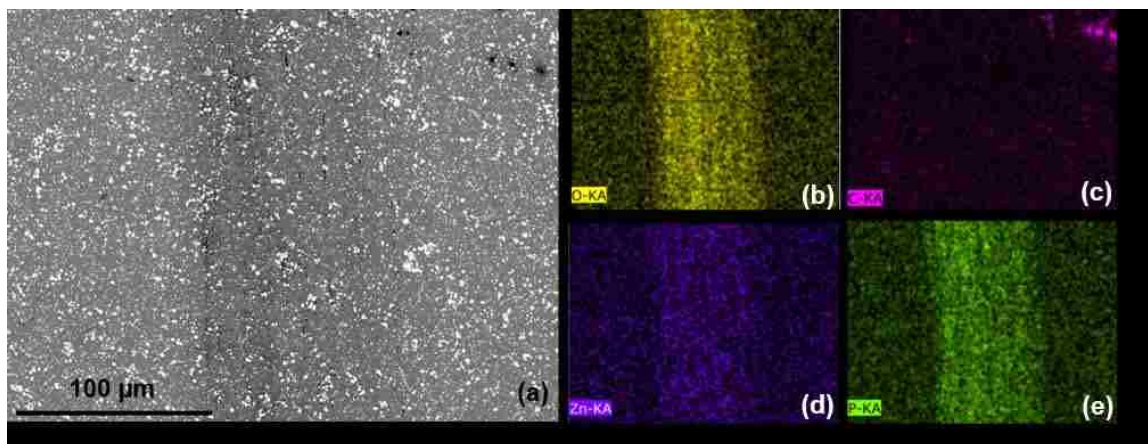
Figure 6.5 (a) Backscattered SEM image of uncoated M2 steel worn surface after sliding against 319 Al in oil for 5×10^3 revolutions at 100 ˚C; (b) Elemental EDS maps taken from (a) showing the distributions of (b) O, (c) C, (d) Zn and (e) P. Arrows in figure (a) show the oil residue layer (ORL).

The lower COF at 100 °C for steel vs Al is because of the formation of MoS_2 tribolayer at higher temperature [21, 33]. It was reported that the MoDTC could only be decomposed at elevated temperature (>room temperature) to form MoS_2 protective and wear reduction layers [34, 35]. **Figure 6.6** shows the EDS maps of Mo and S, the MoS_2 layer is mainly formed on the carbide phase of the steel. Neither Mo nor S was found on the wear track of the steel after room temperature wear test. The MoS_2 layers formed at 100 °C helped to decrease the COF during wear test.

At both room temperature and 100 °C Ti-MoS_2 coatings have lower COF than steel. It was reported that Ti-MoS_2 coatings have good wear performance in dry sliding conditions against Al up to 350 °C [25] in ambient air. The low COF is attributed to the easy-shear structure of MoS_2 coatings [4, 8, 36]. In dry wear condition, the MoS_2 coatings will transfer to the counter surface resulting in MoS_2-MoS_2 wear contact, which leads to low COF.
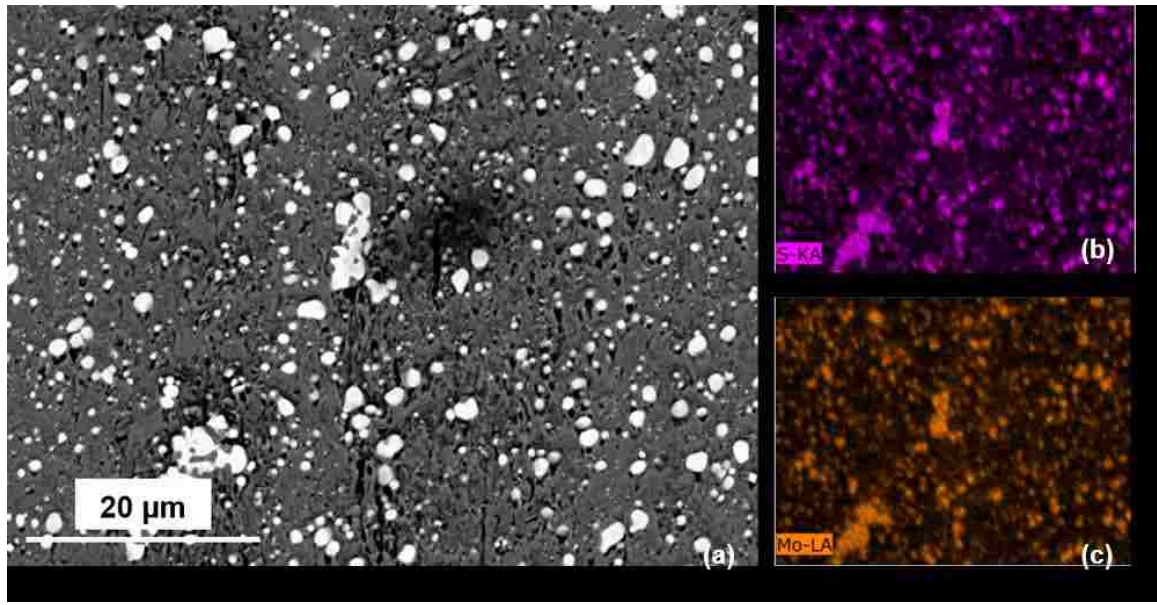
Figure 6.6 (a) Backscattered SEM image of M2 steel worn surface after sliding against 319 Al in oil for 5×103 revolutions at 100 ˚C at higher magnification; Elemental EDS maps taken from (a) showing the distributions of (b) S and (c) Mo.

Though the MoDTC in 5W30 grade engine lubricate oil can only be decomposed at elevated temperature, the Ti-MoS$_2$ coatings can form a transfer layer on the counter surface when the tests are conducted at room temperature. **Figure 6.7** shows SEM image of Al pin after wear against Ti-MoS$_2$ coating in oil at room temperature. The transferred Ti-MoS$_2$ layer could be found at the top parts of the Al pin, which is confirmed by the EDS maps in **Figure 6.7(c), (d) and (e)**. The MoS$_2$ layers formed from the decomposition of 5W30 lowered the COF at 100 °C for steel wear against Al. In the cases for Ti-MoS$_2$ against Al, more MoS$_2$ layers were formed, therefore, lower COF values were achived by Ti-MoS$_2$ coatings.
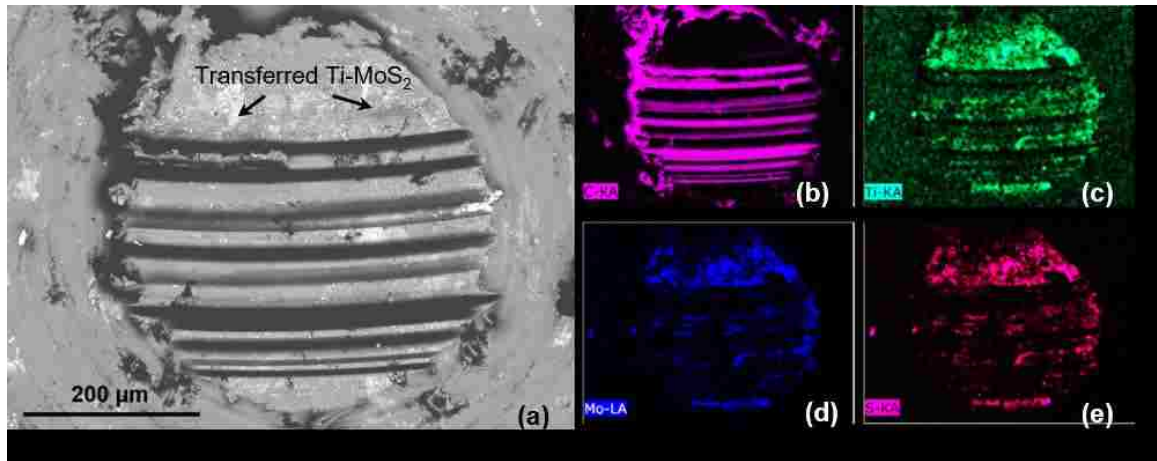
Figure 6.7 (a) Backscattered SEM image of 319 Al worn surface after sliding against Ti-MoS2 coating in oil for 5×103 revolutions at room temperature; (b) Elemental EDS maps taken from (a) showing the distributions of (b) C, (c) Ti, (d) Mo and (e) S.

SEM images and EDS maps of wear tracks of Ti-MoS$_2$ coatings tested at room temperature and 100 °C are shown in **Figure 6.8**. As shown in **Figure 6.3**, the wear rate tested at room temperature is lower. Though the wear track of room temperature is wider than the are conducted at 100 °C. The higher wear rate values of the tests performed at 100 °C are due to the more contact between the wear surfaces.
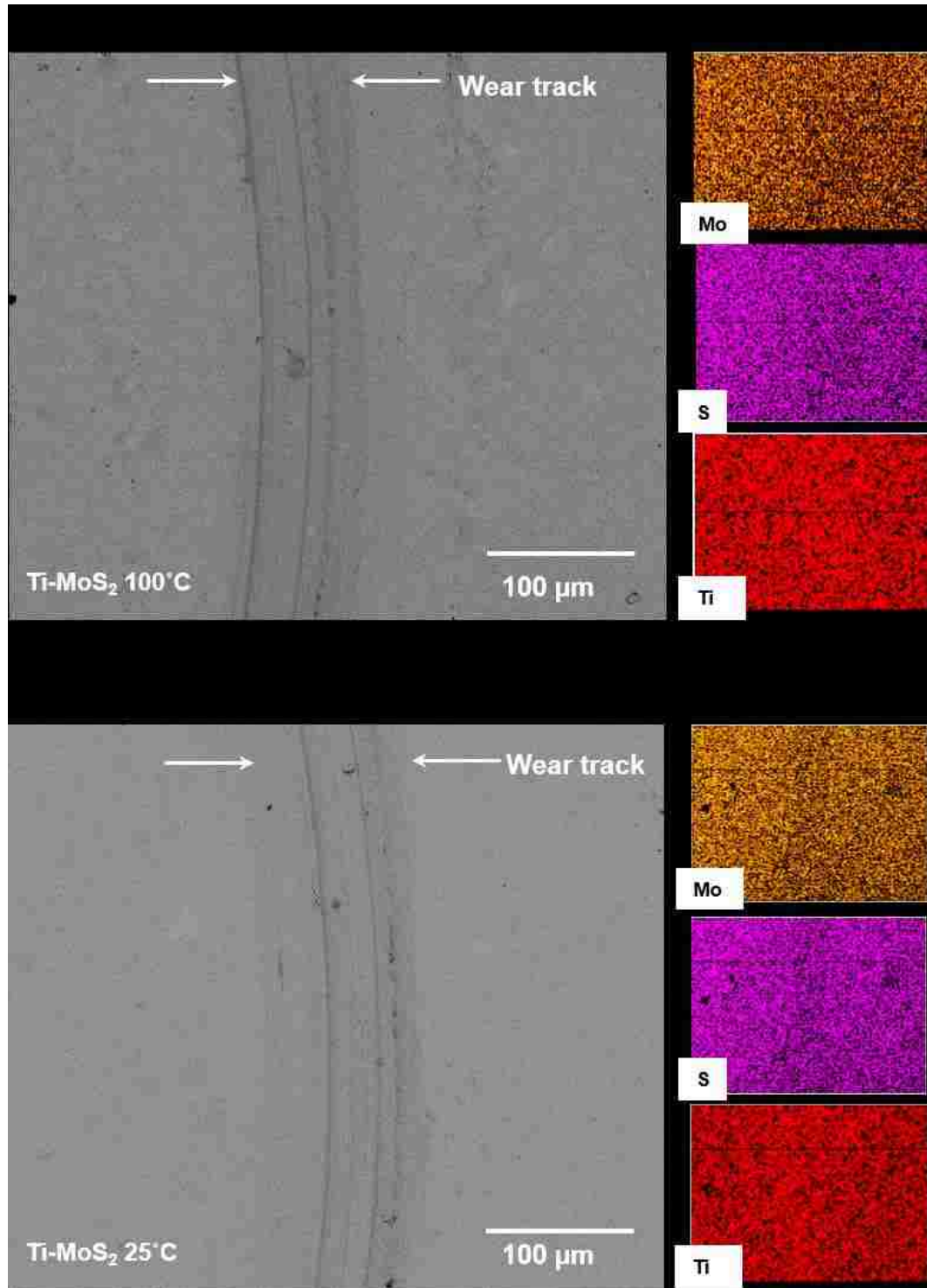
Figure 6.8 (a) Backscattered SEM image of wear tracks on Ti-MoS$_2$ coatings after sliding against 319 Al in oil for 5 × 103 revolutions at 100 ˚C (a) and room temperature (b) and corresponding EDS maps for Mo, S and Ti.

Raman spectra results of wear tracks and tribolayers formed on Al pin are shown in **Figure 6.9**. The typical peaks at 374 and 405 cm^{-1} arising from the vibrations within the S-Mo-S layers [25, 37] are shown in **Figure 6.9(a)** for tribolayers formed after wear against Ti-MoS$_2$ coatings. The MoS$_2$ layers formed on the Al counter face helped reduce COF as presented in Figure 2. There are two possible resources for the MoS$_2$ layers: 1. transferred from the Ti-MoS$_2$ coatings, because of the easy-shear planes for MoS$_2$ structure, it is easy for MoS$_2$ coatings to be transferred to the counter surface to form the friction reduction transfer layer; 2. the decomposition of MoDTC in 5W30, though the decomposition will only occur at elevated temperature. The existence of MoS$_2$ layers on Al counter surface is the reason for lower COF values obtained by Ti-MoS$_2$ coatings. At 100 °C, the MoS$_2$ from decomposed MoDTC further reduced COF by forming more MoS$_2$ layers on the counter surface.

The peaks appeared on tribolayers and wear tracks of tests conducted at 100 °C for Al against steel at 1250, 1480, and 2950 cm^{-1} are attributed to C-H bonds in the ORL [38]. The ORL formed at 100 °C helped to reduce friction during wear.
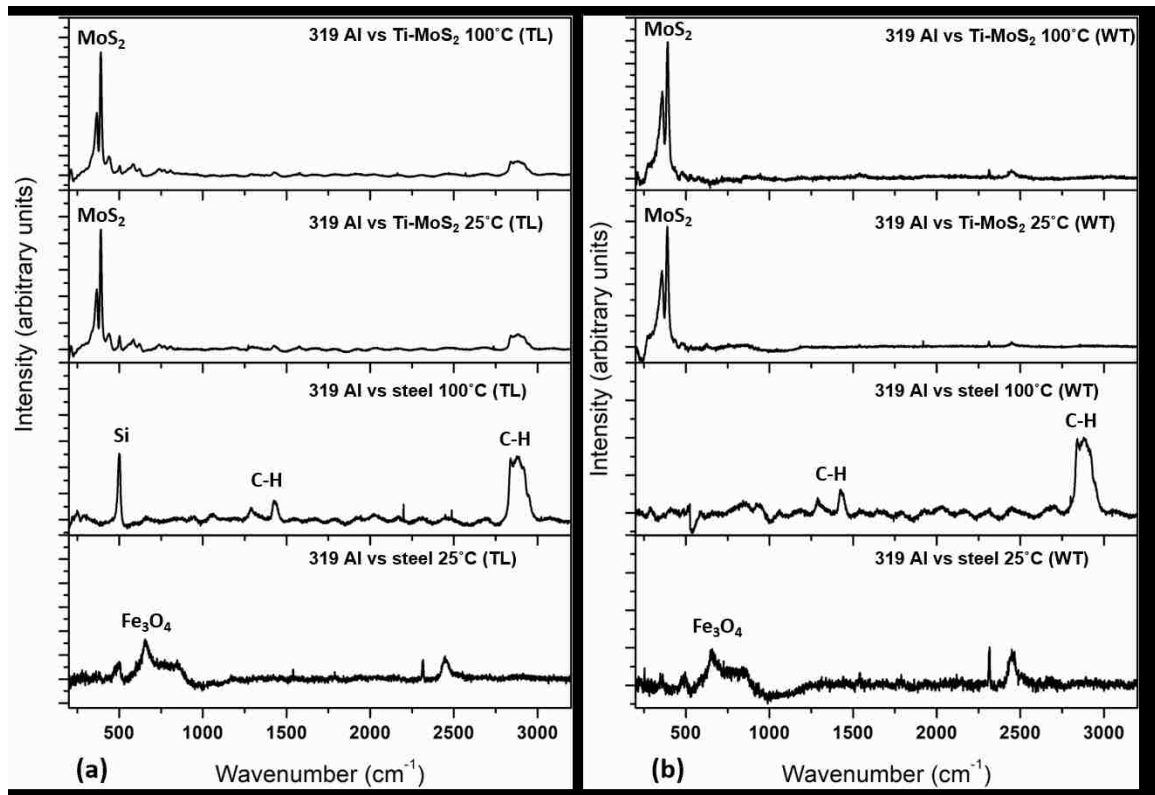
Figure 6.9 (a) Raman spectra of transfer layer (TL) formed on 319 Al surface tested against Ti-MoS$_2$ and M2 steel at room temperature and 100 °C. (b) Raman spectra of wear track on Ti-MoS$_2$ and M2 steel.

6.4   Wear Maps for Advanced Coatings

Figure 6.10 shows the wear behaviour of advanced coatings, namely DLC, B$_4$C and Ti-MoS$_2$ coatings tested against lightweight alloys under different RH levels in ambient air and dry atmospheres. For different kinds of DLC coatings (hydrogenated, non-hydrogenated and F doped), moisture has opposite effect on their wear behaviours. Non-hydrogenated and F-doped DLC coatings have lowest COF and wear rate under highest level humidity, since -OH bonds were formed on transfer layer and coatings with repulsive force to each other resulted in low COF. Whereas the hydrogenated DLC coating is already self-passivated, the moisture between coating and transferlayer generates attraction force, which leads to higher COF.

197
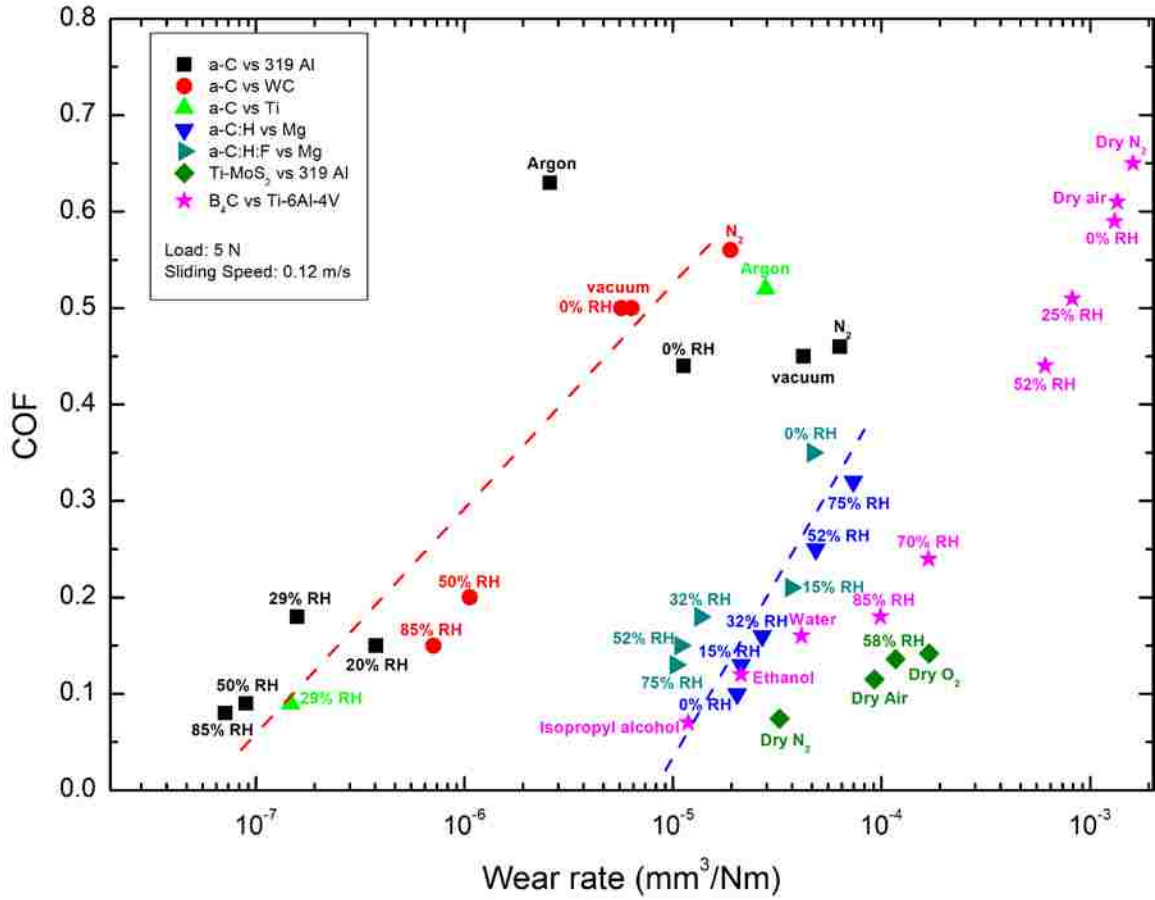
Figure 6.10 COF versus wear rate map for DLC, B_4C and $Ti-MoS_2$ coatings tested against selected alloys under different environments [39-42].

Figure 6.11 shows the wear map of DLC and $Ti-MoS_2$ coatings tested in elevated temperatures under different environments against lightweight alloys.
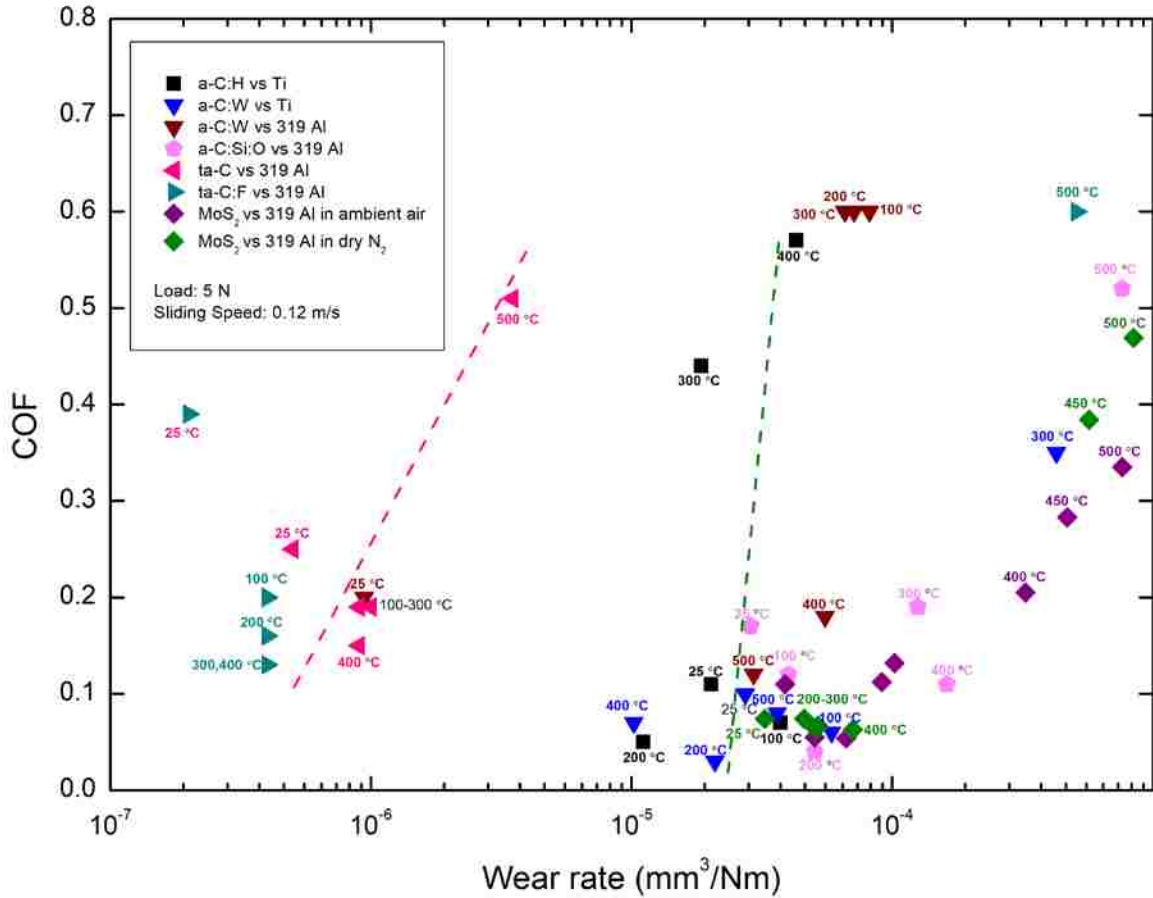
Figure 6.11 the COF versus wear rate map for DLC and Ti-MoS$_2$ coatings tested against lightweight alloys at temperatures from 25 ºC to 500 ºC [26, 43-45].

6.5   Conclusions

1. Tests conducted at higher temperature have lower COF values because of the formation of ORLs for both steel and Ti-MoS$_2$ coatings.

2. Ti-MoS$_2$ coatings at room temperature showed COF values of 0.08 against Al-Si (319Al) compared to steel (0.13). The reduced COF is attributed to the transferred Ti-MoS$_2$ layers on the counter surfaces;

3. For both Ti-MoS$_2$ and steel, COF values at 100 °C (0.06 for Ti-MoS$_2$ and 0.10 for steel) are lower than those at room temperature. It is because of the decomposition of MoDTC forming into MoS$_2$ in tribolayers.

Therefore, the use of Ti-MoS$_2$ coatings could reduce friction and wear for sliding lubricated applications from room temperature to 100 °C.

6.6   Bibliography

[1] L. Rapoport, N. Fleischer, R. Tenne, Applications of WS2 (MoS2) inorganic nanotubes and fullerene-like nanoparticles for solid lubrication and for structural nanocomposites, Journal of Materials Chemistry, 15 (2005) 1782-1788.

[2] R. Tenne, M. Homyonfer, Y. Feldman, Nanoparticles of layered compounds with hollow cage structures (inorganic fullerene-like structures), Chem Mater, 10 (1998) 3225-3238.

[3] M. Chhowalla, G.A.J. Amaratunga, Thin films of fullerene-like MoS2 nanoparticles with ultra-low friction and wear, Nature, 407 (2000) 164-167.

[4] J.M. Martin, C. Donnet, T. Lemogne, T. Epicier, Superlubricity of Molybdenum-Disulfide, Phys Rev B, 48 (1993) 10583-10586.

[5] T.W. Scharf, S.V. Prasad, Solid lubricants: a Review, J Mater Sci, 48 (2013) 511-531.

[6] J.K.G. Panitz, L.E. Pope, J.E. Lyons, D.J. Staley, The Tribological Properties of Mos2 Coatings in Vacuum, Low Relative-Humidity, and High Relative-Humidity Environments, Journal of Vacuum Science & Technology a-Vacuum Surfaces and Films, 6 (1988) 1166-1170.

[7] T. Endo, T. Iijima, Y. Kaneko, Y. Miyakawa, M. Nishimura, Tribological characteristics of bonded MoS2 films evaluated in rolling-sliding contact in a vacuum, Wear, 190 (1995) 219-225.

[8] C. Donnet, Advanced solid lubricant coatings for high vacuum environments, Surf Coat Tech, 80 (1996) 151-156.

[9] T. Spalvins, Lubrication with Sputtered Mos2 Films - Principles, Operation, and Limitations, J Mater Eng Perform, 1 (1992) 347-352.

[10] V.R. Johnson, G.W. Vaughn, Investigation of the Mechanism of MoS2 Lubrication in Vacuum, J Appl Phys, 27 (1956) 1173-1179.

[11] N.M. Renevier, V.C. Fox, D.G. Teer, J. Hampshire, Performance of low friction MoS2/titanium composite coatings used in forming applications, Mater Design, 21 (2000) 337-343.

[12] X.Z. Ding, X.T. Zeng, X.Y. He, Z. Chen, Tribological properties of Cr- and Ti-doped MoS2 composite coatings under different humidity atmosphere, Surf Coat Tech, 205 (2010) 224-231.

[13] X. Wang, Y.M. Xing, S.L. Ma, X.L. Zhang, K.W. Xu, D.G. Teer, Microstructure and mechanical properties of MOS2/titanium composite coatings with different titanium content, Surf Coat Tech, 201 (2007) 5290-5293.

[14] P. Stoyanov, R.R. Chromik, D. Goldbaum, J.R. Lince, X.L. Zhang, Microtribological Performance of Au-MoS2 and Ti-MoS2 Coatings with Varying Contact Pressure, Tribol Lett, 40 (2010) 199-211.

[15] L.L. Wu, B.C. Holloway, D.P. Beesabathina, C. Kalil, D.M. Manos, Analysis of diamond-like carbon and Ti/MoS2 coatings on Ti-6Al-4V substrates for applicability to turbine engine applications, Surf Coat Tech, 130 (2000) 207-217.

[16] G. Sun, S. Bhowmick, A.T. Alpas, Effect of Atmosphere and Temperature on the Tribological Behavior of the Ti Containing MoS2 Coatings Against Aluminum, Tribol Lett, 65 (2017) 158.

[17] P.I. Sanin, G.N. Kuzmina, Y.A. Lozovoi, T.A. Zaimovskaya, Molybdenum Complexes as Synthetic Additives to Lubricating Oils, Petrol Chem+, 26 (1986) 252-257.

[18] Y. Yamamoto, S. Gondo, Friction and Wear Characteristics of Molybdenum Dithiocarbamate and Molybdenum Dithiophosphate, Tribol T, 32 (1989) 251-257.

[19] C. Grossiord, K. Varlot, J.M. Martin, T. Le Mogne, C. Esnouf, K. Inoue, MoS2, single sheet lubrication by molybdenum dithiocarbamate, Tribology International, 31 (1998) 737-743.

[20] Y.R. Jeng, S.J. Hwang, Z.G.H. Fong, J.A. Shieh, The effects of adding molybdenum dithiocarbamate additive to a sulfur-phosphorus gear oil on two roller apparatus performance, Lubr Eng, 58 (2002) 9-15.

[21] L.R. Rudnick, Lubricant Additives: Chemistry and Applications, CRC Press, Taylor & Francis Group, 2017.

[22] J. Graham, H. Spikes, S. Korcek, The friction reducing properties of molybdenum dialkyldithiocarbamate additives: Part I - Factors influencing friction reduction, Tribol T, 44 (2001) 626-636.

[23] M. Kasrai, J.N. Cutler, K. Gore, G. Canning, G.M. Bancroft, K.H. Tan, The chemistry of antiwear films generated by the combination of ZDDP and MoDTC examined by X-ray absorption spectroscopy, Tribol T, 41 (1998) 69-77.

[24] M. Chen, X. Meng-Burany, T.A. Perry, A.T. Alpas, Micromechanisms and mechanics of ultra-mild wear in Al-Si alloys, Acta Mater, 56 (2008) 5605-5616.

[25] A. Banerji, S. Bhowmick, A.T. Alpas, Role of temperature on tribological behaviour of Ti containing MoS2 coating against aluminum alloys, Surf Coat Tech, 314 (2017) 2-12.

[26] S. Bhowmick, A. Banerji, M.Z.U. Khan, M.J. Lukitsch, A.T. Alpas, High temperature tribological behavior of tetrahedral amorphous carbon (ta-C) and fluorinated ta-C coatings against aluminum alloys, Surf Coat Tech, 284 (2015) 14-25.

[27] S. Bhowmick, A. Banerji, M.J. Lukitsch, A.T. Alpas, The high temperature tribological behavior of Si, O containing hydrogenated diamond-like carbon (a-C:H/a-Si:O) coating against an aluminum alloy, Wear, 330 (2015) 261-271.

[28] I.M. Hutchings, Tribology: Friction and Wear of Engineering Materials, Edward Arnold, 1992.

[29] S. Bhowmick, G. Sun, A.T. Alpas, Low friction behaviour of boron carbide coatings (B4C) sliding against Ti-6Al-4V, Surf Coat Tech, 308 (2016) 316-327.

[30] J.M. Martin, C. Grossiord, T. Le Mogne, S. Bec, A. Tonck, The two-layer structure of zndtp tribofilms Part 1: AES, XPS and XANES analyses, Tribology International, 34 (2001) 523-530.

[31] G. Pereira, A. Lachenwitzer, M.A. Nicholls, M. Kasrai, P.R. Norton, G. De Stasio, Chemical characterization and nanomechanical properties of antiwear films fabricated from ZDDP on a near hypereutectic Al-Si alloy, Tribol Lett, 18 (2005) 411-427.

[32] G. Pereira, A. Lachenwitzer, M. Kasrai, P.R. Norton, T.W. Capehart, T.A. Perry, Y.T. Cheng, B. Frazer, P.U.P.A. Gilbert, A multi-technique characterization of ZDDP antiwear films formed on Al (Si) alloy (A383) under various conditions, Tribol Lett, 26 (2007) 103-117.

[33] D.N. Khaemba, A. Neville, A. Morina, New insights on the decomposition mechanism of Molybdenum DialkyldiThioCarbamate (MoDTC): a Raman spectroscopic study, Rsc Adv, 6 (2016) 38637-38646.

[34] A. Neville, A. Morina, T. Haque, Q. Voong, Compatibility between tribological surfaces and lubricant additives - How friction and wear reduction can be controlled by surface/lube synergies, Tribology International, 40 (2007) 1680-1695.

[35] R.K. Gunda, S.K.R. Narala, Tribological studies to analyze the effect of solid lubricant particle size on friction and wear behaviour of Ti-6Al-4V alloy, Surf Coat Tech, 308 (2016) 203-212.

[36] C. Donnet, J.M. Martin, T. LeMogne, M. Belin, Super-low friction of MoS2 coatings in various environments, Tribology International, 29 (1996) 123-128.

[37] B.C. Windom, W.G. Sawyer, D.W. Hahn, A Raman Spectroscopic Study of MoS2 and MoO3: Applications to Tribological Systems, Tribol Lett, 42 (2011) 301-310.

[38] A. Erdemir, G. Ramirez, O.L. Eryilmaz, B. Narayanan, Y.F. Liao, G. Kamath, S.K.R.S. Sankaranarayanan, Carbon-based tribofilms from lubricating oils, Nature, 536 (2016) 67-71.

[39] E. Konca, Y.T. Cheng, A.T. Alpas, Dry sliding behaviour of non-hydrogenated DLC coatings against Al, Cu and Ti in ambient air and argon, Diam Relat Mater, 15 (2006) 939-943.

[40] E. Konca, Y.T. Cheng, A.M. Weiner, J.M. Dasch, A.T. Alpas, Effect of test atmosphere on the tribological behaviour of the non-hydrogenated diamond-like carbon coatings against 319 aluminum alloy and tungsten carbide, Surf Coat Tech, 200 (2005) 1783-1791.

[41] E. Konca, Y.T. Cheng, A.T. Alpas, Sliding wear of non-hydrogenated diamond-like carbon coatings against magnesium, Surf Coat Tech, 201 (2006) 4352-4356.

[42] S. Bhowmick, F.G. Sen, A. Banerji, A.T. Alpas, Friction and adhesion of fluorine containing hydrophobic hydrogenated diamond-like carbon (F-H-DLC) coating against magnesium alloy AZ91, Surf Coat Tech, 267 (2015) 21-31.

[43] S. Bhowmick, A.T. Alpas, The performance of hydrogenated and non-hydrogenated diamond-like carbon tool coatings during the dry drilling of 319 Al, International Journal of Machine Tools & Manufacture, 48 (2008) 802-814.

[44] A. Abou Gharam, M.J. Lukitsch, M.P. Balogh, A.T. Alpas, High temperature tribological behaviour of carbon based (B4C and DLC) coatings in sliding contact with aluminum, Thin Solid Films, 519 (2010) 1611-1617.

[45] F.G. Sen, X. Meng-Burany, M.J. Lukitsch, Y. Qi, A.T. Alpas, Low friction and environmentally stable diamond-like carbon (DLC) coatings incorporating silicon, oxygen and fluorine sliding against aluminum, Surf Coat Tech, 215 (2013) 340-349.

CHAPTER 7

CYCLIC STRAIN-INDUCED CRACK GROWTH IN GRAPHITE DURING ELECTROCHEMICAL TESTING IN PROPYLENE CARBONATE-BASED LI-ION BATTERY ELECTROLYTES

7.1 Introduction

During cyclic charging and discharging cycles Li-ion battery electrodes experience volumetric expansion as a result of lithiation and solvent co-intercalation-induced strains. The degree of volume expansion depends on the type of electrode material, but in most cases, mechanical damage in the form of fracture and fragmentation is expected to occur [1-3]. Mechanical damage could be regarded as one of the important reasons for graphite electrode degradation resulting in impedance growth and capacity loss [4-7]. Many studies have also found that the generation of a solid electrolyte interphase (SEI) on graphite would help to reduce the severity of mechanical damage to electrode materials and maintain the initial capacity of lithium-ion batteries over their lifespan [8-11].

Experimental techniques that were employed in order to observe the damage caused by lithium-ion intercalation/de-intercalation induced strains within a graphite lattice include Raman spectroscopy and atomic force microscopy [12, 13]. Raman observations suggested a "surface structural disordering" phenomenon caused by deformation of the graphene layers and breaking of the C–C bonds. Evidence for fracture and fragmentation of graphite particles during electrochemical cycling (and a decrease in the average graphite crystallite (plate-like, a ≫ c) size) was also provided by Raman spectroscopy [14]. Lithiation-induced strains, estimated by digital image correlation (DIC) in graphite electrodes [15], were as high as 3–4% in regions near the cracks. In-situ Raman spectroscopy revealed that a strain of 0.4% was sufficient to cause fragmentation and particle removal due to lithiation in graphite electrodes [16]. Aurbach et al. [17]

suggested that crack formation mechanisms in graphite anodes include separation of graphite planes due to the intercalation products diffusing to the edges of the exfoliated planes. According to Bhattacharya et al. [4], the solvents' adsorption stage was instantaneous so the crack initiation occurred immediately after the application of a voltage gradient [7]. However, the crack-growth process could occur gradually and may display cyclic growth properties. Thus, the degradation of electrodes can be thought as a cyclic fracture mechanics problem and can be studied using a stress intensity approach. It can be suggested that the rate of crack growth in an electrode material, such as graphite, subjected to a voltage gradient could be determined by the cyclic stress intensity factor, $\Delta K = K_{max} - K_{min}$. Accordingly, an existing crack would open during the lithiation stage reaching the highest stress intensity (K_{max}) and then will be closed (K_{min}) during de-lithiation. Formation of SEI deposits may reduce the effective ΔK value by preventing physical contact of the cracks flanks (and cause crack closure [18]). Therefore, the graphite crack-growth rate is expected to reduce if SEI deposits cover the crack surface or lithium compounds are intercalated at the crack-tip [4]. Once the growth behaviour of cracks is determined, the associated capacity loss in Li-ion batteries due to graphite electrode degradation could be better understood.

A fracture mechanics approach was used in this experimental work to rationalize the crack-growth process in graphite electrochemically cycled (vs. Li/Li+) in propylene carbonate (PC)-based electrolyte solutions. For this purpose, cyclic electrochemical experiments were performed using an applied constant load on pre-cracked graphite bars and the graphite crack propagation rates were determined using in-situ optical microscopy. Electrochemical intercalation in graphite electrodes could lead to the development of compressive stresses ranging from 5 to 12 MPa [19, 20] to 250 MPa [21, 22] depending on the charge/discharge rates. It has been demonstrated that solvent co-intercalation in graphite-based anodes is more pronounced in presence of PC as compared to other electrolytes [23-25]. Therefore, a PC-based electrolyte is expected to cause extensive damage and crack formation in electrochemically cycled graphite. In fact, large internal stresses arising from

solvent intercalation in presence of PC were shown to lead to void formation in graphitic thin film electrodes eventually causing delamination of graphene layers [26]. In this work, the cyclic strain, induced by lithiation/de-lithiation cycles, was measured by micro-Raman spectroscopy performed simultaneously with cyclic voltammetry (CV) tests. Variations in graphite crack-growth rates were discussed in terms of the morphologies of the fracture surface and the deposited solid electrolyte reduction products.

7.2 Materials and Methods

7.2.1 Description of constant load bending experiments during electrochemical tests

Single-edge-notched-bend (SENB) samples with dimensions of 20 mm (L) $\times$ 6 mm (W) $\times$ 2 mm (B) were machined (and polished) from >99% purity graphite (grade GM10) isostatically pressed by GraphtekTM with a density of 1820 kg m^{-3}. The porosity of the graphite, determined by means of image analyses, was 24%. A ~4-mm-long notch was machined in the sample and a sharp crack of length 100 ± 20 μm, with an average radius of 15 ± 5 μm, was introduced at the tip of the notch. A four-point bending fixture was placed inside a test cell, as shown in **Figure 7.1**a. The SENB samples were mounted in the bending fixture with 16-mm-long outer loading span (S1) and an inner span (S$_o$) of 6 mm, following the test configuration of ASTM-C1421 [27]. The cell, constructed from polytetrafluoroethylene (PTFE), was assembled in an Ar-filled (MBraun LABstar) glove box where H_2O and O_2 levels were maintained below 1 ppm. A 99.99% pure Li wire with a resistivity of 9.446 μΩ-cm (at 20 °C) was used as the counter electrode.
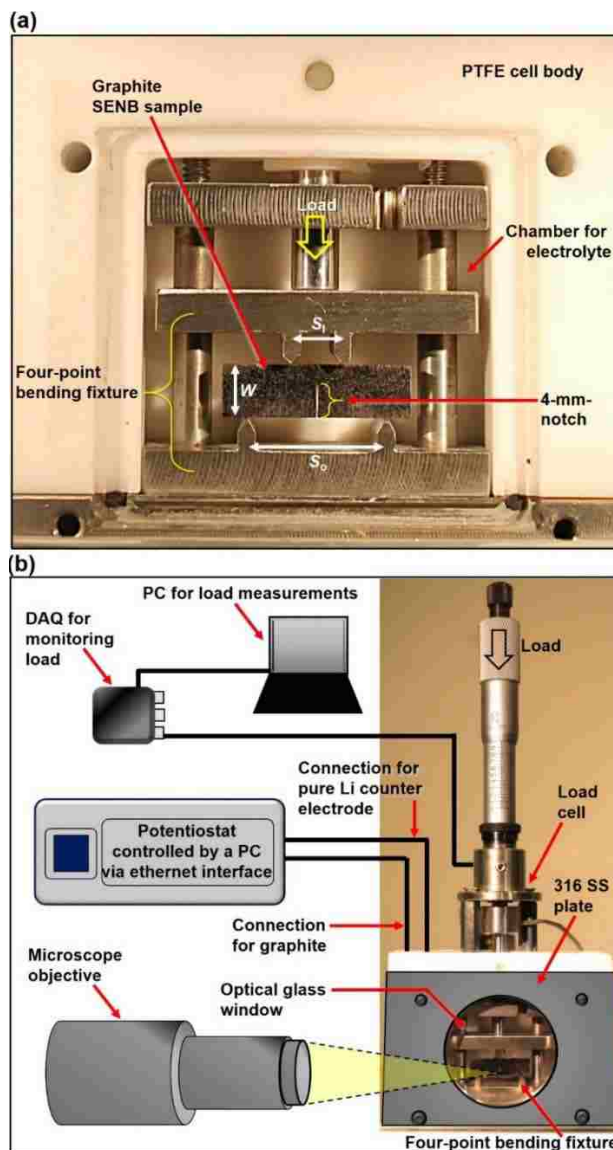
Figure 7.1 a Optical image showing the four-point bending fixture installed in an electrolyte chamber for investigating environment-assisted cracking of graphite SENB samples. b Schematic diagram showing the electrochemical cell used for in-situ observation of electrochemical cycling-induced crack growth under a constant load.

A simulated battery environment was achieved by testing in an electrolyte solution prepared using 1 M $LiClO_4$ (99%) in a 1:1 (by vol.) mixture of PC (99%) and 1,2-dimethoxy ethane (DME, 99%). CV tests were performed in such a way that initially a low voltage of 0.02 V was applied and then the voltage was increased to a maximum of 3.00 V, i.e. V = 0.02 V $\rightarrow$ 3.00 V (vs. Li/Li+) while maintaining a constant scan rate of 20 mVs^{-1} using a Potentiostat/Galvanostat system

(Solartron Modulab System with a high-speed data acquisition rate of up to 1 MS s^{-1}). A schematic of the experimental set-up is shown in **Figure 7.1**b. The load was applied by means of a screw gauge located outside the cell after the first CV cycle. Crack growth was observed using a high depth-of-field optical digital microscope and continuously recorded. The applied load (10 N) was measured using a load cell that was capable of operating in the load range of 0–22.2 N with an accuracy of approximately 4.48×10^{-3} N, corresponding to the smallest unit of 1 µV measured by a data acquisition (DAQ) system.

7.2.2 In-situ Raman spectroscopy for measurement of lithiation/de-lithiation-induced strain

The driving force required for crack growth in graphite is provided by the lithiation/de-lithiation-induced strains. A separate set of cyclic electrochemical experiments were performed with the objective of measuring the global strain that caused damage in graphite. Here, unnotched and cylindrical electrodes, with a diameter of 5.0 mm and a height of 4.5 mm, were micro-wire EDM machined from graphite with the same physical properties as mentioned in the previous section. In this case, the top surface of the graphite electrode, installed inside a cylindrical cell with a quartz glass window, was placed directly under the 50× objective of a Raman spectrometer. The cells were assembled and sealed in the MBraun LABstar workstation where the counter and reference electrodes, machined from Li wires, were installed. A detailed description of the electrochemical cell and the in-situ Raman set-up is provided in [16]. Briefly, a 50 mW Nd-YAG solid-state laser diode emitting a continuous wave laser at the 532-nm excitation line was used to obtain Raman spectra by means of a Horiba spectrometer equipped with a CCD detector. The diameter of the laser spot on the specimen surface was 1 µm.

7.3 Result and Discussion

7.3.1 Constant-load bending of graphite samples in ambient air

Crack-growth behaviour of the graphite samples under constant loading in an ambient air atmosphere are shown in **Figure 7.2**. Crack-growth rates are plotted against stress intensity factor (K_I). The expression for K_I for four-point bending is provided in the Appendix. The crack-growth rate data can be fitted to $da/dt = AK^n$-type functions. Constant load testing of GM10 graphite resulted in a single stage crack-growth behaviour, and da/dt exhibited a high sensitivity to K_I. This observation was consistent with the data reported in the literature where results of experiments conducted on glassy carbon [28], pyrolytic graphite and POCO-grade graphite [29] in air were plotted in **Figure 7.2**. Properties of GM10 graphite and crack growth parameters, n and A, are listed in **Table 7.1** in comparison with those reported for glassy carbon, pyrolytic and POCO graphite obtained by means of double torsion tests. Results of tests performed using compact tension (CT) specimens made from graphite/carbon composite samples, subjected to loading in a simulated physiological environment namely Ringer's solution, are also shown in [30]. A single-stage crack growth behaviour where K_I levels varied between 1.3 to 1.5 MPa.m$^{0.5}$ can be seen in **Figure 7.2**.

7.3.2 Measurement of lithiation/de-lithiation-induced strain in graphite during cyclic electrochemical experiments

CV scans obtained during experiments with the graphite SENB samples performed in PC-based electrolyte solutions are shown in **Figure 7.3**. The difference in the voltammogram areas between the first and the second cycles can be attributed to the irreversible charge consumption due to solid electrolyte formation and usually associated with the drastic drop in capacity in the first cycle [5].
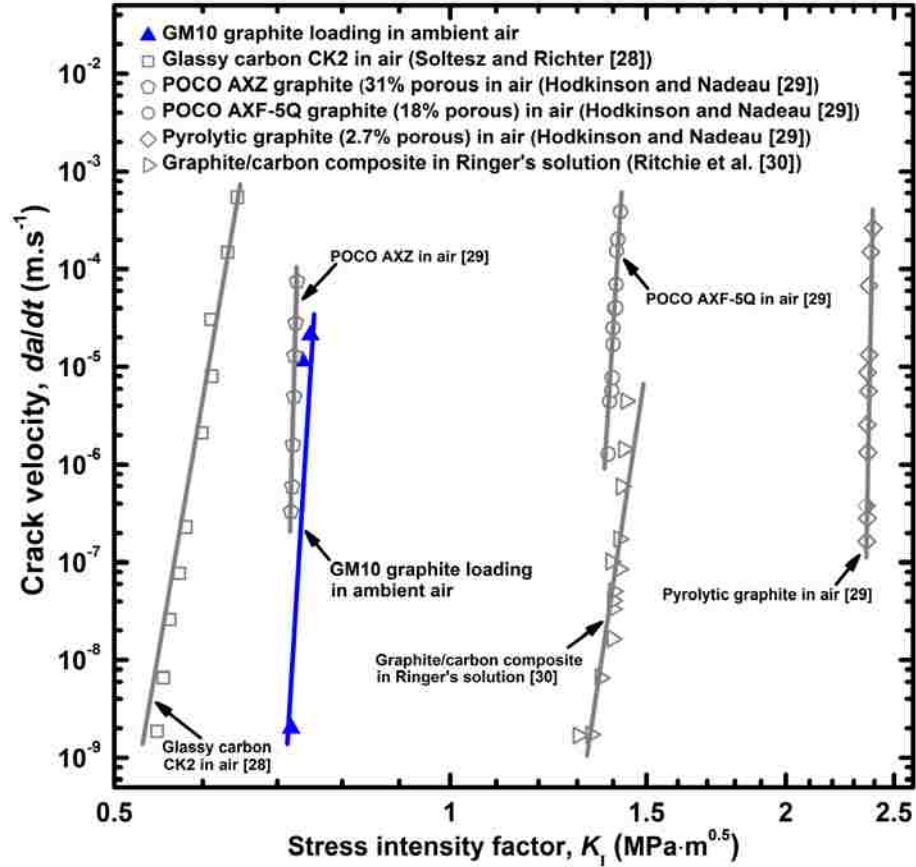
Figure 7.2 Experimental da/dt versus K_I constant-load cracking data of graphite SENB samples in ambient air in comparison with results in the literature for glassy carbon [28], pyrolytic graphite and POCO-grade graphite [29] tested in air and graphite/carbon composite tested in Ringer's solution [30].

Cyclic lithiation and de-lithiation cycles would induce strains in the lattices of graphite. For determining the variations in the strain generated during voltage cycling in PC-based electrolytes, in-situ Raman spectroscopy was performed simultaneously with the CV experiments conducted between 3.00 V → 0.02 V → 3.00 V vs. Li/Li+ at a scan rate of 2.00 mVs^{-1}. A series of in-situ Raman spectra obtained during the first (**Figure 7.4** (a)) and second CV cycles (**Figure 7.4** (b)) at 3.00, 2.00, 1.00, 0.20 and 0.02 V showed that the G-band in graphite shifted from 1580 cm^{-1} (at 3.00 V) to a high wavenumber of 1599 cm^{-1} when the voltage was decreased to 0.02 V.

Table 7.1 Properties and fracture mechanics parameters of carbon materials reported in the literature in comparison with those obtained during four-point bending of notched GM10 graphite in ambient air.

Material	Porosity (%)	Density (Kg m^{-3})	Environment	Test Method	Crack growth parameters $da/dt=AK_I^n$		Fracture toughness, K_{Ic} (MPa·m$^{1/2}$)
					n	logA	
Glassy carbon CK2 [28]	<1%	1500	Air	Double torsion	178	31	0.71
POCO AXZ [29]	31	1550	Air	Double torsion	113	-662	0.73
POCO AXF-5Q [29]	18	1850	Air	Double torsion	218	-1343	1.46
Pyrolytic graphite [29]	2.7	2190	Air	Double torsion	216	-1384	2.50
Graphite/ carbon composite [30]	-	1900	Ringer's solution	Compact tension	74.4	18	1.60
GM10 graphite	24%	1820	Air	4-point bending	186.7	18.72	0.75±0.06
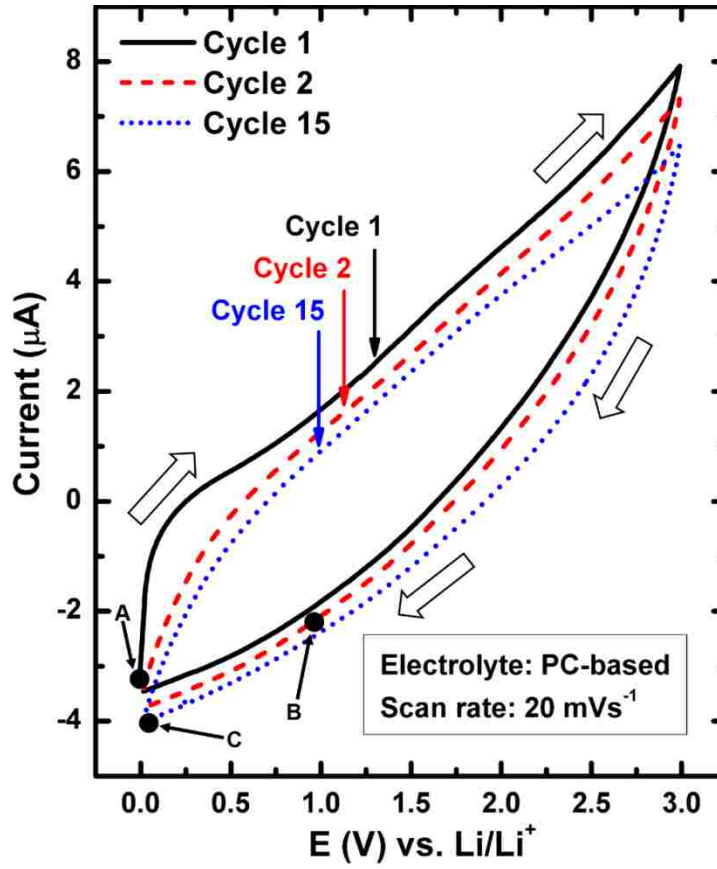
Figure 7.3 Cyclic voltammograms obtained during cycling from V = 0.02 V→3.00 V (vs. Li/Li⁺) at a high voltage scan rate of 20 mVs⁻¹ in PC-based electrolytes.

The frequency shift of the G-band is related to the uniaxial strain and the shear strain—the latter could be ignored due to its minor contribution [31]. The relation between the Raman frequency and the strain could be expressed as [31, 32]:

$$\frac{\Delta\omega}{\omega_o} = \gamma\left(\varepsilon_{xx} + \varepsilon_{yy}\right) \tag{7-1}$$

where ω_o is the G-band frequency; $\Delta\omega$ is the shift in the frequency (from 1580 to 1599 cm⁻¹); $\gamma = 1.59$ is the Grüneisen parameter for graphite [31]; ε_{xx} is the uniaxial strain, while $\varepsilon_{yy} \approx -0.2\,\varepsilon_{xx}$ is the relative strain in the perpendicular direction according to the Poisson's ratio of graphite (= 0.20 [32]). From these values, the maximum ε_{xx} for graphite cycled in PC-based electrolytes was

214

calculated as 9.5×10^{-3}. The shift in the location of the G-band was discussed in terms of the strain increase in the graphite lattice [33, 34]. It could be attributed to intercalation of solvent molecules. The changes in the uniaxial strain are plotted as a function of the time and voltage in **Figure 7.4** (c). When the voltage was increased to 3.00 V during the reverse sweep, the G-band shifted back to only 1583 cm^{-1} in the first cycle and 1585 cm^{-1} in the second cycle, instead of 1580 cm^{-1} measured at the beginning of cycling. This incomplete strain hysteresis resulting from voltage cycling could be attributed to residual strain in the graphite lattice that caused damage and crack growth. The large strain of 0.95% calculated from Eq. 2.1 would be responsible for the accelerated crack growth in graphite as described in the following section.

7.3.3   Crack growth during cyclic electrochemical experiments with graphite

Crack growth during constant loading accompanied by the CV experiments in PC-based electrolyte (described in **Figure 7.3**) was observed at a magnification of 500× and cracks at different stages of propagation are shown in Figure 7.5a–c. A microstructure was obtained corresponding to the point A marked in **Figure 7.3**, and shown in Figure 7.5 (a). The tip of the notch introduced prior to the tests is indicated in this figure. A load of 10 N was applied before the initiation of the CV experiment. In the second cycle at point B in **Figure 7.3**, an approximately 205 µm-long-crack was observed to form in the graphite, as can be seen in Figure 7.5 (b). The lithiation and de-lithiation stages during the CV experiments would induce cyclic strain (as described in the previous section) that would cause crack growth in graphite over a span of several cycles. The rate of crack growth (da/dt) could be plotted as a function of the cyclic stress intensity factor, ΔK. The stress intensity measured in this case, at the point of maximum crack opening during the lithiation step, was $K_I = K_{max}$. It was assumed that $K_{min} = 0$. According to Eqs. 2 and 3, K_{max} for the crack formed in Figure 7.5 (b) was 0.78 MPa.m$^{0.5}$. With progress in cycling, the crack length increased and was measured after 15 cycles at point C in **Figure 7.3**. By this time, the length of the crack had

increased to 400 μm as shown in Figure 7.5 (c), and K_{max} was 0.91 MPa.m$^{0.5}$. Further continuation of electrochemical cycling caused unstable crack growth leading to fracture of the graphite bars.
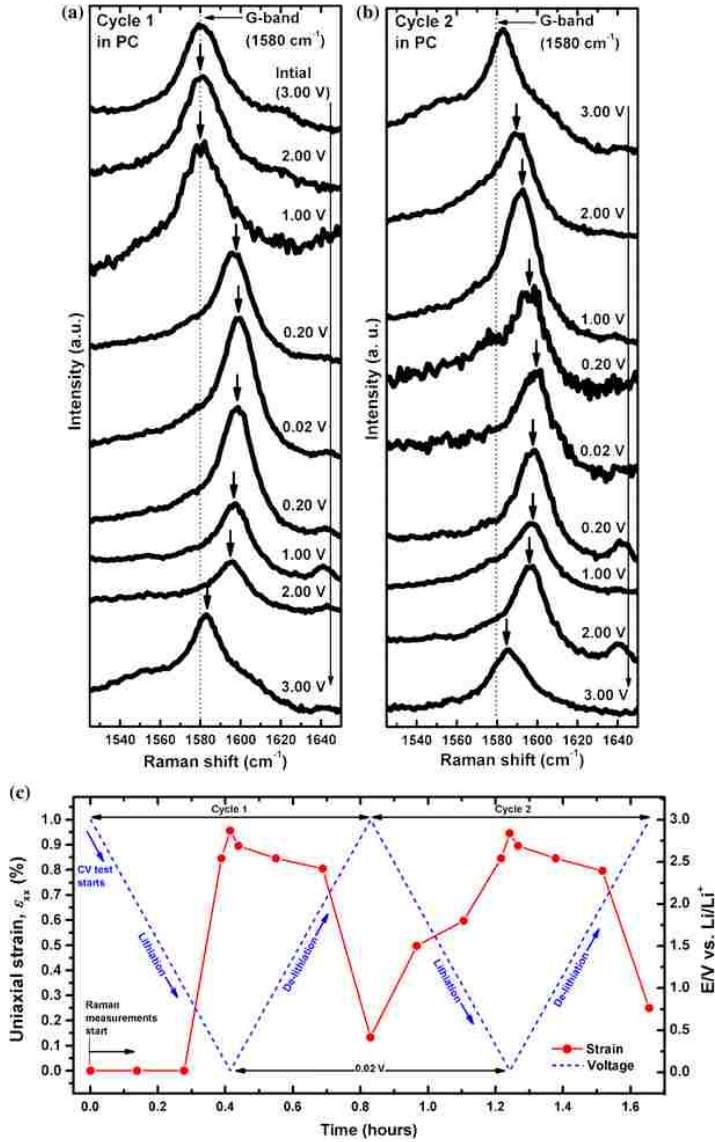
Figure 7.4 In-situ Raman spectra obtained from graphite cycled using PC-based electrolytes in **a** first and **b** second CV cycles while scanning from 3.00 → 0.02 → 3.00 V at a linear scan rate of 2.0 mVs^{-1}. **c** Plot showing changes in the uniaxial strain measured from the shift in the Raman G-band observed in **a** and **b**.

(a)
Before CV test in PC-electrolyte

Graphite

Pores

Crack-tip

100 μm

(b)
Time = 600 s, K_{max} = 0.78 MPa·m$^{0.5}$

Cycle 2, Load = 10 N
Voltage = 1.00 V

Crack

100 μm

(c)
Time = 4200 s, K_{max} = 0.91 MPa·m$^{0.5}$

Cycle 15
Voltage = 0.02 V
Load = 10 N

Crack

100 μm
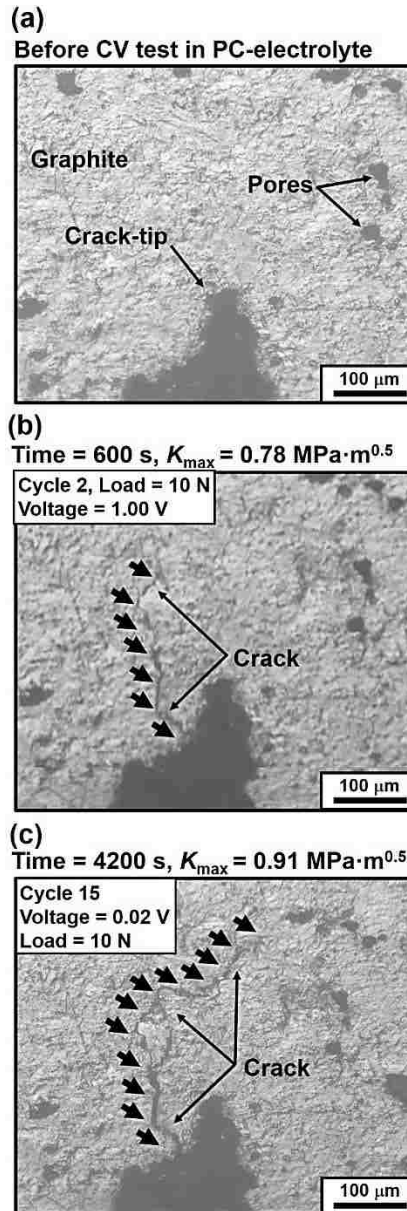
Figure 7.5 In-situ optical micrographs obtained at points marked in **Figure 7.3**, that is **a** point A—before CV experiments in PC-based electrolytes **b** point B—after 600 s (cycle 2) and **c** point C—after 4200 s (cycle 15). A constant load of 10 N was applied simultaneously.

Based on the in-situ microscopic observations, the increase in the crack length due to simultaneous bending and cycling in PC-based electrolyte solutions is plotted as a function of time and voltage cycles in **Figure 7.6** (a). The crack length increased gradually with voltage cycling (from 4000 μm in the first cycle to 4400 μm at the 14th cycle). In the 15th cycle, however, the crack

length increased to 4800 µm before fracture occurred. The subcritical crack-growth behaviour observed in graphite cycled in PC-based electrolyte under constant loading was determined as shown in **Figure 7.6** (b) where da/dt is plotted against K_{max}. The plot of da/dt as a function of K_{max} showed two different stages of crack development. In the first stage, da/dt vs. K_{max} had a high slope. This stage served to estimate the threshold stress intensity factor, K_{Iscc}. In the second stage, the da/dt was less sensitive to the applied stress intensity compared to that observed in the first stage. The fracture parameters, K_{Iscc} and K_{Ic}, along with n and A determined for the two-stage behaviour in PC-based solution (**Figure 7.6** (b)) are presented in **Table 7.2**. The parameters obtained from the single-stage behaviour observed during bending experiments in the air (**Figure 7.2**) are also included in the table for comparison. It was observed that cracking in a PC-based electrolyte increased the K_{Ic} of graphite to 1.42 ± 0.05 MPa.m$^{0.5}$ (from 0.75 ± 0.06 MPa.m$^{0.5}$ tested in air). **Figure 7.5** (b) also illustrates the low sensitivity of crack-growth rate to K_{max} in the second stage which is evident from the low exponent (n = 9.9). The delay in crack growth in the second stage could be discussed in terms of solid electrolyte deposits that were generated on the crack faces. Accordingly, the crack surface morphology obtained after tests in PC-based electrolyte solutions are discussed in the following section.
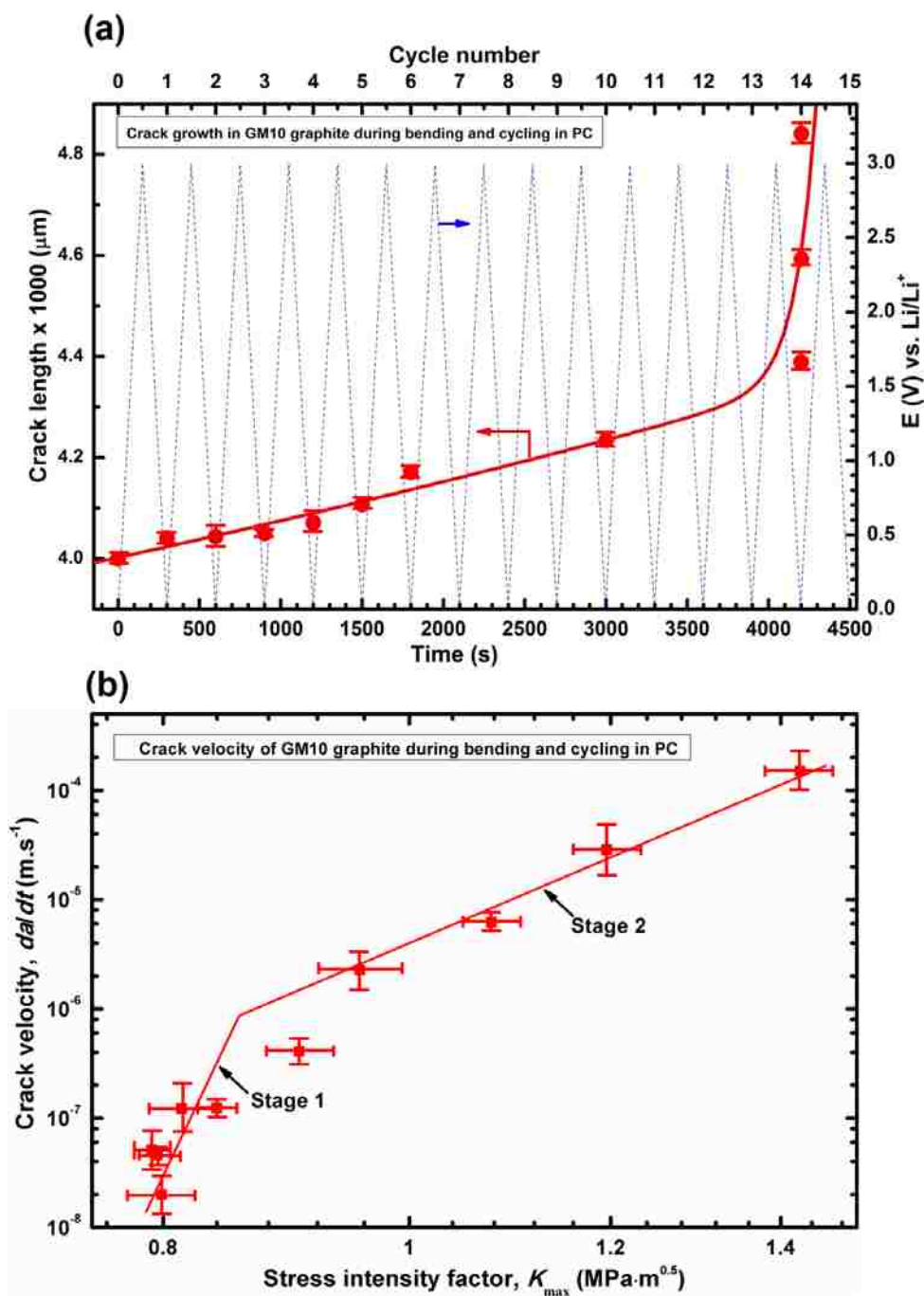
Figure 7.6 a Experimental crack length vs. time plot and **b** da/dt versus K_{max} constant-load data for graphite SENB samples obtained during simultaneous CV and bending experiments in PC-based electrolyte solutions.

Table 7.2 Crack growth parameters obtained from isostatically pressed graphite (porosity: 24%, density: 1820 kg m^{-3}) SENB samples during electrochemical cycling in PC-based electrolytes and under an ambient air atmosphere.

Test conditions	Stage	Threshold stress intensity factor, K_{Iscc} (MPa·m$^{1/2}$)	Crack growth parameters da/dt=A$K_{\mathrm{I}}^{\mathrm{n}}$		Fracture toughness, K_{Ic} (MPa·m$^{1/2}$)
			n	**logA**	
Static loading and voltage cycling in PC	Stage I	0.79±0.05	51.3	-2.30	1.42±0.05
	Stage II		9.9	-5.35	
Static loading in air	Single stage	0.72±0.05	186.7	18.72	0.75±0.06

7.3.4 Observation of graphite fracture surface

The material's resistance to fracture is expected to change with the changes in the crack-tip morphology. Previously, the R-curve behaviour [35] of coarse- and fine-grained graphite were studied [36] using both CT and three-point bend specimens. Using modified CT specimens [37], the crack propagation in polycrystalline nuclear graphite and the mechanisms responsible for the R-curve behaviour were investigated by means of in-situ X-ray tomography. It was suggested that crack closure was caused by frictional contact between the fracture surfaces. The fine-grained graphite showed the lowest resistance, and the high crack-growth-resistance in coarse-grained graphite was attributed to increased crack path deflection and grain bridging. Crack-growth resistance curves for PGA and IM1-24 graphite [38] consisted of an initial rising part, followed by a plateau region indicating resistance to crack growth due to bridging by graphite fragments. The typical morphology of the fracture surface of a graphite specimen after complete failure in the PC-based electrolyte is shown in the secondary electron (SE)-SEM image in **Figure 7.7**. It can be seen that the crack front was rough and uneven with a population of large grains (and pores) indicating the occurrence of intergranular fracture [39, 40]. Cracks possibly nucleated at the pores and the

stepped irregular fracture surfaces showed that a final separation has occurred due to cracks propagating on different crack planes.
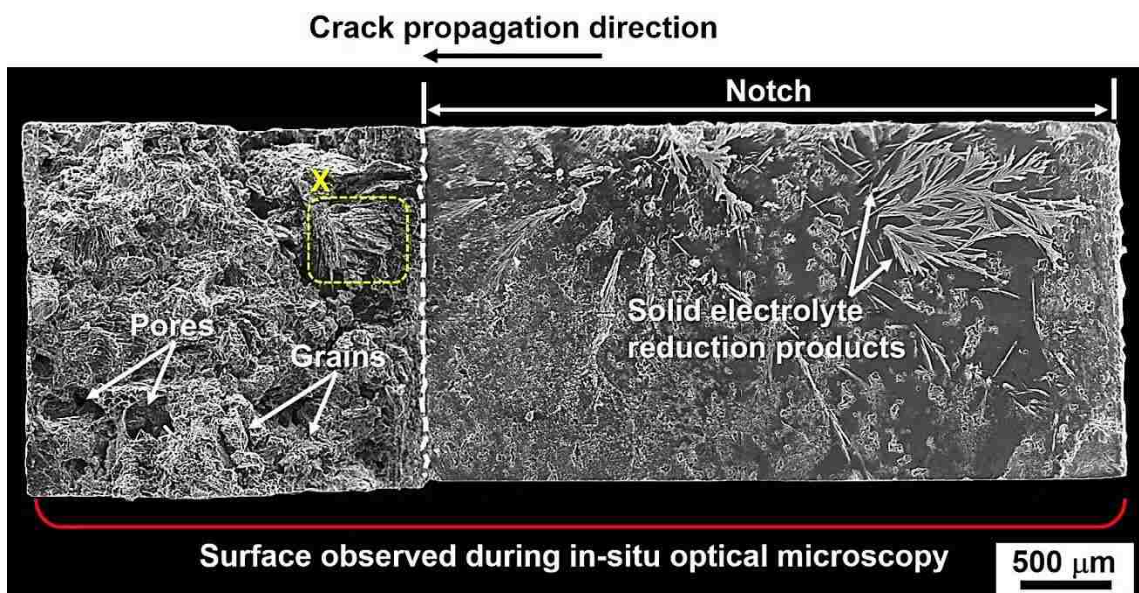
Figure 7.7 SE-SEM image showing the fracture surface of a graphite specimen after fracture due to bending during electrochemical cycling in PC-based electrolyte. The crack propagation direction, the initial notch and the surface observed during the in-situ microscopy are marked.

In some locations, flat facets indicating cleavage fracture were observed in the region of initial crack growth. A typical region is marked in **Figure 7.7** as X and shown in **Figure 7.8** (a). The flat facets occurred due to the separation of graphite layers during crack propagation. A closer inspection of a region marked as (b) in **Figure 7.8** (a), and shown in the SE-SEM image in **Figure 7.8** (b), indicated the presence of deposits with lighter contrast on the separated facets. It is seen in this image that the thickness of the deposits at this location was 4.8 ± 0.5 μm. EDS analyses of the deposits, shown in **Figure 7.8** (c), revealed the presence of chlorine and oxygen, which are both components of the electrolyte salt—$LiClO_4$. Therefore, these deposits were solid electrolyte reduction products [41, 42] that were formed on the graphite surface due to electrochemical reduction during the CV experiments.
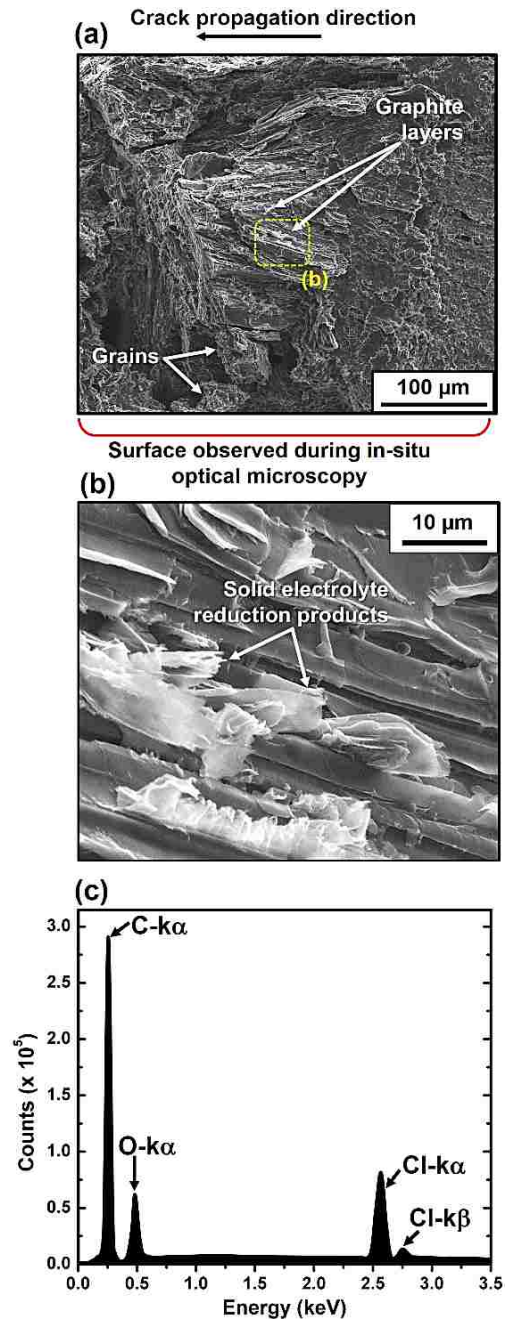
Figure 7.8 SE-SEM images of **a** a region marked as (*x*) in **Figure 7.7** showing flat facets that indicate cleavage fracture within the stable crack-growth region; **b** a region marked as *b* in a showing the presence of solid electrolyte deposits on the crack faces. **c** EDS obtained from the solid electrolyte reduction products.

Some of the deposits that are labelled as the solid electrolyte reduction products in **Figure 7.7** and **Figure 7.8** (b) could be associated with the partially exfoliated facets of the underlying

222

graphite. The presence of these deposits possibly played a role in delaying crack growth that led to the transition in the subcritical crack-growth behaviour from stage I to II as observed in **Figure 7.5** (b) and these are further discussed in the following section.

7.3.5 Mechanism of crack-growth delay due to closure in PC-based electrolyte solutions

The crack-growth mechanisms observed in graphite bars subjected to a constant bending load during cyclic electrochemical testing in PC-based electrolyte solutions are summarized in this section. The stress intensity at the crack tip, K_{max}, was measured and plotted, but stresses induced by cyclic lithiation and delithiation should be also considered. Thus, it is appropriate to describe crack growth rates as a function of the cyclic stress intensity factor, ΔK ($= K_{max} - K_{min}$), where K_{min} is the value of the stress intensity during the delithiation step. In the first stage (**Figure 7.6** (b)), the crack-growth rate was fast in the absence of facets and solid electrolyte deposits. A second stage of crack-growth behaviour was observed in graphite where the value of the exponent (slope), n, was low (9.9) indicating a delay in crack growth (**Figure 7.6** (b)). At this stage, the surface roughness of the crack flanks was high (**Figure 7.7**), and they were covered partially by solid electrolyte deposits formed due to electrochemical reduction (**Figure 7.8**). The mechanisms of crack-growth delay due to crack closure in the presence of PC-based electrolyte solutions are schematically shown in **Figure 7.9**. The surface roughness of the crack flanks was measured to be as high as 22 ± 2 μm. Crack closure due to surface roughness and irregular morphology has been previously reported [18, 43, 44]. In this case, the crack was "wedged-closed" due to the high-fracture surface roughness as shown in **Figure 7.9** (a), which reduced the actual value of "effective" ΔK, ΔK_{eff}. The second mechanism that reduced ΔK was likely due to the presence of solid electrolyte deposits within the crack flanks as shown in **Figure 7.9** (b). These two factors could lead to earlier contact between crack surfaces, thereby raising K_{min} and thus reducing the $\Delta K_{eff} = K_{max} - K_{cl}$ experienced by the crack tip, where K_{cl} ($>K_{min}$) is the stress intensity factor when the crack faces

come into contact. In summary, a fracture mechanics approach could be a valuable tool for understanding the micromechanisms of the electrode damage processes that contribute to capacity fading in Li-ion batteries.
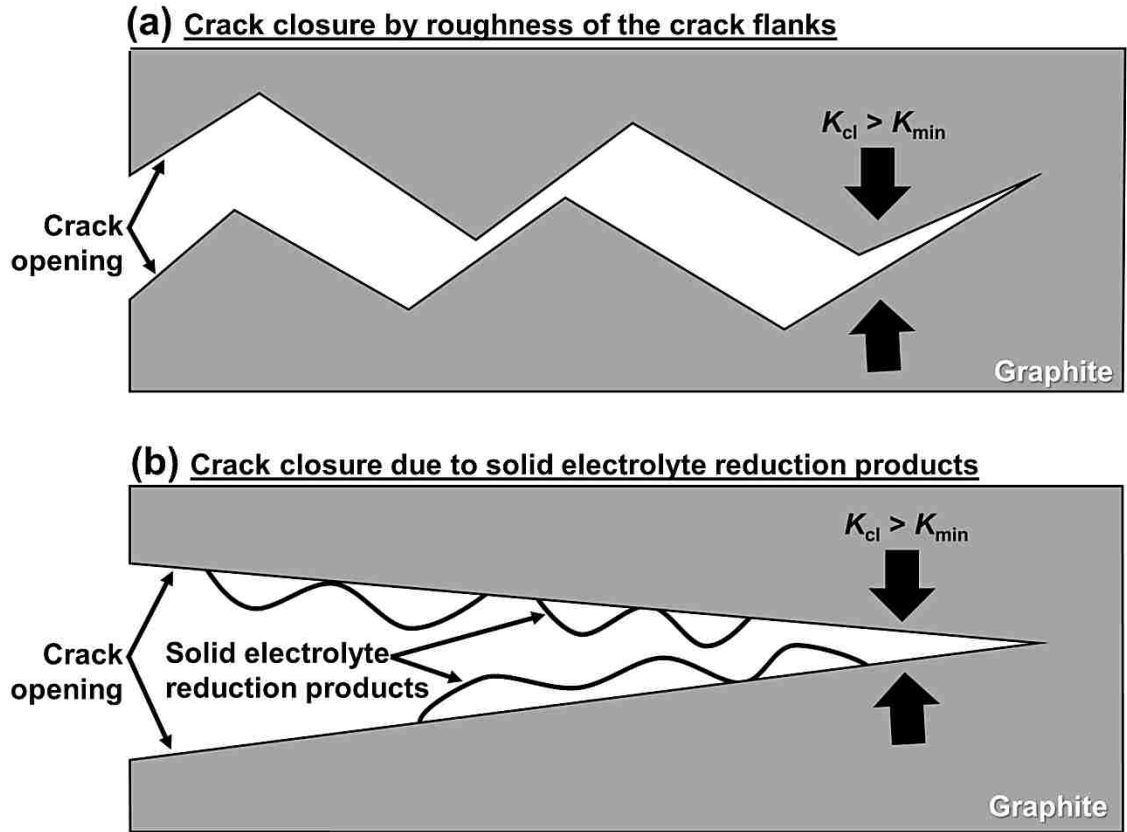
Figure 7.9 Schematic representation of the mechanisms of crack closure induced by **a** roughness and **b** solid electrolyte deposits on the graphite crack flanks that reduced the effective stress intensity for crack growth during bending and electrochemical cycling experiments in PC-based electrolytes.

7.4   Conclusions

This work shows that lithiation/de-lithiation process induces cyclic strains in isostatically pressed graphite. A notched bar bending test at constant load enabled to monitor crack growth in battery electrolyte solutions containing PC. In-situ Raman spectroscopy was used to measure the cyclic strain that provided the driving force for crack growth in graphite. Crack-growth rates (*da/dt*)

were measured by means of in-situ optical microscopy and were related to ΔK as $da/dt = A\Delta K_I^n$. The main conclusions arising from these observations are as follows:

1. A two-stage crack-growth behaviour was observed in PC-based electrolyte solutions (n = 51.3 in stage 1 and n = 9.9 in stage 2) in comparison with a single-stage fast crack-growth behaviour in ambient air (n = 186.7).

2. In the first stage, lithiation/de-lithiation cycles in PC-based electrolytes induced a large cyclic strain of 0.95% in graphite that caused fast crack growth.

3. Premature closing of cracks in the second stage possibly caused by a rough crack face morphology and generation of thick solid electrolyte reduction products on the crack flanks resulted in a reduction of ΔK to ΔK_{eff} and thus reduced the crack-growth rates.

7.5   Acknowledgements

7.6   Appendix

According to ASTM-C1421 [27] for four-point flexure with $0.35 \leqslant a \leqslant 0.60$, K_I (or K_{max}) can be expressed as,

$$K_I \left(K_{max}\right) = f\left[\frac{P(S_0 - S_1)10^{-6}}{BW^{3/2}}\right]\left[\frac{3\left(\dfrac{a}{W}\right)^{1/2}}{2\left(1-\dfrac{a}{W}\right)^{3/2}}\right] \qquad (7\text{-}2)$$

in which, P is the load applied, a is the crack length measured by in-situ optical microscopy, B is the thickness of the test specimen measured perpendicular to a, W is the width measured parallel to a and f is a function of the ratio a/W for four-point flexure expressed as,

$$f = f(a/W) = 1.9887 - 1.326\left(\frac{a}{W}\right) - \frac{\left\{3.49 - 0.68\left(\frac{a}{W}\right) + 1.35\left(\frac{a}{W}\right)^2\right\}\left(\frac{a}{W}\right)\left\{1-\left(\frac{a}{W}\right)\right\}}{\left\{1+\left(\frac{a}{W}\right)\right\}^2} \quad (7\text{-}3)$$

7.7   Bibliography

[1]   Chung GC, Kim HJ, Yu SI, Jun SH, Choi JW, Kim MH (2000) Origin of graphite exfoliation - An investigation of the important role of solvent cointercalation, J Electrochem Soc 147:4391-4398.

[2]   Aurbach D, Zinigrad E, Cohen Y, Teller H (2002) A short review of failure mechanisms of lithium metal and lithiated graphite anodes in liquid electrolyte solutions, Solid State Ionics 148:405-416.

[3]   Cheng YT, Verbrugge MW (2010) Application of Hasselman's Crack Propagation Model to Insertion Electrodes, Electrochem Solid St 13:A128-A131.

[4]   Bhattacharya S, Riahi AR, Alpas AT (2011) A transmission electron microscopy study of crack formation and propagation in electrochemically cycled graphite electrode in lithium-ion cells, J Power Sources 196:8719-8727.

[5]   Woodford WH, Chiang YM, Carter WC (2010) "Electrochemical Shock" of Intercalation Electrodes: A Fracture Mechanics Analysis, J Electrochem Soc 157:A1052-A1059.

[6]   Harris SJ, Deshpande RD, Qi Y, Dutta I, Cheng YT (2010) Mesopores inside electrode particles can change the Li-ion transport mechanism and diffusion-induced stress, J Mater Res 25:1433-1440.

[7]   Bhattacharya S, Riahi AR, Alpas AT (2011) In-situ observations of lithiation/de-lithiation induced graphite damage during electrochemical cycling, Scripta Mater 64:165-168.

[8]   Aurbach D, Koltypin M, Teller H (2002) In situ AFM imaging of surface phenomena on composite graphite electrodes during lithium insertion, Langmuir 18:9000-9009.

[9]   Zhang HL, Li F, Liu C, Tan J, Cheng HM (2005) New insight into the solid electrolyte interphase with use of a focused ion beam, J Phys Chem B 109:22205-22211.

[10] Liu P, Wang J, Hicks-Garner J, Sherman E, Soukiazian S, Verbrugge M, Tataria H, Musser J et al (2010) Aging Mechanisms of LiFePO4 Batteries Deduced by Electrochemical and Structural Analyses, J Electrochem Soc 157:A499-A507.

[11] Bhattacharya S, Alpas AT (2012) Micromechanisms of solid electrolyte interphase formation on electrochemically cycled graphite electrodes in lithium-ion cells, Carbon 50:5359-5371.

[12] Sethuraman VA, Hardwick LJ, Srinivasan V, Kostecki R (2010) Surface structural disordering in graphite upon lithium intercalation/deintercalation, J Power Sources 195:3655-3660.

[13] Kostecki R, McLarnon F (2003) Microprobe study of the effect of Li intercalation on the structure of graphite, J Power Sources 119:550-554.

[14] Markervich E, Salitra G, Levi MD, Aurbach D (2005) Capacity fading of lithiated graphite electrodes studied by a combination of electroanalytical methods, Raman spectroscopy and SEM, J Power Sources 146:146-150.

[15] Qi Y, Harris SJ (2010) In Situ Observation of Strains during Lithiation of a Graphite Electrode, J Electrochem Soc 157:A741-A747.

[16] Bhattacharya S, Riahi AR, Alpas AT (2014) Electrochemical cycling behaviour of lithium carbonate (Li_2CO_3) pre-treated graphite anodes - SEI formation and graphite damage mechanisms, Carbon 77:99-112.

[17] Aurbach D, Markovsky B, Weissman I, Levi E, Ein-Eli Y (1999) On the correlation between surface chemistry and performance of graphite negative electrodes for Li ion batteries, Electrochim Acta 45:67-86.

[18] Suresh S, Zamiski GF, Ritchie RO (1981) Oxide-Induced Crack Closure - an Explanation for near-Threshold Corrosion Fatigue Crack Growth-Behavior, Metall Trans A 12:1435-1443.

[19] Renganathan S, Sikha G, Santhanagopalan S, White RE (2010) Theoretical analysis of stresses in a lithium ion cell, J Electrochem Soc 157(2):A155-A163.

[20] Sethuraman VA, Van Winkle N, Abraham DP, Bower AF, Guduru PR (2012) Real-time stress measurements in lithium-ion battery negative-electrodes, J Power Sources 206:334-342.

[21] Mukhopadhyay A, Tokranov A, Sena K, Xiao X, Sheldon BW (2011) Thin film graphite electrodes with low stress generation during Li-intercalation, Carbon 49:2742-2749.

[22] Mukhopadhyay A, Tokranov A, Xiao X, Sheldon BW (2012) Stress development due to surface processes in graphite electrodes for Li-ion batteries: A first report, Electrochim Acta 66:28-37.

[23] Aurbach D, Koltypin M, Teller H (2002) In situ AFM imaging of surface phenomena on composite graphite electrodes during lithium insertion, Langmuir 18:9000-9009.

[24] Zhao H, Park S-J, Shi F, Fu Y, Battaglia V, Ross PN, Liu G (2014) Propylene carbonate (PC)-based electrolytes with high coulombic efficiency for lithium-ion batteries, J Electrochem Soc 161 (1):A194-A200.

[25] Zhang H-L, Sun C-H, Li F, Liu C, Tan J, Cheng H-M (2007) New insight into the interaction between propylene carbonate-based electrolytes and graphite anode material for lithium ion batteries, J Phys Chem C 111:4740-4748.

[26] Sheldon BW, Tokranov A (2016) Internal stress due to solvent co-intercalation in graphite electrodes for Li ion batteries, Extreme Mech Lett 9:379-385.

[27] ASTM-C1421: Standard Test Methods for Determination of Fracture Toughness of Advanced Ceramics at Ambient Temperature (2016). ASTM International.

[28] Soltesz U, Richter H (1984) Mechanical behavior of selected ceramics. In Metals and Ceramics Biomaterials, Vol. 2, Strength and Surface, P. Ducheyne and G. W. Hastings (Eds.), CRC Press, Boca Raton, pp.23-61.

[29] Hodkinson PH, Nadeau JS (1975) Slow Crack Growth in Graphite, J Mater Sci 10:846-856.

[30] Ritchie RO, Dauskardt RH, Yu WK, Brendzel AM (1990) Cyclic Fatigue-Crack Propagation, Stress-Corrosion, and Fracture-Toughness Behavior in Pyrolytic Carbon-Coated Graphite for Prosthetic Heart-Valve Applications, Journal of biomedical materials research 24:189-206.

[31] Reich S, Jantoljak H, Thomsen C (2000) Shear strain in carbon nanotubes under hydrostatic pressure, Phys Rev B 61:13389-13392.

[32] Thomsen C, Reich S, Ordejon P (2002) Ab initio determination of the phonon deformation potentials of graphene, Phys Rev B 65:073403.

[33] Hanfland M, Beister H, Syassen K (1989) Graphite under Pressure - Equation of State and 1st-Order Raman Modes, Phys Rev B 39:12598-12603.

[34] Panitz JC, Joho F, Novak P (1999) In situ characterization of a graphite electrode in a secondary lithium-ion battery using Raman microscopy, Appl Spectrosc 53:1188-1199.

[35] Broek D (1973) Artificial slow crack growth under constant stress. The r-curve concept in plane stress, In: Engineering Fracture Mechanics, Vol. 5, pp. 45-53.

[36] Fazluddin S (2002) Crack growth resistance in nuclear graphite. PhD Dissertation, University of Leeds.

[37] Hodgkins A, Marrow TJ, Mummery P, Marsden B, Fok A (2006) X-ray tomography observation of crack propagation in nuclear graphite, Mater Sci Tech Ser 22:1045-1051.

[38] Ouagne P, Neighbour GB, McEnaney B (2002) Crack growth resistance in nuclear graphites, J Phys D Appl Phys 35:927-934.

[39] Chi SH (2016) Comparison of fracture toughness (K_{Ic}) and strain energy release rate (G) of selected nuclear graphites, J Nucl Mater 476:188-197.

[40] Kim NH, Kuila T, Kim KM, Nahm SH, Lee JH (2012) Material selection windows for hybrid carbons/poly(phenylene sulfide) composite for bipolar plates of fuel cell, Polym Test 31:537-545.

[41] Harris SJ, Lu P (2013) Effects of inhomogeneities-nanoscale to mesoscale-on the durability of Li-ion batteries, J Phys Chem C 117 (13):6481-6492.

[42] Bhattacharya S, Shafiei M, Alpas AT (2015) Microstructural characterization of nanocrystalline Sn-coated carbon fibre electrodes cycled in Li-ion cells, Metall Mater Trans E 2:208-219.

[43] Mayes IC, Baker TJ (1981) Load transference across crack faces during fatigue crack-growth at positive values of R in low growth-rate regime, Met Sci 15:320-322.

[44] Walker N, Beevers CJ (1979) Fatigue crack closure mechanism in titanium, Fatigue Eng Mater 1:1460-2695.

CHAPTER 8

GENERAL SUMMARY AND CONCLUSIONS

8.1   General Discussion and Summary

The current study has contributed to the ongoing efforts to reduce the energy consumption of automobiles by decreasing the friction losses in energy, employing lightweight materials and new coatings, and utilizing hybrid engines assisted by lithium batteries. New methods were developed to study the fracture behaviour and tribological properties of thermal spray coatings by using an in-situ microscope and observing a four-point bending set-up. Recommendations for optimized microstructural design have been given for ferrous thermal spray coatings deposited on cylinder bores based on the experiments. The tribological behaviours of PVD coatings, such as B_4C and Ti-MoS_2 coatings, were examined under different environments and temperatures. The mechanisms that control the friction and wear behaviour were studied, including material transfer, graphitization, passivation, oxidation, and adhesion. Moreover, suitable environmental conditions that provide low COF and wear rate were determined for these coatings. Hence the possible application of these coatings for demanding operating conditions has been demonstrated. As the the in-situ fracture behaviour set-up was already developed to study thermal spray coating, this approach was also used to study the intercalation damage to graphite electrodes. The crack propagation rates were measured while the graphite was under lithiation/de-lithiation cycles for the first time. The lower sensitivity of crack growth rate to the stress intensity factor was observed, which was attributed to the roughness of the crack surface and deposition of solid electrolyte products. The direct measurement of crack growth rate for lithium battery electrodes can help estimate the time-dependent capacity fading and predict the life cycle of the electrode material. These results will assist new battery material design and development.

The main results of the dissertation can be summarized as follows.

Ferrous thermal spray cylinder bore coatings were investigated. Bending tests were conducted on thermal-spray cylinder-bore steel coatings with an in-situ observation set-up to study the fracture behaviour and effects of the microstructure on the fracture toughness of thermal spray coatings. The crack initiation, propagation, and failure resulting from the coalescence of the cracks were captured. Based on these observations, it was concluded that cracks propagated along oxide layers. The distribution features of oxide layers namely length, orientation angles, and distances between each other were concluded to have been controlling factors with respect to the fracture behaviours of the thermal spray coating. With fracture mechanics analysis, the coating microstructure optimization methods were proposed.

In Chapter 2, four-point bending tests equipped with in-situ crack observation were performed on the thermal spray coatings investigated to understand two key issues: the coating's fracture behaviour, and how the cracks initiate, propagate, and lead to the failure of the coating. A fracture mechanics analysis was applied to understand the influence of the oxide layer distribution on the fracture. K_I values were measured to be in the range of 3.28 to 3.75 MPa·m$^{1/2}$ with the presence of interlocks, influenced by the distribution factors of oxide layers, specifically the angle, length, and distance between layers. Without interlocks, the K_I was decreased to 1.89 MPa·m$^{1/2}$. At the same time, it was found that oxide layers could also stop crack growth if they are distributed perpendicular to each other, which increased the K_I to 6.12 MPa·m$^{1/2}$. Crack coalescence and delamination lead to the fracture of the thermal spray coating. It was observed that the cracks propagated along the oxide veins under the influence of Mode I type stress intensity factor. A fracture mechanics analysis of coating fracture was presented, leading to three recommendations regarding the microstructural design of the coatings: decreasing the oxide layer angle, decreasing the length of oxide layers, or increasing the distance between oxide layers.

Nano- and micro-indentation tests were performed to examine subsurface cracks and measure the hardness, fracture toughness, and elastic modulus. This process determined two types

of fracture mechanisms induced by the indentations: the fracture of brittle FeO aggregates, which occurred at the lowest indentation load, and the separation of the FeO stringers from matrix, which lead to chipping fracture. It was considered that chipping type of fracture was more dangerous since it could lead to the delamination of thermal spray coating splats.

The indentation fracture toughness of the ferrous Fe/FeO coatings can be compared with other thermal spray coatings. Figure 8.1 is a fracture toughness-hardness map comparing ferrous thermal spray coatings with other ceramic thermal spray coatings [1-6]. Although ceramic coatings such as TiO2 and Al2O3 had higher hardness, ferrous thermal spray coatings exhibited the second highest fracture toughness values among all coatings. The high fracture toughness among thermal spray coatings suggests that when used as cylinder bore coating, these coatings have high reliability.
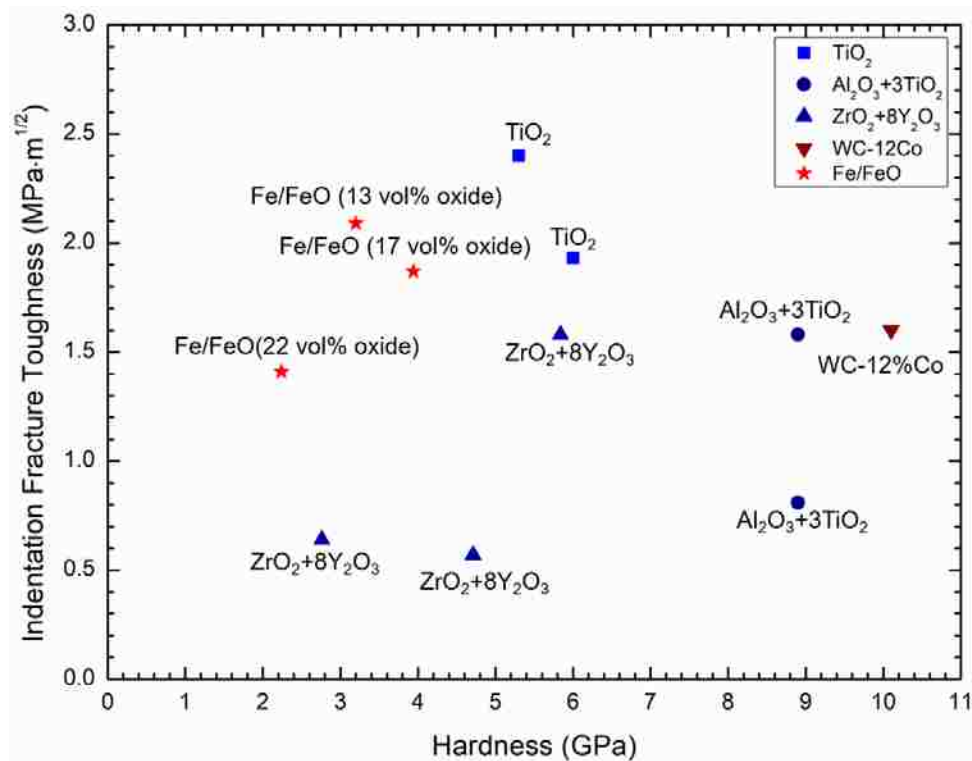

Figure 8.1 Fracture toughness-hardness map for the ferrous thermal spray coatings compared to thermal spray ceramic coatings [1-6].

However, the reliability of the coatings could better be evaluated using a Weibull analysis. **Figure 8.2** shows the Weibull plots for the hardness and fracture toughness values of ferrous thermal spray coatings with different oxide content. The coating with 22 vol% oxide had a Weibull modulus value of 10.44 for hardness data, which was the highest. In contrast, the coating with 17 vol% oxide had Weibull modulus value of 3.65, which was the lowest. It can be observed from **Figure 8.2**(a) that the high hardness values for 17% coating are far removed from the Weibull distribution curve. The low Weibull modulus could be attributed to low load indentations in oxide aggregates; thus, the hardness values presented the hardness of the FeO oxide's hardness rather than that of the Fe/FeO composite coating. For fracture toughness, the coating with 22 vol% had a Weibull modulus value of 3.41, which was the highest in this context, though it has the lowest average fracture toughness (1.41 MPa·m$^{1/2}$). This is because the fracture toughness values were determined by measuring the crack length induced by indentations. The higher oxide content implies that the higher probability indenter will activate the separation of oxide layers, resulting in longer cracks. However, the high oxide content makes the hardness and fracture toughness values of the coating more consistent, even though these two properties are the lowest in three kinds of coatings. It is necessary for automotive and other industries where advanced coatings with multiphase, multilayered structures to determine not only the hardest and toughest component, but also the one that will have the lowest failure probability. These type of probability analyses should be further developed and applied to coatings with complex microstructures, such as the thermal spray coatings.

Chapter 3 used micro-indentations to measure the hardness and fracture toughness of thermal spray steel coating. It was found that the cracks initiate and propagate along the oxide layers in the coating. Micro-indentations caused the fracturing of particles within the FeO aggregates at loads as low as 10 gf. It likewise caused separation of the FeO stringers within the indentation plastic zone: this led to chipping-type fracture in the coating. The dry sliding against CrN coatings

generated iron oxide tribolayers, and the tribolayer that formed on the wear track of the coating was rich in Fe_3O_4 with a hardness of 0.36 ± 0.1 GPa and an elastic modulus of 38.4 ± 5.3 GPa. With the presence of the oxide tribolayer, the resistance to oxide stringer separation was improved: the low carbon coating's Weibull modulus, m, increased from 0.84 to 1.51 due to presence of the tribolayer. The tribolayer acted as an energy-absorbing entity and reduced the driving force required for FeO stringer separation in the low carbon coating. Hence, chipping fracture in presence of the tribolayer occurred only at higher loads.
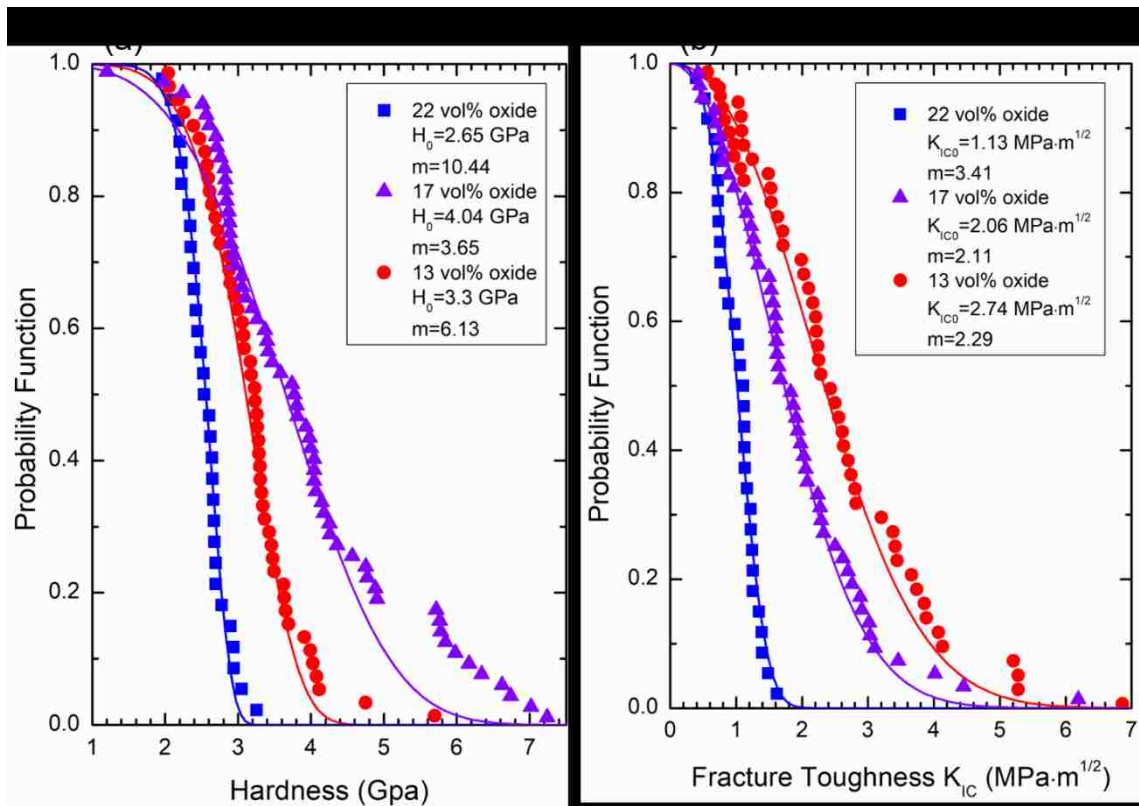
Figure 8.2 Weibull plots for (a) microhardness and (b) fracture toughness of ferrous thermal spray coatings measured by Vickers indentations.

Another important aspect of the analyses was the consideration of tribolayers that were formed during sliding. For this reason, a dry wear test was performed on ferrous thermal spray coating sliding against the CrN ring. A 770-nm-thick sliding-induced tribolayer was formed on the coating, and it was rich in F_3O_4 confirmed by Raman spectroscopy. The chipping-fracture

probability was reduced by the presence of the tribolayer. **Figure 8.3**(a) shows the change in the survival probability of coating failure by chipping ($P_S(L)$) as a function of indentation load L. It was observed that $P_S(L)$ decreased with L. For all values of L, the calculated $P_S(L)$ measured from indentations performed inside the Fe_3O_4-rich tribolayer covered-wear track were higher than those measured for the low-carbon coating outside the wear track.
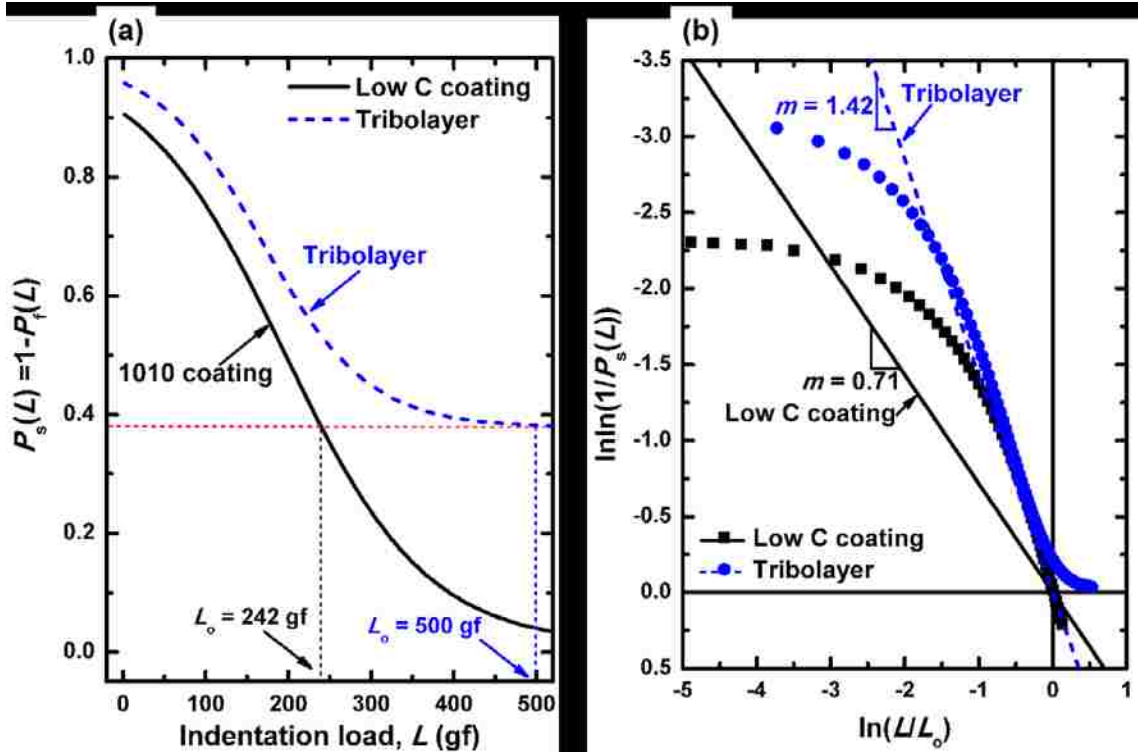

Figure 8.3 (a): Survival probability from chipping fracture due to separation of oxide stringer in the thermal spray coating and the tribolayer generated on the wear track plotted as a function of the indentation load (L); (b) Logarithmic scale plots of Weibull distribution functions and Weibull modulus values.

Subsequently, the values of $P_S(L)$ were fitted with a Weibull distribution. In presence of the tribolayer on the wear track, the Weibull parameter, L_o (for $P_S(L) = 37\%$) was calculated as 500 gf, whereas, for the thermal spray coating, $L_o = 242$ gf. The logarithmic scale plots of the Weibull distribution function are presented in **Figure 8.3**(b). The slope of the fitted linear function provided the Weibull modulus, m, which depicts the variability of the critical indentation load. A higher

value for m, 1.42, for the Fe_3O_4-rich tribolayer implied less variability in stringer separation-induced chipping compared to that for the low carbon coating ($m = 0.71$). The tribolayer could have acted as an energy absorbing entity and reduced the probability of chipping investigated in this indentation-load range. Thus, a critical implication of these analyses is that, during sliding contact, the interface tribological reactions can lead to improved surfaces. Moreover, the mechanical properties of these surfaces could also be improved during sliding. This is critical with respect to designing sliding components in energy saving devices and in automotive applications.

PVD and CVD thin coatings like Ti-MoS_2 and B_4C coatings are widely used for manufacturing lightweight alloys. Wear tests of these coatings against Al-Si and Ti alloys were conducted under different environments and temperature to investigate the effect of environmental factors on the wear behaviour of MoS_2 coatings. The relationship between RH and COF was examined for DLC, B_4C, and Ti-MoS_2 PVD coatings, and wear maps considering moisture and temperature were also constructed. The wear and friction behaviour of these coatings were revealed by these maps. This study will help to understand the failure mechanisms of tribology materials under selected environments and provide design suggestions for improving the performance of these materials.

Figure 8.4 shows the effect of relative humidity (RH) on the COF of different coatings [7, 8]. As the figure shows, for DLC coatings, the COF decreases as a function of relative humidity, whereas, for MoS_2 coatings, COF increases with the increase of the humidity. This is because the H_2O molecules present in DLC coatings help to passivate the tribolayers, which in turn reduces the friction [8, 9]. However, for MoS_2 coatings, the dangling bonds in the edge planes react with the H_2O and oxygen in the surrounding environment to form MoO_3, which increase both COF and wear rate [10, 11].
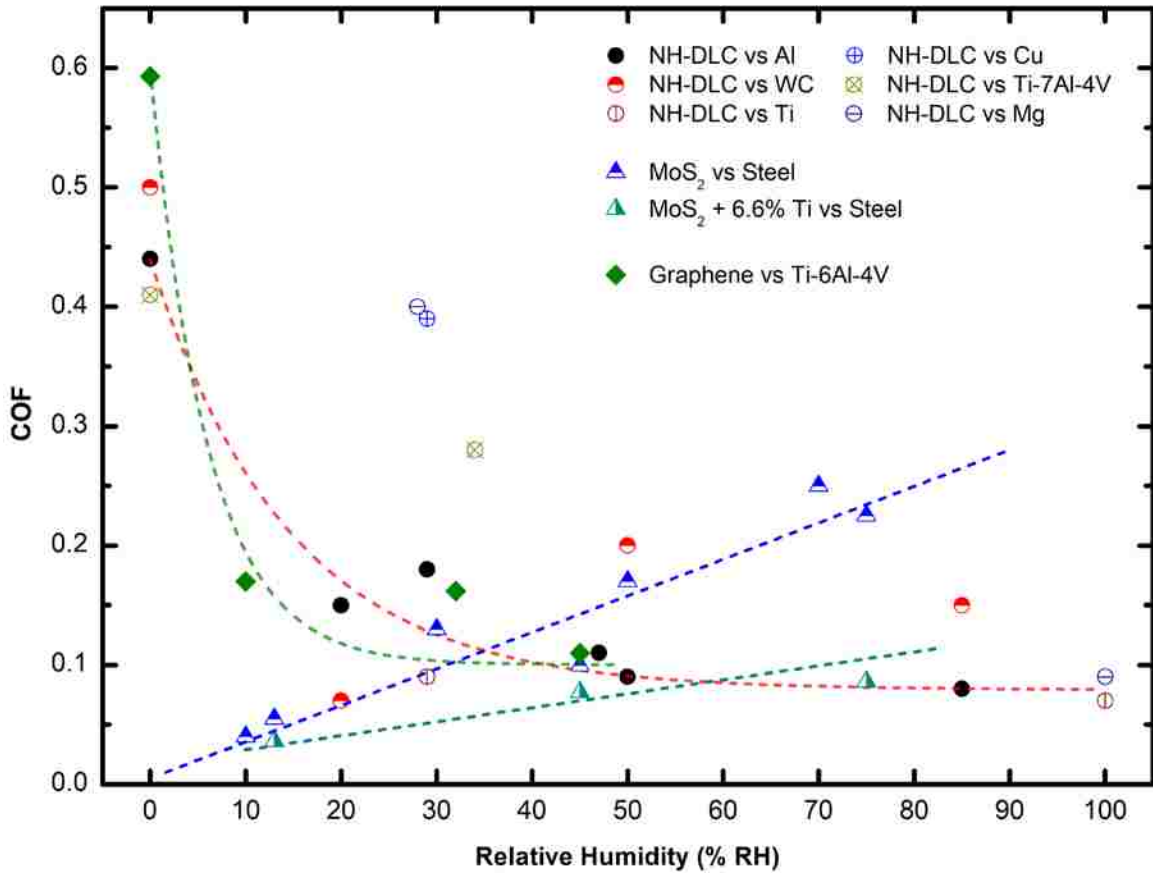
Figure 8.4 COF change for DLC and MoS$_2$ coatings as a function of relative humidity [7-11].

Figure 8.5 shows the wear behaviour of DLC, B$_4$C, and Ti-MoS$_2$ coatings tested against lightweight alloys (Al, Mg and Ti) under different RH levels [7, 8, 12, 13]. Non-hydrogenated, F-doped DLC and B$_4$C coatings had the lowest COF and wear rate in the highest humidity level. This is because the water molecules accelerated formation of transferlayer, which led to the surface graphitization and passivation by H and OH groups. In contrast, when the COF of hydrogenated DLC and Ti-MoS$_2$ coatings increased with the presence of moisture, the humidity damaged the repulsive force between contact surfaces for the DLC coating and oxidized the easy-shear MoS$_2$ layers. Therefore, Ti-MoS$_2$ and H-DLC coatings are ideal candidates for aerospace applications that require low COF in vacuum environments, while B$_4$C and NH-DLC coatings qualify for work conditions with high RH level presence, like water pumps in automotive engines.

Figure 8.5 COF versus wear rate map for DLC, B$_4$C, and Ti-MoS$_2$ coatings tested against selected alloys under different environments [7, 8, 12, 13].

Figure 8.6 shows the wear map of DLC and Ti-MoS$_2$ coatings tested against lightweight alloys at temperatures from 25 to 500 °C [14-17]. As concluded in chapter 5, transferlayer, oxidation and counter material adhesion controlled the wear mechanisms in different temperature regions. Ti-MoS$_2$ maintained the lowest COF at 400 °C in dry N$_2$ environment, indicating its promising high temperature vacuum/aerospace applications. Meanwhile, the high COF and wear rate points in this figure suggested dangerous temperature ranges for these coatings.

Figure 8.6 COF versus wear rate map for DLC and Ti-MoS₂ coatings tested against lightweight alloys at different temperatures [14-17].

Chapter 5 and 6 investigated the tribological behaviour of Ti-MoS₂ coatings, which have a layered structure similar to graphite. Van der Waals forces occur between covalent bonded S-Mo-S sandwiched layers. The low friction of MoS_2 is attributed to the easy-shear basal plane and the formation of transfer layer on the counter surface. However, MoS_2 could be easily oxidized and the friction will increase. This is a controversial phenomenon for hydrogenated DLC coatings since H-DLC will be passivated by water molecules and the friction will be decreased in humid environments. In order to benefit from low COF of Ti-MoS₂ coatings, the working conditions should be monitored and controlled in the application of sliding components and lightweight material machining.

Chapter 5 focused on how temperature and environments affect dry wear test results. It was found that Ti–MoS$_2$ tested in a dry N$_2$ showed a COF value of 0.074 against Al–Si (319 Al), which was lower than tests conducted in ambient air (0.136), dry O$_2$ (0.145) and dry air (0.115). The low COF in N$_2$ was attributed to the MoS$_2$ transfer layer formation on the counterfaces and absence of oxidation. Higher COF values observed in ambient air, dry O$_2$ and dry N$_2$ were attributed to the formation of MoO$_3$ on sliding surfaces. Ti–MoS$_2$ showed low wear rate and low COF throughout the temperature range from 25 to 400 °C under a N$_2$ atmosphere. Dry N$_2$ prevented the oxidation of Ti–MoS$_2$ coatings in the entire temperature range. Accordingly, Ti–MoS$_2$ is a strong candidate for sliding applications at elevated temperatures up to 400 °C that preclude oxidizing atmospheres, such as in space tribology.

Chapter 6 continued the wear test work for Ti-MoS$_2$ coatings and focused on the boundary lubrication wear behaviour in 5W30 engine oil at 25 and 100 °C. Tests conducted at 100 °C have lower COF values because of the formation of ORLs for both steel and Ti-MoS$_2$ coatings. It was found that Ti-MoS$_2$ coatings at room temperature had COF values of 0.08 against Al-Si (319Al) compared to steel (0.13). The reduced COF is attributed to the transferred Ti-MoS$_2$ layers on the counter surfaces at 25 °C. For both Ti-MoS$_2$ and steel, COF values at 100 °C (0.06 for Ti-MoS$_2$ and 0.10 for steel) are lower than those at room temperature because of the decomposition of MoDTC formed MoS$_2$ tribolayers. Thus, findings suggest that the use of Ti-MoS$_2$ coatings could reduce friction and wear for sliding lubricated applications from room temperature to 100 °C.

Carbon based materials are both excellent tribological materials and energy materials for electrodes in lithium batteries. Chapter 7 investigated the fracture behaviour of graphite anodes in lithium battery using the in-situ bending set-up. When the lithium battery is under charging/discharging cycles, lithiation/de-lithiation process will induce cyclic strains in the graphite. In-situ Raman spectroscopy was used to measure the cyclic strain that provided the driving force for crack growth in graphite. In the first cycle, lithiation/de-lithiation cycles in PC-

based electrolytes induced a large cyclical strain of 0.95% in the graphite, which caused rapid crack growth. Crack-growth rates (da/dt) were measured by means of in-situ optical microscopy and were related to ΔK as $da/dt = A\Delta K_I^n$. A single-stage rapid crack-growth behaviour in ambient air (n = 186.7) was observed and compared with data in the literature, whereas a two-stage crack-growth behaviour was found in PC-based electrolyte solutions (n = 51.3 in stage 1 and n = 9.9 in stage 2). The decreased n value in the second stage is due to the premature closing of cracks in the second stage, which was caused by a rough crack face morphology and generation of thick, solid electrolyte reduction products on the crack flanks: this resulted in a reduction of ΔK to ΔK_{eff}.

Physical and chemical reactions between tribology material and environment have significant influence on the performance of these materials with regard to issues such a COF, wear rate, and life time. The lithiation/de-lithiation process introduces strain changes to graphite and accelerates the crack growth. However, the graphite defoliation combined with chemical reaction with PC electrolyte produces solid electrolyte products on the crack surfaces and slows down the crack-growth rate, thereby prolonging the life time of graphite under a certain stress level. For tribological coatings, reaction with water and oxygen will damage the easy-shear basal plane of Ti-MoS$_2$ coatings, leading to an increased COF. In contrast, B$_4$C coatings need -OH groups to form a tribolayer containing H$_3$BO$_3$ to decrease the COF. The stress is the driving force of crack growth for graphite, which leads to the failure of graphite. However, during wear tests, the stress helps the graphitization of B$_4$C and formation of Ti-MoS$_2$ transfer layer on the counter surface. The stress and environment factors combined determine the wear behaviour of tribological materials.

In conclusion, the in-situ bending test provided direct evidence on crack initiation and propagation mechanisms. Based on these results, an optimized microstructure design method focused on oxide layers in the coating is proposed to improve the fracture resistance of the coating. The indentation technique was used to examine the change of mechanical properties of the thermal spray coating before and after dry wear test. The Fe$_3$O$_4$ containing tribolayer increased the survival

243

probability of the coating from chipping fracture. Wear tests were conducted on Mo- and C-based PVD coatings against lightweight alloys in different environments and temperatures. It was found that as long as the oxidation was prevented, the COF was kept low up to 400 °C for Ti-MoS$_2$ coating. B$_4$C coating was the passivation that controlled the COF, and the more passivating groups, such as OH, there are, the lower the COF was. The in-situ bending tests on graphite electrode in lithium battery found the rough fracture surfaces and solid electrolyte depostion slowing down the crack growth rate, which could inform the selection of electrolyte and electrode materials that can improve battery capacity retention.

8.2   A Summary of Original Contributions of This Work

The current study has established six key conclusions regarding (1) microstructural design methods for thermal sprays coatings, (2) fracture mechanisms on thermals spray coatings, (3) graphitization and passivation of B$_4$C coating, (4) high temperature wear performance of Ti-MoS$_2$ coating, (5), wear behaviour of Ti-MoS$_2$ coating in boundary-lubricated condition, and (6) the crack-growth rate in graphite electrodes.

1. The fracture toughness of the thermal spray coatings with complex microstructure—which were mixed with oxide layers, pores, splats and ferrite matrix—were measured by in-situ four-point bending tests. K_I values were measured to be from 3.28 to 3.75 MPa·m$^{1/2}$ with the presence of interlocks at the coating/substrate interface. Without interlock, the K_I was decreased to 1.89 MPa·m$^{1/2}$. The in-situ bending tests determined that the crack initiation, propagation path, and final coalesce. Oxide layers provided crack initiation sites and propagation paths. However, it was found that perpendicular distributed oxide layers could increase the K_I to 6.12 MPa·m$^{1/2}$, acting as crack propagation inhibitor. Based on these results, it was suggested that three microstructural design methods could increase the fracture resistance of the coatings: decreasing the oxide layer angle, decreasing the length of oxide layers, and increasing the distance between oxide layers.

2. Two fracture mechanisms were found by indentations: local fractures at oxide aggregates, and oxide layer/stringer separation. The oxide stringer separation was considered to be more dangerous. When the indentation brought enough energy to the coating, the chipping fracture occurred due to the oxide separation, and it may cause particles to become detached from the coatings. However, dry-wear sliding induced tribolayer, while reduced the chipping fracture probability. Raman spectroscopy confirmed the tribolayer consisted of Fe_3O_4. The tribolayer had lower hardness and elastic modulus than those of thermal spray coating: it acted as an energy-absorbing entity and reduced the driving force necessary for FeO stringer separation in the low carbon coating. In presence of the oxide tribolayer, the chipping fracture probability was decreased and resistance to oxide stringer separation was improved. This was possible because the Weibull modulus, m, increased from 0.71 in the low carbon coating, to 1.42 in presence of the tribolayer.

3. The graphitization and passivation controlled the wear behaviour of B_4C coating in different environments. Raman, FTIR and XPS analyses found graphitization of B_4C coating was induced by sliding contact to the alloy, and the graphitized layer transferred to the counter surface. The repulsive force between the passivated graphitized layers resulted in low COF. The OH-bonds in the water molecules and organic solution were the major resource for passivation. Therefore, the iso-propyl alcohol containing higher levels of OH-bonds helped B_4C coating maintain the lowest COF.

4. As long as it was not oxidized, the layered-structure orientation was the reason for low COF of $Ti-MoS_2$ coatings. The low COF could be maintained up to 400 °C when the oxidation was prevented, and the room temperature wear tests in different environments showed that the lowest COF was achieved in dry N_2, while the highest was in dry O_2. It was concluded that the oxidation would damage the parallel oriented Ti-MoS2 layers, leading to increased COF. High temperature wear tests in dry N_2 explored the upper limit of the working condition for $Ti-MoS_2$ coating.

5. In boundary-lubricated condition, the easily transferred Ti-MoS$_2$ coating had a low COF at room temperature before the decomposition of MoDTC. The formation of MoS$_2$ tribolayer, through the decomposition of MoDTC in formula engine oil (5W30), is a key mechanism for low COF. However, MoDTC could only decompose at temperatures above 40 °C. Ti-MoS$_2$ coating provided MoS$_2$ transferlayer when worn against Al-Si and steel maintaining a lower COF. Ti-MoS$_2$ coatings are optimal for reduced friction in oil starvation and cold start conditions.

6. The crack-growth rate in graphite electrodes of lithium battery was measured in-situ during bending tests. The lithium ions intercalation induced the cyclic strain and cracks in the graphite electrode during the charging/discharging processes. The cyclic strain was measured with the in-situ Raman spectrometer. The crack growth rates were measured with an in-situ crack length measurement by using a large depth optical microscope. With respect to the crack-growth rate dependency on stress intensity factor K as it is applied to the graphite electrode by static load and cyclic strain from intercalation this measure demonstrated that there are two factors that slow this crack-growth rate: the rough fracture surface morphology of the crack, and the deposition of solid electrolyte reduction.

Conclusion. Exploring the failure mechanisms and wear behaviour of different kinds of coatings for lightweight materials provides insights required to create more effective design methods for thermal spray coatings. Measurements of the crack-growth rate of graphite electrodes in working lithium batteries provided insights into material design and electrolyte selection for high efficiency batteries, which could help develop more energy efficient engines and batteries for automotive applications.

8.3 Bibliography

[1] J. Li, S. Forberg, L. Hermansson, Evaluation of the Mechanical-Properties of Hot Isostatically Pressed Titania and Titania Calcium-Phosphate Composites, Biomaterials, 12 (1991) 438-440.

[2] K.A. Habib, J.J. Saura, C. Ferrer, M.S. Damra, E. Gimenez, L. Cabedo, Comparison of flame sprayed Al2O3/TiO2 coatings: Their microstructure, mechanical properties and tribology behavior, Surf Coat Tech, 201 (2006) 1436-1443.

[3] S.R. Choi, D.M. Zhu, R.A. Miller, Mechanical properties/database of plasma-sprayed ZrO2-8wt% Y2O3 thermal barrier coatings, Int J Appl Ceram Tec, 1 (2004) 330-342.

[4] M.M. Lima, C. Godoy, J.C. Avelar-Batista, P.J. Modenesi, Toughness evaluation of HVOF WC–Co coatings using non-linear regression analysis, Materials Science and Engineering: A, 357 (2003) 337-345.

[5] W.G. Mao, J. Wan, C.Y. Dai, J. Ding, Y. Zhang, Y.C. Zhou, C. Lu, Evaluation of microhardness, fracture toughness and residual stress in a thermal barrier coating system: A modified Vickers indentation technique, Surf Coat Tech, 206 (2012) 4455-4461.

[6] M.M. Lima, C. Godoy, P.J. Modenesi, J.C. Avelar-Batista, A. Davison, A. Matthews, Coating fracture toughness determined by Vickers indentation: an important parameter in cavitation erosion resistance of WC-Co thermally sprayed coatings, Surf Coat Tech, 177 (2004) 489-496.

[7] E. Konca, Y.T. Cheng, A.T. Alpas, Dry sliding behaviour of non-hydrogenated DLC coatings against Al, Cu and Ti in ambient air and argon, Diam Relat Mater, 15 (2006) 939-943.

[8] E. Konca, Y.T. Cheng, A.M. Weiner, J.M. Dasch, A.T. Alpas, Effect of test atmosphere on the tribological behaviour of the non-hydrogenated diamond-like carbon coatings against 319 aluminum alloy and tungsten carbide, Surf Coat Tech, 200 (2005) 1783-1791.

[9] F.G. Sen, Y. Qi, A.T. Alpas, Tribology of fluorinated diamond-like carbon coatings: first principles calculations and sliding experiments, Lubr Sci, 25 (2013) 111-121.

[10] S. Prasad, J. Zabinski, Lubricants - Super slippery solids, Nature, 387 (1997) 761-763.

[11] K. Matsumoto, M. Suzuki, Tribological performance of sputtered MoS_2 films in various environment - influence of oxygen concentration, water vapor and gas species, Proceedings of the 8th European Space Mechanisms and Tribology Symposium, 438 (1998) 43-48.

[12] E. Konca, Y.T. Cheng, A.T. Alpas, Sliding wear of non-hydrogenated diamond-like carbon coatings against magnesium, Surf Coat Tech, 201 (2006) 4352-4356.

[13] S. Bhowmick, F.G. Sen, A. Banerji, A.T. Alpas, Friction and adhesion of fluorine containing hydrophobic hydrogenated diamond-like carbon (F-H-DLC) coating against magnesium alloy AZ91, Surf Coat Tech, 267 (2015) 21-31.

[14] S. Bhowmick, A.T. Alpas, The performance of hydrogenated and non-hydrogenated diamond-like carbon tool coatings during the dry drilling of 319 Al, International Journal of Machine Tools & Manufacture, 48 (2008) 802-814.

[15] A. Abou Gharam, M.J. Lukitsch, M.P. Balogh, A.T. Alpas, High temperature tribological behaviour of carbon based (B4C and DLC) coatings in sliding contact with aluminum, Thin Solid Films, 519 (2010) 1611-1617.

[16] F.G. Sen, X. Meng-Burany, M.J. Lukitsch, Y. Qi, A.T. Alpas, Low friction and environmentally stable diamond-like carbon (DLC) coatings incorporating silicon, oxygen and fluorine sliding against aluminum, Surf Coat Tech, 215 (2013) 340-349.

[17] S. Bhowmick, A. Banerji, M.Z.U. Khan, M.J. Lukitsch, A.T. Alpas, High temperature tribological behavior of tetrahedral amorphous carbon (ta-C) and fluorinated ta-C coatings against aluminum alloys, Surf Coat Tech, 284 (2015) 14-25.

APPENDIX

Chapter 5

SPRINGER NATURE LICENSE
TERMS AND CONDITIONS

Jun 04, 2018

This Agreement between Mr. Guanhong Sun ("You") and Springer Nature ("Springer Nature") consists of your license details and the terms and conditions provided by Springer Nature and Copyright Clearance Center.

License Number	4362141145367
License date	Jun 04, 2018
Licensed Content Publisher	Springer Nature
Licensed Content Publication	Tribology Letters
Licensed Content Title	Effect of Atmosphere and Temperature on the Tribological Behavior of the Ti Containing MoS2 Coatings Against Aluminum
Licensed Content Author	G. Sun, S. Bhowmick, A. T. Alpas
Licensed Content Date	Jan 1, 2017
Licensed Content Volume	65
Licensed Content Issue	4
Type of Use	Thesis/Dissertation
Requestor type	academic/university or research institute
Format	print and electronic
Portion	full article/chapter
Will you be translating?	no
Circulation/distribution	<501
Author of this Springer Nature content	yes
Title	Failure Mechanisms in Tribological Coatings and Energy Materials in Different Environments and Temperatures
Instructor name	Dr. Ahmet T. Alpas
Institution name	University of Windsor
Expected presentation date	Jun 2018
Requestor Location	Mr. Guanhong Sun 401 Sunset Avenue Windsor, ON N9B3P4 Canada Attn: Mr. Guanhong Sun
Billing Type	Invoice
Billing Address	Mr. Guanhong Sun 401 Sunset Avenue. Windsor, ON N9B3P4 Canada Attn: Mr. Guanhong Sun
Total	0.00 USD

Terms and Conditions

Springer Nature Terms and Conditions for RightsLink Permissions

Springer Customer Service Centre GmbH (the Licensor) hereby grants you a non-exclusive, world-wide licence to reproduce the material and for the purpose and requirements specified in the attached copy of your order form, and for no other use, subject to the conditions below:

1. The Licensor warrants that it has, to the best of its knowledge, the rights to license reuse of this material. However, you should ensure that the material you are requesting is original to the Licensor and does not carry the copyright of another entity (as credited in the published version).

   If the credit line on any part of the material you have requested indicates that it was reprinted or adapted with permission from another source, then you should also seek permission from that source to reuse the material.

2. Where **print only** permission has been granted for a fee, separate permission must be obtained for any additional electronic re-use.

3. Permission granted **free of charge** for material in print is also usually granted for any electronic version of that work, provided that the material is incidental to your work as a whole and that the electronic version is essentially equivalent to, or substitutes for, the print version.

4. A licence for 'post on a website' is valid for 12 months from the licence date. This licence does not cover use of full text articles on websites.

5. Where 'reuse in a dissertation/thesis' has been selected the following terms apply: Print rights for up to 100 copies, electronic rights for use only on a personal website or institutional repository as defined by the Sherpa guideline (www.sherpa.ac.uk/romeo/).

6. Permission granted for books and journals is granted for the lifetime of the first edition and does not apply to second and subsequent editions (except where the first edition permission was granted free of charge or for signatories to the STM Permissions Guidelines http://www.stm-assoc.org/copyright-legal-affairs/permissions/permissions-guidelines/), and does not apply for editions in other languages unless additional translation rights have been granted separately in the licence.

7. Rights for additional components such as custom editions and derivatives require additional permission and may be subject to an additional fee. Please apply to Journalpermissions@springernature.com/bookpermissions@springernature.com for these rights.

8. The Licensor's permission must be acknowledged next to the licensed material in print. In electronic form, this acknowledgement must be visible at the same time as the figures/tables/illustrations or abstract, and must be hyperlinked to the journal/book's homepage. Our required acknowledgement format is in the Appendix below.

9. Use of the material for incidental promotional use, minor editing privileges (this does not include cropping, adapting, omitting material or any other changes that affect the meaning, intention or moral rights of the author) and copies for the disabled are permitted under this licence.

10. Minor adaptations of single figures (changes of format, colour and style) do not require the Licensor's approval. However, the adaptation should be credited as shown in Appendix below.

Appendix — Acknowledgements:

For Journal Content:
Reprinted by permission from [the Licensor]: [Journal Publisher (e.g.

Nature/Springer/Palgrave)] [JOURNAL NAME] [REFERENCE CITATION (Article name, Author(s) Name), [COPYRIGHT] (year of publication)

For Advance Online Publication papers:
Reprinted by permission from [the Licensor]: [Journal Publisher (e.g. Nature/Springer/Palgrave)] [JOURNAL NAME] [REFERENCE CITATION (Article name, Author(s) Name), [COPYRIGHT] (year of publication), advance online publication, day month year (doi: 10.1038/sj.[JOURNAL ACRONYM].)

For Adaptations/Translations:
Adapted/Translated by permission from [the Licensor]: [Journal Publisher (e.g. Nature/Springer/Palgrave)] [JOURNAL NAME] [REFERENCE CITATION (Article name, Author(s) Name), [COPYRIGHT] (year of publication)

Note: For any republication from the British Journal of Cancer, the following credit line style applies:

Reprinted/adapted/translated by permission from [the Licensor]: on behalf of Cancer Research UK: : [Journal Publisher (e.g. Nature/Springer/Palgrave)] [JOURNAL NAME] [REFERENCE CITATION (Article name, Author(s) Name), [COPYRIGHT] (year of publication)

For Advance Online Publication papers:
Reprinted by permission from The [the Licensor]: on behalf of Cancer Research UK: [Journal Publisher (e.g. Nature/Springer/Palgrave)] [JOURNAL NAME] [REFERENCE CITATION (Article name, Author(s) Name), [COPYRIGHT] (year of publication), advance online publication, day month year (doi: 10.1038/sj. [JOURNAL ACRONYM])

For Book content:
Reprinted/adapted by permission from [the Licensor]: [Book Publisher (e.g. Palgrave Macmillan, Springer etc) [Book Title] by [Book author(s)] [COPYRIGHT] (year of publication)

Other Conditions:

Version 1.0

Chapter 7

Total   0.00 USD

Terms and Conditions

Springer Nature Terms and Conditions for RightsLink Permissions

Springer Customer Service Centre GmbH (the Licensor) hereby grants you a non-exclusive, world-wide licence to reproduce the material and for the purpose and requirements specified in the attached copy of your order form, and for no other use, subject to the conditions below:

1. The Licensor warrants that it has, to the best of its knowledge, the rights to license reuse of this material. However, you should ensure that the material you are requesting is original to the Licensor and does not carry the copyright of another entity (as credited in the published version).

   If the credit line on any part of the material you have requested indicates that it was reprinted or adapted with permission from another source, then you should also seek permission from that source to reuse the material.

2. Where **print only** permission has been granted for a fee, separate permission must be obtained for any additional electronic re-use.

3. Permission granted **free of charge** for material in print is also usually granted for any electronic version of that work, provided that the material is incidental to your work as a whole and that the electronic version is essentially equivalent to, or substitutes for, the print version.

4. A licence for 'post on a website' is valid for 12 months from the licence date. This licence does not cover use of full text articles on websites.

5. Where 'reuse in a dissertation/thesis' has been selected the following terms apply: Print rights for up to 100 copies, electronic rights for use only on a personal website or institutional repository as defined by the Sherpa guideline (www.sherpa.ac.uk/romeo/).

6. Permission granted for books and journals is granted for the lifetime of the first edition and does not apply to second and subsequent editions (except where the first edition permission was granted free of charge or for signatories to the STM Permissions Guidelines http://www.stm-assoc.org/copyright-legal-affairs/permissions/permissions-guidelines/), and does not apply for editions in other languages unless additional translation rights have been granted separately in the licence.

7. Rights for additional components such as custom editions and derivatives require additional permission and may be subject to an additional fee. Please apply to Journalpermissions@springernature.com/bookpermissions@springernature.com for these rights.

8. The Licensor's permission must be acknowledged next to the licensed material in print. In electronic form, this acknowledgement must be visible at the same time as the figures/tables/illustrations or abstract, and must be hyperlinked to the journal/book's homepage. Our required acknowledgement format is in the Appendix below.

9. Use of the material for incidental promotional use, minor editing privileges (this does not include cropping, adapting, omitting material or any other changes that affect the meaning, intention or moral rights of the author) and copies for the disabled are permitted under this licence.

10. Minor adaptations of single figures (changes of format, colour and style) do not require the Licensor's approval. However, the adaptation should be credited as shown in Appendix below.

Appendix — Acknowledgements:

For Journal Content:
Reprinted by permission from [the Licensor]: [Journal Publisher (e.g.
Nature/Springer/Palgrave)] [JOURNAL NAME] [REFERENCE CITATION
(Article name, Author(s) Name), [COPYRIGHT] (year of publication)

For Advance Online Publication papers:
Reprinted by permission from [the Licensor]: [Journal Publisher (e.g.
Nature/Springer/Palgrave)] [JOURNAL NAME] [REFERENCE CITATION
(Article name, Author(s) Name), [COPYRIGHT] (year of publication), advance
online publication, day month year (doi: 10.1038/sj.[JOURNAL ACRONYM].)

For Adaptations/Translations:
Adapted/Translated by permission from [the Licensor]: [Journal Publisher (e.g.
Nature/Springer/Palgrave)] [JOURNAL NAME] [REFERENCE CITATION
(Article name, Author(s) Name), [COPYRIGHT] (year of publication)

**Note: For any republication from the British Journal of Cancer, the following
credit line style applies:**

Reprinted/adapted/translated by permission from [the Licensor]: on behalf of Cancer
Research UK : [Journal Publisher (e.g. Nature/Springer/Palgrave)] [JOURNAL
NAME] [REFERENCE CITATION (Article name, Author(s) Name),
[COPYRIGHT] (year of publication)

For Advance Online Publication papers:
Reprinted by permission from The [the Licensor]: on behalf of Cancer Research UK:
[Journal Publisher (e.g. Nature/Springer/Palgrave)] [JOURNAL NAME]
[REFERENCE CITATION (Article name, Author(s) Name), [COPYRIGHT] (year
of publication), advance online publication, day month year (doi: 10.1038/sj.
[JOURNAL ACRONYM])

For Book content:
Reprinted/adapted by permission from [the Licensor]: [Book Publisher (e.g.
Palgrave Macmillan, Springer etc) [Book Title] by [Book author(s)]
[COPYRIGHT] (year of publication)

Other Conditions:

Version 1.0

Questions? customercare@copyright.com or +1-855-239-3415 (toll free in the US) or
+1-978-646-2777.

254

VITA AUCTORIS

NAME: Guanhong Sun

PLACE OF BIRTH: Harbin, Heilongjiang, China

YEAR OF BIRTH: 1984

EDUCATION: Harbin Institute of Technology, B. E., Harbin,

Heilongjiang, China, 2006

Harbin Institute of Technology, Master, Harbin, Heilongjiang, China, 2008

Harbin Institute of Technology, Ph. D, Harbin, Heilongjiang, China, 2013

University of Windsor, Ph.D, Windsor, Ontario, Canada, 2018